Selection and Reconstruction of ν_μ and $\overline{\nu}_\mu$ CC π^0 Production Interactions on Argon with the Short-Baseline Near Detector

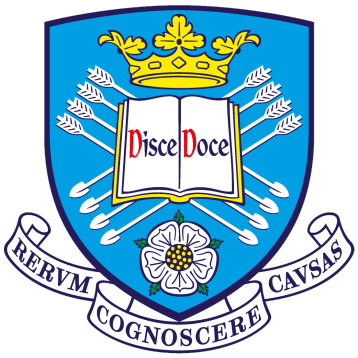

Ala Zglam

Supervisor: Prof. N. J. C. Spooner

Department of Physics and Astronomy
The University of Sheffield

This dissertation is submitted for the degree of
Doctor of Philosophy

February 2024

To my family

Declaration

The content of this thesis represents the original work by the author, unless explicitly cited otherwise. The work presented here has not been submitted for any other academic degree or qualification, whether at this university or any other institution. Given the collaborative nature of modern particle physics experiments, this research builds upon the contributions of fellow researchers and collaborators associated with SBND, as detailed in the following sections.

In Chapter 2 and 3, the discussion on neutrino physics and LArTPC that the author did not contribute, and credit for the content and figures presented in these chapters is attributed to the referenced sources. The outline of SBND presented in Chapter 4 is built upon the collective efforts of the entire SBND collaboration, with a significant reference to the SBND proposal [1]. Any plots that were not created by the author are clearly attributed to their original sources.

The data-driven noise model discussed in Chapter 5 was primarily created in MicroBooNE and repurposed by A. Scarff for SBND use before the author involvement. However, the author conducted all the assessments of the low-level reconstruction performance and the tuning of the hit finding threshold. Similarly, the author evaluated the Pandora pattern recognition package, assessed neutrino identification, and reconstructed performance, including the identification of common failure modes, as part of their work with the reconstruction group, guided by D. Brailsford. Likewise, all the plots presented in the high-level reconstruction of tracks described in Chapter 6 were originally created by the author as part of the assessment model for track reconstruction written for the ciSystem. Also, the evaluation of shower reconstruction, including the event display and photon shower cheater, was conducted by the author with guidance from D. Brailsford and E. Tyley, which led to an improvement in shower reconstruction through the tuning of reconstruction tools.

The selection approach discussed in Chapter 7 makes use of the Common Analysis Framework (CAF) established within the SBN project. This framework originated from the initial development within the NuMI Off-axis ν_e Appearance experiment (NOνA) and later in the Deep Underground Neutrino Experiment (DUNE). This framework was created through collaborative efforts of numerous individuals, including the author, C. Backhouse, D. Mendez,

B. Howard, F. Psihas, and G. Putnam. In addition, the SBND production team created the simulated samples used to evaluate the performance of the selection process and to extract cross-section. The selection process is built upon common components used in various analyses within the SBN program. Specifically, the techniques for cosmic ray rejection were primarily developed by T. Brooks, while flash matching techniques were introduced by M. Stancari and I. de Icaza, and the Razzle and Dazzle MVA-trained algorithms were developed by E. Tyley. On the other hand, the author carefully selected and optimised all the selection criteria approaches and cuts to achieve the highest performance in identifying the desired signal. Finally, the measurement of cross-section conducted in Chapter 8 was entirely implemented by the author, building upon the information provided by E. Tyley.

Chapters 9 and 10 represent original contributions entirely derived from my own research, conducted under the guidance and support of A. Ezeribe, while also building upon the foundational work previously conducted by D. Barker and E. Tyley.

Ala Zglam
February 2024

Acknowledgements

First, I would like to give special thanks to my supervisor, Prof. Neil Spooner, for all his support and guidance throughout my entire PhD, especially during the Covid-19 pandemic. His regular attention has kept me focused, and I cannot thank him enough for the opportunity and support, even before I came to the UK to officially start my PhD.

My experience with SBND has been entirely positive, and there are numerous individuals to whom I am deeply grateful. The support I have received from the conveners of SBND working groups, with whom I have been working, has been instrumental in completing this thesis. I would like to extend my special thanks to Dom Brailsford, Vishvas Pandey, Andrew Furmanski, and Ornella Palamara for their invaluable support and guidance at various steps of my PhD.

I would like to extend my heartfelt gratitude to the individuals at the University of Sheffield for their unwavering support and guidance throughout my entire PhD journey, with special thanks to Dom Barker, Ed Tyley, Anthony Ezeribe, Andrew Scarff, Rhiannon Jones, Lan Nguyen, and Harry Scott. I greatly appreciate your assistance and support, which have contributed to my positive experience during my PhD and made me feel truly welcomed in Sheffield.

I would also like to express a dedicated thank you to the people who assisted with the Sheffield liquid argon test stand. I am grateful for all the work that has been done before me, especially by Dom Barker, Ed Tyley, and Andrew Scarff. Thank you for all your hard work. Also, without the support and the knowledge of these people I would have never left the Lab: Matt Wright, Anthony Ezeribe, Dom Barker and Andrew Scarff. Finally, saving the best for last, special thanks to Anthony Ezeribe. Without his unwavering support, guidance, and hard work, the two tests with liquid argon would have been impossible. I deeply appreciate your invaluable assistance.

Lastly, I am immensely grateful to my family for their unconditional support, especially my wonderful parents. They have been by my side from the beginning of this PhD journey and continue to stand by me, and I can not express my gratitude enough. I hope that my accomplishments have filled you with pride, knowing that your unwavering support and guidance have played an integral role in my journey.

Abstract

As the field of neutrino physics moves into the precision era, where all parameters related to neutrino oscillations have been determined, it has become imperative to further enhance our understanding of neutrino-nucleus interactions to support the upcoming generation of oscillation experiments. Improvements in both theoretical modelling and experimental measurements of these interactions are required for progress in this regard. The Short-Baseline Near Detector (SBND) represents a significant step in this direction. It is a 112-ton Liquid Argon Time Projection Chamber (LArTPC) designed to reduce uncertainties for the search for sterile neutrinos as part of the Short-Baseline Neutrino (SBN) program. Additionally, SBND aims to provide precise interaction measurements within the Booster Neutrino Beam (BNB), which is set to commence in 2024. The ability of SBND to measure the cross section for ν_μ Charged Current (CC) π^0 production interactions is assessed in this thesis. Enhancements to SBND reconstruction process, specifically in relation to photon showers, are introduced, resulting in an improved capability to both identify and measure these interactions. These ν_μ CC π^0 production interactions are selected with an efficiency of 39.44% and a purity of 67.16%, effectively rejecting over 98.45% of neutrino-induced events and 99.997% of cosmogenic background events. A procedure for conducting an exclusive cross section analysis of the ν_μ CC π^0 production interactions is outlined, taking into account both statistical and systematic uncertainties. It is found that the integrated cross-section values, derived from the reconstructed information, exhibit a minor discrepancy of approximately 0.14% when compared to the true calculated value.

Table of contents

List of figures

List of tables

Nomenclature

Acronyms / Abbreviations

ADC Analog-to-Digital Converter

ALEPH Apparatus for LEP Physics

ANL Argonne National Laboratory

APAs Anode Plane Assemblies

ARAPUCA Argon R&D Advanced Program at UniCAmp

arb Arbitrary Unit

ArgoNeuT Argon Neutrino Test-stand

ASIC Application-Specific Integrated Circuit

BDT Boosted Decision Tree

BNB Booster Neutrino Beam

BNL Brookhaven National Laboratory

BSM Beyond Standard Model

BUU Boltzmann-Uehling-Uhlenbeck

BY Bodek-Yang

CC Charged Current

CCQE CC Quasi-Elastic

CF ConFlat

CFG Correlated Fermi Gas

CL Confidence Levels

CPA Cathode Plane Assembly

CRT Cosmic Ray Tagger

CSV Central Spline Variation

CV Central Value

DAQ Data Acquisition

DCA Distance of Closest Approach

dE/dx Energy per Unit Distance

DIS Deep Inelastic Scatterings

DONUT Direct Observation of the NU Tau

DUNE Deep Underground Neutrino Experiment

FC Fully Contained

FFT Fast Fourier Transform

FPGA Field-Programmable Gate Array

FS Feynman Scaling

FSI Final State Interactions

FU Flux Unisim

FV Fiducial Volume

GAr Argon gas

GHF GausHitFinder

HEP High Energy Physics

HV High-Voltage

ICARUS Imaging Cosmic And Rare Underground Signals

ILC International Linear Collider

IMB Irvine Michigan Brookhaven

IO Inverted Ordering

*JSNS*2 J-PARC Spallation Neutron Source

JUNO Jiangmen Under- ground Neutrino Observatory

KamioKande Kamioka Neutrino Detection Experiment

KATRIN Karlsruhe Tritium Neutrino Experiment

KE Kinetic Energy

LAr Liquid Argon

LAr TPC Liquid Argon Time Projection Chamber

LArIAT Liquid Argon In A Testbeam

LArTPC Liquid Argon Time Projection Chambers

LEP Large Electron-Positron Collider

LFG Local Fermi Gas

LGC Langau-Gaussian Convolution

LN_2 Liquid Nitrogen

LSND Liquid Scintillator Neutrino Detector

M_a Axial Mass

MCS Multiple Coulomb Scattering

MEC Meson Exchange Current

MEP Mean Free Path

MINERvA Main Injector Neutrino ExpeRiment to study ν-A interactions

MINOS Main Injector Neutrino Oscillation Search

MIP Minimum Ionising Particle

MVA MultiVariate Analysis

N Normalisation

NC Neutral Current

NCE NC Elastic

NO Normal Ordering

NOvA NuMI Off-axis ν_e Appearance experiment

$np-nh$ n-particle n-hole

NuMI Neutrinos at the Main Injector

PC Partially Contained

PCA Principal Component Analysis

PCB Printed Circuit Board

PDFs Parton Distribution Functions

PDS Photon Detection System

PE Photo-Electron

PFO Particle Flow Object

PID Particle IDentification

PMNS Pontecorvo-Maki-Nakagawa-Sakata

PMT Photo-Multiplier Tube

POT Protons On Target

PPM Parts Per Million

psia Pound per square inch

QE Quantum Efficiency

QES Quasi-Elastic Scattering

RFG Relativistic Fermi Gas

RES Resonant Interactions

ROI Region Of Interest

RPA Random Phase Approximation

SAGE Sovient-American Gallium Experiment

SBN Short-Baseline Neutrino

SBND Short-Baseline Near Detector

SBR Signal-to-Background Ratio

SCE Space Charge Effect

SciBooNE SciBar Booster Neutrino Experiment at Fermilab

SERDES Serializer/Deserializer

SHV Safe High Voltage

SiPMs Silicon Photo-Multipliers

SK Super-Kamiokande

SM Standard Model

SNO Sudbury Neutrino Observatory

SNR Signal-to-Noise Ratio

SRC Short Range Correlations

SS Stainless Steel

SSM Solar Standard Model

SW Sanford-Wang

T2HK Tokai to Hyper-Kamiokande

T2K Tokai to Super-Kamiokande

TPB TetraPhenyl Butadiene

TPC Time Projection Chamber

VPM Volumes per Million

VUV Vacuum Ultra-Violet

WIB Warm Interface Board

Y Collection Plane

U and V Induction Planes

Chapter 1

Introduction

The intriguing characteristics of neutrinos have captivated scientists since their initial proposal and discovery, underscoring the indispensable role of neutrino physics in acquiring profound insights into the fundamental aspects of matter, energy, and the governing forces of the universe. Chapter 2 offers a concise historical account of neutrino physics, with an emphasis on neutrino oscillations and the motivation behind the Short-Baseline Neutrino (SBN) program, which is driven by the challenges in measuring sterile neutrino oscillations. It also provides an overview of neutrino-nucleus interactions, encompassing theoretical models and existing measurements, with specific attention to ν_μ Charged Current (CC) π^0 production interactions pertinent to this thesis.

Chapter 3 presents a historical overview of Liquid Argon Time Projection Chamber (LArTPC) detector technology, highlighting their potential as neutrino detectors, along with an examination of significant experiments. It then delves into the operational principles of these detectors, elucidating the fundamental physical processes driving their performance. Additionally, an overview is given of the ongoing development of novel readout methods, with a specific focus on a noteworthy 3D pixel readout technique, relevant to the work presented in Chapter 9 and Chapter 10.

In Chapter 4, the study turns its attention to the SBN program, consisting of three LArTPCs. The chapter begins by exploring the physics objectives, primarily centred around detecting sterile neutrino-induced oscillations. Following this, the discussion shifts to the Booster Neutrino Beam (BNB), the context in which the Short-Baseline Near Detector (SBND) operates, detailing the design of the beam and the flux through SBND. The goals of SBND are then presented, with a primary focus on the cross section measurements relevant to this thesis, as well as the design of the detector, including a breakdown of its individual subsystems. Lastly, it introduces the simulation and the reconstruction of SBND subsystem processes.

The SBND event processing and reconstruction methods are elucidated in Chapter 5, with a focus on enhancements in noise simulation and the hit-finding process. This includes evaluation of the effectiveness of low-level reconstruction through the hit finding threshold tuning. Subsequently, it provides an overview of the Pandora pattern recognition package employed in SBND. Lastly, it delves into an assessment of the performance of track-shower characterisation, identifying the key failure modes within the characterisation process, along with an assessment of neutrino identification and reconstruction performance.

In Chapter 6, the subsequent high-level reconstruction process is discussed, which includes distinct pathways for track and showers. It begins by providing an overview of a reconstruction framework designed for showers, evaluating the performance of various approaches for each feature. Next, an evaluation of how the enhancements in shower reconstruction influence the high-level reconstruction process is presented. Finally, the reconstruction and performance of π^0 diphoton showers are introduced.

A selection process has been developed to identify ν_μ Charged Current (CC) π^0 production interactions while minimising background interference. This is discussed in Chapter 7. This starts with defining the signal criteria and implementing specific cuts to ensure the quality of reconstructed events. The rejection of cosmogenic backgrounds is then explored, utilising various subsystems in SBND. Additionally, the identification and selection of ν_μ CC interactions through the detection of muon tracks are detailed. Lastly, the criteria applied to photon candidate showers to mitigate electron and misidentified tracks contamination, along with analysis of the final outcomes of the selection process, are presented.

Chapter 8 covers evaluation of the potential of SBND for conducting an analysis of the exclusive cross section for ν_μ CC π^0 production interactions. The assessment commences with an outline of the employed cross section extraction method. Subsequently, the chapter explores the systematic uncertainties considered in this analysis, addressing their origins and the approach taken in their treatment. Finally, the analysis of the cross section of selected signal events outcomes is presented, including future developments.

The SBND detector in part aimed to serve as a wire TPC prototype for the Deep Underground Neutrino Experiment (DUNE) far detector, but the high pile-up at the DUNE near detector makes the current wire plane readout unfeasible due to readout ambiguities. New readout methods, including a 3D pixel approach, are under development. A liquid argon rig at the University of Sheffield has been developed to test these new electronics and readouts for future liquid argon experiments. This is discussed in Chapter 9. The test stand consists of four primary systems: the LAr dewar, purification system, condenser system, and detection system. The assessment of these systems has been conducted at the individual, subgroup, and group levels, with a focus on their collective functionality. Specifically, the assessment

included evaluating components within the LAr dewar, conducting leak tests, evaluating external CRTs, testing the pixel-readout equipment and connection up to the pixel board, and successfully performing an argon recirculation test. A summary of the findings and the overall performance of the Sheffield LAr test stand is provided in this chapter.

Expanding upon Chapter 9, Chapter 10 discusses results from an extended three-week operational evaluation of the test stand, with a specific emphasis on the performance of the pixel readout system, observed through charge deposition on the pixel board. The system operation and performance for the three weeks of running using liquid argon are detailed. Next, a three-step processing procedure used for data obtained from the CRT system is discussed. Subsequently, it presents the noise filtering and hit-finding algorithms employed to analyse the pixel readout data, along with the 2D and 3D event displays used to observe charge deposition on the pixel plane using external triggers from the CRT system.

Finally, the thesis ends with Chapter 11, a brief conclusion summarising the main outcomes of the work.

Chapter 2

Fundamentals of Neutrino Physics

The discovery of the electron in 1897 marked the beginning of elementary particle physics, challenging the idea of atoms as the fundamental constituents of matter. Exploring smaller scales and higher energies with accelerators led to the discovery of numerous new particles and the establishment of the Standard Model (SM) of particle physics. Despite these advances, neutrinos remain one of the least understood particles in the SM, driving extensive research and independent experiments to measure their properties, including masses and oscillation parameters. Neutrinos also hold crucial significance beyond the SM, potentially offering solutions to the flavour problem and playing a role in explaining the strong CP problem through hidden symmetries in the quark sector.

The first section, Section 2.1 provides a concise historical overview of the neutrino, including the proposal and discovery of its various flavours along with a description of the main sources of neutrinos. Section 2.2 discusses neutrino oscillations, including experimental anomalies, theoretical formulation, verification, and the current status of this phenomenon. In Section 2.3, the supporting and opposing evidence regarding the existence of sterile neutrinos is examined. In Section 2.4, a summary of neutrino interactions is presented, covering interaction mechanisms, nuclear models, and the current state of measurements in this field. This section emphasises the importance of further studying interaction cross sections, the central focus of this thesis, to enhance our understanding of interactions and nuclear physics, as well as to improve oscillation measurements.

2.1 Historical Overview and Introduction

Neutrinos are electrically neutral, possess an astonishingly tiny mass and traverse vast distances without interacting with matter. Despite their elusive nature, neutrinos play a fundamental role in numerous particle physics and astrophysical phenomena. From their

origins in nuclear reactions to their ability to change flavours, neutrinos continue to intrigue researchers, offering insights into particle physics, astrophysics, and cosmology. The progression of neutrino physics exemplifies how advancements in theoretical understanding and experimental techniques to propel scientific knowledge forward.

2.1.1 Neutrino Proposal and Discovery

Ellis and Wooster demonstrated in 1927 that the energy distribution of electrons resulting from the decay of "Radium E" was observed to be continuous, which contradicted the anticipated sharp peak that would be expected from a two-body decay process, (see Figure 2.1) [4]. During β decay, an atomic nucleus with an atomic number Z undergoes transformation into a nucleus with reduced mass and an increased atomic number, Z+1, accompanied by the emission of an observed electron, described by Equation 2.1:

$$ {}^{A}_{Z}X \rightarrow {}^{A}_{Z+1}X' + e^{-} \tag{2.1} $$

In a hypothetical scenario of a two-body decay, the electron would acquire a constant amount of kinetic energy, equal to the difference in masses between the nuclei involved. However, experimental observations indicated that β decay exhibited continuous distributions of electron energy, as depicted in Figure 2.1, deviating from the expected discrete values.

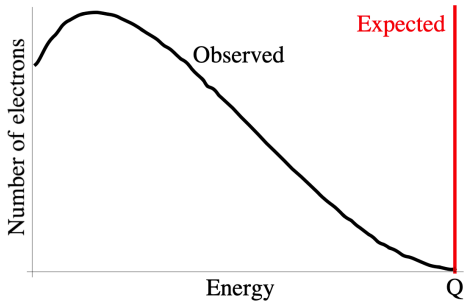

Figure 2.1: The continuous energy spectrum of electrons emitted in β decay (black line) contradicts the expected spectrum (red line) based on the conventional two-body model, necessitating a violation of the conservation of energy. Figure from [5].

Furthermore, the spin characteristics of both the parent and daughter nuclei, which possessed either integer or half-integer spins, were incompatible with the expectation of only an electron emission with a spin of $\frac{1}{2}$. This inconsistency suggested a violation of the conservation laws governing energy and angular momentum at the atomic scale.

Wolfgang Pauli made a revolutionary proposal by suggesting the existence of an extremely lightweight, neutral particle with a spin of $\frac{1}{2}$ that exhibits very weak interactions with matter [6]. This particle is emitted alongside the electron in β decay, effectively accounting

for the continuous energy spectrum and successfully addressing both problems of non-conservation [6]. In 1934, E. Fermi, who formulated the theory of β decay, coined the term "neutrino" for this hypothetical particle. The concept emerged as part of Fermi's explanation of the decay process, in which the recently discovered neutron would transform into a proton, an electron, and a antineutrino [7].

It took 25 years for the existence of the neutrino to be experimentally confirmed, and in 1956, Cowan, Reines, et al. observed the interactions of electron antineutrinos through a process known as inverse β decay [8], described by Equation 2.2.

$$\overline{\nu}_e + p \rightarrow \beta^+ + n \tag{2.2}$$

The experiment took place in the vicinity of the Savannah River nuclear reactor, employing a detector setup comprising two water tanks containing dissolved $CdCl_2$. These tanks were positioned between three tanks filled with liquid scintillator and were readout by photomultipliers [8]. The characteristic indication of this signal manifested as a pair of scintillation pulses: the first pulse represented the β^+ emission, followed by a delayed pulse indicating the neutron capture on dissolved Cadmium within the scintillator. The successful detection of this signal, along with observed correlations between the detection rate and the power of the detector, provided strong evidence for the existence of neutrinos [8]. Additionally, the number of measured neutrinos aligned with the theoretical predictions of the cross section at that time.

Prior to the experimental verification of neutrino existence, the discovery of the muon took place [9]. Subsequently, in 1959, Pontecorvo posed a fundamental question regarding the relationship between neutrinos produced alongside electrons and those produced with muons: Are ν_e and ν_μ equivalent ($\nu_e = \nu_\mu$) or distinct ($\nu_e \neq \nu_\mu$) [10]. The question was resolved through the groundbreaking work of Danby et al. in 1962, by observing ν_μ interactions [11]. In their experiment, a spark chamber was positioned within a neutrino beam created through the in-flight decay of pions. The setup enabled the measurement of muon and electron rates by distinguishing the unique topological signatures of outgoing muons and electrons in the detector, which were produced by ν_μ and ν_e interactions, respectively.

The prediction of a third flavour of neutrino arose following the discovery of the tau lepton in the 1970s [12]. The measurement of the Z-boson decay width at the Large Electron-Positron Collider (LEP) conducted by the Apparatus for LEP Physics (ALEPH) experiment to ascertain the number of neutrino flavours reinforced the prediction [13, 14]. The outcomes were in agreement with the existence of only three flavours of weakly interacting neutrinos, each having a mass less than half of that of the Z-boson; details can be found in [13]. In 2001, the Direct Observation of the NU Tau (DONUT) experiment provided experimental

evidence for the existence of the ν_τ [15]. The DONUT experiment utilised nuclear emulsion targets and identified "Tracks" with kinks, which indicated the presence of τ leptons in a neutrino beam generated from the Tevatron, for details see [15].

2.1.2 Key Neutrino Sources and Properties

Neutrinos are recognised as one of the most abundant particles in the universe. It is estimated that every cubic centimetre of the universe contains over 300 relic neutrinos that originated shortly after the Big-Bang. Additionally, neutrinos originate from a range of sources, including both natural and artificial origins. Figure 2.2 depicts a diverse range of neutrino sources based on the corresponding characteristic energy of neutrinos emitted in each specific environment. Natural sources offer the advantage of producing neutrinos in significant quantities, allowing for a better understanding of the underlying physics processes, which can be quite intricate in certain cases. In contrast, artificial sources generate fewer neutrinos, but their properties, such as energy, direction, flavour, and travel distance, are well understood. As a result, systematic effects associated with artificial neutrino sources are more effectively controlled compared to those arising from natural sources.

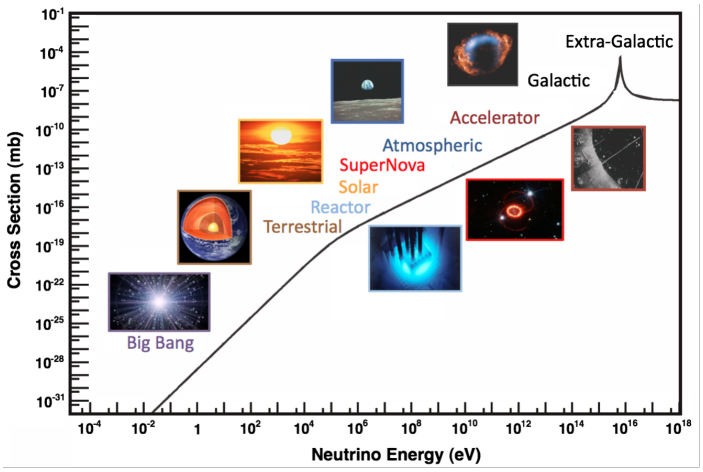

Figure 2.2: The relative cross section of different neutrino sources as a function of their energy. Figure from [16].

The Sun is the most dominant and close-by source of neutrinos, primarily generated through proton-proton fusion. However, there are more potent sources of neutrinos, such as supernovae [17, 18]. On Earth, neutrinos are created through geothermal reactions within the core of the Earth, and there is a substantial flux of atmospheric neutrinos resulting from cosmic particles interacting in the upper atmosphere. Additionally, radioactive materials emit neutrinos as they decay through weak interactions.

Artificial neutrino sources, such as nuclear reactors, though possessing a lower magnitude than the Sun, offer the advantage of allowing neutrino experiments to operate in close proximity. This proximity can result in a potentially higher local neutrino flux. Notably, advanced artificial neutrino sources are generated at accelerator complexes like Fermilab, CERN, and J-PARC. These artificial neutrino beams offer a high-intensity neutrino source across a wide energy range, along with various additional advantages, as discussed in section 4.2.

2.2 Neutrino Oscillations and Masses

In 1939, Bethe formulated the theory of solar fusion, which predicted the production of neutrinos by the Sun [19]. However, it was anticipated that only electron neutrinos would be involved in beta decay and the inverse process. The observation of solar neutrinos by Davis et al. in 1968 revealed a capture rate significantly lower than expected, only one-third of the predicted number, leading to the solar neutrino problem [20]. Before this discovery, Pontecorvo, Maki, Nakagawa, and Sakata had proposed neutrino oscillation as a mechanism, suggesting that neutrinos are superpositions of mass eigenstates, which can explain this deficit but require massive neutrinos [21–23]. However, the Standard Model (SM) required massless neutrinos, like the Fermi theory, causing initial hesitation to adopt the theory of neutrino oscillations [23, 24]. Anomalous results in atmospheric neutrino data from various experiments [25, 26] further supported the idea of massive oscillating neutrinos, which was subsequently confirmed by the Super-Kamiokande experiment [27]. The discovery of massive neutrinos also prompted a shift in understanding, where it became evident that neutrinos have exclusively left-handed chirality rather than the previously believed helicity [28].

Covered firstly in this section is a summary of the experimental deviations that suggested the presence of neutrino oscillations. Following that, the theoretical concept and mathematical framework of neutrino oscillations will be introduced and a discussion of the experimental confirmation of neutrino oscillations. Lastly, a highlight of ongoing and upcoming neutrino oscillation experiments is presented, along with the most recent global best-fit parameter values for these oscillations.

2.2.1 Neutrino Experimental Anomalies

Following the successful detection of neutrinos emitted by nuclear reactors and neutrino beams, endeavours were undertaken to detect the neutrinos generated through nuclear fusion within the Sun, as mentioned above [20]. In the late 1960s, Davis et al. established

an experiment aimed at measuring solar neutrinos within the Homestake Mine in South Dakota [20]. The experiment was located 4400 m below the surface, and its configuration included a tank containing 390,000 litres of liquid tetrachloroethylene (C_2Cl_4) to facilitate the neutrino capture reaction $Cl^{37}(\nu,\ e^-)Ar^{37}$, which produces a radioactive isotope, as depicted in Equation 2.3:

$$\nu_e + n(Cl^{37}) \rightarrow e^- \ + \ p(Ar^{37}) \tag{2.3}$$

Afterward, the quantity of argon produced was measured by counting the number of Ar^{37} decays, allowing for the calculation of the neutrino flux. The published results in 1968 came as surprise since the upper limit on the solar ν_e flux was approximately three times lower than the prediction of the Solar Standard Model (SSM), leading to what is known as the solar neutrino anomaly [29].

Several years following the first discovery of the solar neutrino anomaly, further measurements conducted by the Kamioka Neutrino Detection Experiment (Kamiokande) using a water Cherenkov detector, as well as GALLEX and the Sovient-American Gallium Experiment (SAGE), provided additional confirmation [30–35]. Figure 2.3a presents a comparison between the experimentally measured rate and the theoretical predictions using various detector technologies that are sensitive to distinct energy ranges. In this comparison, a noticeable deficit can be observed. Although each experiment detects a distinct deficit of neutrinos, the variability arises due to different minimum detection thresholds and the non-constant nature of the solar neutrino flux across different energy levels, as shown Figure 2.3b. Consequently, it strongly suggests that resolving the Solar Neutrino Problem requires an explanation that incorporates a dependence on neutrino energy, aligning with the concept of neutrino oscillations.

The issue with neutrino flux was not limited to solar observations alone. Another anomaly was detected in neutrinos within Earth's upper atmosphere. Atmospheric neutrinos are generated when cosmic rays, typically composed of protons or helium nuclei, collide with atmospheric nuclei. These collisions give rise to mesons, like pions, which subsequently decay into leptons and neutrinos [37]. The energy distribution of these cosmic rays is known as they constitute anticipated primary backgrounds in both the Irvine Michigan Brookhaven (IMB) and Kamiokande experiments. Upon comparing the rate of atmospheric neutrinos to the backgrounds in these experiments, an additional deficit became apparent, known as the atmospheric neutrino anomaly [38–41].

The presence of anomalies in both solar and atmospheric neutrino observations indicated that the deviations were not solely due to miscalculations of neutrino fluxes but rather pointed towards a novel phenomenon exhibited by neutrinos known as neutrino oscillation.

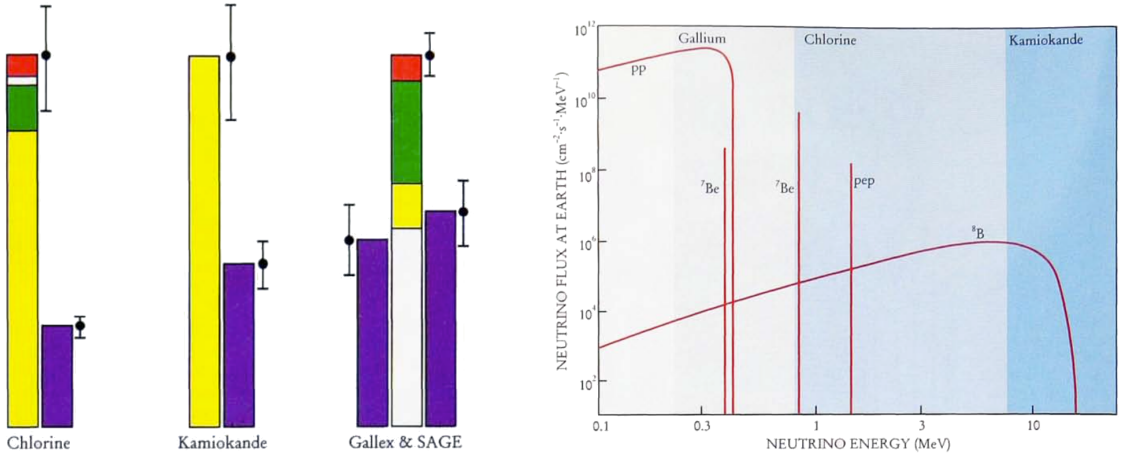

(a) (b)

Figure 2.3: Solar neutrino deficit (a) and flux (b), and the relevant region for the various detectors/materials. (a): The observed solar neutrino fluxes (purple) from the first detectors exhibit significant deficits compared to predictions based on SSM. The predicted total fluxes, normalised to unity, encompass distinct solar processes represented by different colours: white for p-p fusion, green for electron capture by Be^7, yellow for B^8 decay, and red for the stellar carbon-nitrogen-oxygen cycle, which has a minimal impact on solar activity. Figures from [36].

2.2.2 Theoretical Aspects of Neutrino Oscillation

After the introduction of the concept of neutrino oscillation by Pontecorvo, subsequent mathematical formalisation by Maki, Nakagawa, and Sakata resulted in the formulation of the Pontecorvo-Maki-Nakagawa-Sakata (PMNS) matrix [23]. According to this theory, there exist two distinct forms of neutrinos: weak eigenstates, which interact through weak force, and the mass eigenstates that represent the neutrino propagation. The mass eigenstates are characterised by their adherence to the Schrödinger equation [42], as outlined in Equation 2.4:

$$i\hbar(\frac{d}{dt}|\nu\rangle) = \hat{H}|\nu\rangle = E|\nu\rangle \tag{2.4}$$

The observed weak eigenstates in neutrino interactions are derived from a combination of the mass eigenstates, as illustrated in Equation 2.5:

$$|\nu_\alpha\rangle = \sum_i U^*_{\alpha i}|\nu_i\rangle \tag{2.5}$$

The weak eigenstates are represented by Greek letters (α,β,γ), belonging to the set [e, μ, τ], while the mass eigenstates are denoted by Latin letters (i, j, k), belonging to the set [1, 2, 3]. The PMNS matrix, denoted as U and described in Equation 2.6:

$$U_\nu = \begin{pmatrix} U_{e1} & U_{e2} & U_{e3} \\ U_{\mu 1} & U_{\mu 2} & U_{\mu 3} \\ U_{\tau 1} & U_{\tau 2} & U_{\tau 3} \end{pmatrix} = \begin{pmatrix} 1 & 0 & 0 \\ 0 & C_{23} & S_{23} \\ 0 & -S_{23} & C_{23} \end{pmatrix} \begin{pmatrix} C_{13} & 0 & S_{13}e^{-i\delta} \\ 0 & 1 & 0 \\ -S_{13}e^{i\delta} & 0 & C_{13} \end{pmatrix} \begin{pmatrix} C_{12} & S_{12} & 0 \\ -S_{12} & C_{12} & 0 \\ 0 & 0 & 1 \end{pmatrix} \tag{2.6}$$

The matrix is separated into three distinct mixing matrices, each defined by a unique mixing angle θ_{ij}, where C_{ij} represents $cos(\theta_{ij})$ and S_{ij} represents $sin(\theta_{ij})$. There is also a phase called δ_{cp}, which introduces CP violation by distinguishing between neutrino and antineutrino oscillations. It is worth noting that the presence of an additional Majorana phase, dependent on the nature of neutrinos, is excluded from consideration as it does not contribute to oscillations [28, 43].

The solution to the Schrödinger equation can be obtained by employing a plane wave solution, as indicated in Equation 2.7, where $|\nu\rangle$ refers to the neutrino state at time t = 0.

$$|\nu(t)\rangle = e^{-iEt}|\nu\rangle = \sum_i U^*_{\alpha i} e^{-iE_i t}|\nu_i\rangle \tag{2.7}$$

Hence, the probability of observing a neutrino of flavour α as flavour β after a time t can be expressed by Equation 2.8:

$$P_{\alpha\to\beta}(t) = \left|\langle\nu_\beta(t)|\nu_\alpha\rangle\right|^2 = \left|\sum_{i,j} e^{-iE_j t} U^*_{\alpha i} U_{\beta i}\langle\nu_j|\nu_i\rangle\right|^2 \tag{2.8}$$

Given that $\langle\nu_j|\nu_i\rangle$ is equivalent to δ_{ij}, this relationship can be rearranged and represented as Equation 2.9

$$P_{\alpha\to\beta}(t) = \left|\sum_i e^{-iE_i t} U^*_{\alpha i} U_{\beta i}\right|^2 = \sum_{i,j} e^{-i(E_i - E_j)t} U^*_{\alpha i} U_{\beta i} U_{\alpha j} U^*_{\beta j} \tag{2.9}$$

The energy E_i associated with a specific mass eigenstate of a neutrino can be calculated using the formula provided in Equation 2.10. In this equation, the assumption of $m \ll E$ is made to justify the Taylor expansion and simplify the approximations, such as $P_i = E$.

$$E_i = \sqrt{P_i^2 + m_i^2} = |\mathbf{p}_i|.\left[1 + \left(\frac{m_i}{P_i}\right)^2\right]^{1/2} \to E + \frac{m_i^2}{2E} \tag{2.10}$$

As a consequence, the probability of oscillation is obtained, where Δm^2_{ij} represents the difference in squared masses $(m_i^2 - m_j^2)$, and the relationship between time and length is given by factors of $c(t = L)$ [44]:

$$P_{\alpha\to\beta}(t) = \sum_{i,j} U^*_{\alpha i} U_{\beta i} U_{\alpha j} U^*_{\beta j}\, exp\left(\frac{-i\Delta m^2_{ij} L}{2E}\right) \tag{2.11}$$

which can be reformulated as follows:

$$\begin{aligned} P_{\alpha\to\beta}(t) = \delta_{\alpha\beta} - 4\sum_{i,j}^{i\neq j} \Re\left(U^*_{\alpha i} U_{\beta i} U_{\alpha j} U^*_{\beta j}\right) \sin^2\left(\frac{-i\Delta m^2_{ij} L}{4E}\right) \\ +2\sum_{i,j}^{i\neq j} \Im\left(U^*_{\alpha i} U_{\beta i} U_{\alpha j} U^*_{\beta j}\right) \sin\left(\frac{-i\Delta m^2_{ij} L}{2E}\right) \end{aligned} \tag{2.12}$$

In the simplified scenario of oscillation between two flavours, the mixing matrix can be represented using a single angle, as illustrated in Equation 2.13

$$U_\nu = \begin{pmatrix} cos(\theta) & sin(\theta) \\ -sin(\theta) & cos(\theta) \end{pmatrix} \tag{2.13}$$

Hence

$$P_{\alpha\to\beta} = \sin^2(2\theta)\sin^2\left(\frac{\Delta m^2 L}{4E}\right) \tag{2.14}$$

The values of mass splittings (Δm^2) and matrix elements (U_{ij}) are constants that require determination through experimentation. The value of L/E can be selected to maximise sensitivity to the mixing parameter.

When neutrinos traverse through matter instead of a vacuum, additional matter effects must be considered due to the coherent scattering between neutrinos and matter [44, 28]. These effects result in enhancements or suppressions of the neutrino oscillation probability, depending on the value and sign of δ_{cp}, while also producing the opposite effect on antineutrinos. The study of the disparity between neutrino and antineutrino oscillations caused by these matter effects allows modern and future oscillation experiments to determine the value of δ_{cp} [45].

2.2.3 Experimental Evidence

The Super-Kamiokande (SK) experiment, which succeeded the Kamiokande experiment that initially identified a deficit of atmospheric neutrinos, successfully resolved the atmospheric anomaly in 1998 [26]. The SK detector, consisting of a 22.5 kiloton water fiducial volume Cherenkov detector with around 11,000 PMTs, sought to determine the flux ratio (ν_μ/ν_e) by observing particles resulting from neutrino interactions occurring in ultra-pure water. A ν_e

interaction generates a distinct "electron-like" Cherenkov ring, which appears more blurred compared to the well-defined "muon-like" ring. This observation highlighted the correlation between the deficits of atmospheric muon neutrinos and their zenith angular and energy dependence, aligning with the concept of neutrino oscillations, as seen in Figure 2.4 [26]. The plot on the left depicts the Up/Down asymmetry of the neutrino rates observed for electrons and muons as functions of momentum. The electron data aligns with the shaded boxes, representing Monte Carlo (MC) expectations with no oscillations, displaying no significant asymmetry. However, the muon data exhibits a pronounced asymmetry that contradicts the no-oscillation hypothesis. The dashed line represents the best fit for the oscillation parameters with $\sin^2(2\theta) = 1.0$, $\Delta m^2 = 2.2 \times 10^{-3} eV^2$. Moreover, SK analysed the ratio of the neutrino flux in the recorded data to the expected MC flux, denoted as $R = \Phi Data/\Phi MC$, in order to assess any deviations from the nominal value of $R = 1$, as shown in Figure 2.4 (right). The observed value was approximately $R \approx 0.6$, indicating strong agreement with the two-flavour atmospheric neutrino oscillation hypothesis [26, 46].

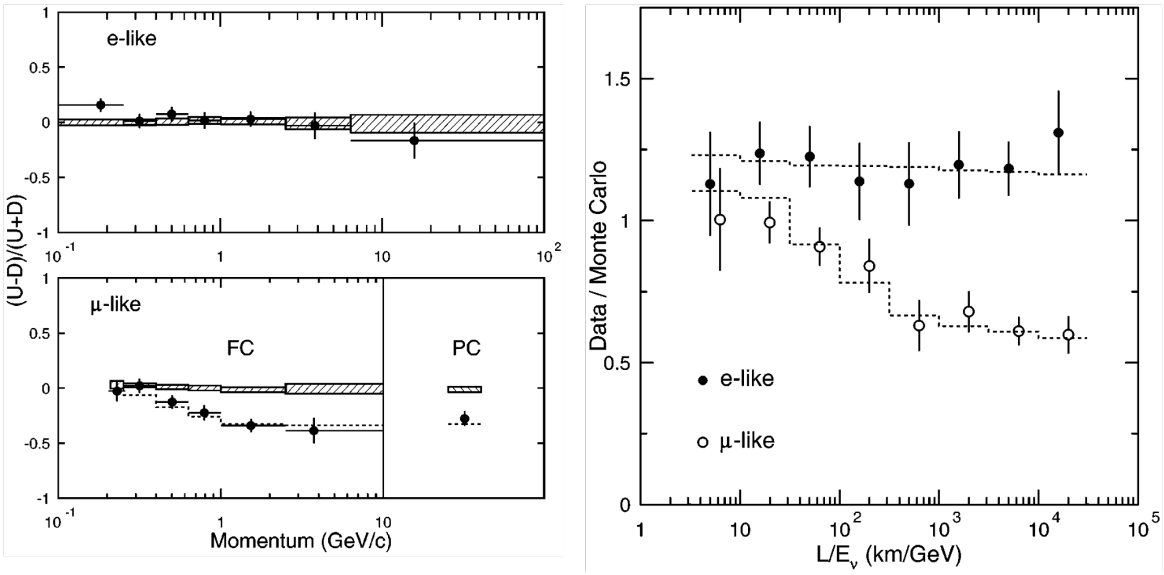

Figure 2.4: The SK experiment reported indications of an oscillatory pattern in atmospheric neutrino oscillations. On the left, the Up/Down asymmetry is shown as a momentum-dependent function for Fully Contained (FC) e-like, μ-like, and Partially Contained (PC) events. PC events, though lacking assigned momenta, have an estimated mean neutrino energy of 15 GeV. The hatched region represents the Monte Carlo expectation without neutrino oscillations, incorporating statistical and systematic errors in quadrature. On the right, the graph displays the ratio of FC data events to FC MC events plotted against the reconstructed L/E$_\nu$. The data points indicate the observed ratio in comparison to the MC expectation without oscillations. In both plots, the dashed lines present the expected shape for $\nu_\mu \leftrightarrow \nu_\tau$ at $\Delta m^2 = 2.2 \times 10^{-3} eV^2$ and $\sin^2 2\theta = 1$. Figure from [26]

Subsequently, the solution to the solar neutrino anomaly was achieved through the Sudbury Neutrino Observatory (SNO) experiment, which offered additional verification of neutrino oscillations within solar neutrinos [47]. As the Davis et al. and Kamiokande experiments primarily observed high-energy neutrinos originating from solar B^8 decay, the SNO experiment differed by measuring both the flux of electron neutrinos (through charged-current (CC) interactions, $\nu_e + d \rightarrow p + p + e^-$, which exclusively occur for electron neutrinos) and the total neutrino flux (via flavour-independent neutral-current (NC) interactions, $\nu_x + d \rightarrow p + n + \nu_x$). This was achieved through the introduction of deuterium into the water Cherenkov detector utilised by the SNO experiment. Figure 2.5 shows the combined measurements from CC, NC and ES channels to determine the overall neutrinos flux, which is further categorised into $\phi\nu_e$ and $\phi\nu_{\mu\tau}$. The three interaction modes, represented by red (CC), blue (NC), and green (ES), are depicted along with the SSM theoretical prediction, indicated as a dashed diagonal line. The optimal alignment between these channels revealed that one-third of the total solar flux consisted of ν_e, while the remaining portion had undergone oscillation into muon and tau neutrinos.

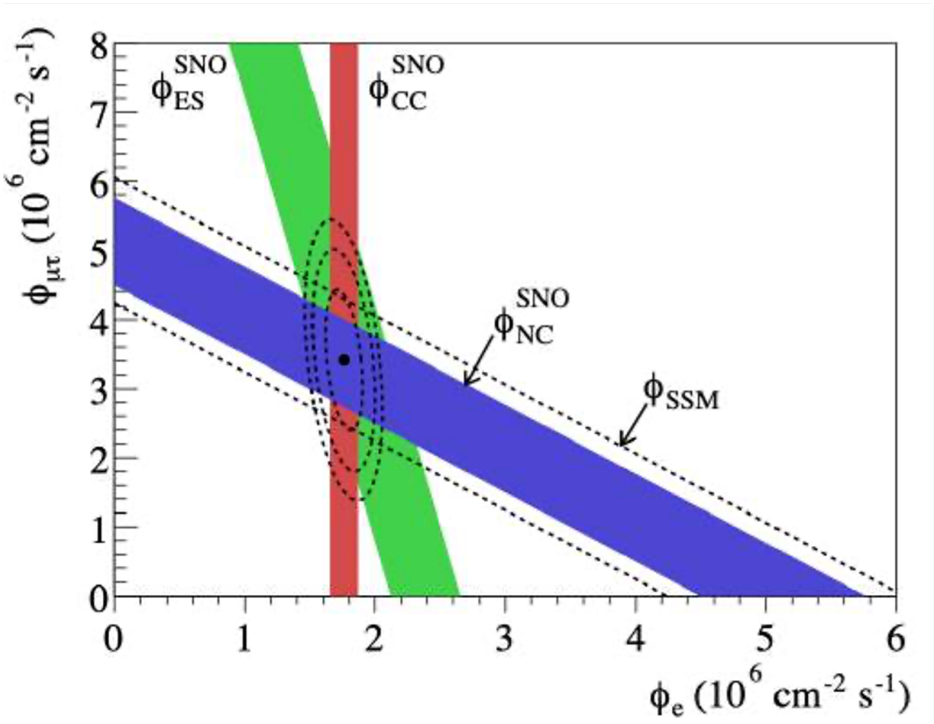

Figure 2.5: The SNO experiment measured total fluxes of solar neutrinos, including both ν_e and $\nu_{\mu\tau}$. The predicted total flux by the SSM is shown as diagonal dashed lines, while the measured total flux using the NC reaction in SNO is represented by diagonal blue bands. The intercepts of these bands with the axes indicate the $\pm 1\sigma$ errors. Figure from [47].

2.2.4 Status of Active Neutrino Oscillation Experiments

Numerous experiments following the discovery of neutrino oscillations have consistently strengthened the evidence and improved measurements of this phenomenon. The evidence now overwhelmingly supports the occurrence of neutrino oscillations, shifting the field's focus towards accurately determining the theoretical parameters that define this phenomenon, such as mass splittings, mixing angles, and δ_{cp}. Experiments commonly observe the appearance and disappearance (or both) of specific weak eigenstates from various neutrino sources such as solar, atmospheric, reactor, and neutrino beams. The sensitivity of a particular experiment to oscillation parameters relies on the energy and baseline of the detected neutrinos. Subsequently, global fits integrate the outcomes from multiple experiments across different sources to extract the complete set of mixing parameters collectively.

Measuring the absolute mass of individual active neutrinos is a considerably more intricate matter compared to determining the mass splittings, which is the squared differences between the mass eigenstates. Dedicated experiments like Karlsruhe Tritium Neutrino Experiment (KATRIN) are necessary to accurately measure these quantities, see [48]. At the time of writing, the current upper limit on the neutrino mass is m_ν<0.8 eV [48–51].

Experimental measurements have confirmed that the magnitudes of $|\Delta m^2_{32}|$ and $|\Delta m^2_{31}|$ are approximately $10^{-3}eV^2$, representing the atmospheric mass splitting, denoted as Δm^2_{atm}. This atmospheric mass splitting is roughly two orders of magnitude larger than Δm^2_{21}, which is approximately $10^{-5}eV^2$ and known as the solar mass splitting, Δm^2_{sol} [52]. The sign of Δm^2_{atm} has not been determined; the third neutrino mass eigenstate can have larger or smaller mass than the first and second eigenstates. The concept of "Mass Ordering" refers to the arrangement of neutrino masses in terms of size, where $m_3 > m_2 \approx m_1$ corresponds to the "Normal Hierarchy" while $m_3 < m_2 \approx m_1$ corresponds to the "Inverted Hierarchy", as shown in Figure 2.6 [53]. Due to a certain degeneracy, the neutrino mixing parameters (including the mixing angles and δ_{cp}) are interconnected with the mass hierarchy. As a result, many measurements of the mixing parameters are provided for both the normal and inverted mass hierarchies to account for this degeneracy.

Recent findings from solar neutrino experiments, SK, SNO and Borexino, have provided robust constraints on the oscillation parameters θ_{12} and Δ^2_{12} [55–57]. KamLAND, on the other hand, examines reactor neutrinos over a longer baseline of 180 km and is capable of detecting the identical oscillation parameters as solar experiments (θ_{12} and Δ^2_{12}) [58]. The combined observations of these solar oscillation parameters are generally consistent and further reinforce the overall constraint on the parameters. Conversely, shorter baseline reactor experiments like DayaBay [59], RENO [60], and Double Chooz [61] are generally more sensitive to θ_{13} and a combination of Δ^2_{32} and Δ^2_{31}.

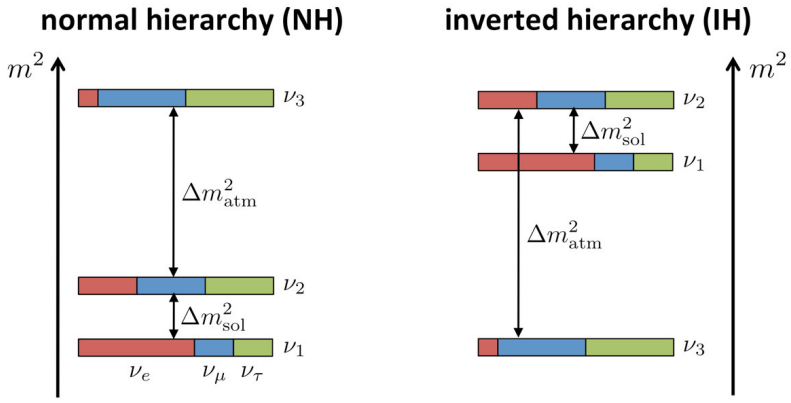

Figure 2.6: Diagram illustrating the two potential hierarchies on neutrino masses based on the sign of Δm^2_{atm}. On the left is the normal hierarchy, where the third mass eigenstate is the heaviest, while on the right is the inverted hierarchy, where the third mass eigenstate is the lightest. The colours represent the probability of interacting as each of the flavours. Figure from [54].

Long-baseline neutrino experiments, such as Tokai to Super-Kamiokande (T2K) and NuMI Off-axis ν_e Appearance experiment (NOνA), utilising accelerator-based neutrino beams, are sensitive to various oscillation parameters that include solar and reactor mixing angles. These experiments gain additional sensitivity to the neutrino mass hierarchy due to matter effects induced by the long path of neutrinos through the ground. By comparing oscillation measurements between ν and $\overline{\nu}$ optimised beam modes, these experiments also probe matter-antimatter asymmetry quantified by δ_{cp}. In recent findings, the T2K collaboration has presented evidence of δ exhibiting CP-violating values exceeding the 2σ significance level [62, 63]. Recent data from the NOνA experiment indicate a preference for values of δ_{cp} near 0.8π in the case of normal mass ordering, suggesting a potential CP-violating effect. The NOνA experiment has also excluded certain values of δ_{cp} for the inverted mass ordering [64]. T2K, on the other hand, exhibits slightly enhanced sensitivity to δ_{cp} for the inverted neutrino mass ordering, while both experiments demonstrate comparable sensitivity for the normal neutrino mass ordering.

Experiments that study atmospheric neutrinos, generated from cosmic ray interactions in the atmosphere, play a crucial role in determining the remaining oscillation parameters, namely θ_{23} and Δm_{23}. Notably, the latest global analyses incorporate data from SK and the DeepCore detector of the IceCube experiment [65, 66].

The NuFIT group combines the results from various experiments to perform a global fit, as depicted in Figure 2.7. This representation showcases the regions in which the mixing

angles, mass splittings, and δ_{cp} values are permitted. The results indicate a preference for the "Normal" mass ordering, as evidenced by a lower χ^2 value for $\Delta m^2_{23} > 0$ compared to

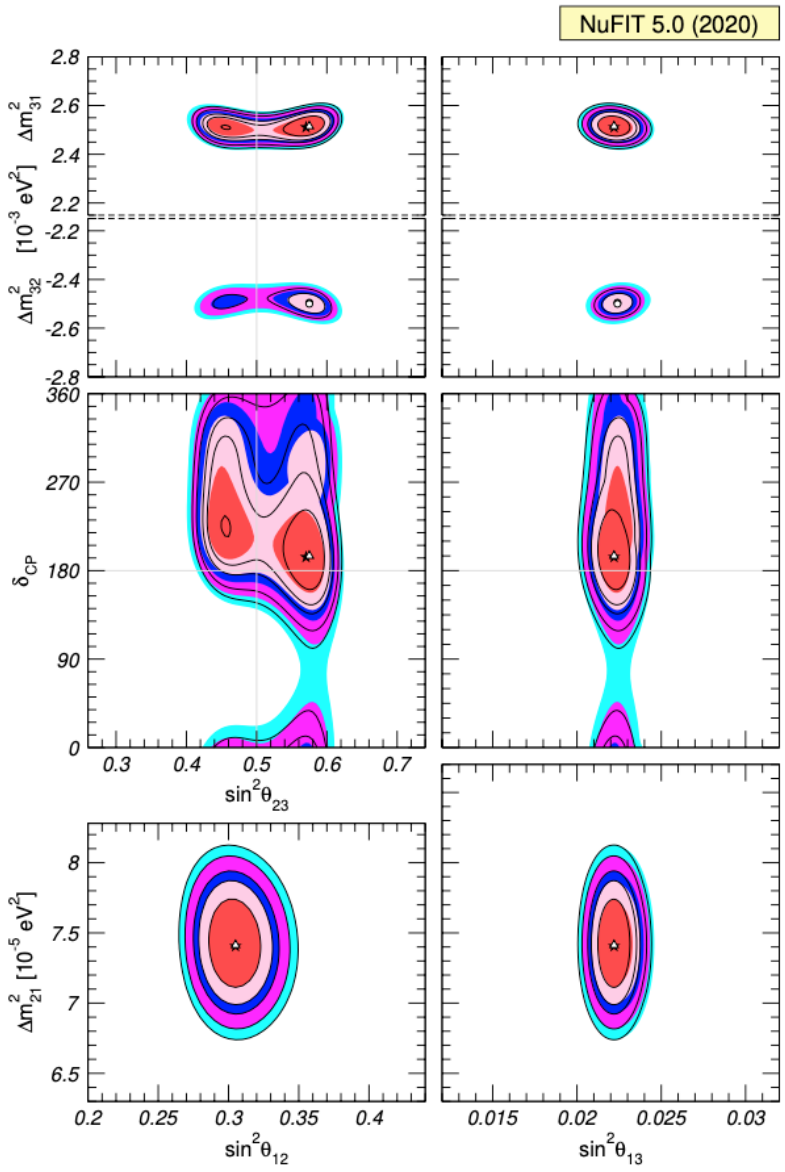

Figure 2.7: Presentation of Global 3ν oscillation analysis by NuFit. Each panel displays the 2D projection of the allowed region in six dimensions, obtained after minimising the undisplayed parameters. The lower four panels depict regions determined through the minimisation of $\Delta\chi^2$ concerning the mass ordering. Within these panels, the contours correspond to confidence levels (CL) of 1σ, 90%, 2σ, 99%, and 3σ for 2 degrees of freedom. The coloured regions (with black contour curves) correspond to the analysis without (with) the inclusion of the tabulated $SK-atm\Delta\chi^2$. The atmospheric mass-squared splitting is denoted as Δm^2_{31} for the normal ordering (NO) and Δm^2_{32} for the inverted ordering (IO). Figure from [67].

$\Delta m^2_{23} < 0$. However, the determination of the $\sin 2\theta_{23}$ octant (whether it is greater or less than 0.5) and the specific value of δ_{cp} remain inadequately constrained because of discrepancies observed between the T2K and NOνA experiments.

Upcoming long baseline experiments, including the Deep Underground Neutrino Experiment (DUNE) and Tokai to Hyper-Kamiokande (T2HK), have the objective of providing definitive measurements for these parameters [68, 69]. Additionally, the Jiangmen Underground Neutrino Observatory (JUNO) experiment, which focuses on reactor neutrinos across different baselines, will investigate the reactor oscillation parameters and mass hierarchy [70]. Consequently, the field of neutrino oscillation analyses is rapidly advancing into a precision era.

2.3 Sterile Neutrinos

The LEP experiments support the existence of three light, weakly interacting neutrino flavours, but others suggest a possible fourth type: the sterile neutrino [13, 71]. Sterile neutrinos are hypothetical neutral leptons that do not participate in standard weak interactions. Coined by Pontecorvo in 1967, the term "sterile" describes neutrino oscillations into undetectable sterile neutrinos [22]. Sterile neutrinos are primarily influenced by gravitational interactions arising from the curvature of space-time. Hence, unlike other neutrino flavours, sterile neutrinos do not interact via weak force and cannot be directly observed. However, by extending the PMNS matrix to accommodate a fourth neutrino, neutrinos produced in weak interactions can undergo oscillations to sterile neutrinos. This extension involves expanding the 3×3 matrix to a 4×4 matrix. Oscillation experiments can probe the presence of this additional neutrino, resulting in enhanced disappearance or appearance effects [72–74].

The Liquid Scintillator Neutrino Detector (LSND) experiment at the Los Alamos National Laboratory observed potentially anomalous neutrino mixing. Using a short-baseline Cherenkov detector, LSND studied the $\overline{\nu}_\mu$ flux up to 53 MeV [75]. The goal was to detect ν_e events by observing the Cherenkov and scintillation light produced by the e^+ and the delayed 2.2 MeV gamma-ray from capturing a neutron in the inverse beta decay process in Carbon [75]. Key backgrounds at LSND included standard $\overline{\nu}_e$ production in the beam stop and misidentification of μ^+ as e^+ in π^- decay followed by $\overline{\nu}_\mu + p \rightarrow \mu^+ + n$. The experiment, as shown in Figure 2.8, observed an excess of $87.9 \pm 22.4(stat.) \pm 6.0(syst.)$ $\overline{\nu}_e$ events over the expected backgrounds at a 3.8σ CL [75].

MiniBooNE was specifically designed to investigate the LSND findings with improved accuracy [76–78]. Positioned 540 m downstream from the Booster Neutrino Beam (BNB), MiniBooNE employed a mineral oil detector optimised for detecting Cherenkov light emitted

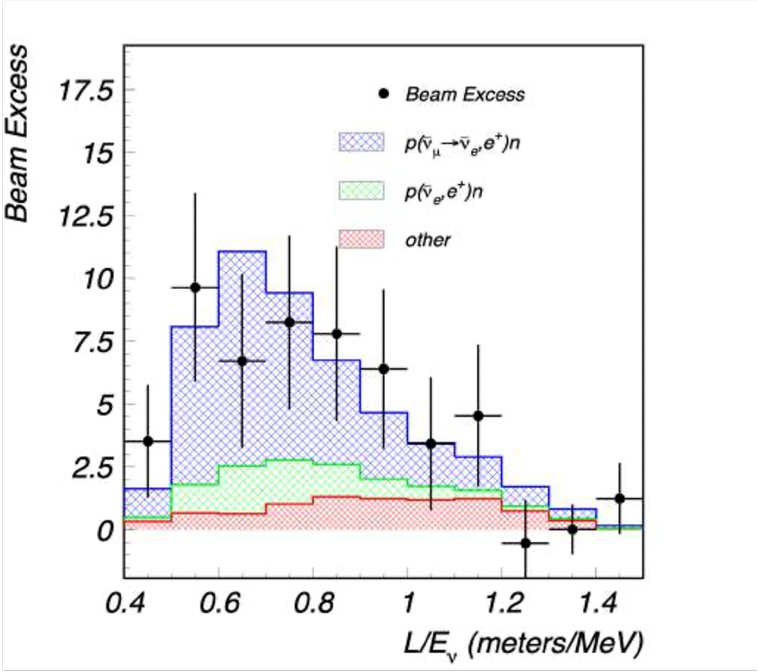

Figure 2.8: The observed excess of $\overline{\nu}_e$-like events correlates with the distance travelled by the neutrinos (L) and their energy (E_ν). The data align closely with expectations from neutrino background and oscillations at Δm^2 approximately 1 eV^2. Figure from [75].

by electrons and muons. Although MiniBooNE had distinct energy configurations and event signatures, its higher energy and longer baseline allowed it to probe the same range of L/E as LSND, thus ensuring sensitivity to a mass squared splitting of approximately 1 eV^2. A low-energy interactions excess involving ν_e ($\overline{\nu}_e$) was detected when the BNB operated in ν ($\overline{\nu}$) mode, with a slightly larger excess detected in neutrino mode.

Figure 2.9 shows the excess rate observed by MiniBooNE versus reconstructed neutrino energy, along with the best-fit prediction based on the sterile neutrino hypothesis. The combined excesses observed in both ν and $\overline{\nu}$ modes at MiniBooNE yield an overall significance of 4.8σ. Figure 2.10 also displays the allowed parameter space for sterile neutrino oscillation, which aligns with the LSND allowed region, indicating general agreement between the two experiments.

Sterile neutrinos could result in the appearance of ν_e and also lead to the disappearance of both ν_e and ν_μ. Evidence of ν_e disappearance has been observed in certain reactor experiments, as shown in the global fit depicted in Figure 2.11. This figure illustrates the allowed regions in the phase space and compares them to exclusion contours from atmospheric and solar experiments. However, the absence of ν_μ disappearance in multiple experiments contradicts the measurements of ν_e appearance and disappearance, as shown in Figure 2.11. This figure displays exclusion contours for ν_μ disappearance and the region where the Mini-

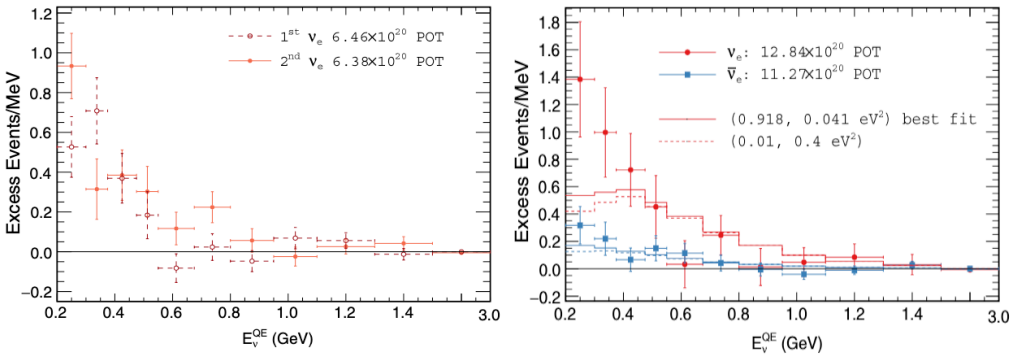

Figure 2.9: The left plot displays the event excesses observed in MiniBooNE's neutrino mode, representing the first and second set of data as a function of E_ν^{QE}. The right plot shows the combined event excesses from both neutrino and antineutrino modes. The solid curve represents the best fit to the data, while the dashed curve represents the 1σ fit point, both assuming two-neutrino oscillations. The last energy bin covers the range from 1.5 to 3 GeV. Figure from [76].

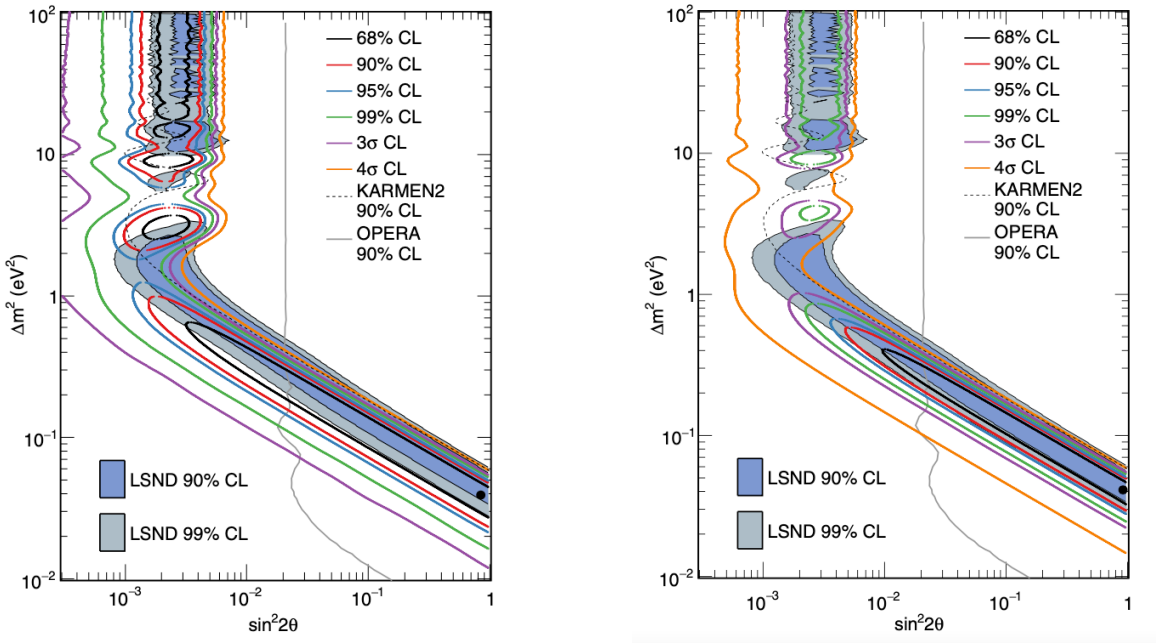

(a) ν only mode

(b) ν and $\overline{\nu}$ mode

Figure 2.10: The MiniBooNE analysis focuses on the allowed regions in neutrino (a), and neutrino with antineutrino (b) modes for events with an E_ν^{QE} between 0.2 and 3 GeV, using a two-neutrino oscillation model. The shaded regions represent the 90% and 99% CL allowed regions for LSND $\overline{\nu}_\mu \rightarrow \overline{\nu}_e$ oscillations. The MiniBooNE best fit point is represented by black point. Additionally, the analysis includes the 90% CL limits from the KARMEN and OPERA experiments [79, 80]. Figures from [76].

BooNE low-energy excess is permitted, connecting these parameter spaces via the best-fit point for ν_e disappearance. The global fit integrates information from accelerator-based experiments, such as MINOS/MINOS+ (Main Injector Neutrino Oscillation Search [81]) and MiniBooNE [82], as well as atmospheric experiments, like SK [83], IceCube [65], and DeepCore [65], to address ν_μ disappearance. The overlapping region between the MiniBooNE permissible region and the exclusion contours for ν_μ disappearance highlights the substantial inconsistency between measurements of neutrino appearance and disappearance.

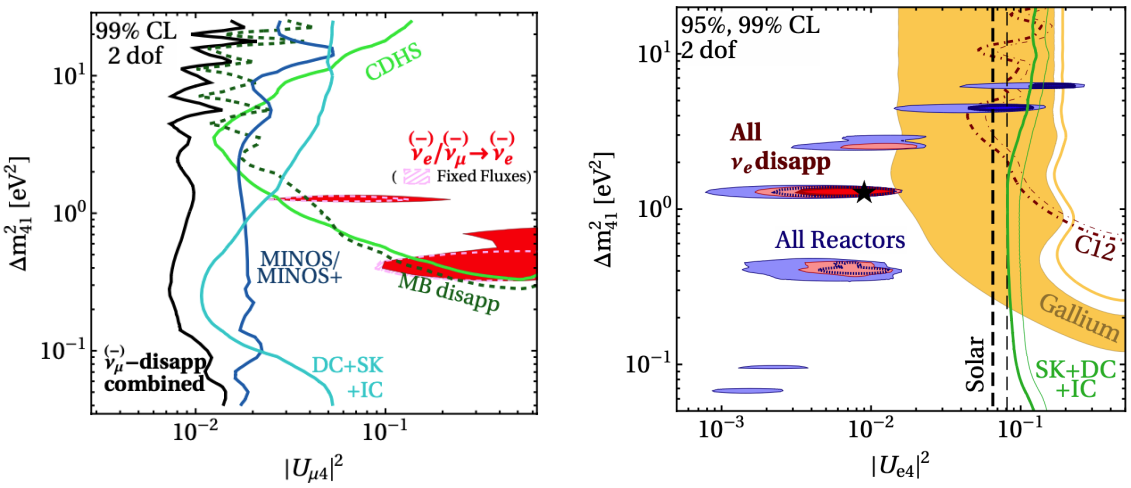

(a) ν_μ Disappearance

(b) ν_e Disappearance

Figure 2.11: The global limits for ν_μ (left) and ν_e (right) are shown. The MiniBooNE allowed region for ν_e appearance is also extended into the realm of disappearance, highlighting the disparity in measurements between these two phenomena. Figures from [84].

New experiments are underway to enhance experimental limits and address the discrepancies observed between different measurements. The JSNS2 experiment at J-PARC Spallation Neutron Source aims to directly investigate the LSND observation by searching for anomalous ν_e appearance using a stopped muon source [85]. Likewise, the SBN program, consisting of three detectors of the same technology, will directly probe the MiniBooNE low-energy excess in the BNB beam, enabling simultaneous measurement of ν_e appearance and ν_μ disappearance channels to mitigate systematic uncertainties [1]. Initial results from MicroBooNE, the first SBN detector, have not shown any signs of the excess [86, 87]. Further details on the SBN program, with an emphasis on the Short-Baseline Near Detector (SBND), will be discussed in Chapter 4. Additional reactor neutrino experiments such as DANSS [88], Neutrino4 [89], PROSPECT [90], and STEREO [91], with varying baselines and improved calibration, are expected to enhance ν_e disappearance sensitivity. Long-baseline accelerator experiments like NOνA and T2K are also improving the constraints on ν_μ disappearance,

while IceCube and other experiments are enhancing sensitivity through the search for atmospheric neutrino disappearance [92, 93]. The primary goal of these upcoming experiments is to effectively resolve the discrepancy between the appearance and disappearance modes.

2.4 Neutrino-Nucleus Interactions

Researching neutrino interactions plays a crucial role in unravelling the nature of weak force and nuclear structure. By examining the cross section that quantifies the likelihood of neutrino interactions, valuable insight can be gained. Accurate measurements of neutrino oscillations heavily rely on understanding these interactions, as they contribute to uncertainties in long baseline analyses [94–97]. While efforts have been made to minimise systematic uncertainties through the use of near and far detectors, variations in neutrino flux and detector acceptance make complete cancellation challenging, especially in cases where detectors employ different nuclear targets. As the study of neutrino oscillations advances into an era of precision measurements, the focus shifts from acquiring sufficient statistics to reducing uncertainties related to neutrino-nucleus cross sections across different target materials, neutrino energies, flavours, and interaction final states for precision measurements [98].

Additionally, numerous experiments aiming to detect ν_e appearance heavily depend on assumptions about the ν_e/ν_μ cross section ratio, primarily due to the limited availability of ν_e cross section measurements [99]. Accurately measuring the ν_e cross section poses significant challenges since neutrino beams primarily produce ν_μ, leading to measurements with significant background contributions [100–102]. Backgrounds arising from neutral pion (π^0) production in neutrino interactions can restrict the sensitivity of oscillation searches, such as those pursued by the SBN Program and DUNE, which are seeking neutrino $\nu_\mu \rightarrow \nu_e$ oscillations [1, 103–105], see Chapter 6. Therefore, precise cross section measurements are essential for the success of the next generation of oscillation experiments in achieving their physics objectives.

Neutrino-nucleus interactions are commonly modelled by factoring the process into components such as nuclear models, primary interactions, and the generation and transportation of hadrons. Using an event generator, such as GENIE [106], these models are then combined to create predictions that can be contrasted to and calibrated with experimental data. This modular approach simplifies model building, allowing for the identification of the optimal combination of nuclear, interaction, and hadron models. Figure 2.12 shows the combined cross section of these interaction channels at typical accelerator neutrino energies, alongside a compilation of experimental data [16]. As observed in Figure 2.12, the available data primarily covers higher energy interactions, and for the limited data in the 1 GeV region, there are considerable uncertainties, especially for the antineutrino measurements.

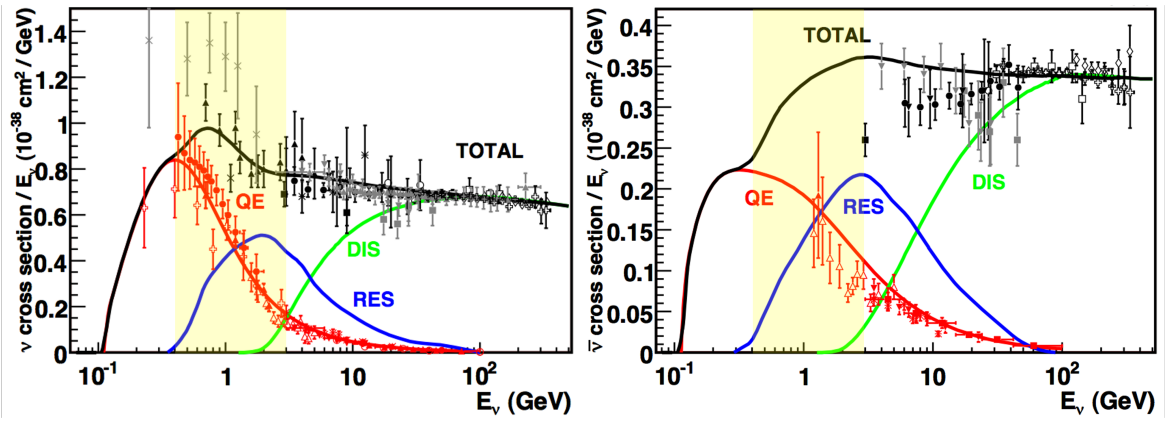

Figure 2.12: Neutrino (left) and antineutrino (right) cross sections per nucleon in charged current interactions, presented versus neutrino energy. The combined cross section is presented along with the contributions from separate interaction channels and exclusive channel measurements. The highlighted region corresponds to the energy range of the neutrino beam utilised by the SBN Program. Figure from [107].

2.4.1 Neutrino Interaction Channels

The neutrino, being electrically neutral, interacts only through the weak and gravitational forces, though measuring the gravitational effect is challenging. To detect neutrinos, experiments rely on observing the particles resulting from the interaction of neutrinos with nuclear targets via the exchange of Z or W bosons. The exchange of a Z boson results in a Neutral Current (NC) interaction, with the neutrino remaining in the final state. On the other hand, the exchange of a W boson results in Charge Current (CC) interactions, generating a charged lepton in the final state that matches the flavour of the interacting neutrino. As shown in Figure 2.12, in the GeV energy range, neutrino interactions with nuclear targets exhibit various energy-dependent processes with cross sections, including (Quasi-)Elastic Scattering (QE), Resonant interactions (Res), and Deep Inelastic Scatterings (DIS).

(Quasi-)Elastic Scattering

At energies below approximately 1 GeV, the main interaction process is CC Quasi-Elastic (CCQE) and NC Elastic (NCE) scattering, as illustrated by Feynman diagrams in Figure 2.13. CCQE interactions are particularly valuable for experimental measurements because the kinematics of the outgoing lepton provides insights into the incoming neutrino's energy. Additionally, the simplicity of this interaction makes it easier to model, allowing for probing of fundamental form factors and nuclear models. Commonly used to model this process is the Llewellyn-Smith formalism [108], which is based on the Axial Mass (M_a) and form factors describing the density of charges in the nucleus.

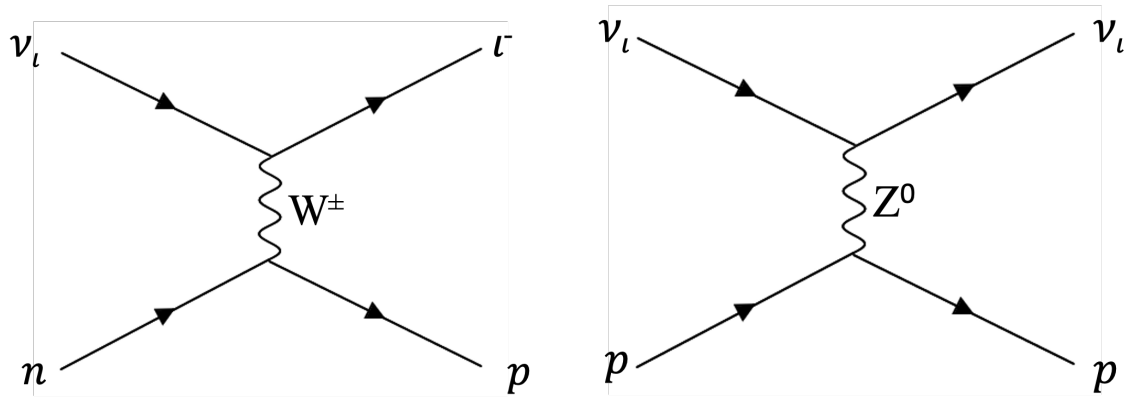

(a) CCQE (b) NCE

Figure 2.13: Feynman diagrams representing Charged Current Quasi-Elastic and Neutral Current Elastic interactions, where l = (e, μ or τ).

As the energy increases, studies from electron and neutrino scattering experiments have revealed the significance of multi-nucleon emission [109]. As modern neutrino experiments, heavier and more complex nuclear targets like carbon or argon are used, simple QE models need to be extended to incorporate interactions between nucleons, including Meson Exchange Current (MEC). The neutrino, in these multi-nucleon interactions, interacts not with one nucleon but with a pair (or sometimes more) of interacting nucleons, which are commonly known as n-particle n-hole (np-nh). Understanding these np-nh processes is a current focus in the development of theories related to neutrino-nucleus cross sections, as they require precise descriptions of the entire nucleus. Leading efforts in this area are being made by research groups such as Valencia [110, 111], SuSA [112], Martini-Ericson [113], Ghent[114], and others. Figure 2.14 presents an example diagram contributing to two-body (2p-2h) currents.

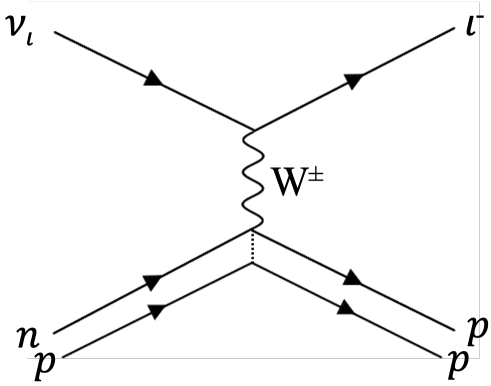

Figure 2.14: Feynman Diagram for 2p-2h interaction channel.

The MEC interactions were first introduced in GENIE using an empirical model calibrated to electron scattering data [115]. On the other hand, the Valencia model takes a different approach by incorporating both QE and multi-nucleon processes, while also considering polarisation and Coulomb corrections [110].

Resonant Interactions

In the neutrino energy range of 1 to 5 GeV, resonant interactions (RES) become dominant. During these interactions, as more energy is transferred to the nucleus (higher Q^2), there is a higher likelihood of exciting the nucleus. Usually, nucleons are excited to a baryon resonance, like a Δ^{++}, which rapidly decays into, commonly, a pion and a nucleon. Example Feynman diagrams for CC π^0 production can be seen in Figure 2.15. The Rein-Sehgal model has historically been widely used for simulating resonant interactions [116, 117]. However, the more recent Berger-Sehgal model improves upon the older one by incorporating experimental pion scattering data and including leptonic mass correction terms [118].

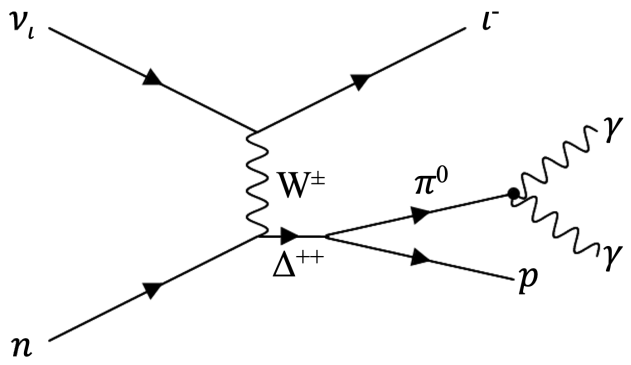

Figure 2.15: A CCπ^0 Feynman diagram propagated via a nucleon resonance, Δ^{++}.

Deep Inelastic Scattering

At energies beyond approximately 5 GeV, the cross sections for CCQE and RES interactions decrease, while the cross section for Deep Inelastic Scattering (DIS) rises. The cross section increases relatively linearly with neutrino energy at high energies. In this regime, the neutrino is capable of resolving individual quarks within nucleons, leading to the breakup of the final-state nucleus and resulting in a hadronic shower, as exemplified in Figure 2.16. This process is commonly described by the Bodek-Yang (BY) model that utilises Parton Distribution Functions (PDFs) to characterise the components of the nucleon [119]. Subsequently, the kinematics of the final state particles are modelled by employing a hadronisation model [120].

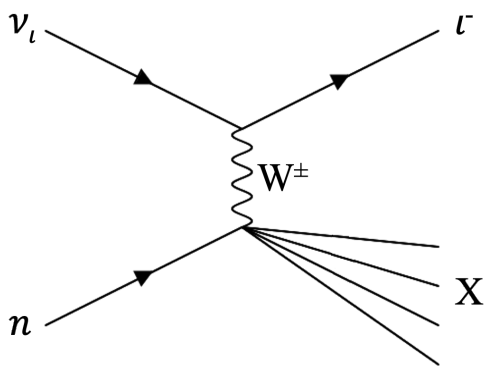

Figure 2.16: Deep Inelastic Scattering Feynman diagram, with X representing the hadronic shower.

At GeV-scale energies, CCQE and RES are the most prevalent types of neutrino interactions, which are particularly relevant to the research discussed in this thesis. However, at lower energies, other interaction processes may contribute with less significance. In addition to the resonance mode mentioned earlier, pions can also be generated in coherent scattering. In coherent scattering, a low-energy neutrino interacts inelastically with the entire nucleus, resulting in the production of either a charged or neutral pion. Similar to resonant production, the modelling of coherent pion production utilises either the Berger-Sehgal or Rein-Sehgal models [118, 116].

2.4.2 Nuclear Effects

Many of the neutrino interaction models assume free, stationary nucleon targets. However, for a comprehensive understanding of neutrino interactions, it is essential to consider more sophisticated systems. Neutrino detectors are composed of atoms, so the targets should be seen as part of a complex structure rather than isolated nucleons. The presence of nuclei as targets disrupts the assumption of free nucleons and involves continuous strong and weak interactions between protons and neutrons within the nucleus. Although the QE, RES, and DIS models have been relatively successful with light targets like deuterium and tritium in bubble chamber experiments, further studies are required to better understand nuclear effects in neutrino experiments using heavy nuclei such as liquid argon, carbon, or iron [16].

The Relativistic Fermi Gas (RFG) model, introduced by Smith and Moniz, is the basis for many modern models [121]. It considers the nucleus as a "gas" of non-interacting fermions uniformly distributed within a potential well defined by the nuclear radius. Nucleons occupy all energy levels from the lowest to the maximum threshold known as the Fermi energy.

While the Fermi energies for protons and neutrons can differ, they are equal for isoscalar nuclei. The RFG model assumes a flat momentum distribution for nucleons, with the Fermi momentum, p_f, defined by the Fermi energy. Additionally, a constant binding energy is included in the model, representing the energy required to remove a nucleon from the nucleus. See Figure 2.17 for a schematic illustration of the RFG model.

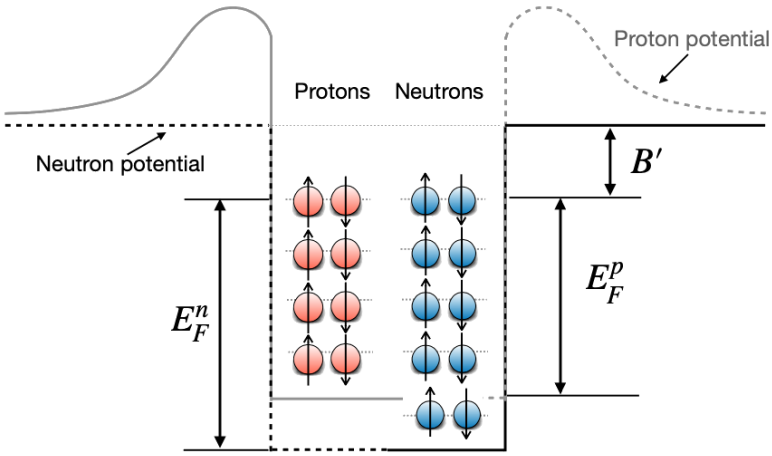

Figure 2.17: Illustration of the Relativistic Fermi Gas model featuring a non-isoscalar nucleus with a number of protons and neutrons, where E_F^n is the Fermi energy of neutrons, E_F^p is the Fermi energy of protons and B' is the binding energy. Figure from [122].

Neutrino-nucleon interactions with a momentum transfer $|\vec{q}| < 2p_f$ are limited due to Pauli blocking, where the final state nucleon cannot occupy energy levels already filled. The RFG model does not consider nucleons with momenta greater than the Fermi momentum. To address this, Bodek and Ritchie introduced the high-momentum tail model, allowing non-zero probabilities for nucleons with momenta larger than prescribed by the RFG model.

The Local Fermi Gas (LFG) model extends the RFG model by considering a non-uniform nucleus density and varying nucleon momentum. Using the local density approximation theory, the LFG model connects nucleon momentum to its distance from the nucleus centre, affecting the binding energy with stronger binding for nucleons closer to the centre [123, 124]. Additionally, the LFG model introduces an extra degree of freedom for Pauli blocking based on nucleon distance from the centre. Moreover, the Correlated Fermi Gas (CFG) model incorporates Short Range Correlations (SRC) between nucleons, resulting in a high momentum tail for nucleons above p_f. Figure 2.18 presents a comparison of predicted proton momentum distributions for each model, revealing significant differences.

In nuclear interactions, incorporating correlations between nuclei, whether short or long range, is commonly achieved using the Random Phase Approximation (RPA), and this is

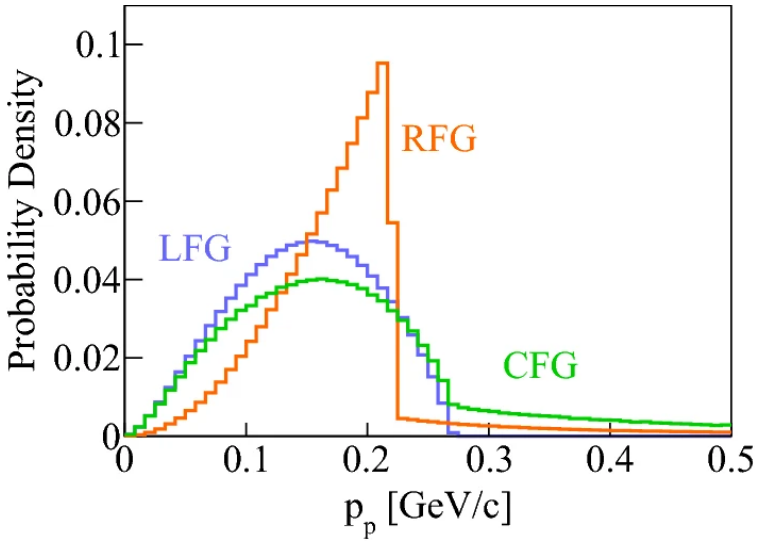

Figure 2.18: Comparison of predicted proton momentum using various GENIE nuclear models. Figure from [125].

especially crucial for heavy nuclei. An example of such correlations is the MEC interactions, in which two nucleons interact via the exchange of a virtual meson, and they have been found to play a significant role in multi-nucleon 2p-2h interactions [126, 127].

Furthermore, Final State Interactions (FSI) pose challenges in measuring neutrino-nucleus cross sections, as outgoing particles need to propagate out of the nucleus after the neutrino interactions [128], as depicted in Figure 2.19. While the outgoing lepton remains largely unaffected, emitted mesons and nucleons need to traverse the nuclear medium before detection. This makes it difficult to definitively deduce the true interaction, except for hydrogen or helium targets.

Generators model particle propagation through the nucleus, mostly using intra-nuclear cascade models, or more realistically, transport theory as in the GiBUU generator, which employs the Boltzmann-Uehling-Uhlenbeck (BUU) equation [130, 131]. However, propagating model uncertainties through re-weighting is challenging, so transport theoretical approaches are not widely employed in neutrino experiments. The discussion of this re-weighting can be found in Chapter 8. The GENIE [106] generator, employed in this thesis, utilises the hA and hN models, simulating effective interactions and performing full intra-nuclear cascade simulations to predict final states, for details refer to [3, 132, 133].

Experiment measurements are commonly reported based on final state multiplicity, such as "QE-like" for $1p0\pi$ observed events, including both true QE interactions and other modes affected by FSI. More details on these measurements and distinguishing kinematic variables will be discussed in the next section.

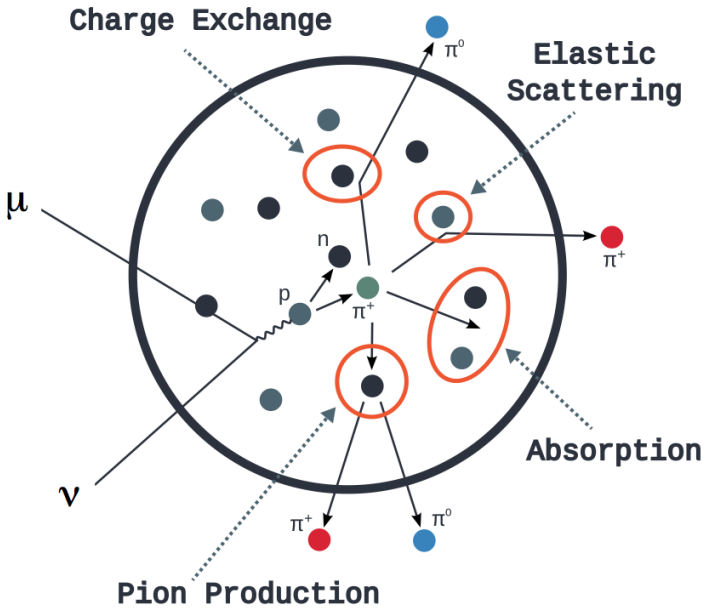

Figure 2.19: Diagram illustrating potential final state interactions within a nucleus. Figure from [129].

2.4.3 Experimental Measurements

Interaction cross section measurements have played a fundamental role in the development and optimisation of the interaction and nuclear models mentioned earlier. These measurements encompass both integrated and differential cross sections, considering various variables such as the energy and angular distributions of observed particles. Additionally, they can be inclusive, covering all possible final state interactions, or exclusive, focusing on specific requirements, such as the number of hadrons produced. In recent times, there has been a shift towards more exclusive and differential final state measurements to address complexities in the parameter space of heavier nuclear models. This progress is made possible by modern detectors with enhanced Particle IDentification (PID), resolution, and higher rates of neutrino interactions.

During the 1970s and 1980s, the first experiments that conducted neutrino cross section measurements utilised bubble chambers [134–136]. These experiments primarily employed hydrogen and deuterium targets, minimising the complexities arising from nuclear effects mentioned earlier. As such, measuring CCQE interactions was equivalent to determining the Axial Mass, M_a. The world average obtained from bubble chamber experiments yielded $M_a = 1.026 \pm 0.021$ GeV, demonstrating good agreement with data from pion decay [137]. However, as depicted in Figure 2.20, the cross section measurements for ν_μ QE interactions

in experiments using heavier nuclei, such as mineral oil (CH_2) in MiniBooNE [77], exhibited tension with axial mass measurements acquired from bubble chamber experiments.

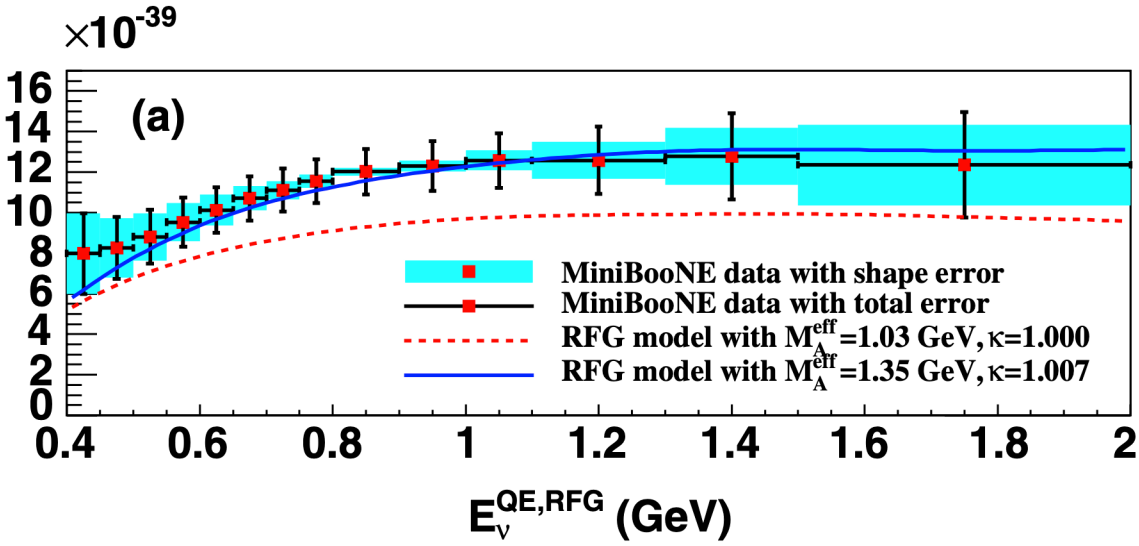

Figure 2.20: Comparison of MiniBooNE cross section data with predicted cross section for various values of M_a. Figure from [138]

The earliest measurements of CC single-π^0 production were conducted in 1976 by Barish using a 3.65 m deuterium bubble chamber experiment at Argonne National Laboratory (ANL). Using a neutrino beam with energies below 1.5 GeV, they studied charged and neutral pion production channels, including $\nu_\mu\ d \rightarrow \mu^- p \pi^0 p_s$ where p_s represents the spectator proton from the deuterium following the interaction [139]. A similar experiment was later performed by Radecky in 1982 at ANL with increased statistics in the same energy range, focusing on the same measurements with enhanced statistical data [140]. Approximately 56 events of CC single-π^0 production were observed in the first run, while in the second run, the number of events increased to 273 [139, 140]. Both experiments presented event rates for the invariant mass of nucleon-pion and the four-momentum transfer Q^2, using simulations relying on Adler's model [141].

Similar studies were conducted at Brookhaven National Laboratory (BNL) using a 2.13 m deuterium bubble chamber in a beam with an average energy of 1.6 GeV [142]. The BNL study had a larger signal sample of 853 events and covered an energy range up to 3 GeV [142]. Figure 2.21 displays the event rates of the ANL and BNL bubble chamber experiments plotted against the four-momentum transfer Q^2.

Later bubble chamber experiments provided valuable insights into the nucleon-pion invariant mass and higher resonances. The SKAT Collaboration employed a high-energy neutrino beam ranging from 3 to 30 GeV with a heavy liquid bubble chamber, while the

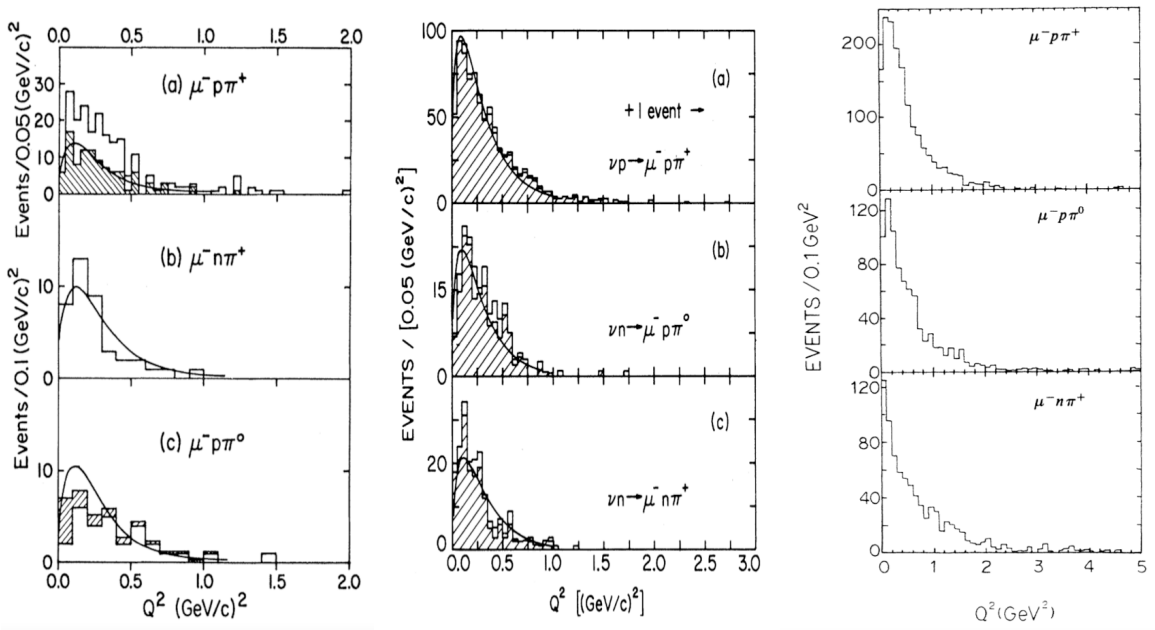

Figure 2.21: Event rates for pion production in the deuterium bubble chamber experiments at ANL (a, b) and BNL (c), with simulations based on Adler's pion production model. Figures from [139, 140, 142], respectively.

Big European Bubble Chamber at CERN employed a higher neutrino beam with an upper threshold of 54 GeV [143, 144]. Both experiments observed resonant peaks at hadronic masses beyond $\Delta(1232)$. In the early 2000s, efforts were made to explain the data from bubble chamber experiments and incorporate it into models [145–148]. Concurrently, Monte Carlo-based neutrino event generators such as NUANCE [149], NEUT [150], and NeuGen [151] were developed for the next generation of experiments, aiming to extend measurements to more complex targets beyond bubble chambers to further test their simulation models.

Between 2007 and 2008, the SciBar Booster Neutrino Experiment at Fermilab (SciBooNE) conducted data-taking in the BNB. In 2010, the SciBooNE collaboration published cross-section ratios $\frac{\sigma(NC\pi^0)}{\sigma(CC)}$ and $\frac{\sigma(NCcoh\pi^0)}{\sigma(CC)}$ using an average neutrino energy of 0.7 GeV and employing the SciBar plastic scintillator tracker (C_8H_8) as the target material [152]. Additionally, in 2014, a SciBooNE thesis [153] presented a measured CCπ^0 cross section based on 308 final selected data events to be:

$$\langle \sigma_{\mathrm{CC}-\pi^0} \rangle_\phi = (5.6 \pm 1.9_{\mathrm{fit}} \pm 0.7_{\mathrm{beam}} \pm 0.5_{\mathrm{int}} - 0.7_{\mathrm{det}}) \times 10^{-40}\,\mathrm{cm}^2/\mathrm{N} \tag{2.15}$$

In 2011, the K2K experiment presented a cross section ratio ($\frac{\sigma(CC\pi^0)}{\sigma(CCQE)}$) focusing on CC production instead of NC, using a beam with an average energy of approximately 1.3 GeV

interacting with a plastic scintillator target [154]. Also in 2011, MiniBooNE conducted measurements using a 12 m diameter spherical water Cherenkov detector filled with mineral oil (CH_2) as the target, with a neutrino beam peaking at 0.6 GeV. The MiniBooNE results included various CCπ^0 differential cross sections based on kinematic variables such as π^0 momentum and angle, and Q^2. Figure 2.22 presents the results from both K2K, on the left, and MiniBooNE, on the right, experiments on CCπ^0 production [155].

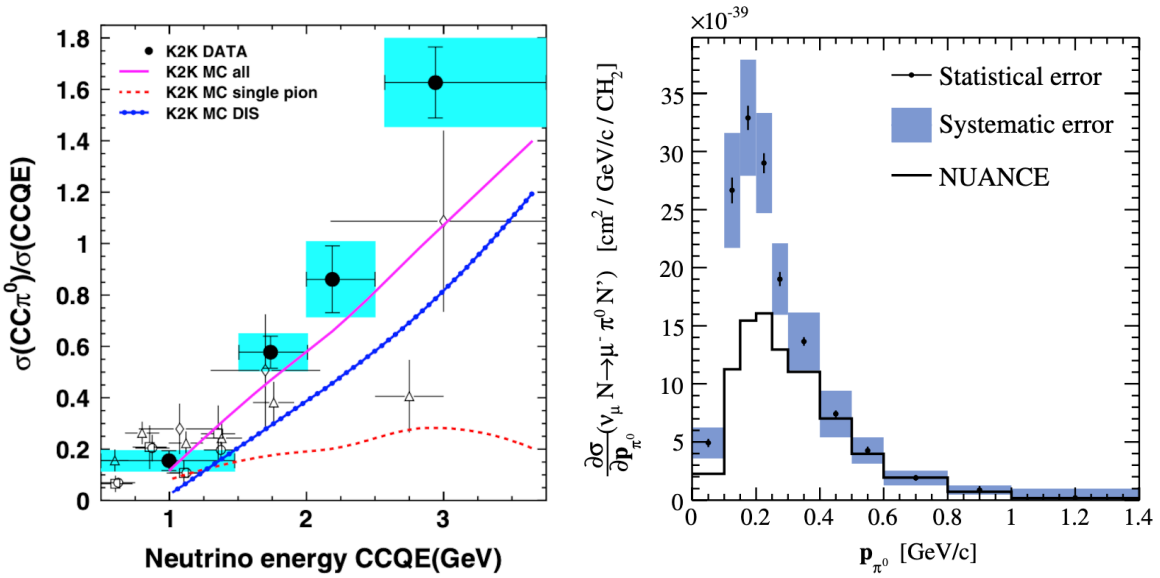

(a) (b)

Figure 2.22: Published results on CCπ^0 production from K2K and MiniBooNE collaborations. Figure 2.22a shows variation of CCπ^0-to-CC-QE cross section ratio with neutrino energy, as observed in the K2K experiment [154]. Figure 2.22b presents the flux-averaged differential cross section in $|P_{\pi^0}|$ at an energy range of 0.5 to 2.0 GeV with a total systematic uncertainty of 15.9%, plot from MiniBooNE experiment [155].

Data obtained from these experiments encompassed various energy regimes and diverse final states, including $NC\pi^0$ and $CC\pi^0$ productions, as well as $CC\pi^+$ production results from MiniBooNE [156]. These experimental results served as a foundation for the development of other phenomenological models aimed at explaining the observed data. Notably, extensive studies focused on resonant pion production and inelastic scatterings within these models [156–159].

The ANL and BNL bubble chamber data were re-analysed using modern techniques due to the initial high uncertainty and discrepancies with other data and models [160]. The re-analysis revealed that the disagreements were primarily attributed to inadequate modelling of the neutrino flux and statistical limitations, resulting in better agreement between the

ANL and BNL data [160]. Additionally, this re-analysis extension provided valuable insights to fine-tune certain simulation parameters used by GENIE in predicting resonant and non-resonant pion production [161].

In 2015, the MINERνA (Main Injector Neutrino ExpeRiment to study ν-A interactions) experiment conducted measurements of $\overline{\nu}_\mu$ CC π^0 differential cross sections against various variables using polystyrene as the target material [162]. MINERνA operated in the Neutrinos at the Main Injector (NuMI) beamline at Fermilab, focusing on an energy range of 2-10 GeV. The measurement signal is similar to MiniBooNE's but requires a μ^+ rather than a μ^- in the final state. More recently, in 2017, MINERνA published a study on ν_μ induced CC single π^0 differential cross section, with the signal definition excluding charged mesons from the final state [163].

MINERνA utilised GENIE as their neutrino event generator, employing version 2.6.2 for $\overline{\nu}_\mu$ CC π^0 analysis and 2.8.4 for the ν_μ CC π^0 analysis. Both ν and $\overline{\nu}$ measurements presented cross sections in terms of muon and π^0 kinematics, as well as Q^2. Notably, a significant discrepancy between the data and the simulation was observed in the differential cross section for $Q^2 < 0.2\ GeV^2$, as depicted in Figure 2.23.

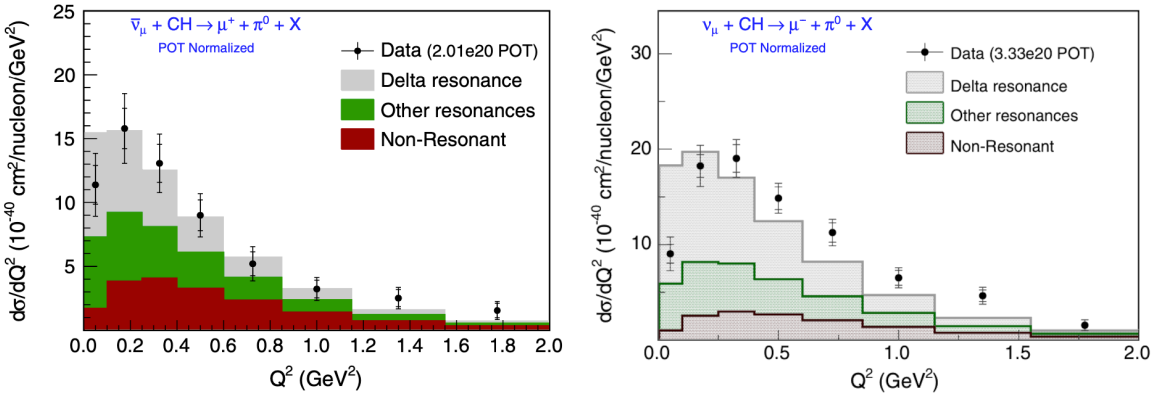

(a) $\overline{\nu}_\mu$ CC π^0 measurement

(b) ν_μ CC π^0 measurement

Figure 2.23: Differential cross section $\frac{d\sigma}{dQ^2}$ in CCπ^0 production channels for both neutrino and antineutrino interactions reported by MINERνA. The simulation models utilised for these analyses are GENIE versions 2.6.2 ($\overline{\nu}_\mu$ CC π^0) and 2.8.4 (ν_μ CC π^0). Figures from [164, 163].

The observed deficiency of data compared to the prediction at low Q^2 values, as depicted in Figure 2.23, is known as low-Q^2 suppression. This suppression cannot be attributed to coherent or diffractive production, as these interactions do not lead to neutral pion production in any of the CC channels. Rather, the deficit in π^0 production at low Q^2 can be explained by the absence of a different interaction model in the simulation and the influence of final-state

interactions on π^0 production. Considering these inconsistencies, a dedicated study was undertaken to tune the GENIE prediction for pion production using the available data at that time [165].

The study led to the tuning of GENIE parameters to better align with MINERνA data in $\overline{\nu}_\mu$ CC π^0, ν_μ CC π^0, and other pion production channels, resulting in improved agreement with the data, except for the low-Q^2 regime. Consequently, the MINERνA Collaboration developed empirical low-Q^2 suppression models for each channel, a combined model incorporating all channels, and an additional model to account for the suppression observed in MINOS [166]. These models currently provide the most accurate estimation of low-Q^2 suppression when utilising a scintillator target.

Liquid Argon Time Projection Chambers (LArTPC) are commonly known as 'modern bubble chambers' because of their high-resolution capabilities down to the millimetre scale and low-energy particle tracking thresholds [167]. Consequently, LArTPCs have the capacity to perform precise measurements of particle kinematics and excellent particle identification abilities for selecting specific final states.

As of the time of writing, the MicroBooNE experiment stands as the first and only LArTPC experiment to conduct a cross section measurement of $\nu_\mu CC\pi^0$ production on argon [168]. MicroBooNE made the measurement by requiring one or more reconstructed photons, resulting in the selection of 771 candidate events from the data sample, with an estimated purity of 56% and efficiency of 16% [168]. The measurement employed completely automated reconstruction techniques and successfully demonstrated its capacity to reject cosmic ray backgrounds that affect surface detectors, highlighting essential capabilities for future SBN measurements.

Figure 2.24 shows the MicroBooNE measurement of CC single-π production in neutrino-argon scattering compared to a collection of models incorporated within the GENIE and NUWRO [169] neutrino event generators, which, validated by prior measurements, effectively characterise this process on lighter nuclei. Both ANL and MiniBooNE measurements align with the predictions from GENIE models, except for a slight deficit (1.2σ) observed in the case of argon. In addition, the systematic uncertainties, mainly influenced by flux, and statistical uncertainties create challenges in making meaningful comparisons between generators [168].

In recent years, considerable progress has been made in both theoretical models and experimental measurements. Notably, nuclear effects, such as removal energy, Fermi momentum, and FSI, are now better modelled and constrained. Nevertheless, extending these models to heavier nuclei, like argon, still poses challenges. The comprehension of these effects is crucial not only for advancing our understanding of nuclear physics but also for realising

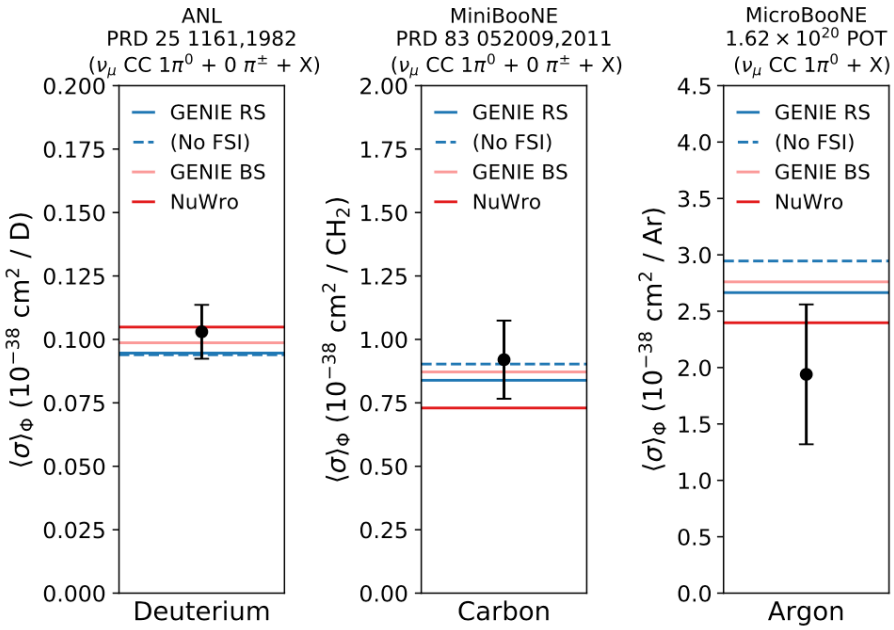

Figure 2.24: Total cross sections of ν_μ CC single π^0 interactions measured by ANL, MiniBooNE, and MicroBooNE, including total uncertainty represented by the bars. Figure from [168]

the full physics potential of upcoming generation oscillation measurements, especially for projects like SBN and DUNE.

2.5 Summary

Since the discovery of neutrinos, significant progress has been made in experimental and theoretical research to better comprehend their properties and behaviour. Notably, the observation of neutrino oscillation was the first evidence beyond the standard model. Ongoing efforts to characterise neutrino oscillation and interactions are essential to measure its parameters and explore anomalous outcomes. Improved modelling of neutrino-nucleus interactions underpins these efforts. However, continued efforts are needed to unlock the full potential of upcoming neutrino experiments, particularly those using heavy nuclear targets like Ar in projects such as DUNE. This thesis focuses on assessing SBND capability to measure ν_μ CC π^0 production cross sections, advancing the current statistically limited measurements.

Chapter 3

Liquid Argon Time Projection Chambers for Neutrino Detection

Liquid Argon Time Projection Chambers (LArTPCs) are an advancing detector technology in neutrino physics, often likened to modern bubble chambers. LArTPCs have undergone substantial development and have emerged as highly effective particle detectors with remarkable precision and detection capabilities. This technology uses the unique properties of liquid argon, utilising it both as the target material for particle interactions and as the detection medium. As mentioned in Chapter 2, the ongoing Short-Baseline Neutrino (SBN) program and the upcoming Deep Underground Neutrino Experiment (DUNE) are prime examples of experiments harnessing the potential of LArTPC technology. It is crucial to understand the characteristics of the effects of the detector in order to achieve the desired scientific objectives of these experiments.

This chapter presents an overview of LArTPC detector technology, its historical context, operational principles, and ongoing development of novel readout methods. Firstly, in Section 3.1 presents a historical and general introduction to LArTPCs with the properties of liquid argon and the operating principles of LArTPCs. Following that, Section 3.2, a comprehensive summary is provided regarding how particles distribute their energy within the detector. Next, the trajectory of the resulting electrons and photons generated by these energy depositions towards the detectors responsible for their detection is elucidated in Section 3.3. Lastly, the electrons and photons detection, emphasising the vital readout technologies employed in this process, is presented in Section 3.4.

3.1 LArTPC Technology Overview and Development

The Liquid Argon Time Projection Chamber (LArTPC) is a highly effective technology employed for capturing high-resolution representations of particle interactions. It offers valuable information about the topology and calorimetry of charged particles that pass through the detector. LArTPC technology was proposed in 1977 by Carlo Rubbia to overcome limitations of choosing between high-resolution and event rate in experimental neutrino physics. Rubbia's solution was an "electronic bubble chamber" that electronically collects and computationally reconstructs highly detailed images of all neutrino interaction products [167]. As a result, LArTPCs emerged as an optimal instrument for investigating phenomena such as neutrino oscillations and other fundamental physics.

Using noble liquid elements, such as liquid argon, in neutrino detectors offers significant advantages. The high density of liquids compared to gases increases the number of interaction targets for neutrinos within a given volume. Moreover, the increased density results in higher energy loss by charged particles, enhancing the detector's calorimetry capabilities and forcing particles to deposit more energy in a shorter range. Liquid Argon (LAr) is an excellent choice as a neutrino detection medium due to its density, stopping power, high scintillation light yield and transparency to its scintillation radiation. The key physical properties of liquid argon relevant to LArTPCs are summarised in table 3.1 [170, 2, 51].

As argon is the third most abundant gas in the Earth's atmosphere, it can be acquired in significant quantities through cryogenic distillation of air. As a result, the abundant availability of LAr at a reasonable cost makes it a feasible choice for constructing neutrino detectors ranging from a few tons to several kilotons in scale. Additionally, pure LAr possesses several advantageous characteristics, including enabling extended drift times, a remarkably low ionisation capture rate, and high electron mobility. The detection of ionisation charge, coupled with the use of scintillation light, renders LAr detectors highly appealing for the identification and analysis of charged particles.

The time projection chambers are essentially large vessels containing a medium, LAr in this case, which enable the reconstruction of charged particle interactions by effectively capturing ionisation charges. Figure 3.1 illustrates the fundamental operations of a LArTPC. When particles traverse the bulk of the detector, they cause the ionisation of argon atoms along their trajectory. An electric field is applied across the detector, enabling the drift of these charges towards the designated collection point, where their readings signify the presence of ionisation and, thus, the passage of particles in the detector.

At one of the TPC sides, there is a mesh of wires serving as the data collection points. These wires align with the direction of the electric field. The TPC includes three wire planes: two induction planes (U and V) and one collection plane (Y), as seen in Figure 3.1. The

Property	Symbol	Value	Unit
General and Thermodynamic properties			
Atomic weight		39.948	u
Normal boiling point	T_{NBP}	87.303(2)	K
Density	ρ_{NBP}	1.3954	g/cm^3
Electron Transportation (0.5 kV/cm at 87.3 K)			
Electron mobility	μ	318.5779	$cm^2V^{-1}s^{-1}$
Electron drift velocity	v	0.1593	$cm/\mu s$
Effective longitudinal electron energy	ε_L	0.0208	eV
Longitudinal diffusion coefficients	D_L	6.6156	cm^2/s
Transverse diffusion coefficients	D_T	13.2099	cm^2/s
Electron lifetime (for 0.1 ppb O^2)	τ	2.9931	ms
Response to ionization radiation			
W-value for ionization	W_i	23.6(3)	$eV/pair$
Fano factor	F	0.107	–
Moliere radius	R_M	9.04	cm
Radiation length	X_0	14	cm
Nuclear interaction length	λ_i	85.7	cm
Critical energy, $e^{\pm}$	$E_{c,e}$	32.8	MeV
Critical energy, $\mu^{\pm}$	$E_{c,\mu}$	485	GeV
Mininum specific energy loss	$(dE/dx)_{MIP}$	2.12	MeV/cm
Scintillation properties			
W-value for scintillation	W_s	19.5	$eV/photon$
W-value for Cerenkov radiation	W_c	2700	$eV/photon$
Scintillation emission peak	λ_{scint}	128(10)	nm
Decay time (singlet, triplet)	τ_{scint}	6(2), 1590(100)	ns
Dielectric constant	ε	1.505(3)	–
Index of refraction (at 128 nm)	n	1.38	–
Rayleigh scattering length (at 128 nm)	L_R	95	cm
Absorption length (>128 nm)	L_A	>200	cm

Table 3.1: Key physical characteristics of liquid argon essential to LArTPCs [2].

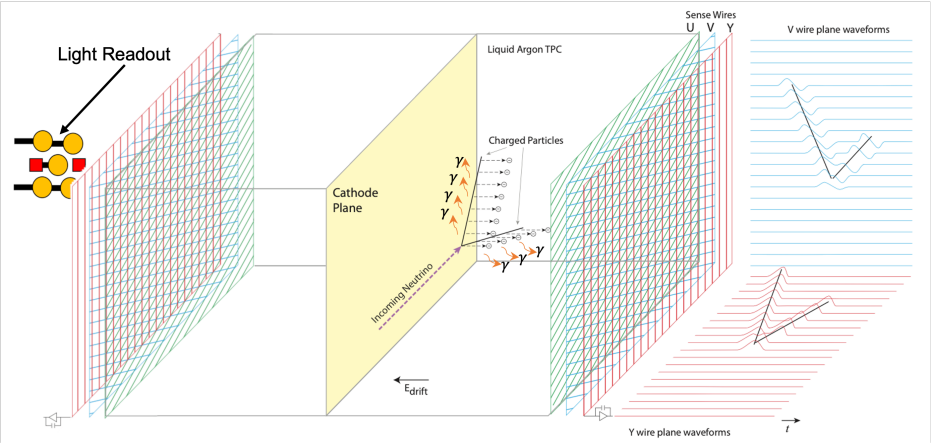

Figure 3.1: Diagram illustrates the fundamental operations of a LArTPC [171].

induction planes, at a lower electric potential, allow electrons to drift past and generate a current. The induction planes' currents enable 2D projections of the charge within the detector. The collection plane (Y-plane) gathers electrons as a current, resulting in an additional signal. Furthermore, situated behind the wire planes is a photon detection system (PDS) designed to capture the scintillation photons produced alongside the drift electrons as will be discussed the next sections. Through the analysis of signals detected on the segmented wire planes, the arrival times of the drifting electrons and timing information from scintillation photons, it becomes possible to achieve comprehensive three-dimensional (3D) reconstruction and calorimetry of the ionisation track.

For surface LArTPC experiments, only electrons reaching the wire planes within a specific readout window are recorded, excluding those outside. This readout window is synchronised with the beam spill time and lasts for the longest drift time of ionisation electrons resulting from neutrino interaction events. The purpose of this approach is to reduce the recording of cosmic rays that pass through the detector during the readout window [1].

Figure 3.2 shows an event display of a simulated ν_μ Charged Current (CC) interaction with a final state topology involving a π^0, where the colour reflects the charge deposition. The visible neutrino interaction is emphasised by the deposited charge arising from low-energy hadronic activity and resulting in the emergence of two-photon showers generated by π^0 decay, a muon track, and a proton track. The clear presence of the anticipated Bragg peak, characteristic of a stopping particle, is observed as the energy deposition along the length of the proton track increases. Conversely, the photon showers display complex substructures due to stochastic showering processes. This event display effectively demonstrates the capacity of LArTPC to provide comprehensive information in terms of both calorimetry and the topological aspects of neutrino interactions.

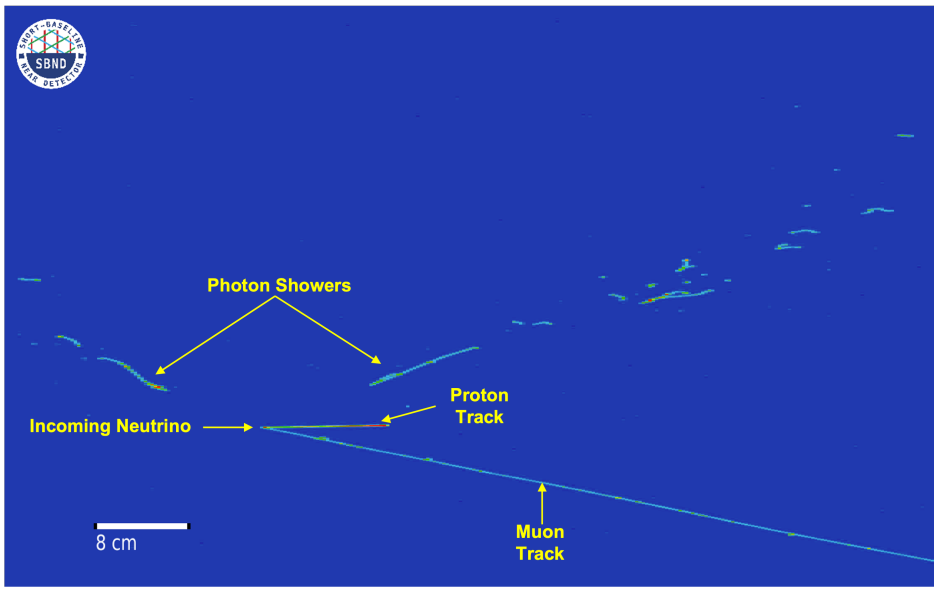

Figure 3.2: Event display of a simulated ν_μ CC π^0 interaction in SBND, generating two photon showers from π^0 decay, muon and proton tracks.

In the 1989, Imaging Cosmic And Rare Underground Signals (ICARUS) collaboration utilised this technology in their proposed detectors, aiming to study solar neutrinos, proton decay, and cosmic neutrino interactions across different energy ranges [172]. These aims were to be achieved through a two-step experimental process, the first of which was the construction of a small-scale LArTPC detector prototype [173]. The second step was the construction of a large-scale detector referred to as the ICARUS T600, which consisted of two cryostats accommodating an active target mass of 235 tons each [174]. During its operation at the Gran Sasso underground laboratory, the ICARUS experiment effectively showcased the hardware and reconstruction capabilities of LArTPCs [175, 176]. Eventually, ICARUS was relocated to Fermilab to become the far detector within the Short Baseline Neutrino program (SBN) [1].

Another significant liquid argon detector was the Argon Neutrino Test-stand (ArgoNeuT), located in Fermilab's Neutrinos at the Main Injector (NuMI) beam. This achieved groundbreaking cross-section measurements on argon despite its limited active mass of 24 kg [177]. ArgoNeuT was positioned upstream of the Main Injector Neutrino Oscillation Search (MINSO) new detector, allowing for energy estimation of tracks that are not fully contained. ArgoNeuT provided additional evidence of the capacity of LArTPCs to achieve accurate measurements of neutrino interactions, characterised by low thresholds and exceptional Particle IDentification (PID) capabilities, employing semi-autonomous reconstruction techniques[178–184]. Later, the cryostat, originally used in ArgoNeuT, was reused for the

Liquid Argon In A Testbeam (LArIAT) experiment, which focused on measuring the hadronic interaction cross-sections of particles generated in a testbeam [185]. These essential testbeam experiments contribute to the accurate modelling of particle interactions in LArTPCs [186].

The 85-ton MicroBooNE was the next LArTPC to be built. It was positioned upstream of MiniBooNE in the Booster Neutrino Beam (BNB) and used examine the low energy excess, as discussed in Section 2.3 [171]. Advancements were made to enhance detector technology and reconstruction techniques, with a focus on addressing challenges associated with high cosmic ray rates in surface detectors. Utilising both the BNB and the off-axis NuMI beam, MicroBooNE conducted various cross-section measurements, further showcasing the LArTPC capabilities [187, 188]. Notably, it achieved the first measurement of ν_μ CC single π^0 production on argon cross-section and highlighted the effective reconstruction and analysis of neutrino interactions leading to electromagnetic showers in the final states [168]. However, despite the search for the low energy excess reported by MiniBooNE, MicroBooNE found no supporting evidence, adding further complexities to the field [189, 190].

Next, the SBN program at Fermilab was proposed to investigate the low energy excesses from LSND and MiniBooNE. It involves three detectors at different baselines along the BNB, aiming to search for oscillations caused by sterile neutrinos. The program, described in more detail in Chapter 4, includes the Short-Baseline Near Detector (SBND), MicroBooNE, and a rebuilt ICARUS serving as the near, intermediate, and far detectors, respectively. Additionally, the upcoming DUNE detector aims to make precise long-baseline measurements of neutrino oscillations, including the measurement of δ_{cp} [69]. DUNE will feature four 10 kt LArTPCs, significantly larger than previous detectors. The scalability of the detector technology was demonstrated by the protoDUNE prototypes, with a mass of 530 tons [191]. New readout technologies that enhance performance within high-multiplicity environments have also been demonstrated, driven in part by the near detector requirements [192, 193]. New work in this area, notable the development of pixel charge readout, is presented in Chapter 9 and 10.

3.2 Ionisation and Scintillation in LAr

In the context of particle interactions in a LArTPC, it is important to understand how heavy charged particles, such as muons, pions, kaons, and protons, deposit energy per unit distance (dE/dx) due to their distinct properties. These particles generate track-like features in the detector and follow the Bethe-Block formalism [194], an example can be seen in Figure 3.2. Figure 3.3 presents an illustration of the mass-stopping power of muons in copper, calculated using the Bethe-Block equation. It is worth noting that these underlying mechanisms can be applied to argon as well [194]. In the central region of the figure, the stopping power aligns

with the the Bethe-Block formalism. However, at higher energies, radiative effects begin to dominate, causing the emission of photons that carry away the particle's energy. Similarly, at lower energies, the velocity of the particles approaches that of atomic electrons, rendering the Bethe-Bloch equation unreliable in these scenarios [194].

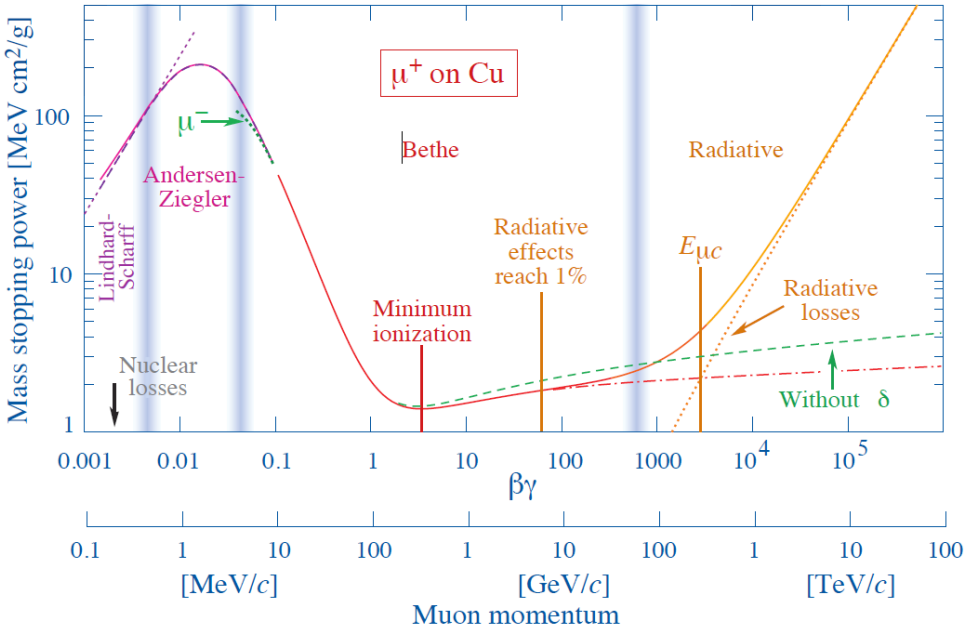

Figure 3.3: The energy loss of particles in a medium, demonstrated by the case of a muon in copper. The mass-stopping power of muons in copper is depicted across various energy and momentum ranges. The energy loss for tracks and showers is represented by the Bethe-Block and radiative regimes, respectively. In LArTPC experiments, muons typically have energies below 10 GeV, resulting in an average deposited energy per length of 2.2 MeV/cm. At lower energies, the increase in stopping power corresponds to the observation of Bragg peaks as particles come to rest within a detector. Plot from [194].

Tracks in a detector generally exhibit linear energy deposition through ionisation, but are subject to Multiple Coulomb Scattering (MCS) depending on the momentum of the particle. The energy deposition per unit length (dE/dx) remains relatively constant in the MIP region, although exhibiting a rise known as the Bragg peak as the particle approaches rest. This energy loss profile varies based on particle mass making it useful for particle identification [177]. Energy depositions in MIP tracks are described by a Landau-Gaussian Convolution (LGC) with occasional deviations from the Most Probable Value.

Electromagnetic showers result from the interaction of electrons/positrons, following the principles of the Bethe-Bloch formalism, or photons. Electrons primarily release energy through Bremsstrahlung, leading to the deposition of MIPs. Photons, on the other hand,

undergo energy loss via the photoelectric effect and Compton scattering at low energies, a few MeVs, while pair production becomes dominant at higher energies. The electron-positron pair further contributes to photon production via Bremsstrahlung. This process persists until photons lack sufficient energy for pair production and electrons can no longer emit photons through Bremsstrahlung, generating shower-like phenomena as depicted in Figure 3.2.

The types of electromagnetic activity may appear visually similar, in most cases, but they can be distinguished by the dE/dx at the beginning of the shower. When the photon undergoes pair production, it leaves a signature indicative of two times the MIPs. Hence, the dE/dx at the beginning of the shower can be used to determine between single MIP, indicating an electron shower, and double MIP, indicating a photon shower. In addition, before interacting with the argon, photons travel a certain distance without causing any ionisation due to their neutral nature, resulting in the presence of a noticeable gap known as a conversion gap. Figure 3.4 depicts the distance travelled by photons in argon before interacting [195]. At low energies, photons interact mainly through Compton scatter, while at higher energies, they predominantly undergo pair production into e-e+ pairs, enabling differentiation between electrons and photons based on conversion gaps and energy loss profiles, discussed in details in Section 6.2.

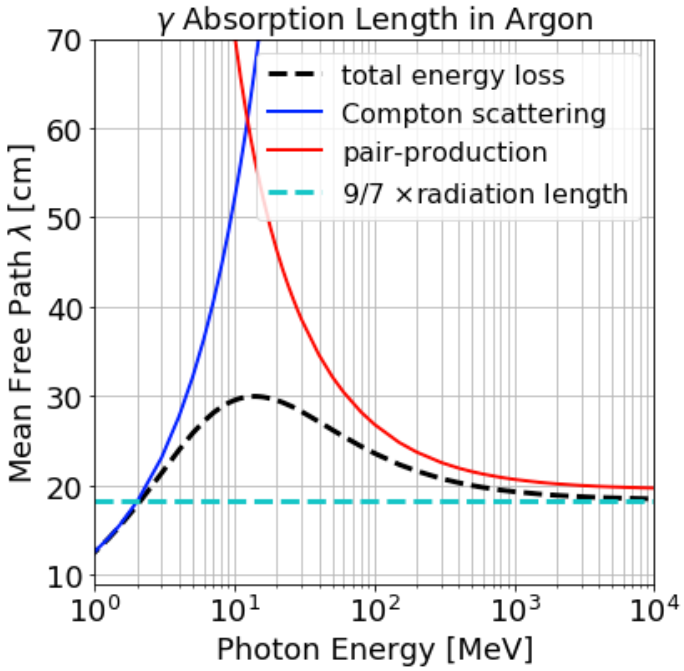

Figure 3.4: Presentation of the energy-dependent mean free path of photons, depicting contributions from various interaction modes in conjunction with the total and asymptotic limits. Plot from [195].

Charged particles passing through argon lose energy through ionisation and excitation of argon atoms. The production of ionisation and excitation of argon atoms is depicted in Figure 3.5. The released electrons can then either recombine with the argon ions, referred to as recombination, or escape and subsequently drift towards the anode. Additionally, the excited argon atoms, resulting from collisions or recombination, commonly form excimers that decay by emitting a 128 nm Vacuum Ultra-Violet (VUV) photon with 9.69 eV energy to return to a stable state, facilitating their return to a stable state [196].

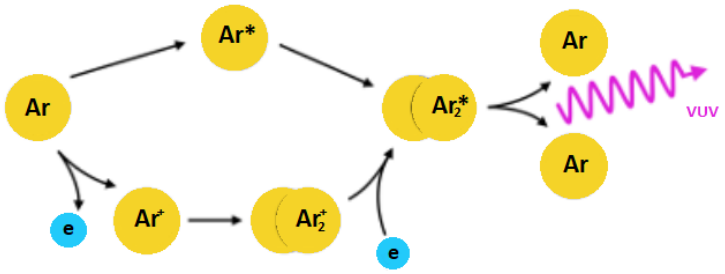

Figure 3.5: Diagram depicting the process of argon atoms becoming excited (top) or ionised (bottom) when a charge particle passes in close proximity [197].

After the production of ionisation electrons, they may thermalise by interacting with the surrounding medium and recombine with nearby ions, in which recombination plays a crucial role in determining the overall behaviour of electron-ion pairs. The recombination rate of the electron-ion process is commonly assessed using the recombination survival probability, recombination factor, (R). This factor represents the ratio of electrons that escape to the initial number of electron-ion pairs formed (and can be estimated using equation 3.1). The recombination process relies on two primary factors: the strength of the external electric field [198] and the density of ionisation [199]. In the presence of stronger electric fields, a greater number of ionisation electrons and ions are drifted from the region of deposition before recombination occurs, thereby contributing to the overall deposited charge. Conversely, at weaker electric fields, the likelihood of recombination decreases, leading to reduced charge and increased production of scintillation light. In the case of ionisation density, the recombination process increases as a result of the decreased distance between electrons and ions, leading to the generation of a more densely populated ionisation cloud. Hence, The recombination factor can be estimated using:

$$R = \frac{W_{ion}\frac{dE}{dx}}{\frac{dQ}{dx}} \tag{3.1}$$

where W_{ion} represents the energy necessary for ionising an argon atom, which is equal to 23.6 eV [200], and dE/dx and dQ/dx denote the energy and charge loss per unit length.

The recombination factor is commonly described through the implementation of either the modified box model or the Birks model, can be found in references [201] and [202], respectively. The original box model is founded on the concept of columnar theory encompassing the charge deposition, subsequently refined by incorporating experimentally derived parameters to enhance its alignment with data, particularly at low charge densities [201, 199]. The Box model considers ion mobility and electron diffusion to be insignificant during the process of recombination within liquid argon. In the Birks model, it considers a Gaussian spatial dispersion surrounding the particle's trajectory throughout the recombination phase, and that ions and electrons exhibit equal charge mobility. These models determine the recombination survival fraction of ionisation electrons depend on factors such as the density of electron-ion pairs, the electric field, the distance between electron and ions after thermalisation, the particle angle relative to the electric field direction, and the diffusion coefficient in the Birks model. Figure 3.6 presents a comparison of these models, illustrating their non-linear relationship with dE/dx. Understanding of recombination plays a crucial role in accurately reconstructing the deposited energy based on the detected charge in the detector.

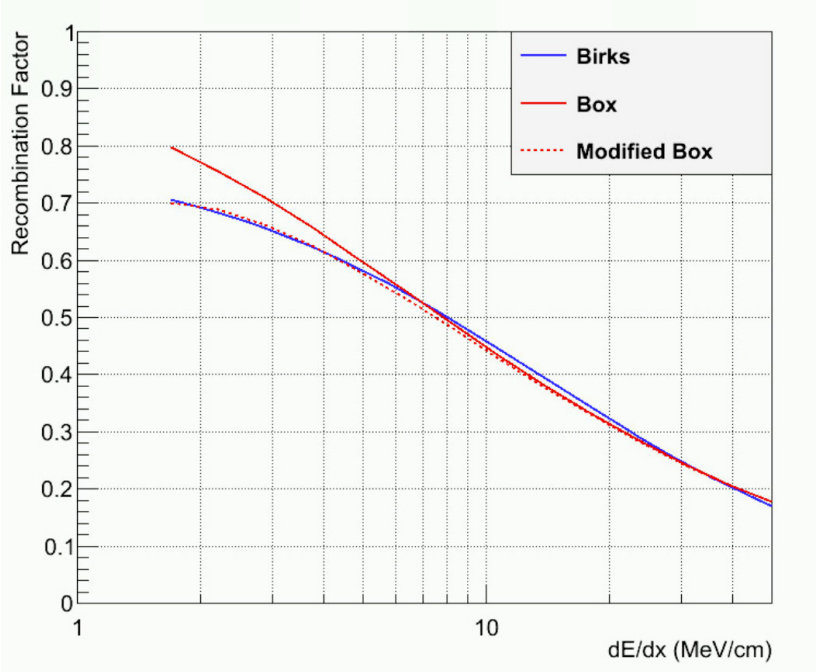

Figure 3.6: The recombination process, which represents the proportion of electrons that remain unrecaptured by argon ions, is dependent on the energy density deposited at 500 V/cm electric field strength [199].

The generation of argon excitons and excimers can undergo a quenching process, resulting in heat production instead of light emission. The presence of impurities, such as oxygen and water, may impact the rate of this quenching phenomenon [203]. Excimers can exist in two states, namely singlet and triplet states, with respective decay times of approximately 6 ns and 1300 ns [204]. Additionally, particles moving at high velocities can generate Cherenkov light, although its light yield is considerably lower than that of scintillation light [205].

3.3 Electron and Photon Transport in Argon

After escaping recombination with argon ions, the liberated electrons are subsequently guided by an electric field generated through the application of a high negative voltage to a cathode as illustrated in Figure 3.1. The mobility of electrons travelling through argon depends primarily on the temperature and density of the argon. Under typical conditions in a LArTPC with a drift field of 500 Vcm^{-1}, the electrons move away from the cathode at a speed of 160 cm/ms [170]. These factors collectively govern the dynamics of ionisation electrons resulting from neutrino-argon interaction as they traverse the detector.

Moreover, the movement of electrons in the LArTPC is influenced by diffusion, which occurs in both the longitudinal (drift) direction, represented by the coefficient D_L, and the transverse direction, represented by D_T. The magnitude of the electric field, along with the values of D_L and D_T, determines the extent of diffusion and thus imposes constraints on the dimensions of the drift region within the LArTPC. The pulse time-width is described by the following model:

$$\sigma^2(t) = \sigma_t^2(0) + \left(\frac{2D}{v_d^2}\right) t \tag{3.2}$$

where σ is the measured time-width of the signal which depends on various factors, including the initial width $\sigma_t(0)$, the effective diffusion coefficient D with a minor contribution from transverse diffusion, the drift velocity v_d, and the drift time t [206]. Measured values of the diffusion coefficients under similar standard conditions can be found in Table 3.1.

The ions generated during ionisation drift towards the cathode with a velocity of 0.8 cm/s, which can result in the alteration of the electric field distribution within the LArTPC [207]. This phenomenon referred to as the Space Charge Effect (SCE) results in a deviation in the reconstructed position of ionisation electrons in the signal. In surface LArTPC detectors, this effect is mainly attributed to the ionisation rate caused by cosmic rays, which continuously drift within the chamber [208]. The distortions in the electric field can impact both the calorimetric and spatial aspects of energy depositions. Calorimetric effects arise from the

influence of the local electric field on the recombination process. Spatial deviations occur as electrons drift along a distorted field, resulting in curved tracks and shifting the endpoints away from the edges of the detector. If left uncorrected, these effects can introduce distortions in calorimetry, impacting PID and energy resolution, as well as inaccuracies in track lengths and positions. To assess and mitigate these effects, a combination of muon tracks from cosmic ray and specialised laser calibration systems can be employed [208]. By measuring these effects, spatial and calorimetric corrections can be implemented to mitigate their impact.

Drifting electrons may be captured by impurities in the argon, including oxygen and water, which results in a reduction of signal amplitude upon reaching the wires. For instance, ProtoDUNE, which employs the same cryostat technology as SBND, has achieved oxygen-equivalent purity levels of 3.4 ppt, resulting in lifetimes exceeding 100 ms [209]. Since the drift time of SBND is 1.25 ms, the effect of this level of impurity if found in SBND would be negligible. However, corrections are still implemented during calorimetric reconstruction to compensate for this attenuation, as outlined in Chapter 6.

As stated earlier scintillation light is also generated by particle interactions in liquid argon. The photons from this travel through the detector, its detection probability determined by the detectors' solid angle. However, Rayleigh scattering can occur, causing elastic scattering of photons off nuclei and reducing light yield over long distances [210]. The distance of photon propagation before scattering depends on the wavelength, typically ranging from 66 to 90 cm for 128 nm light [211, 212]. In order to mitigate against Rayleigh scattering and enhance the number of detected photons, a strategy involving the employment of a light shifting technique that shifts the wavelength to a longer range is pursued. In SBND wavelength-shifting foils coated with TetraPhenyl Butadiene (TPB) are applied on the cathode to reflect the incoming light towards the light detectors positioned behind the anode [1, 213].

3.4 Ionisation Charge and Scintillation-Light Detection

After electrons travel through the argon and reach the anode planes, they generate a signal on a readout system. As outlined in Section 3.1 this is achieved traditionally using multiple wire planes comprising parallel wires typically spaced a few millimetres apart. The first planes are biased with a voltage to ensure that drifting electrons passing through these planes are collected on the final plane. These planes are commonly known as induction and collection planes, respectively, based on the shapes of the induced signals (see Figure 3.1). In addition, Figure 3.7 shows the signal characteristics of the LArTPC on each wire plane [214]. The induction planes, denoted as U and V, display small bipolar signals resulting from the passage of electrons, while the collection plane, labelled as Y, exhibits unipolar signals.

Typically, there are three planes positioned 60 degrees apart, minimising the impact of tracks aligned parallel to a wire plane. Incorporating signals from these planes enables accurate reconstruction of the energy deposition position in the perpendicular plane.

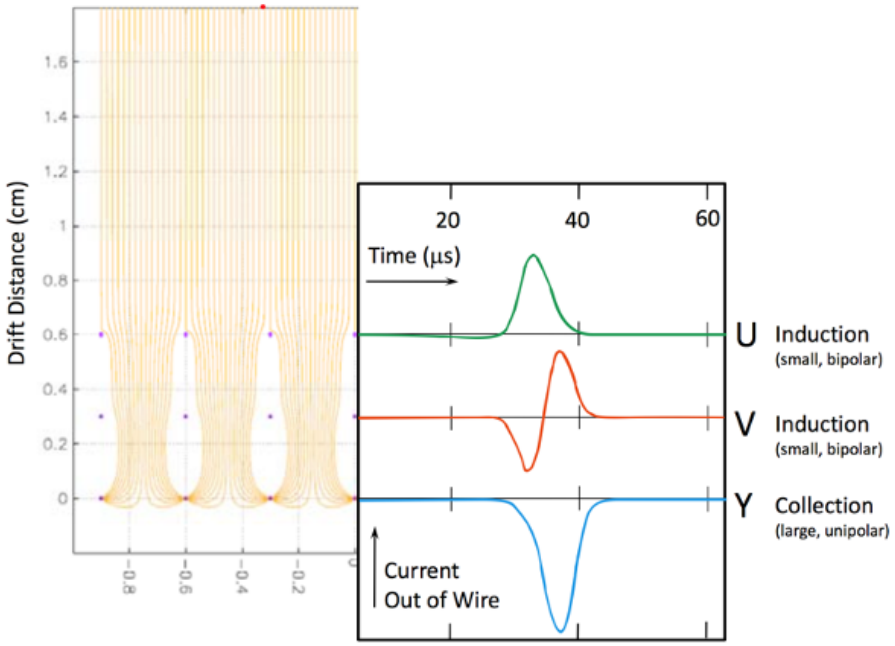

Figure 3.7: The signal characteristics of the LArTPC on the wire planes [214].

The induced signals on the wires undergo shaping, amplification, and digitisation by cold electronics, which are placed within the LAr, then recorded by the Data Acquisition (DAQ) system. This placement significantly reduces noise compared to warm electronics located outside the LAr, thanks to decreased thermal interference and cable lengths, leading to reduced capacitance [215]. Typically, the data is captured during a drift window, which accounts for the time it takes for the charge to traverse the entire distance between the cathode and the anode, with additional padding to capture cosmic rays occurring outside the trigger time. In modern LArTPCs, a significant portion of the noise originates from the inherent capacitance of the TPC wires rather than external wiring or electronics. To mitigate this noise and improve the Signal-to-Noise Ratio (SNR), filtering techniques, both hardware and software based, can be implemented [215].

The VUV light generated during the ionisation process in a LArTPC can be detected using a wavelength shifter, often TPB, which converts the light to a longer wavelength suitable for detection, usually by a Photo-Multiplier Tube (PMT). This is commonly achieved by coating the PMTs with TPB, but TPB-coated reflective foils can also be employed. TPB

has demonstrated high efficiency, approaching 100%, although it may introduce a time delay as a result of de-excitation processes [204].

Efforts have been undertaken to enhance the capabilities of LArTPC through advancements in readout technologies for efficient charge collection and scintillation light detection. Pixelated readout have shown the capability to achieve complete 3D reconstruction without the ambiguities associated with wire-based systems [216, 193], details in Chapter 9. New work in this area is discussed further in Chapter 9. This is of significant importance for detectors with high occupancy rates, such as the planned DUNE near detector. Additionally, dual-phase readouts, where electrons are extracted to a gaseous phase for signal amplification and subsequently read out using a Printed Circuit Board (PCB), holds promise for potentially improving the SNR, see [217].

In the case of VUV light detection systems, ARAPUCA (Argon R&D Advanced Program at UniCAmp) offers an alternative approach to photon detection by using wavelength shifters and dichroic filters to trap the light. The dichroic filters are reflective but allow a narrow range of wavelengths to pass through [218]. Coating the dichroic filter with a wavelength shifter ensures the incident VUV light is shifted to a longer wavelength, preventing it from exiting the filter. The trapped light is internally reflected until it reaches a series of Silicon Photo-Multipliers (SiPMs). In the refined X-ARAPUCA design, a wavelength shifting light guide guides the light to the SiPMs [219]. Figure 3.8 presents the ARAPUCA and X-ARAPUCA working principle. These detector are specifically developed for the DUNE detector, addressing the space limitations between the anode planes for conventional PMTs. Moreover, their ability to operate in an external electric field presence, provides more placement options.

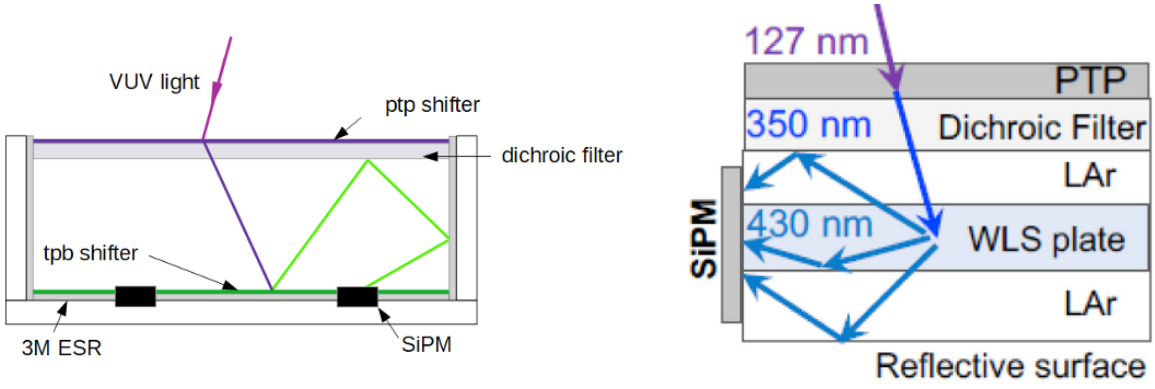

(a) ARAPUCA (b) X-ARAPUCA

Figure 3.8: ARAPUCA and X-ARAPUCA working principle [220, 221]

3.5 Summary

Since 1977, LArTPCs have evolved significantly and proven to be effective as particle detectors with high acceptance and low detection thresholds. LArTPC technology is a type of particle detector that utilises liquid argon as both the target material and the detection medium. Charged particles passing through the liquid argon create ionisation trails and scintillation light. These ionisation trails are then drifted towards an anode using an electric field, and by measuring the charge distribution on the anode, the position and energy of the particles can be reconstructed. To detect the ionisation trails, various readout technologies are employed. Traditional methods involve wire planes, where parallel wires separated by a few millimetres are used to collect the charge. Induction and collection planes are utilised to shape the signals induced by the passage of electrons. To capture the scintillation light generated during ionisation, a wavelength shifter, typically TPB, is employed to transform the VUV light into a longer wavelength that can be sensed by PMTs or other light detectors. This enables the detection of both ionisation and scintillation signals, providing complementary information for event reconstruction. Continuous technical advancements have expanded the application of LArTPCs, enabling the development of larger detectors and more suitable readout technologies for environments with high particle multiplicity. The upcoming generation of LArTPCs aims to further advance our knowledge of neutrino interactions and oscillations, such as employed in the SBN program.

Efforts are ongoing to improve LArTPC technology, including enhancing readout capabilities and exploring alternative readout methods, discussed further in Chapter 9. These efforts involve exploring alternative readout options, such as pixelated readouts and dual-phase readouts, which improve spatial reconstruction without the ambiguities of wire-based systems and enhance the SNR of the detected signals. In addition to readout technologies, other techniques are used to detect light produced in LArTPCs. For instance, the ARAPUCA project uses a combination of wavelength shifters and dichroic filters to trap light, which is then detected by SiPMs.

Overall, LArTPC technology continues to evolve and adapt, offering improved precision and capabilities for particle detection and analysis in the field of particle physics research. SBND, as a prime example of this, and the subject of this work, is described next in Chapter 4.

Chapter 4

The Short-Baseline Near Detector

The Short-Baseline Neutrino (SBN) program aims to investigate the anomalies observed in the LSND and MiniBooNE experiments by searching for evidence of oscillations induced by sterile. The program utilises three Liquid Argon Time Projection Chambers (LArTPCs) - SBND (Short-Baseline Near Detector), MicroBooNE, and ICARUS - positioned at different distances from the Booster Neutrino Beam (BNB) where MiniBooNE observed its excesses. SBND, specifically, has a significant impact on reducing systematic uncertainties in oscillation measurements and also pursues an extensive physics agenda of its own.

The chapter begins, covered in Section 4.1 by providing an overview of the SBN program and its underlying physics objectives. Subsequently, in Section 4.2, the details of the Booster Neutrino Beam (BNB) utilised in the SBN program, emphasising the importance of understanding the neutrino flux that reaches the SBND detector is presented. The chapter then proceeds, in Section 4.3, to outline the specific physics goals of SBND and provides comprehensive technical information about the detector itself, including the configuration of its time projection chamber (TPC) with drift regions and anode planes, the photon detection system (PDS), and the cosmic ray tagger (CRT) subsystem. In Section 4.4, a detailed discussion on the simulation workflow is presented, elucidating the employment of the LArSoft framework, event generators for both neutrino interactions and cosmic rays, GEANT4 for particle propagation, and the intricate simulations involved in charge and light propagation within the detector. Finally, section 4.5 presents a comprehensive overview of the signal processing and reconstruction methodologies employed in the various subsystems of SBND, highlighting their significance in the overall analysis of the collected data.

4.1 Short-Baseline Neutrino Program

The Short Baseline Neutrino (SBN) program encompasses a series of three LArTPC experiments strategically positioned at different distances along the Booster Neutrino Beam (BNB) at Fermilab. Figure 4.1 illustrates the arrangement of these detectors [1, 222]. The experiment configuration includes the Short Baseline Near Detector (SBND), the middle detector known as MicroBooNE, and the far detector named ICARUS T600. These detectors leverage the same BNB as MiniBooNE and employs the unique capabilities of LArTPCs. By placing these detectors at baselines of 110 m, 479 m, and 600 m respectively, the SBN program aims to comprehensively investigate the anomalies observed in the LSND and MiniBooNE experiments, while also paving the way for a deeper understanding of neutrino properties and potential new physics phenomena, detailed further in Section 4.1.1.

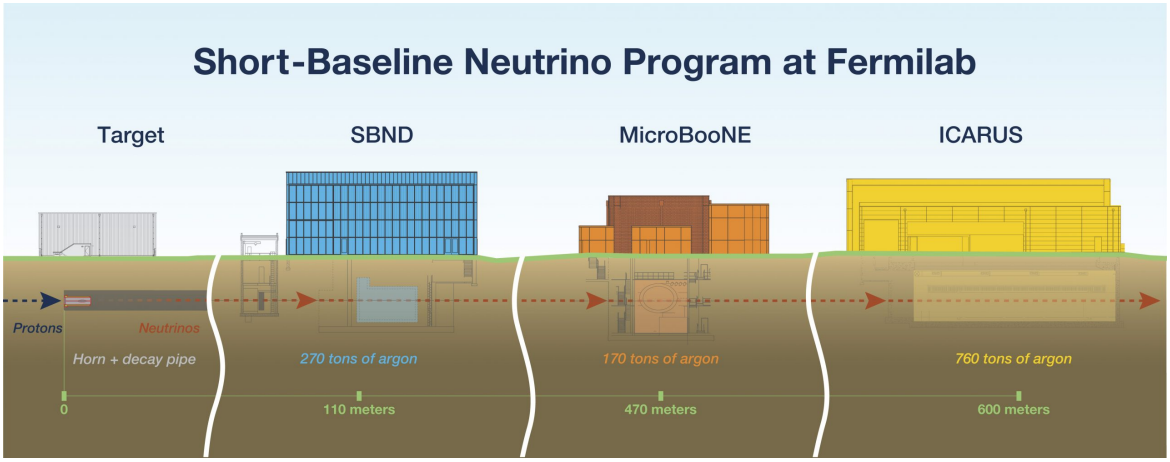

Figure 4.1: Diagram illustrates the arrangement of SBN program detectors with respect to the BNB neutrino beam. The individual masses of the experiments are also displayed in correlation with their respective distances from the BNB target [1].

The primary objective of the SBN program is to investigate sterile neutrinos through a coordinated effort involving three similar detectors. These detectors are strategically located to maximise sensitivity to important oscillation regions, thereby reducing uncertainties in sterile neutrino searches. By utilising the LArTPC technology, the program is able to distinguish and mitigate key background sources, such as photon-induced showers, thus enhancing its ability to draw conclusions regarding the 3+1 sterile neutrino model. Additionally, each experiment will independently explore novel detection techniques and conduct its own search for new physics. Extensive research into neutrino interactions on heavy nuclei will be conducted, and the program aspires to amass high-resolution data from millions of neutrino events in the few-GeV energy range, leveraging the dense nature of argon, the neutrino beam intensity,

and the essential features of the LArTPC detector technology. Ultimately, the SBN program aims to advance our understanding of sterile neutrinos and contribute to both nuclear and Beyond Standard Model (BSM) physics.

4.1.1 SBN Physics Aims

The primary objective of the SBN program is to investigate neutrino oscillations within the short baseline anomalies and analyse them in relation to sterile neutrino oscillations. Additionally, the program will have the capability to extensively study neutrino interactions on argon, benefiting from a substantial number of expected events, estimated at millions per year. These studies will enable precise measurements of cross-sections in various neutrino-argon interaction channels, which contributes to the advancement of future LAr experiments like DUNE. Notably, the SBN program provides an opportunity to explore theories in neutrino physics beyond the standard model, offering the potential to investigate a range of exotic hypotheses [223].

The baseline in SBN program has been carefully selected to achieve optimal sensitivity towards sterile neutrino oscillations within the framework of the (3+1) hypothesis across all three channels of short-baseline neutrino oscillation. Figure 4.2 displays the probabilities of ν_e appearance in these oscillation channels at the near and far detectors within the SBN program, considering the baselines and peak energy. These probabilities were computed for two different values of the mixing angle and mass splitting, aligning with the established limits derived from existing sterile neutrino data [223].

The ratios of oscillation probability between the far and near detectors, at the two-parameters limits, indicate that SBND will primarily be sensitive to observing oscillations when the mass splitting approaches the upper limits of its sensitivity range. However, the SBND will play a crucial role in constraining uncertainties in the oscillation analysis. The use of identical detector technology across all three detectors, resulting in correlated uncertainties in the BNB flux and neutrino-argon interaction cross-sections, which can be effectively mitigated in the joint oscillation analyses. MicroBooNE and ICARUS, due to their respective locations and energy ranges, are better suited for measuring the oscillated neutrino beam content [223].

The deviations observed in LSND and MiniBooNE experiments, as outlined in Chapter 2, currently stand at 3.8σ and 4.8σ respectively [75, 77]. Both MiniBooNE and LSND faced a significant challenge in dealing with topological backgrounds, specifically photon-induced electromagnetic showers, while attempting to interpret the anomalies in their quest to identify electron neutrino interactions. The distinguishing capability of LArTPCs to effectively discriminate electron and photon showers, which was not possible in MiniBooNE, plays

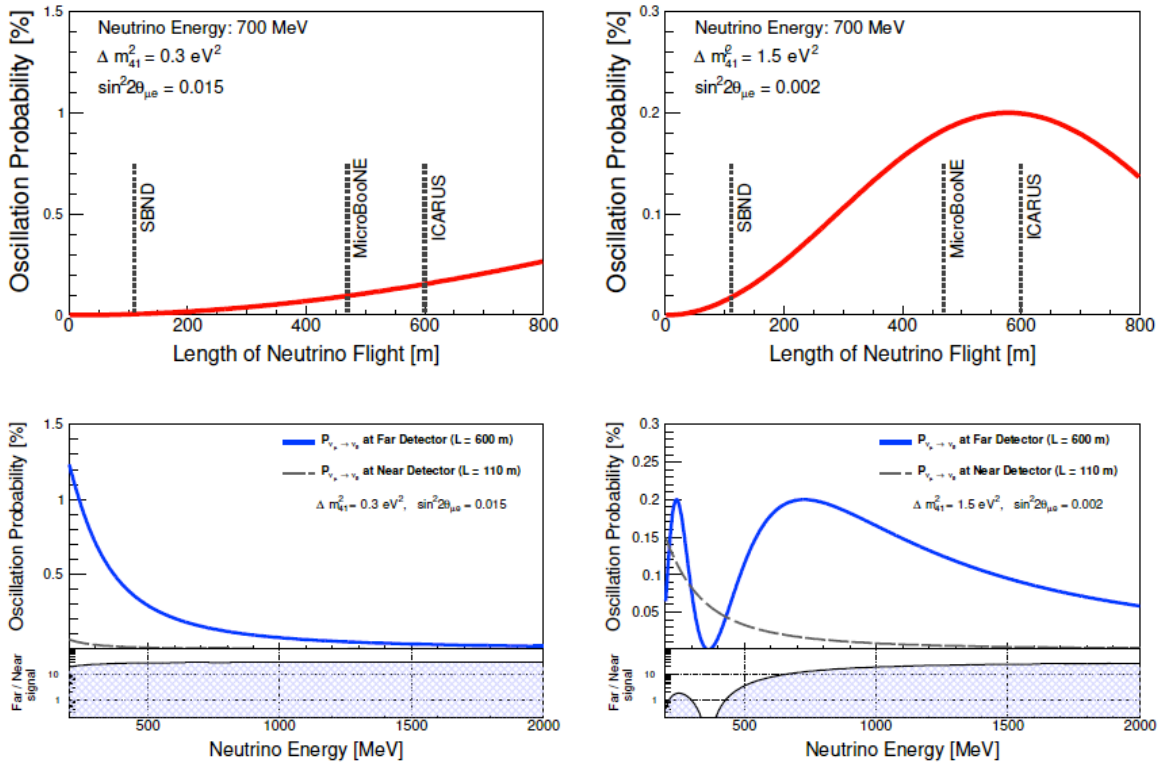

Figure 4.2: The upper plots show the oscillation probability of ν_e appearance for a 700 MeV neutrino, varying with the baseline. Two different benchmark points are considered in the context of a (3+1) sterile neutrino scenario. In the lower panels, the oscillation probabilities of ν_e appearance are shown at distances of 110 m and 600 m, as the neutrino energy varies, still considering the same benchmark points. Additionally, the ratio of appearance probabilities between the far and near detectors is shown [223].

a vital role in both background rejection and understanding the underlying cause of the excess [184]. Although initial searches conducted by MicroBooNE have not found any indications of excess in the electron or photon channels, a comprehensive analysis through the complete SBN program is necessary to conclusively address these discrepancies [189, 190, 224].

Figure 4.3 shows the SBN program exclusion sensitivity for both the disappearance of ν_μ and the appearance of ν_e. On the right plot it can be seen that the SBN program significantly surpasses the existing constraints, as indicated by the dashed lines, and excludes the shaded LSND allowed region at nearly 5σ in the ν_e appearance channel. Likewise, for ν_μ disappearance, the program widens the excluded region beyond the boundaries set by previous experiments. Leveraging its capacity to simultaneously investigate both appearance and disappearance modes, the SBN program intends to definitively resolve the low energy excesses observed by LSND and MiniBooNE.

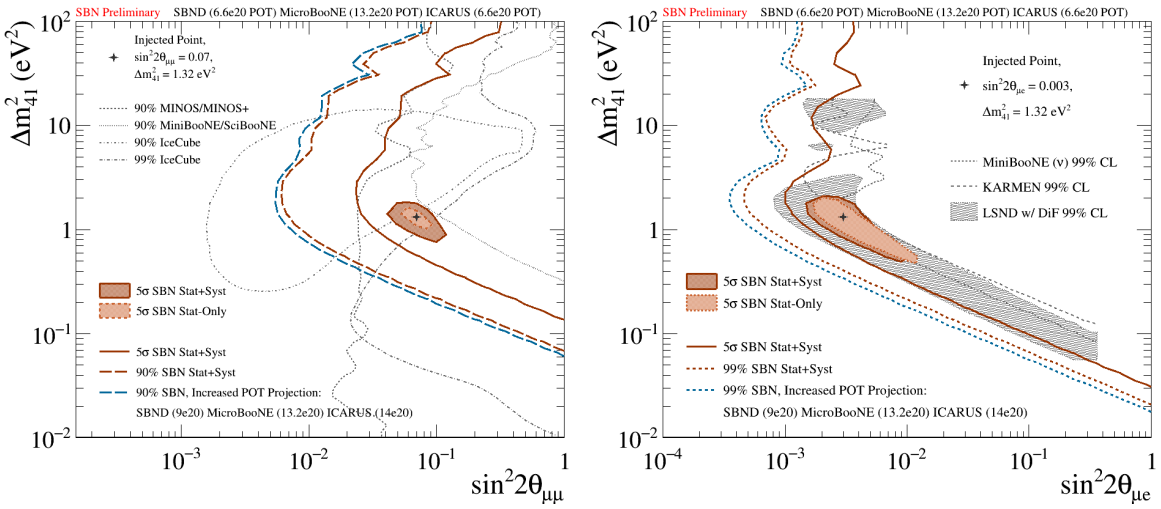

Figure 4.3: SBN program's sensitivity to ν_μ disappearance (Left) and ν_e appearance (Right). Plots modified from [225] with external data from [226, 81, 227, 84].

SBN also has a unique advantage in allowing the study of electron and muon neutrino interactions with the heavy argon nucleus. Using advanced LArTPC detector technology, SBN can achieve exceptional precision in measuring neutrino-argon scattering cross-sections across various charged current and neutral current topologies. The significant event rate, particularly in the SBND, will reduce statistical uncertainties to below the per cent level, making systematic uncertainties the primary concern for most measurements in SBN [223]. An accurate understanding of interaction cross-sections is crucial for precise neutrino oscillation measurements needed to explore new physics. This is particularly important in experiments with heavy-nuclei like argon, where complex neutrino scattering can lead to multiple observed final states due to nuclear effects and varying neutrino energies within the beam [228]. SBND, positioned at a baseline of 110 m, will experience a neutrino flux approximately 10 times that of the other two detectors [1]. With an expected event count of around 6 million during the full experiment run, SBND is well-positioned for conducting measurements of cross-sections for neutrino interactions with argon with high precision. Additionally, MicroBooNE has been operational since 2015, accumulating statistical data in the tens of thousands and already yielding accurate cross section measurements within the 1 GeV energy range [168, 187].

In recent decades, the exploration of using neutrinos to investigate novel physics has rapidly expanded, particularly after the discovery of neutrino oscillations. Numerous untested theories have emerged, and the SBN program, with its LArTPC detector technology and powerful neutrino flux from the BNB, is well-positioned to conduct various searches for

these exotic phenomena [223]. In addition to searching the 3+1 sterile neutrino model, the SBN program offers opportunities to explore various other BSM scenarios. Some of these possibilities include 3+N models involving sterile neutrino decays [229], the impact of large extra dimensions on neutrino mass [230], examinations of heavy neutrino decays and Majorana or Dirac neutrino classifications [231], as well as exploring light dark matter through meson decays [232].

4.1.2 Current status of the SBN program

The MicroBooNE detector has been in operation since October 2015, providing a significant amount of exposure. Currently, MicroBooNE has concluded its data collection and is generating groundbreaking outcomes with high statistical significance in studying interactions between neutrinos and argon nuclei, using both BNB and NuMI beams, covering both inclusive and exclusive channels. Simultaneously, efforts are underway to examine the unanticipated low-energy excess observed by MiniBooNE to explore the existence of sterile neutrinos. The ICARUS T600 detector was transported to Fermilab in 2017 and subsequently filled with LAr in August 2020. It is presently operational, collecting neutrino data from both the BNB beam and NuMI beam since March 2021. The installation phase of the near detector, SBND, is currently in progress, and it is expected that it will be filled with liquid argon by the end of 2023. The SBND is designed to exclusively gather data on neutrino interactions originating from the Booster Neutrino Beam (BNB) and is expected to provide a total exposure of 6.6×10^{20} POT,corresponding to three years of running, for the SBN oscillation analysis [223]. A detailed and exhaustive list of opportunities in BSM physics can be found [223].

4.2 The Booster Neutrino Beam

In order to understand the complicated characteristics of neutrino interactions within any given medium, it is essential to have a detailed knowledge of the characteristics of neutrino source. The substantial statistical data available in the SBN datasets leads to uncertainties dominated by systematic effects in all measurements, and a significant contribution arises from the prediction of neutrino flux, as discussed in Chapter 8. Hence, it is essential to accurately constrain the flux to achieve the desired precision in the SBN physics measurements [233].

The main neutrino beam utilised in the SBN program is the Booster Neutrino Beam (BNB) which is Fermilab's lower energy neutrino beam. Initially, the BNB was developed

by the MiniBooNE collaboration for their Cherenkov-style detector, which aimed to detect the appearance of electron neutrinos. Since the main background in MiniBooNE arising from photons generated by neutral pion production within the detector, originating from higher-energy neutrinos, the BNB flux was deliberately optimised to suppress neutrinos with energies exceeding approximately 1 GeV.

The neutrino beam is generated by the BNB facility through firstly ionising the hydrogen gas molecules to induce the detachment of electrons, resulting in the generation of protons (H^+). The protons are subsequently accelerated in the booster ring to generate a proton beam with a maximum energy of 8 GeV. The ring has a capacity to accommodate up to 84 proton bunches, although only 81 of them are filled. Each bunch consists of around 6.2×10^{10} protons and is characterised by a width of 2 ns and a spacing of 19 ns between adjacent bunches when they are transferred from the ring to the target hall [233]. The release of the entire 81 bunches, which corresponds to about 5×10^{12} protons over a duration of 1.6 μs, is referred to as a "spill" and occurs at a rate of up to 5 Hz [233]. Experiments equipped with precise, nanosecond-level timing resolution can take advantage of the bunch structure to distinguish and reject cosmic activity occurring outside the proton bunches. The intensity of the protons exiting the booster is measured using two toroids, while the beam position monitors and a resistive wall monitor measure the beam's timing and position [233]. These measurements are utilised to determine the systematic uncertainties associated with the beam.

Figure 4.4 illustrates a schematic diagram depicting the neutrino generation process through the BNB beam. The proton beam emerging from the booster is directed towards an air cooled beryllium cylinder, measuring 71.1 cm in length and 0.51 cm in width. Upon interaction with the target, the protons generate secondary hadrons, such as those shown in black. These hadrons are subsequently focused using a 170 kA electromagnetic horn,

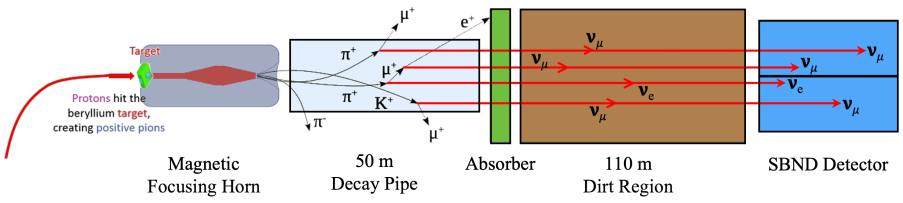

Figure 4.4: A schematic diagram of neutrino beam production at BNB facility. When the incoming protons collide with the beryllium target, they produce secondary hadrons. Depending on the chosen polarity, a magnetic horn (grey) either focuses or defocuses these hadrons. The focused hadrons decay inside the decay pipe (light blue), giving rise to neutrinos that can then travel through the soil (dirt-brown) and reach the SBND detector (Blue). The residual mesons are eliminated as the beam passes through the absorber (green) located after the decay pipe.

depicted in grey. By adjusting the polarity of the horn, either positive or negative hadrons can be focused, enabling operation in neutrino-enhanced or antineutrino-enhanced modes, respectively. The directed particles subsequently pass through a decay region (light blue), 50 m, ending with a steel and concrete absorber (green). In the decay region, hadrons undergo decay to create neutrinos (red) while the absorber serves to reduce the in-flight of long-lived muons, thereby minimising the generation of ν_e. Finally, the neutrinos travel through a region of dirt prior to arriving at the SBND detector.

The beam is modelled using the GEANT4 framework, with the hadronic interaction cross-section adjusted based on HARP data [233, 234]. Figure 4.5 illustrates the modelled flux at SBND front face, categorised by neutrino flavour and plotted against neutrino energy. Most of the beam is composed of ν_μ, accounting for around 90.2% of the total, followed by $\bar{\nu_\mu}$ with a contribution of about 9.1%, while ν_e and $\bar{\nu}_e$ contribute only minimally with 0.6% and 0.1% respectively.

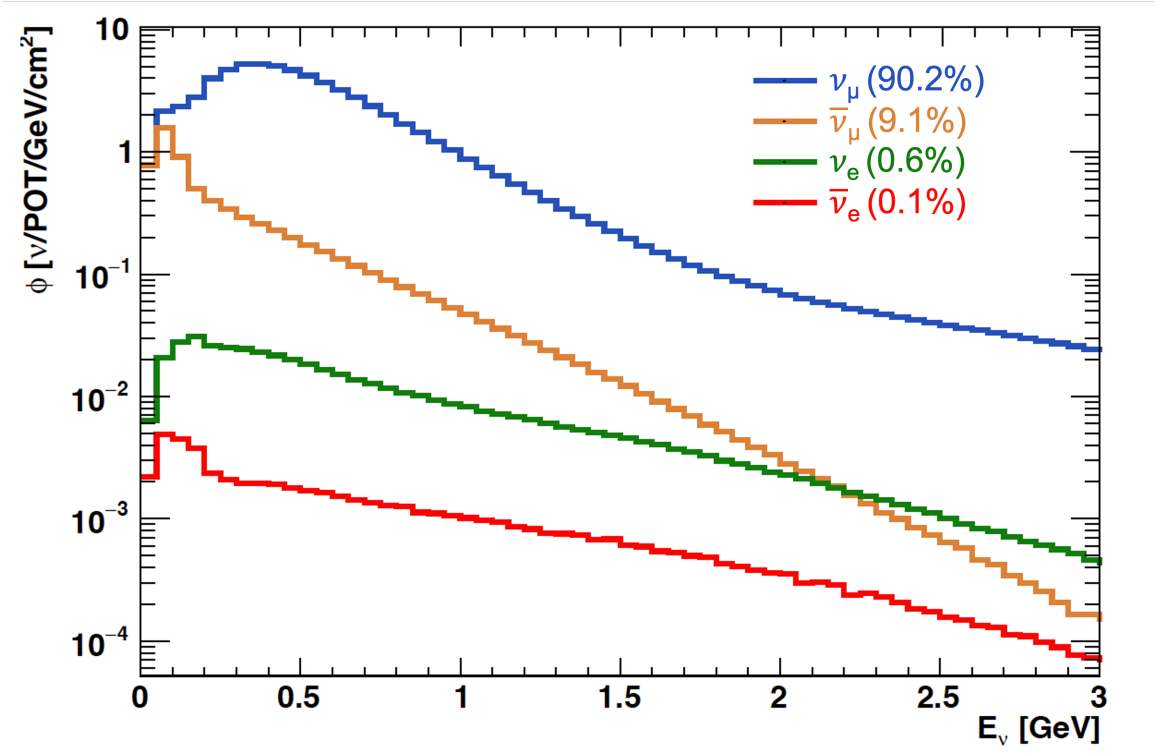

Figure 4.5: Neutrino flavours flux composition simulated to reach the SBND detector.

4.3 The Short-Baseline Near Detector

SBND, illustrated in Figure 4.6, is designated as the near detector among the three LArTPCs within the SBN program situated in the BNB at Fermilab. Although attempts have been made to establish standardisation among the three detectors, there are notable variations present. SBND is a large LArTPC with an active volume of 112 tonnes and positioned at a distance of 110 m away from the BNB target. The detector measures 5 m in length and 4 m in height, and it is comprised of two distinct TPCs that share a common Cathode Plane Assembly (CPA) each with a drift length of 2 m. the anode planes are located at the termination of each 2 m drift length. This serves two purposes: firstly, it reduces the distance travelled by the drifting electrons within the volume, thereby minimising diffusion; second, it allows for scalability of the TPC, resulting in a larger active volume overall. Behind each anode plane, there is a complete Photon Detection System (PDS) that includes reflective foils coated with TPB within the cathode. Additionally, the TPC is housed within a membrane cryostat, which is encircled by seven planes of Cosmic Ray Tagger (CRT) that provide nearly full coverage. The detector design and technology are optimised to maximise neutrino interactions while effectively mitigating cosmic background in order to achieve the physics goals of the experiment.

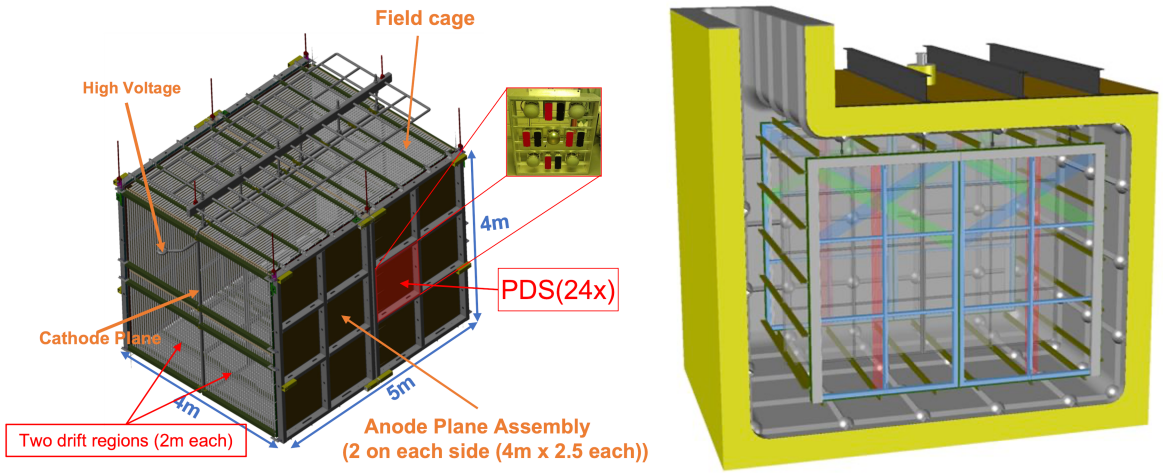

Figure 4.6: A diagram illustrating the SBND detector and its cryostat (right) and the dimensions, APA and CPA (left).

4.3.1 SBND Physics Aims

Aside from studying the low energy excess, each of the experiments in the SBN program has its own extensive physics research objectives. SBND, being the near detector, experiences the highest neutrino flux among the three detectors. The high flux expected to yield over 5.5 million neutrino interactions during the course of three years of operation. The breakdown of these interactions according to their hadronic final state can be found in Table 4.1. These figures signify a substantial increase in magnitude compared to the current measurements of argon cross sections [168].

Hadronic Final State	GENIE (G18_10a) Prediction Event Rate
ν_μ Charged Current	
Inclusive	3,998,310
$\rightarrow 0p$	175,219
$\rightarrow 1p$	2,107,538
$\rightarrow 2p$	746,517
$\rightarrow \geq 3p$	969,051
$\rightarrow 0\pi$	3,224,194
$\rightarrow 1\pi + X$	665,977
$\rightarrow 2\pi + X$	90,737
$\rightarrow 1\pi^0 + X$	405,174
ν_e Charged Current	
Inclusive	29,841
$\rightarrow 0p$	2,377
$\rightarrow 1p$	14,524
$\rightarrow \geq 2p$	12,939
$\rightarrow 0\pi$	21,630
$\rightarrow 1\pi + X$	6,401
$\rightarrow 1\pi^0 + X$	4,316
ν Neutral Current	
Inclusive	1,570,640
$\rightarrow 0\pi$	1,304,762
$\rightarrow 1\pi + X$	221,173
$\rightarrow 1\pi^0 + X$	250,805
$\rightarrow e^-$	393

Table 4.1: SBND event rates for 6.6×10^{20} POT after approximately 3 years.

The abundance of interactions results in reduced statistical uncertainties, enabling the study of exclusive and multi-dimensional differential cross sections. The LArTPCs' low threshold and exceptional particle identification abilities, facilitate exclusive final states selec-

tion and particle kinematics measurements. In the context of this thesis, the anticipated rate of around 400k events ν_μ Charged Current interactions with π^0 production is of significant interest, representing yet another substantial increase compared to the existing measurement of 771 selected events, as detailed in Chapter 2 [168]. However, the existence of substantial background and the difficulty in accurately reconstructing the energy of photon showers present the most significant challenges.

SBND also has the capability to explore rare phenomena, such as neutrino-electron elastic scatters, which involves the interaction of neutrinos with electrons rather than atomic nuclei. These interaction, being purely electroweak processes with a well-defined cross section, can be utilised to constrain flux predictions using a LArTPC for the first time [235]. Additionally, SBND's unique detector features, discussed in more detail in next sections, enable it to achieve world-leading measurements of cross section and conduct searches for BSM physics with great precision [223].

The LArTPC, despite being proposed in 1977, is a novel technology that is still being optimised. As the DUNE detector design is near completion and substantial funding has been allocated, it is crucial to ensure stable operation of key detector components under realistic conditions [197]. The protoDUNE experiment was motivated by this goal [191]. Additionally, SBND will play a significant role in achieving this goal, as it shares essential components including the membrane cryostat, cathode design, front-end electronics, and light detection systems [223].

4.3.2 Time Projection Chamber

As mentioned above, SBND features two independent TPCs in its active region, each with a 2 m long drift and connected in the middle by the Cathode Plane Assembly (CPA). At the end of each drift region, there are two Anode Plane Assemblies (APAs) that house all of the sense wires [236]. The CPA and APAs are positioned facing each other and surrounded by a field cage, as illustrated in Figure 4.6. The dimensions of the detector measure 5 m in the direction of the beam and 4 m in both the drift and vertical directions. The image in Figure 4.7 shows the main components of the SBND TPC, including the CPA, APAs and field cage.

The cathode consists of two CPAs connected in the middle, with each consisting of eight mesh frames sealed together (see Figure 4.7). The design and materials of cathode have been chosen to reduce the side effects that could occur when operating at a high voltage, such as the high fields at the edges of the mesh. The sub-frames are composed of a TPB-coated reflective foil, which assists the Photon Detection System (PDS), and a wire mesh that provides the necessary bias voltage. The foils, which enhance scintillation light, improve

the efficiency of photon detectors and promote uniformity throughout the drift region by converting and reflecting light that would typically be lost near the CPA. The cathode will be operated at around -100 kV to achieve a 500 V/cm drift field in the detector. This allows the electrons to be drifted in the opposite direction [223, 1].

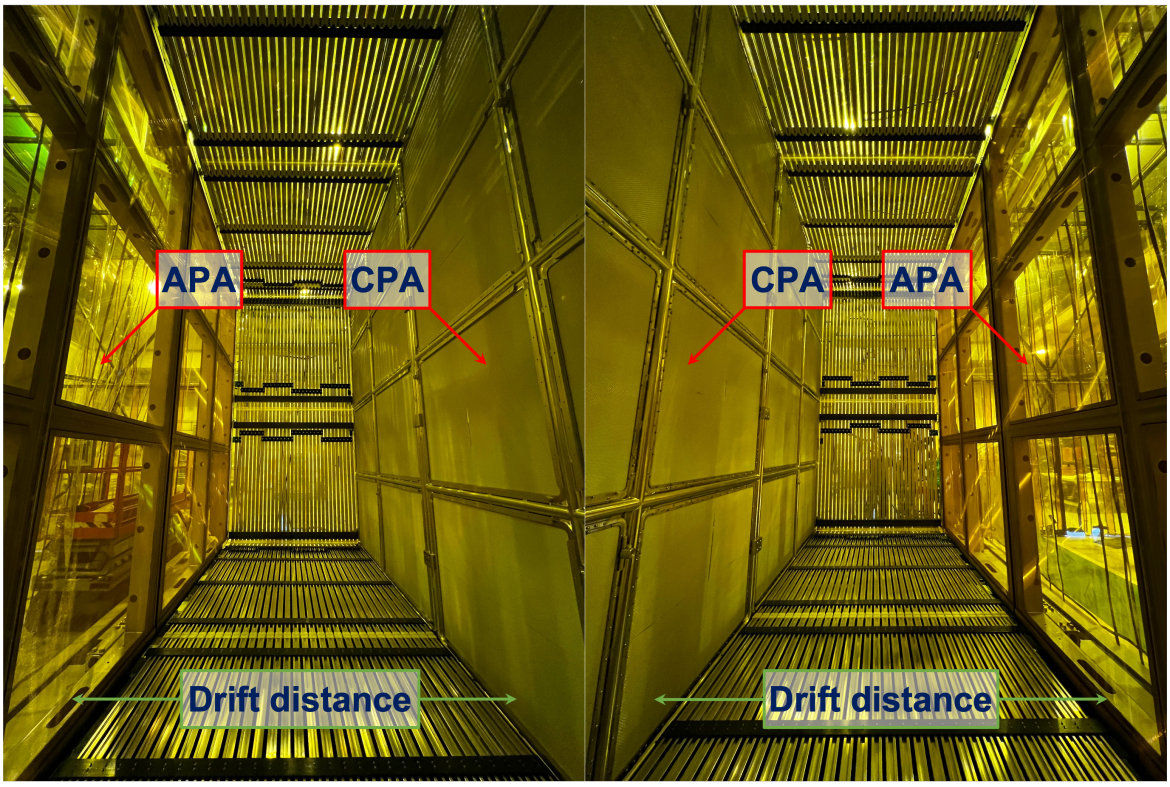

Figure 4.7: An image shows the SBND detector being assembled at Fermilab, showing the central CPA and the front, top, and bottom sections of the field cage visible as a series of metal bars at the far side, top and bottom of the picture.

The SBND APA is equipped with three wire plane configurations: two induction planes, U and V, positioned at ± 60 degrees from the vertical collection plane, Y, as represented by the green, blue, and red colours in Figure 4.8. These wire planes are made up of copper-beryllium wires with a diameter of 150 μm, spaced at intervals of 3 mm. To ensure stability when cooled by the liquid argon, the wires are tensioned to 7 N to prevent sagging[223, 236].

The wire planes within the TPC are spaced 3 mm apart and are maintained at voltages of -200 V for the U plane and 500 V for Y plane, while the V plane is biased at 0 V. This arrangement ensures induction planes electrical transparency and collection plane collection efficiency. Each TPC comprises two interconnected APAs, utilising jumper cables to bridge the induction planes through a 15 mm gap, thereby forming a unified electronic channel. Figure 4.8 shows a depiction of coupled APAs, with the U, V, and Y planes illustrated in

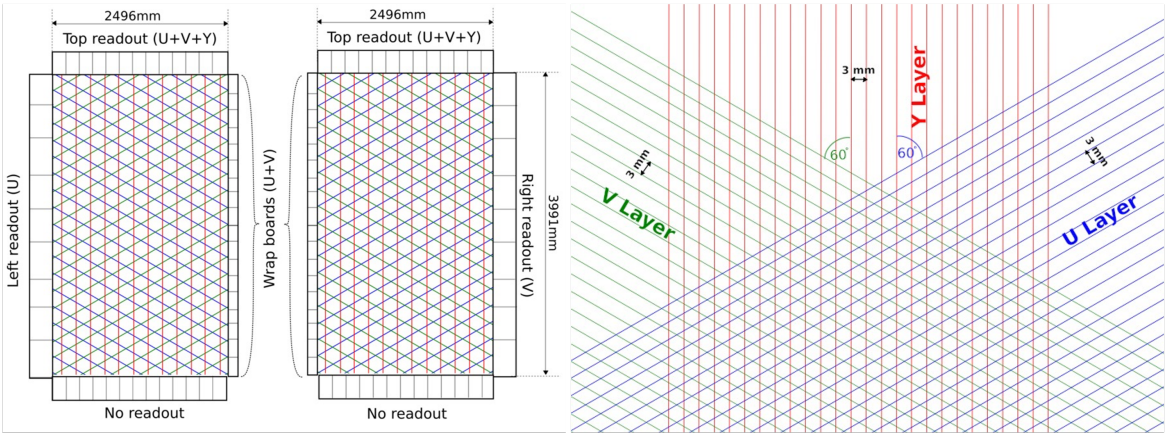

Figure 4.8: The illustration shows a pair of interconnected APAs, forming an APA plane. The U, V, and Y wires are represented in blue, green, and red, respectively, along with the electronic readout boards. The APAs (diagram on the left) are linked at the centre of the diagram, with the induction channels (U and V) bridging the gap between them. Figure from [236].

blue, green, and red, respectively. Each TPC consists of a total of 5,632 wires, with 1984 in each induction plane and 1664 in the collection plane.

The wires in each APA are connected to the cold electronics positioned at the top and sides of the assembly, within the LAr, to minimise thermal noise and cable lengths. This collective set of components is commonly known as the cold electronics (depicted in Figure 4.9), and includes a 16-channel front-end Application-Specific Integrated Circuit (ASIC) responsible for shaping and amplifying the signal at a 2 MHz rate with a resolution of 12 bits. Subsequently, the signal is directed to an Analog-to-Digital Converter (ADC) ASIC, followed by a mezzanine Field-Programmable Gate Array (FPGA), which multiplexes the data from 128 channels across 8 ASICs. The data is later transmitted out of the cryostat to a Warm Interface Board (WIB) through a Serializer/Deserializer (SERDES) mezzanine. Upon exiting the cryostat, the data is further transferred via a fibre optic cable from the WIB to the Data Acquisition (DAQ) system, which will determine whether to store the data on magnetic tape depending on the available trigger information.

The data collected will be divided into readout windows, each representing the time it takes for the charge to drift from the cathode to the wires planes, approximately 1.25 ms. To enable a complete reconstruction of background sources that might have passed through the TPC before or after the trigger, an additional readout window will be saved on both sides of the triggered window.

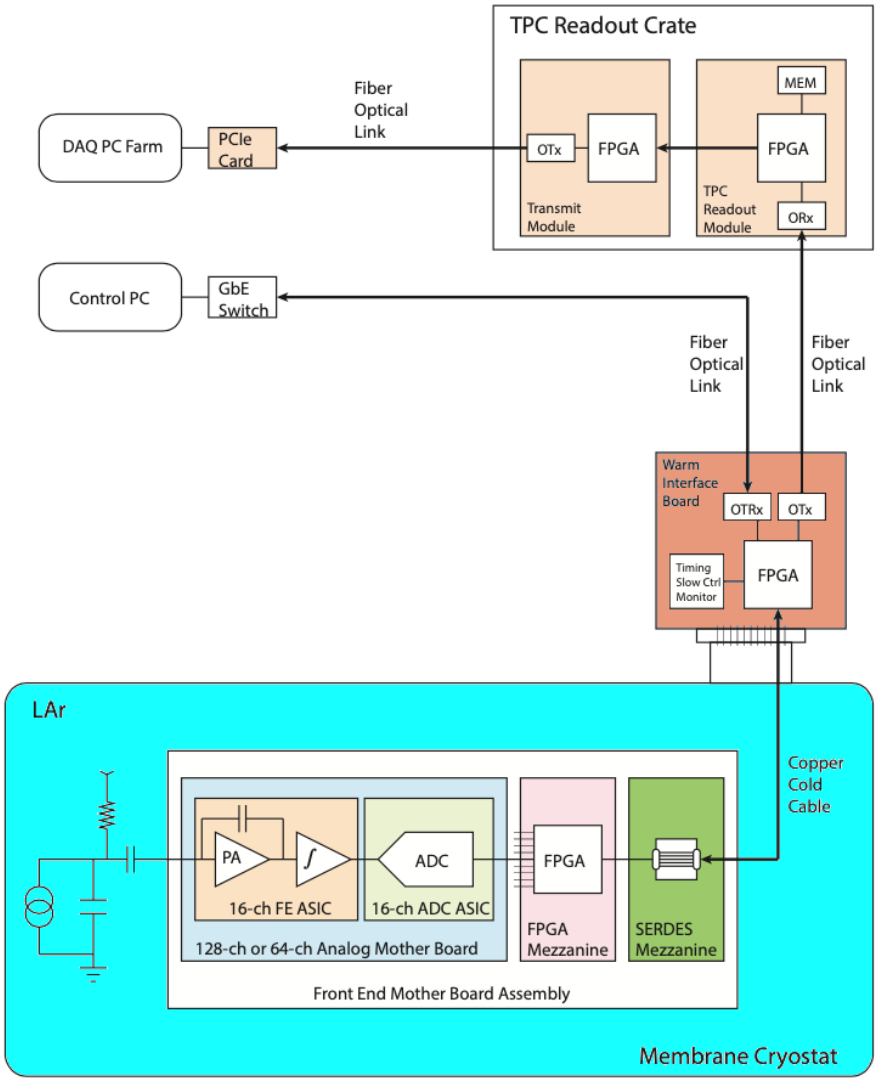

Figure 4.9: Diagram illustrating the information pathway of an individual TPC readout channel. Figure from [1].

The field cage of the TPC is constructed using stainless steel strips that are arranged perpendicularly to the drift direction, as can be seen in Figure 4.6 and Figure 4.7. A resistive divider network is utilised to reduce the voltage by approximately 3 kV per strip between the CPA and APA. The purpose of the field cage is to maintain a uniform 500 V/cm electric field, allowing the electrons to drift perpendicularly to the APA and minimising track distortions.

4.3.3 Photon Detection System

Since scintillation light is faster compared to ionisation electrons, the Photon Detection System (PDS) provides information for event triggering. Achieving timing resolutions of few 100 ns and 1-2 ns is necessary to reject background events outside the beam spill and utilise the spill's bucket structure, respectively [233]. SBND incorporates an extensive light detection system that not only supports the physics objectives but also contributes to R&D for future experiments. The PDS in SBND, positioned behind the wire planes, offers significantly improved sensitivity, with approximately 40% photocathode coverage compared to other neutrino LArTPC detectors like MicroBooNE. It incorporates two light detection technologies capable of measuring direct scintillation light and wavelength-shifted light reflected from the reflective foils mounted on the cathode.

The region behind the wire planes is equipped with 120 Hamamatsu (R5912-MOD) PMTs measuring 8 inches in diameter, offering a timing resolution of 1 ns, along with 192 ARAPUCAs [219]. These PMTs divided into modular "PDS boxes" with a total of 24 boxes divided evenly between the two sides of the APA, shown in Figure 4.10. Each box consists of five PMTs, with four PMTs coated with TPB and one uncoated, and 8 ARAPUCAs distributed in four pairs of VUV and VIS detectors. The front face of the 96 PMT is coated

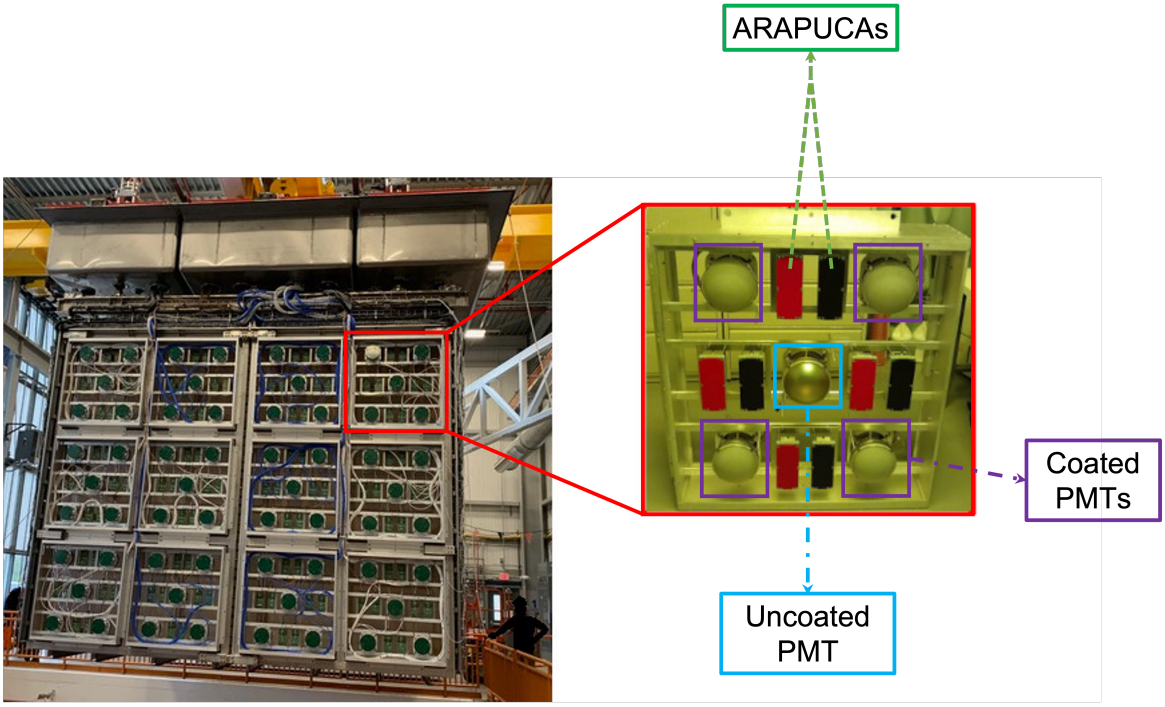

Figure 4.10: An image of SBND PDS located behind APA. It consists of 12 boxes, each containing 5 coated PMTs, one uncoated PMT, and 8 ARAPUCAs.

with TPB using an evaporation process, preceded by sandblasting the glass surface to enhance adhesion and effective surface area. The remaining 24 uncoated PMTs are sensitive only to scintillation light reflected off the cathode foils, providing better estimation of event position in the drift direction. The integration of both conventional PMTs and innovative ARAPUCAs enables a direct evaluation of their respective performances, offering research and development insight for the Deep Underground Neutrino Experiment (DUNE).

The PMTs have a readout frequency of 500 MHz, providing a timing resolution of 2 ns, whereas the ARAPUCAs have a readout rate of 80 MHz and a timing resolution of 12.5 ns. Hence, this capability significantly enhances cosmic rejection, improving it by an order of magnitude compared to associating with the entire BNB spill.

4.3.4 Cosmic Ray Tagger

Since SBND is located on the surface with limited concrete shielding of only 1 m, it is exposed to a high flux of charged particles, primarily muons, originating from cosmic ray showers in the atmosphere, reaching frequencies of 3-4 kHz. The high rate of cosmic ray muons passing through the detector presents a significant background for all studies, as it exceeds the drift velocity of ionisation electrons. The process of matching reconstructed objects in the TPC with light flashes in the PDS lacks precise position resolution. To address this, SBND incorporates a set of Cosmic Ray Tagger (CRTs), offering nearly complete coverage of the TPC [237]. This approach compensates for the limited precision in position resolution when matching reconstructed TPC objects with PDS light flashes.

The system consists arrays of scintillator strips that are 12 cm wide and 1 cm thick, connected to a pair of SiPMs using wavelength shifting optical fibres, depicted in Figure 4.11 (left). Each strip is read out when both SiPMs exceed the threshold simultaneously, achieving a ns-level time resolution. The measurement of the charge detected by each SiPM allows for the accurate determination of the hit position within the 12 cm width of the strip. Multiple sets of strips, oriented perpendicularly to each other, are integrated to create a unified CRT plane, shown in Figure 4.11 (right). The occurrence of simultaneous hits in the overlapping strips enables the determination of the particle's path through the plane in two dimensions.

CRT planes are positioned on all sides of the detector, as depicted in Figure 4.12 (left). However, the coverage of the detector bottom is limited primarily due to the presence of the cryostat support structure, resulting in certain areas with only one-dimensional coverage, as illustrated in Figure 4.12 (right). Additionally, approximately 19% of the back face of the detector does not have coverage due to allocated space for cryogenic equipment. The top two planes are arranged in a telescopic array configuration, enabling the identification of vertically stopped cosmic rays, which can be utilised for calibration purposes.

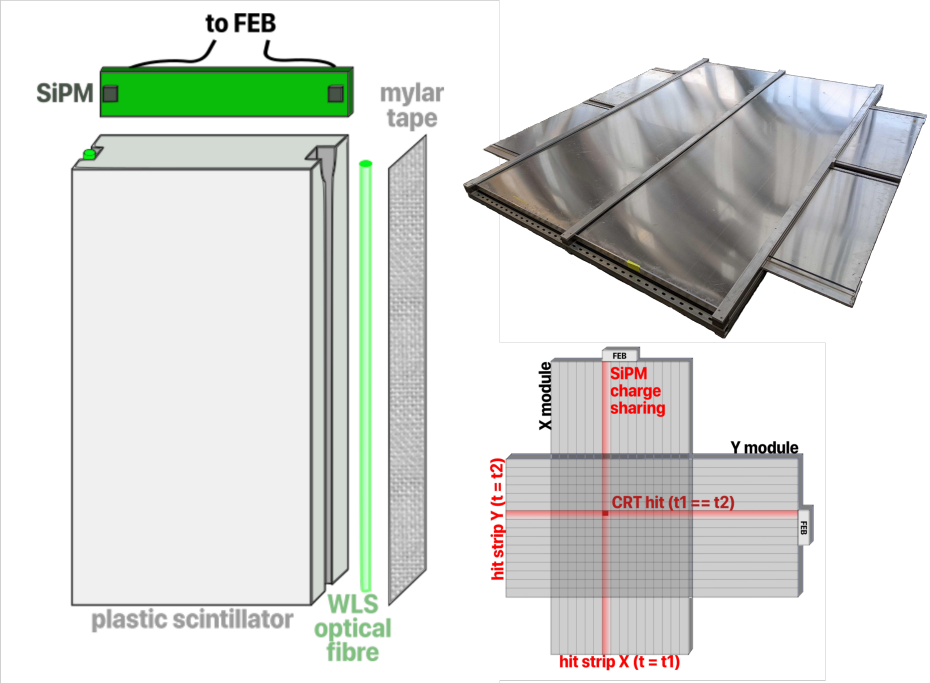

Figure 4.11: Schematic of a CRT strip (left) composed of a plastic scintillator connected to a pair of readout SiPM through wavelength shifting optical fibers. Multiple strips are combined in a series-parallel configuration to create a plane, and perpendicular planes from a module (right bottom), and a picture of 2x2 module is shown on top right. CRT hits are generated by identifying coincident and overlapping hits across the planes in a module. Figure from [1]

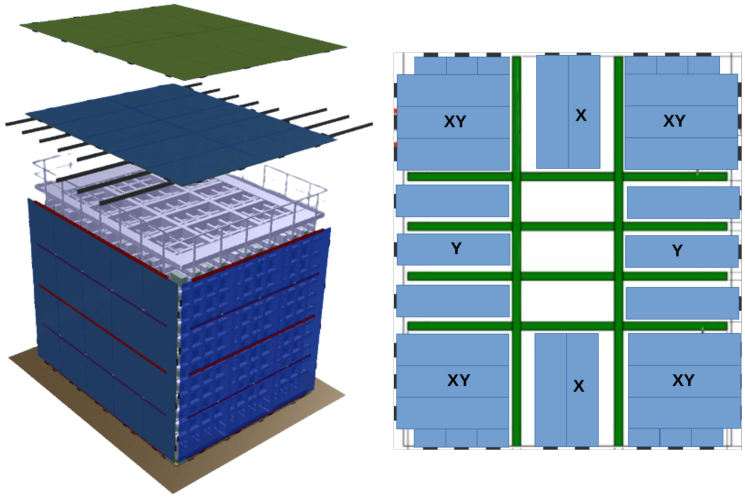

Figure 4.12: Diagram illustrating the geometry of the SBND CRT system (left), featuring seven planes distributed on each side of the detector and a telescopic array positioned at the top. The bottom plane (right) exhibits limited coverage due to the presence of the cryostat support structure, depicted in green. Figure from [1].

4.4 SBND Event Simulation

Simulations play a crucial role in the development of event reconstruction and selection in neutrino experiments. Typically, these simulations employ Monte Carlo (MC) methods, which involve random sampling from predefined distributions. In SBND, the simulation and reconstruction processes are facilitated through the LArSoft framework [238], which is based on the art event processing framework [239] and utilises the ROOT data analysis package [240]. The LArSoft framework enables the sharing of essential code for simulation, reconstruction and analysis among various LArTPC experiments such as ArgoNeut, MicroBooNE, ICARUS, SBND and DUNE.

The simulation workflow for SBND is depicted in Figure 4.13, which starts with an event generator that generates primary particles, whether they are neutrinos, cosmic particles, or BSM. These primary particles are then simulated as they pass through the detector, taking into account the energy loss and production of daughter particles. Next, the detector response is simulated for both the TPC and CRT subsystems, including the calculation of charge and light yield from energy depositions. The simulation also includes the propagation and detection of charge and light, aiming to generate waveforms that closely resemble real data.

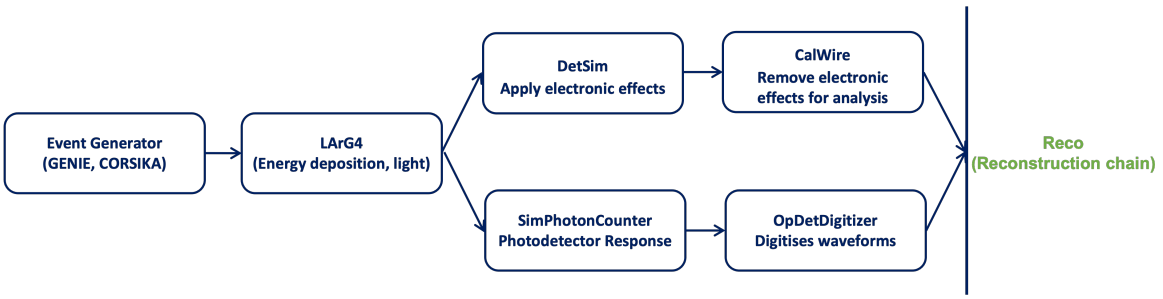

Figure 4.13: Illustration depicting the simulation process for the SBND.

Accurately predicting the interactions within a detector is crucial for understanding its performance and reconstruction capabilities. Therefore, dedicated event generators are employed to model the underlying processes based on global data fits. Two event generators, namely CORSIKA and GENIE, are used in SBND where CORSIKA is used to simulate cosmic rays while GENIE is to simulate neutrino interactions. Although other generators may be incorporated for comparison in the future, these two are currently the only ones integrated, and an overview is presented in the next sections.

4.4.1 Neutrino Interaction Generator

Accurate modelling of neutrino interactions with argon is vital for SBND physics objectives. Limited neutrino scattering data on heavy targets like argon introduces significant cross-section uncertainties, which can impact physics measurements. In addition, due to historical discrepancies in experimental cross section data, the presence of competing models, and variations in generator parametrisations, it is essential to minimise reliance on specific models during reconstruction. The GENIE [106] generator integrates both theoretical and empirical models by adjusting and refining them, a process known as "tuning," through the comparison of predictions with data obtained from experiments involving neutrino and electron scattering. These tunes cover a wide energy range from MeV to PeV, including the change from non-perturbative to perturbative regimes within the few-GeV range, which is important for accelerator-based neutrino experiments like SBND.

GENIE employs a multi-step process to simulate neutrino interactions. It starts by selecting a nuclear model to describe nucleon momenta and potential energy. The cross section model is then incorporated, providing the probability of a neutrino interaction given the neutrino flux. Subsequently, the differential cross section is utilised to identify the specific type of interaction and its kinematics, including Quasi-Elastic (QE), Baryonic Resonant Scattering (RES), Deep Inelastic Scattering (DIS), Coherent Scattering (COH) and neutrino-electron elastic scattering. These models account for interactions with the nucleus, individual nucleons, quarks, and atomic electrons, based on the energy of the neutrino involved.

Hadronisation refers to the generation of hadrons within the nuclei when interacting with free targets, which is especially relevant for DIS interactions. Furthermore, intra-nuclear re-scattering can also happen as these hadrons traverse through the nucleus, affecting the detected kinematics of the interaction. Accurately modelling these Final State Interactions (FSI) is essential for understanding the event patterns detected in neutrino interactions, especially for heavy nuclear targets like argon. Alongside the numerous available models and tunes, a comprehensive re-weighting scheme is also provided to assess the systematic uncertainties inherent in the models.

4.4.2 Cosmic Ray Generators

Understanding the anticipated cosmic ray background is of utmost importance for SBND, as it is a surface-level detector. Unlike neutrino interactions, the cosmic ray background can be studied in anti-coincidence with the beam, providing a pure sample of cosmic rays for validating the simulation and constraining expected backgrounds. In addition to its role in background analysis, cosmic rays are also valuable for calibration studies. By collecting

cosmic ray data during beam-off periods, cosmic ray backgrounds can be subtracted, reducing the necessity for high model accuracy in comparison to the neutrino generator. Nevertheless, simulations retain importance in training reconstruction algorithms prior to detector operation. Incorrect simulations can introduce biases that may require time-consuming corrections, particularly when employing trained machine learning algorithms.

The CORSIKA [241] generator utilised in SBND simulates high-energy primary particles interacting with the Earth's atmosphere. In SBND, only proton primaries are employed to achieve better agreement with MicroBooNE data, although primaries up to iron nuclei are also available. The simulation accounts for interactions with air and secondary decays as the particles propagate through the atmosphere. This propagation goes on until the produced particles reach the surface, with the model extending just above the roof of the near detector building for SBND. The particles that have reached the surface are saved for later retrieval and propagation to the detector, employing the GEANT4 simulation toolkit.

4.4.3 Detector Simulation

After particle generation, the next step involves propagating them through the detector using GEANT4, an MC toolkit for particle transport. GEANT4 simulates the movement of particles through the detector and its subsystems, accounting for scattering, interactions, and decays. This process produces comprehensive particle trajectories, capturing energy depositions in different materials and the hierarchy of particles resulting from interactions and decays. The energy depositions are passed through the detector simulation, which includes the calculation of charge and light production using the modified box model, considering the electric field and energy density. The simulation also takes into account alterations in the electric field induced by the Space Charge Effect (SCE). These alterations affect the calculation of recombination and the perceived position of energy depositions [199].

The electrons remaining after the recombination process are then directed towards the readout wires, assuming a direct path along the drift field. The charge reaching the wires is attenuated to account for electron capture on impurities, utilising an electron lifetime of 10 ms. Longitudinal diffusion is used to introduce variability in the electrons' arrival time on the wires, and transverse diffusion distributes a fraction of the charge to nearby wires. Subsequently, these energy deposits on each wire are entangled with the electric field and the readout electronics response of the detector [242]. Noise is then incorporated, considering the wire length and based on findings from test benches of the detector electronics [215].

Photons, unlike electrons, cannot be accurately modelled as moving in a straight line across the drift direction because of their isotropic emission, scattering, and reflection. Simulating the propagation of a large number of photons for every event is computationally

challenging, given the low scintillation energy threshold of LAr. To address this, a common approach involves utilising a lookup table that offers the probability of photon detection based on its initial position. In SBND, a novel approach is used that incorporates corrections for Rayleigh scattering into geometric approximations in order to assess how effectively photons from interacting particles can be detected by the PDS. By sampling the visibility and considering the photodetectors' quantum efficiency, the expected number of photons reaching each detector and their arrival time distribution can be determined. This information is then used to generate photodetector waveforms, incorporating noise and convolving with the expected detector response, similar to the wire process [243, 244].

The CRT simulation is simpler, directly converting deposited energy into simulated hits without generating waveforms. This is made possible due to the ability of CRT strips to have a low dark rate and self-triggering capability. A strip is triggered if both SiPMs surpass a specified threshold within a 100 ns coincidence window. The simulation involves converting deposited energy into scintillator light yield and applying corrections for SiPM collection efficiency based on the location of energy deposition. The hit time is estimated from the energy deposition time and a light propagation delay determined by the distance between the deposition and the SiPM.

4.5 SBND Subsystem Reconstruction

The process of reconstruction involves extracting meaningful information about particle interactions from the raw data recorded by the detector. The conversion of raw LArTPC images in SBND involves a three-step process: low-level reconstruction for signal processing and hit-finding, pattern recognition to identify 2D hits and clusters, and high-level reconstruction for calorimetric analysis and particle identification. In Photon Detection System (PDS) signal processing, waveform deconvolution determines the number of detected Photo-Electrons (PEs) and identifies optical hits based on threshold crossings. Optical flashes are generated by combining reconstructed hits. In CRT processing, hits and tracks are identified without waveform data, allowing for integration with TPC tracks to resolve drift-time ambiguity and identify beam spill activity. The information from this subsystem is subsequently correlated with the TPC data, leveraging the enhanced timing resolution to assist in filtering out cosmogenic activity. This is covered in more details in Chapter 7. The following subsections provide a comprehensive overview of the signal processing and reconstruction methodologies employed in the PDS and CRT subsystems of SBND. A more detailed exploration of the TPC image processing and reconstruction techniques is presented in Chapter 5 and 6.

4.5.1 PDS Signal Processing and Reconstruction

The light reconstruction process starts by deconvoluting the detected waveform using a measured single Photo-Electron (PE) response. This deconvoluted waveform signifies the number of PEs detected by the photodetector. Optical hits are then identified by detecting waveform points above a specified threshold, and the hit time is determined based on when the threshold is crossed, unlike the TPC where the central time is used. These hits combine all PEs arriving within a certain time window from the initial hit, providing an estimation of the incident light on the photodetector. The procedure mainly emphasises the capture of the fast component of the light, excluding the slow component, and therefore does not account for all of the generated light, as discussed in Chapter 3. For a more detailed understanding of the process of light detection and reconstruction, Chapter 10 provides a comprehensive exploration of a similar approach.

Optical flashes are generated by combining the reconstructed hits from specific types of optical detectors, such as coated or uncoated PMTs. The centre of the flash in the Y-Z plane is calculated using the centre of PE weighted of the optical detectors involved in the hit. Estimating the X-position of the flash can be achieved either by assessing the dispersion of light or by inspecting the proportion of PMTs with and without coatings. Timing corrections can also be implemented to consider the time it takes for photons to travel, taking into account the proximity of the flash to the photodetectors. These flashes can be further correlated with TPC activity, providing timing information to identify events occurring simultaneously with the beam spill, as discussed in Chapter 7 and 10.

4.5.2 CRT Signal Processing and Reconstruction

In CRT reconstruction, waveforms are not saved in simulation or data because of the detectors' high Signal-to-Noise Ratio (SNR), low dark rate, and self-triggering capability; hence, the signal time and peak height are only saved. The reconstruction process begins with identifying hits on each SiPM in a CRT strip, followed by estimating the position within the strip based on the relative number of PEs detected on each SiPM and an estimate of the total PEs within the strip. Afterwards, 2D hits are created by identifying overlapping hits in adjacent strips within a specific plane, as illustrated in Figure 4.11. Subsequently, corrections are applied to the PE measurements to account for the light attenuation within the strip. Additionally, CRT tracks can be reconstructed by identifying 2D hits in opposing planes. The track reconstruction rate is lower than that of hits due to coverage gaps and cosmic rays that do not cross the TPC, stopped within the drift region.

After forming CRT hits and tracks, the next step involves matching them with TPC tracks. The matching process starts by shifting the TPC tracks in the drift direction to align with the CRT hit's timing, compensating for any timing discrepancies. Matches where the TPC track extends beyond the active volume are considered invalid and discarded. Then, a metric is computed to evaluate the goodness of fit for each possible match. Regarding CRT hits, this involves extending the TPC track to the CRT plane and determining the Distance of Closest Approach (DCA). In the case of CRT tracks, it is possible to estimate the DCA for both CRT planes, and consider the alignment in angle between the CRT and TPC tracks. CRT tracks provide additional information compared to CRT hits, resulting in higher purity, although the coverage is reduced.

The combination of CRT and TPC information enables the integration of the high-resolution timing of the CRT system with the TPC. This is valuable for determining activity coinciding with the beam spill window and resolving the drift-time ambiguity in LArTPC, as discussed in Chapter 3, for calibration.

4.6 Summary

The SBN program at Fermilab consists of three experiments: SBND, MicroBooNE, and ICARUS T600, utilising LArTPC technology to enhance sensitivity and mitigate background sources. Addressing the anomalies observed in LSND and MiniBooNE experiments, the SBN program aims to study neutrino oscillations. SBND, located at a distance of 110 m from the BNB target, serves as the near detector with its unique physics research objectives. With a high neutrino flux and expected yield of over 5.5 million interactions, SBND enables studies of exclusive final states, multi-dimensional differential cross-sections, as well as investigations of BSM scenarios and rare phenomena such as neutrino-electron elastic scattering.

The Booster Neutrino Beam (BNB) is the main neutrino beam used in the SBND of the SBN program at Fermilab. The BNB is optimised to suppress higher-energy neutrinos to study low-energy neutrino interactions, delivering a predominantly ν_μ flux with minimal contamination of only 0.5% ν_e, and an average energy of 800 MeV. The TPC in SBND consists of interconnected Anode Plane Assemblies (APAs) with three sets of wire planes. It uses a field cage constructed with stainless steel strips to maintain a uniform electric field. SBND incorporates a Photon Detection System (PDS) with Hamamatsu PMTs and ARAPUCAs to measure scintillation light for event triggering, providing improved sensitivity. To address cosmic ray muons passing through the detector, SBND includes Cosmic Ray Taggers (CRTs) with scintillator strips read out by SiPMs, enabling accurate particle path

determination. Each of these subsystems incorporates unique characteristics to aid SBND in accomplishing its physics objectives.

Simulation plays a crucial role in understanding and developing reconstruction tools in SBND. It enables the study of detector performance, event reconstruction, and background sources. Utilising event generators such as GENIE and CORSIKA, and sophisticated simulation tools like GEANT4, particle interactions and detector responses are accurately modelled. By integrating information from various detector systems and performing reconstruction, fundamental particle interactions within the detector can be understood. PDS signal processing involves waveform deconvolution to determine detected Photo-Electrons (PEs) and identify optical hits. Optical flashes are formed by combining reconstructed hits. CRT processing, without waveforms, integrates with TPC tracks to resolve drift-time ambiguity and identify beam spill activity. Correlation of this subsystem information with TPC data, leveraging improved timing resolution, aids in filtering out cosmogenic activity. The processing and reconstruction of TPC data events in the SBND detector is discussed in the next chapter.

Chapter 5

Event Processing and Reconstruction In The SBND Detector

In the SBND experiment, the conversion of raw LArTPC images into analysis-level physics quantities can be summarised as a three-step process: low-level reconstruction, pattern recognition, and high-level reconstruction. The low-level reconstruction step involves signal processing, noise filtering, and hit-finding, followed by pattern recognition which transforms the resulting 2D images into sparse 2D hits, clusters, and a hierarchy of 3D particles. Finally, the high-level reconstruction step incorporates calorimetric reconstruction and particle identification to further analyse the output of the pattern recognition step and generate the final physics quantities. Figure 5.1 shows a schematic representation of the reconstruction workflow employed in the SBND experiment.

The low-level reconstruction tools are introduced, encompassing signal processing and hit finding, which play a crucial role in extracting meaningful information from the raw data collected by the detector. Following their introduction, the effectiveness of these reconstruction steps is evaluated using simulated events and diverse noise models. This comprehensive evaluation holds paramount importance in informing the development of subsequent high-level reconstruction algorithms and analyses. Specifically, it involves comparing the performance of different noise models and assessing the capabilities of the reconstruction tools to ensure accurate and efficient event reconstruction. Section 5.2 provides a comprehensive overview of the Pandora algorithms employed to tackle the intricate event topologies encountered in LArTPCs. Furthermore, the evaluation encompasses an analysis of the Pandora algorithm's performance in characterising Particle Flow Objects (PFOs) as either track-like or shower-like, a crucial aspect of data analysis. The evaluation sheds light on the challenges associated with accurately distinguishing between low-energy tracks and electromagnetic showers. Additionally, the assessment includes an evaluation of the reconstruction efficiency in the context of neutrino event reconstruction.

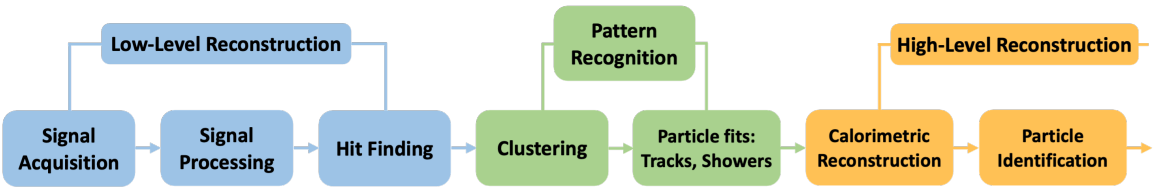

Figure 5.1: Reconstruction Workflow in SBND Experiment

5.1 Low-Level Reconstruction

Reconstruction in particle physics is the process of extracting high-level quantities from raw data collected by the detector in response to fundamental particle interactions. The schematic of the SBND reconstruction workflow is presented in Figure 5.1, which begins with the acquisition of signals as waveforms from either true or simulated events. Next, signal processing, the first stage of the offline data processing chain, is aimed at mitigating noise and detector effects in order to restore the true energy depositions of particle interactions, and generate distributions of charge arrival times and positions based on the input waveforms. Following signal processing, the subsequent step in the low-level reconstruction involves hit-finding, which entails the identification of individual energy depositions from the wires. The output of the low-level reconstruction is then utilised in subsequent reconstruction stages, including pattern recognition. The low-level reconstruction will be discussed in more detail in the following subsection.

5.1.1 Signal Processing

Signal processing is the first stage of the reconstruction chain, and it is the most crucial step in extracting valuable information about the properties of charged particles interacting within the SBND detector. The accuracy and reliability of the results are highly dependent on the quality of the signal processing stage, as it enables the recovery of the true energy depositions by mitigating noise and other detector effects [245]. The TPC signal is formed through a three-part process: the response of the electric field to the drifting of a point ionisation charge, which induces currents on the sense wires, the response of the electronics to the resulting current waveform, involving amplification and shaping of the signal input to each channel, and the initial distribution of the ionisation charge within the detector [245]. These detector effects are addressed through a deconvolution process to recover the initial distribution of the ionisation charge within the detector. The process of deconvolution is of significant importance for the induction planes, as it enables the conversion of the bipolar signal into

a unipolar signal, which allows the waveform integral to be an estimate of the deposited charge.

A neutrino interaction introducing a number of tracks measured on the U-plane from MicroBooNE data at various signal processing stages shown in Figure 5.2. The event display (a) shows the waveform of the raw signal, measured in units of average baseline-subtracted ADC and scaled by a factor of 250 per 3 μs. The raw signal waveform, as shown on the left (a), exhibits high levels of noise, making it difficult to observe the tracks, especially those that are moving vertically along the wires. After the application of software noise filtering, as illustrated in Figure 5.2b, the excess TPC noise is significantly reduced making the tracks more visible. After applying noise filtering techniques, a 1D deconvolution is used to eliminate the bipolar character of the signals, which is evident from the colour scheme in plane (c) of the event display. The 1D deconvolution procedure, which assumes that the current induced each wire is unrelated to the spatial distribution of the charge creating the signals, results in significant distortion and some tracks, including the one located at the top left of the event display window (c), remain barely visible. However, after applying 2D deconvolution, the distortion is eliminated and the missing track and the electromagnetic shower activity, located at the top left and the bottom of the event display window (d), respectively, are recovered. Due to its involvement of both the time and wire dimensions,

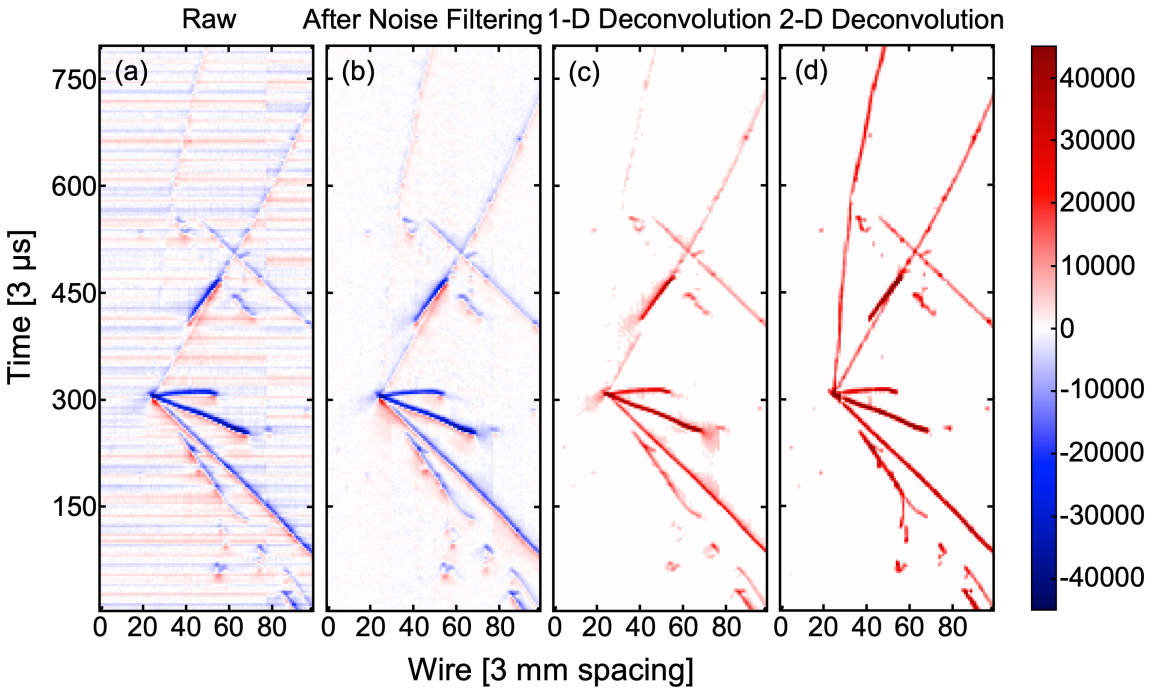

Figure 5.2: MicroBooNE event display showing the raw signal (a), followed by the signal with only noise filtering applied (b), and after 1D (c) and 2D (d) deconvolutions [245, 246].

the 2D deconvolution technique enables a more precise recovery of the ionisation electron distribution. The impact of signal deconvolution on the induction planes is evident in Figure 5.2, whereas for the collection plane, its effect is comparatively minor, as discussed in [246].

At present, SBND employs 1D convolution and deconvolution techniques in its simulation and signal processing, with efforts underway to upgrade to 2D. Gaussian filtering is used for deconvolution since it is more effective in preserving the signal shape than Wiener filtering, despite the latter having a higher Signal-to-Noise Ratio (SNR) with a lower mean square error [245]. To accelerate the deconvolution process and decrease the data size, a Region Of Interest (ROI) finding process is used, which restricts the deconvolution to a small time window comprising the signal. This is achieved by locating the areas on the wire where the signal surpasses a predetermined threshold, tuned such that only 10% of the ROIs are due to noise. To ensure complete containment of energy deposition, an additional 5μs is added before and after the threshold passing for each region. The identified ROI window is then applied to the deconvolved charge distribution after Gaussian filtering, and the ionisation charge is extracted. After forming the ROIs, the next step is to perform a hit finding to obtain information about the energy depositions.

5.1.2 Hit Finding

After the signal processing stage is completed by identifying and implementing the ROIs to the deconvolved charge distribution, the next step in the reconstruction chain involves running hit finding to detect and distinguish event signals from background noise and extract the energy deposition information. In SBND, the process is carried out by the GausHitFinder (GHF) algorithm [247] in LArSoft by fitting multiple Gaussians to the waveform from the deconvolved signals on wires. the GHF module starts by locating a segment where the charge deposited on a wire surpasses a given threshold, followed by determining the number of peaks in this segment, achieved by analysing the waveform differential to identify the number of maxima. After this, a corresponding number of Gaussians are fitted to each peak to find its centre, height and width. Each peak within the segment fitted with Gaussian distribution is classified as a hit, providing information about the magnitude, location, and time of the drift electron signals on the wires.

An event display of a neutrino interaction is shown in Figure 5.3, with examples of waveforms fitted with Gaussians for electromagnetic shower-like and muon track-like particles shown on the bottom left and right, respectively. The lower left window shows a time segment for a given wire that represents a waveform with five peaks above threshold, which are fitted with five Gaussians. Notably, four of the peaks are contiguous and are fitted and grouped as

a single "snippet". This phenomenon occurs typically at the beginning of a vertex, when two charged particle paths cross, or in electromagnetic showers, where charge deposition above the threshold occurs over a period of time in a wire. Conversely, track-like particles usually have only one peak, and are therefore fitted with a single Gaussian, as shown in the bottom right window.

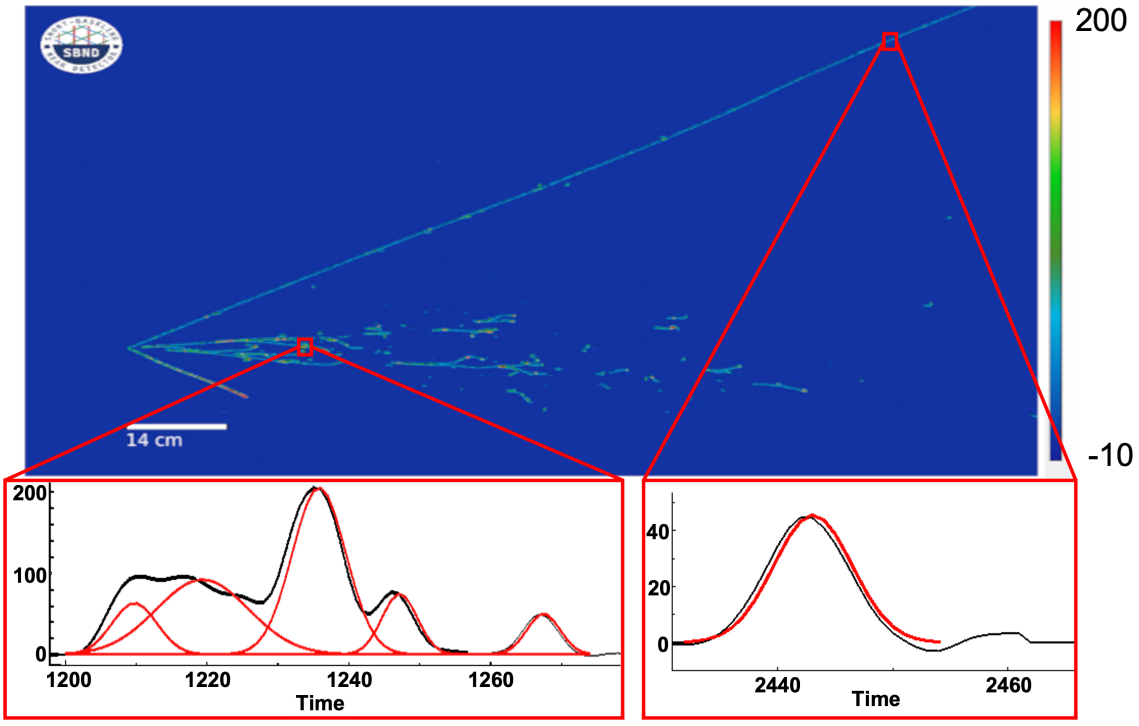

Figure 5.3: A demonstration of an event display showcasing a neutrino interaction with $\mu\pi^0$ final state topology, where the colour scale indicates the amount of charge gathered on a wire, and the y-axis signifies time. A segment of time of a given wire is highlighted in the lower part of the display, showing the waveform (black) and the corresponding Gaussian fits (red).

The peak time of a hit, which corresponds to the arrival time of the charge at the wires, is used to determine the drift position of the hit and to match coincident hits between planes. Meanwhile, the Gaussian fitting height and width are utilised for the estimation of the charge deposited on the wire by calculating the pulse integral. The accurate extraction of ionisation electron information, particularly from complex induction plane signals, is a critical factor for successful 3D event reconstruction in single-phase LArTPCs. Therefore, evaluating and enhancing the low-level reconstruction, specifically the hit finding process, are essential to ensure the effectiveness of advanced reconstruction techniques. The evaluation of the hit finding process and the overall low-level reconstruction chain can be performed by using

simulated events, in which the true ionisation hit parameters are readily available and can be used to optimise the reconstruction tools.

5.1.3 Evaluation of Low-Level Reconstruction

Low-level reconstruction is a critical step in the event reconstruction process in particle physics experiments as it involves the initial steps of signal processing to mitigate noise and other detector effects, and hit finding, which provides the foundational information for subsequent stages of event reconstruction. The accuracy and efficiency of low-level reconstruction directly impact the subsequent high-level reconstruction algorithms and analyses such as interaction classification, particle identification, and event topology reconstruction.

Simulation-based approaches are employed to evaluate the efficacy of reconstruction tools by accessing the true parameters of ionisation hits derived from the generator. In SBND, the event simulation process follows multiple stages, starting with an event generator that creates MC objects representing the primary particles entering the detector, as discussed in section 4.4. Subsequently, the propagation of particles through the detector, including the process of energy loss and the production of secondary particles, are simulated. After that, electronic effects such as the electronic response function and noise model are applied to produce the anticipated signal from the detector. Therefore, in order to enhance the fidelity of the simulation and better approximate the signal observed in real data, a study on the noise module was conducted. In addition, an assessment of the low-level reconstruction chain using this simulation was undertaken, including measurements of reconstructed charge resolution and efficiency.

To meet its physics requirements, SBND as a large-scale neutrino experiment demands exceptionally low noise levels. To mitigate background noise from various sources, cold electronics [248] will be employed as the LArTPC readout solution.Nevertheless, the detector will continue to have two primary sources of noise: the digitisation circuits and the readout electronics, for details see [248] [249].

For the development and evaluation of analysis reconstruction tools, background noise has been simulated. A newly developed data-driven noise model based on MicroBooNE data, credit to A. Scarff for repurposing the module, was implemented in the SBND simulation to replace the standard white noise model, a random noise model. The data-driven noise model is a more accurate representation of the anticipated noise in the SBND detector than the standard white noise model, thereby enhancing the precision of the SBND simulations. Notably, the key distinctions between the white noise and data-driven models lie in the gain constants and noise frequency. The white noise model exhibits a flat frequency response, while the data-driven noise model has a low-frequency peak. Figure 5.4a shows FFTs for

the data-driven noise model of the collection plane, revealing a noticeable peak around 0.2 MHz. In contrast, the white noise model exhibits a flat frequency response, represented by a horizontal line spanning magnitudes between 100 and to 150 arbs. Figure 5.4b shows the peak amplitude of the noise from the two models deposited on collection plane wires. Both noise models exhibit amplitude values below 10 ADC; however, it is noteworthy that the data-driven noise model demonstrates higher noise amplitudes, from 4 ADC and above, compared to the white noise model.

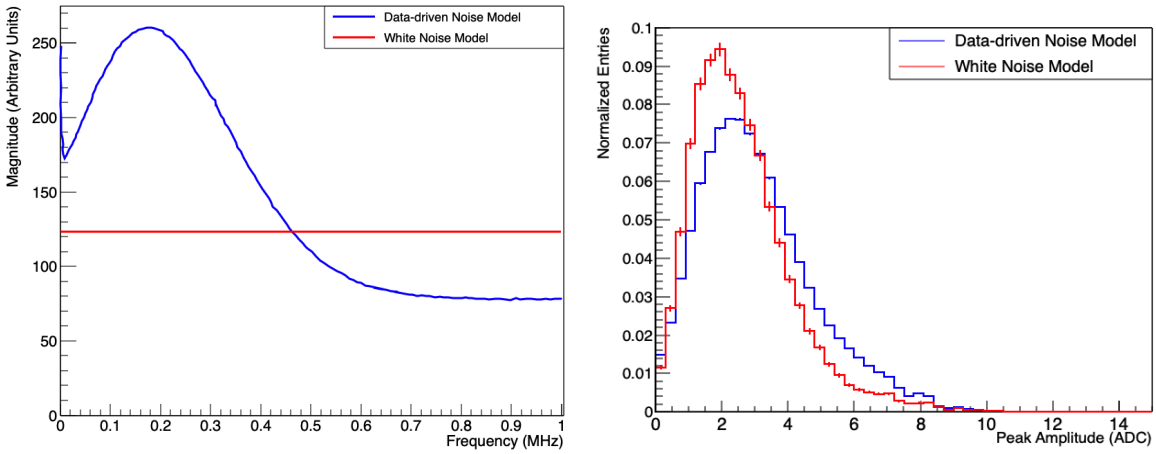

(a) (b)

Figure 5.4: Comparison of noise models in SBND for collection plane. The left plot shows an example of FFT analysis for both noise models, and the right plot presents the peak amplitude of the noise hits on the collection plane, the error bars are Poissonian.

The evaluation of the low-level reconstruction performance involves investigating the ability to accurately recover simulated signals resulting from charged particle interaction within the detector, using a measure derived from the multiplication of signal recovery efficiency and purity. The hit efficiency refers to the fraction of simulated signals that are successfully recovered, while the purity represents the fraction of recovered signals that are actually caused by charged particle interactions. The efficiency can be expressed as follows:

$$\varepsilon = \frac{\text{Number of successfully recovered signals}}{\text{Total number of simulated signals}} \tag{5.1}$$

and purity:

$$\rho = \frac{\text{Number of recovered signals caused by charged particle interactions}}{\text{Total number of recovered signals}} \tag{5.2}$$

and effectiveness of the low-level reconstruction:

$$\text{Effectiveness} = \varepsilon \times \rho \tag{5.3}$$

These parameters were employed to evaluate the performance of low-level reconstruction using samples generated by either the white noise model or the data-driven noise model, thus integrating the latter into the SBND simulation framework. Using the data-driven noise model, three samples of ten thousand muon, proton, and electron events were simulated, alongside comparable samples generated using the white noise model. These samples were simulated with the standardised hit-finding threshold of 10 ADC for all three wire planes. A summary of the low-level reconstruction performance results for both noise model samples is provided in Figure 5.5 and Table 5.1.

Figure 5.5 shows a comparison of low-level reconstruction effectiveness between data-driven and white noise models for electromagnetic shower hits. The effectiveness of low-level reconstruction for the sample simulated with the data-driven noise model is presented in blue, while the results for the white noise model sample are depicted in red. As can be seen, the low-level reconstruction tools are capable of completely recovering signals with amplitudes exceeding 20 ADC across all three planes, encompassing both noise models samples. This implies that the efficiency and purity of recovered signals within this amplitudes range exhibit a 100% accurate correspondence to the simulated charged particles. However, the effectiveness of low-level reconstruction tools is considerably lower for hits with amplitude less than 20 ADC in the case of the data-driven noise sample, whereas it remains high for white noise sample up to the threshold value. The decline in effectiveness observed in the data-driven sample can be attributed to the heightened noise levels, particularly at lower frequencies, as previously mentioned. This reduction in effectiveness resulted from the low purity of the recovered hits by the low-level reconstruction tools, as evidenced in Table 5.1.

Table 5.1 shows the efficiency, purity, and effectiveness mean of low-level reconstruction tools for the two induction and collection planes, respectively, summarising the results obtained from generated samples using both the white and data-driven noise models. The results indicate a slightly higher efficiency for the data-driven noise samples compared to the white noise samples. Conversely, the data-driven noise samples exhibited a significant reduction in the purity of reconstructed hits, with a decline of up to 90% observed across the induction planes when compared to the white noise samples. In addition, the lower hit purity in proton samples, especially data-driven noise sample, can be attributed to the comparatively shorter proton length within the detector resulting in fewer signal hits compared to the simulated noise hits in either noise model.

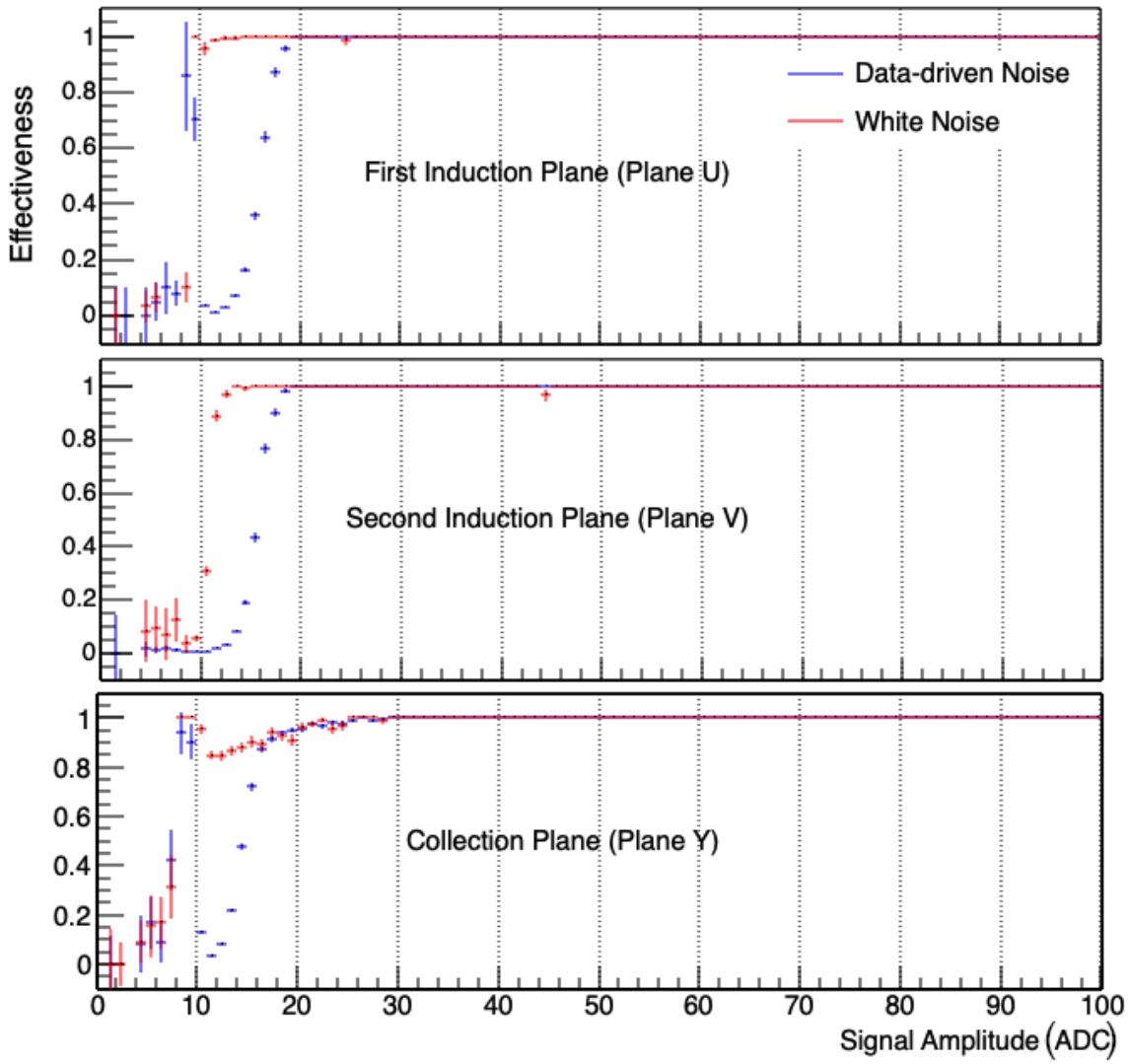

Figure 5.5: Comparison of low-level reconstruction effectiveness between data-driven and white noise models for electromagnetic shower hits. The effectiveness of low-level reconstruction in terms of the amplitude of hits on wire planes for the first and second induction and collection planes are shown at the top, middle and bottom windows, respectively.

In order to improve the purity of recovering the hits from data-driven noise samples, a study was conducted to reassign the threshold. Two methods were used to study the threshold and optimise the effectiveness of low-level reconstruction tools. The aim of maximising effectiveness is to allow reconstruction of as many real time hits as possible while rejecting noise hits, thereby improving the performance of subsequent stages in the reconstruction process and reducing the time and cost associated with running the reconstruction algorithms.

The first method involved manual adjustment of the threshold at intervals of 5 ADC, ranging from 5 to 30 ADC, to identify the optimal range for maximising effectiveness. The

Planes	White noise samples			Data-driven noise samples		
	electron	muon	proton	electron	muon	proton
Efficiency (%)						
U	85.29±0.46	99.46±0.03	91.35±0.09	87.2±0.2	99.57±0.03	88.15±1.07
V	85.76±0.42	99.36±0.04	90.31±0.1	86.37±0.26	99.5±0.03	89.78±0.92
Y	90.26±0.34	99.57±0.03	91.34±0.1	81.96±0.47	91.97±0.15	85.7±0.25
Purity(%)						
U	99.95±0.02	99.95±0.01	93.12±0.16	17.12±0.1	5.163±0.02	2.88±0.01
V	93.02±0.25	92.67±0.14	11.62±0.07	11.76±0.07	4.25±0.02	2.19±0.01
Y	97.66±0.14	98.54±0.06	32.28±0.18	99.61±0.14	99.44±0.05	55.75±0.43
Effectiveness (%)						
U	99.81±0.06	99.89±0.02	92.05±0.23	17.09±0.10	5.136±0.02	2.5±0.2
V	92.83±0.25	92.61±0.14	50.46±0.38	11.74±0.07	4.713±0.02	2.3±0.08
Y	97.53±0.15	88.91±0.23	78±0.1	82.82±0.47	91.66±0.16	73.8±0.72

Table 5.1: Summary of low-level reconstruction performance for white and data-driven noise samples. The first column in each row indicates the wire planes, with the first and second induction planes denoted as U and V, respectively, and the collection plane denoted as Y. The errors are Poissonian.

second method utilised a machine-learning algorithm known as Bayesian Optimisation to further optimise the effectiveness within the range identified by the first method. Bayesian Optimisation leverages Bayesian inference and Gaussian processes to efficiently identify the maximum value of an unknown function within a minimal number of iterations, for further details refer to reference [250].

Figure 5.6 shows the effectiveness variation with threshold adjustment at intervals of 5 ADC for the three planes in the data-driven noise model generated samples. As can be seen, the initial effectiveness values are low across all samples and planes. Subsequently, with an improvement in purity achieved through increasing the threshold, the effectiveness values gradually rise, reaching their maximum before exhibiting a decline which can be attributed to a decrease in efficiency. Based on the data presented in Figure 5.6, the threshold values of 10 ADC and 20 ADC were selected as the optimal range for further optimisation of effectiveness using the Bayesian Optimisation method.

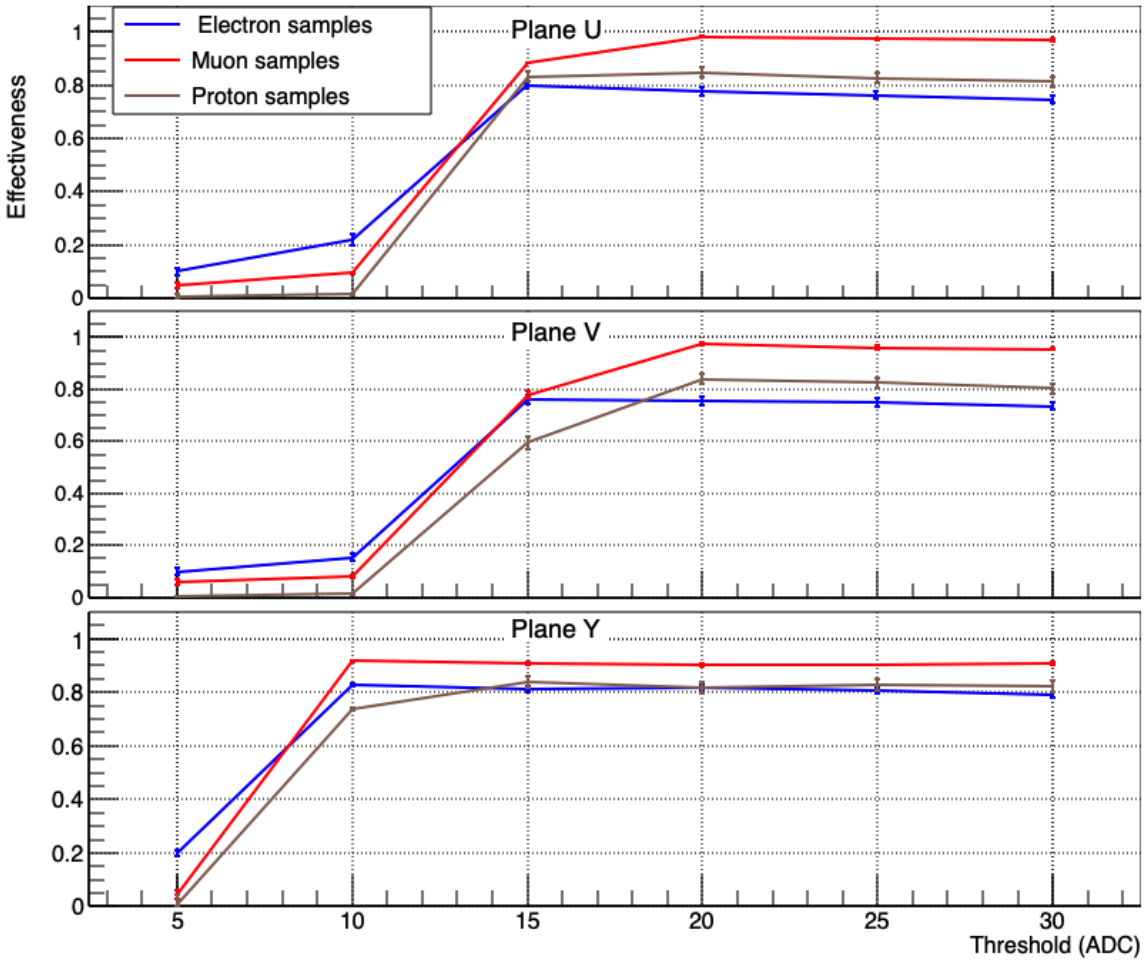

Figure 5.6: Effectiveness variation with threshold adjustment at intervals of 5 ADC (5-30 ADC) for the three planes in the data-driven noise model generated samples. The error bars are based on the Poisson distribution.

An example of Bayesian Optimisation iterations for first induction plane is shown in Figure 5.7. The graph shows the variation of threshold (left-blue) and effectiveness (right-red) as a function of the number of iterations in the Bayesian Optimisation process. Also, the figure illustrates the operational behaviour of the Bayesian Optimisation code, which alternates between the highest and lowest threshold values while evaluating the corresponding maximum effectiveness values. During each iteration, the code gradually decreases the difference between the highest and lowest threshold values until it converges to the maximum effectiveness value. The outcomes of the Bayesian Optimisation process are succinctly summarised in Table 5.2.

Following the optimisation of the threshold using the data-driven samples, threshold values of 14, 17, and 10 ADC were identified for the U, V, and Y planes, respectively, to be

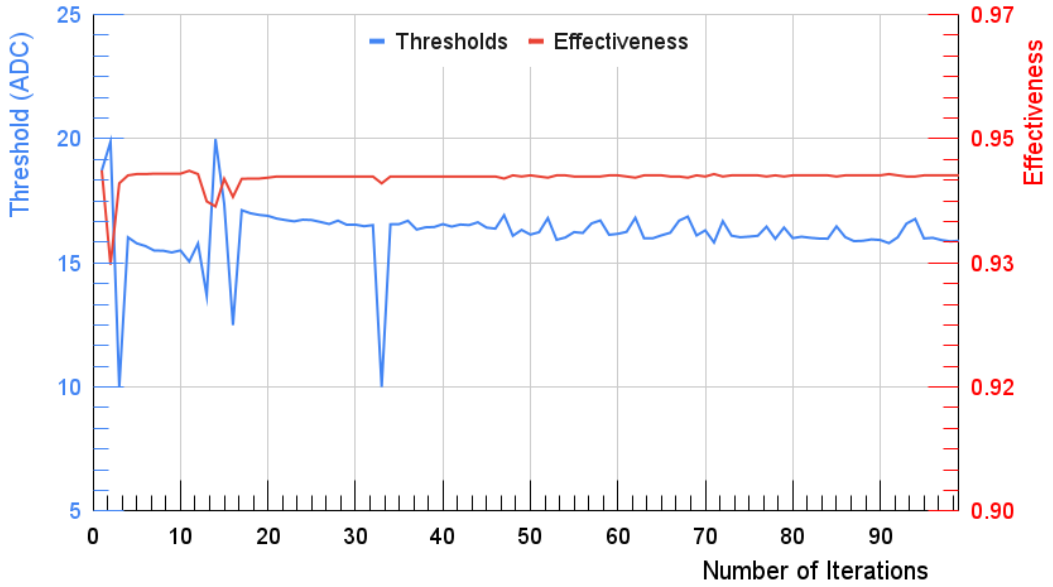

Figure 5.7: A graph shows the threshold (left -blue) and effectiveness (right-red) versus the number of Bayesian Optimisation iterations for U-plane.

employed within the hit-finding tool, aiming to achieve optimal effectiveness. By referring to Table 5.1 and Table 5.2, it is evident that the effectiveness of low-level reconstruction has been maximised and significantly improved for samples generated using the data-driven noise model. Furthermore, it successfully restores its performance in comparison to the samples generated using the white noise model.

Samples	Threshold			Effectiveness		
(Data-driven noise)	Plane U	Plane V	Plane Y	Plane U	Plane V	Plane Y
Electron	14.412	17.085	10.668	0.799	0.749	0.835
Muon	16.080	18.380	10.390	0.945	0.927	0.936
Proton	16.890	20.0	12.350	0.819	0.804	0.845

Table 5.2: Summary of low-level reconstruction performance data-driven noise samples after optimising the threshold.

Through the utilisation of the data-driven noise model and the optimisation of threshold values, the effectiveness of low-level reconstruction was maximised and improved, allowing for a more accurate recovery of the signal hits while reducing the impact of noise. Hence, it will enhance the performance of the subsequent high-level reconstruction algorithms and analyses, as these processed signals, 2D images, provide a foundation for pattern recognition algorithms to operate upon. Pattern recognition algorithms then leverage the reconstructed

data to identify and classify sparse 2D hits, form clusters, and establish a hierarchical structure of 3D particles. The following section, Section 5.2, covers the issues of pattern recognition in more detail.

5.2 Pattern Recognition

Pattern recognition constitutes a critical intermediate step within the reconstruction pathway, following the completion of the low-level reconstruction chain. Pattern recognition encompasses the process of identifying and associating individual recovered hits that are likely products of the same particle, thereby enabling the inference of particle properties based on these associations.

Constructing automated pattern recognition algorithms for LArTPCs poses a substantial challenge due to the complex and diverse topologies encountered. Additionally, LArTPCs face extended exposure times, characterised by lengthy drift times of up to a few milliseconds, along with a notable cosmic-ray background in surface-based detectors like SBND. Consequently, employing a single clustering approach is unlikely to effectively handle the intricacies of these complex topologies. Instead, a multi-algorithm approach is often used, combining the strengths of various algorithms to achieve better performance and accuracy in pattern recognition tasks. In the case of SBND, the Pandora pattern recognition is used to perform this task, which is widely used in other LArTPC experiments [251, 252].

In this section. an extensive review of Pandora algorithms utilised for handling complex event topologies in LArTPCs is presented. Additionally, Pandora's ability to classify Particle Flow Objects (PFOs) as either track-like or shower-like, a pivotal aspect of data analysis, is assessed. The evaluation addresses challenges in distinguishing low-energy tracks from electromagnetic showers and evaluates reconstruction efficiency in the context of neutrino event reconstruction.

5.2.1 Pandora Overview

Pandora, originally developed in 2007 for the International Linear Collider (ILC) to introduce particle flow calorimetry, is a multi-algorithm pattern recognition approach that has since been extended to include LArTPCs, starting with MicroBooNE [251, 252]. Pandora was developed as a solution to tackle the intricate challenge of distinguishing energy depositions attributed to individual particles in detectors employed by High Energy Physics (HEP) experiments [252, 253].

This approach involves subjecting the input hits to a multitude of decoupled algorithms, including over 100 algorithms available in SBND. Each algorithm is developed to address specific event topologies and manages operations such as clustering hits, merging or splitting clusters, and collecting clusters to construct a particle representation in the detector. Each algorithm performs pattern recognition operations safely by deferring complex topologies to subsequent algorithms, thereby maintaining decoupling and minimising inter-algorithm tension, resulting in a gradual and robust reconstruction process [252].

Two distinct Pandora multi-algorithm reconstruction paths, namely PandoraCosmic and PandoraNu, have been developed for analysis purposes. An overview of these two reconstruction paths within the Pandora chain is presented in Figure 5.8. PandoraCosmic is specifically optimised for reconstructing cosmic-ray muons and their associated delta-rays, focusing on track-oriented reconstruction. As a result, primary particles represent cosmic-ray muons, with assumed delta-ray showers added as daughter particles. Additionally, the reconstructed vertex, start-point, is determined based on the high-y coordinate of the muon track.

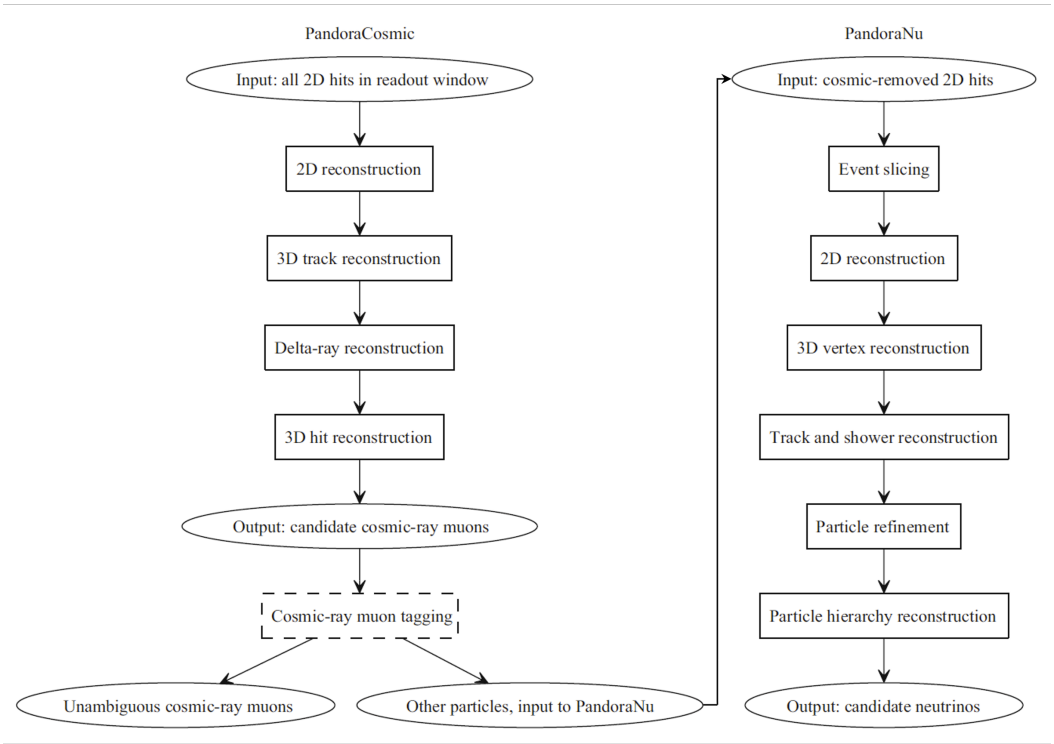

Figure 5.8: Overview of the two reconstruction paths in Pandora [252].

PandoraNu, on the other hand, is optimised for reconstructing neutrino interactions, with a special emphasis on identifying the interaction vertex and reconstructing particles originating from it. In PandoraNu, a neutrino interaction vertex is identified, aiding the

reconstruction of particles emerging from that position. Both tracks and showers are carefully treated, with the reconstructed visible particles added as daughters of the neutrino. While distinct features arise from the algorithm selection, there are also shared algorithms between the PandoraNu and PandoraCosmic paths.

The chain of Pandora algorithms begins the reconstruction, each wire plane independently, by employing a basic clustering approach to group hits that form continuous straight lines, assuming a track-like nature for all entities. Subsequent algorithms are executed to merge these clusters across detector gaps and resolve complex scenarios involving intersecting or interacting particles. The merged clusters are then matched to clusters in other planes by identifying candidate clusters with similar drift spans. Upon finding a series of candidate matches, they can be combined to create a Particle Flow Object (PFO). This combination is based on evaluating the consistency between clusters by projecting their overlap onto a third plane and calculating a goodness-of-fit metric to determine if the match is favourable. Additional algorithms, including those targeting delta-rays from cosmics, are applied to improve the goodness-of-fit metric by merging or splitting clusters as needed. Pandora further endeavours to determine a 3D position, known as a space-point, for each hit by applying sliding linear fits to the matched clusters.

The first step involves running PandoraCosmic and eliminating all clusters and their associated hits that are identified as unequivocally attributed to cosmic-ray particles. This involves grouping PFOs that are likely to have originated from the same source by evaluating their separation and directional characteristics. Various examinations are then performed on these PFOs to assess their consistency with a neutrino-like topology. These checks include verifying the containment of PFO end-points within the detector volume, ensuring that all space-points lie within the detector volume at the trigger time, considering the vertical and straight nature of the tracks, and examining the positions of end-points in relation to the top and bottom of the detector. The slicing algorithm within Pandora is subsequently used to process the remaining clusters, which are considered potential neutrino interactions. This algorithm divides the event into segments known as slices, each aiming to contain all hits originating from a single source, such as particles produced by primary cosmic-ray or a neutrino interaction, based on the proximity and direction of the constituent clusters.

Following reapplying certain 2D clustering algorithms used in PandoraCosmic, Pandora then attempts to identify the vertex of the neutrino interaction for each slice. Initially, Pandora generates a list of vertex candidates by matching the end points of clusters across the different planes. Subsequently, a series of scoring metrics are applied to assess each vertex candidate. These metrics include the Energy Kick Score, which considers transverse energy and the closest approach distance, the Asymmetry Score, which compares the number of hits

upstream and downstream relative to the beam direction to reduce candidates along tracks, and the Beam Deweighting Score, which evaluates the position of the vertex relative to the beam direction, accounting for the expected downstream travel of primary particles.

Pandora then uses Multivariate Analysis (MVA) to select the best vertex candidate by combining scores and predictors. The process involves region finding to approximate the vertex area and vertex finding to select the best candidate within that region. The MVA considers both "Event" and "Candidate" features, capturing event-wide metrics and specific candidate information. These features are subsequently provided to the MVA in a structured format comprising Event Features, followed by Candidate-1 Features and Candidate-2 Features. The MVA returns a score indicating the preference for candidate-1 (positive score) or candidate-2 (negative score). The event features include metrics such as event showeryness, event energy, event volume, longitudinality, and the number of hits, clusters and vertex candidates. The vertex features modify the previous scores, including local and global, which differentiate based on the hit distance from the candidate, and shower asymmetries exclusively consider hits originating from shower-like clusters.

After identifying the vertex, the event can be expanded outward using distinct algorithms for tracks and showers. Characterisation algorithms are employed throughout this process to classify individual clusters as either track-like or shower-like at different stages. This classification determines the further processing of the cluster, either as a track utilising sliding linear fits or a shower using cones. The classification is performed at multiple stages within Pandora, incorporating additional information as it becomes available, such as the transition from 2D clusters to 3D PFOs. A combination of cut-based characterisation and an MVA is employed to assign a score to each PFO, which ultimately determines its track-like or shower-like classification. The MVA is specifically applied to the final classification step, as it establishes the path for higher-level reconstruction following Pandora. After executing the algorithms, Pandora generates a PFO output for each 3D cluster, including a vertex, a set of 3D space-points (along with corresponding 2D hits), and a hierarchy of particle flows. The hierarchy originates with a "Neutrino" particle containing a vertex and primary daughters, which may further possess their distinct hierarchies.

Figure 5.9 shows the progressive stages of the Pandora reconstruction process for the neutrino interaction scenario featuring the production of a muon, proton and two photons. The initial unclustered hits in each of the three planes, serving as the input for Pandora, are displayed in Figure 5.9a, while the subsequent 2D reconstructed clusters in each plane are depicted in Figure 5.9b. Notably, Pandora successfully clusters the hits, resulting in two track-like clusters corresponding to the muon and proton tracks, as well as three shower-like clusters originating from π^0 decay (two showers) and the muon decay (Michel Electron) at

the terminus of the muon track, within each plane. It is important to note that the colours assigned to individual clusters in each plane are not cross-correlated. Figure 5.9c shows a comprehensive 3D reconstruction of the event generated by Pandora, wherein the information derived from all planes has been integrated.

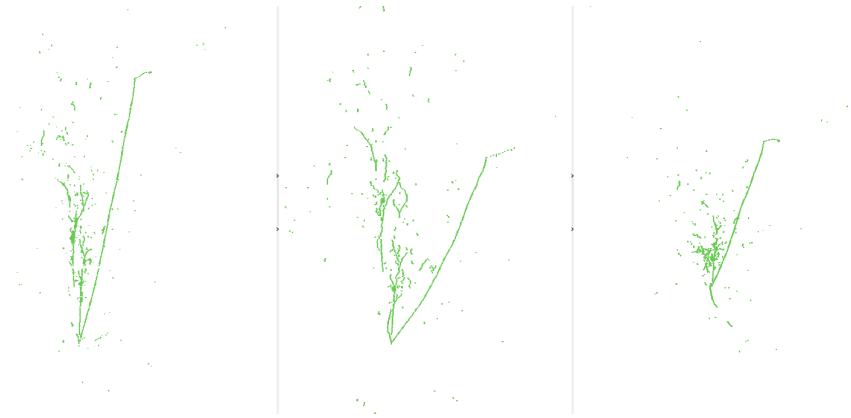

(a)

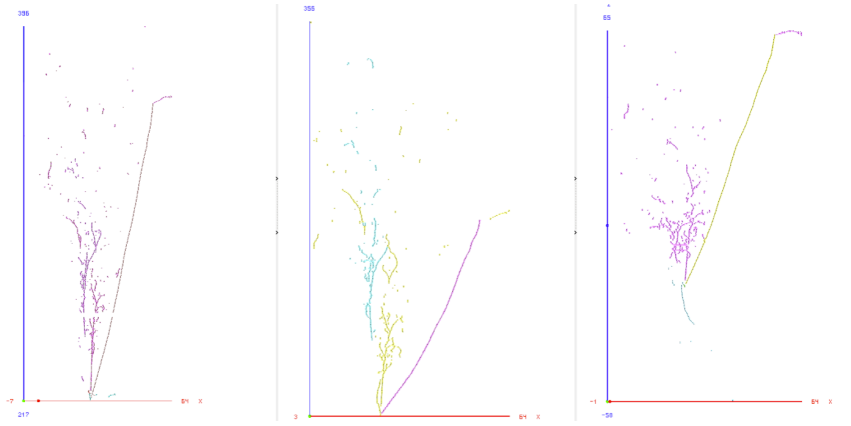

(b)

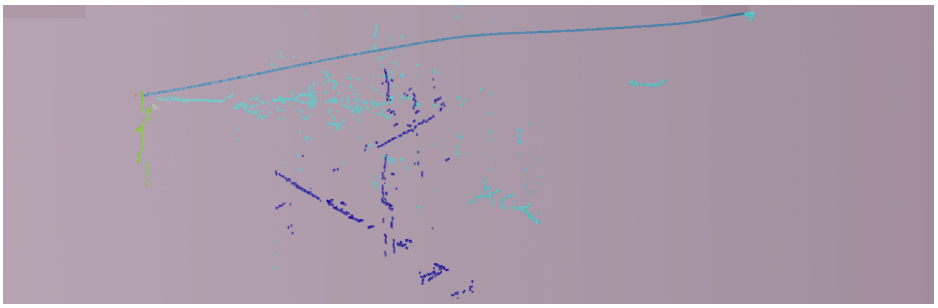

(c)

Figure 5.9: Visualisation of Pandora clustered ν_μCC interaction with π^0 in the final state: U, V, and Y views (left, centre, and right, respectively) pre-clustering and post-clustering, with full 3D reconstruction displayed at the bottom.

5.2.2 Performance of Track-Shower Characterisation

The characterisation of Particle Flow Objects (PFOs) in Pandora involves determining their classification as either track-like, attributed to particles with high mass and momentum such as muons, protons, pions, and kaons, or shower-like, associated with an electromagnetic activity. This classification is important because it determines how the PFO will be further processed. Misclassification of clusters can result in tracks and showers with low purity and/or incomplete reconstruction, thereby impacting the subsequent higher-level reconstruction conducted after Pandora. Therefore, the accurate characterisation of PFOs is a critical step in data analysis, enabling the generation of high-quality tracks and showers by Pandora.

Two samples were generated to assess the performance of Pandora in characterising PFOs as either track-like or shower-like. The first sample consisted of 10k events of ν_e *CC* interactions, while the second sample comprised 100k events of ν_μ *CC* interactions with final state neutral pions. Figure 5.10 shows the classification of clusters identified as shower-like particles in both samples. Figures 5.10a and 5.10b show the number of showers as a function of true particle energy in GeV for photons and electrons samples, respectively. At the bottom of each plots, ratio plots depict the metrics of purity and completeness, indicating the accuracy and comprehensiveness of clustering the hits from the respective particle. Both Figures 5.10a and 5.10b display histograms representing different classifications of clusters. In both cases, the blue histogram corresponds to true electromagnetic showers that were correctly clustered and classified as showers in the reconstruction. The red histogram represents true track-like particles that were mistakenly clustered and classified as showers. The dark grey histogram represents a group of hits that were separated from true electromagnetic showers but were still clustered and classified as showers. Lastly, the green histogram represents a group of hits from true track-like particles that were erroneously clustered and classified as showers.

In the photon showers sample (Figure 5.10a), the majority of reconstructed showers below 400 MeV align with true electromagnetic showers, as indicated by the blue histogram. However, there is a minor fraction of showers around 200 MeV and 50 MeV that are associated with either true track-like particles or fragments of actual showers, respectively. Similarly, in the sample of electron showers (Figure 5.10b), most reconstructed showers below 900 MeV match with true electron showers. The classification of clusters as showers at energies of approximately 200 MeV and 50 MeV exhibits a similar pattern to the photon sample, with a small fraction of showers attributed to either true track-like particles or fragments of genuine showers. In both samples, it is observed that clusters originating from track-like particles, particularly protons within the energy range of 0.9 GeV to 1.3 GeV, are misclassified as showers. This misclassification primarily arises from the resemblance in behaviour between low-energy tracks and electromagnetic showers, making it challenging to

differentiate and categorise them accurately as tracks. Additionally, protons demonstrate a lower likelihood of being classified as showers in photons sample when compared to electrons sample. Figure 5.11b and Figure 5.11a show event display misclassified proton-track and an accurately classified proton-track, respectively.

The electron sample exhibits a higher overall purity in the reconstructed showers, approximately 55%, compared to the photon sample, which achieves a purity of around 45%. This disparity can be attributed to the overlapping hits from both photons showers originating from decay, particularly when the angle between the two photons is narrow. In terms of completeness, both samples exhibit an average value of approximately 85%, with some minor fluctuations observed as a function of particle energies, as depicted by the violet colour in Figures 5.10a and 5.10b.

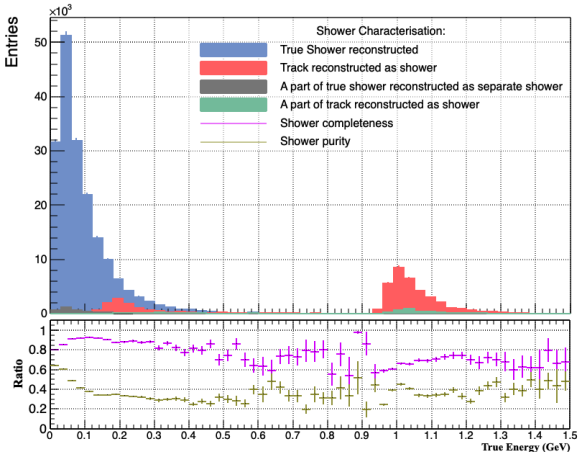

(a) Photon Showers Sample

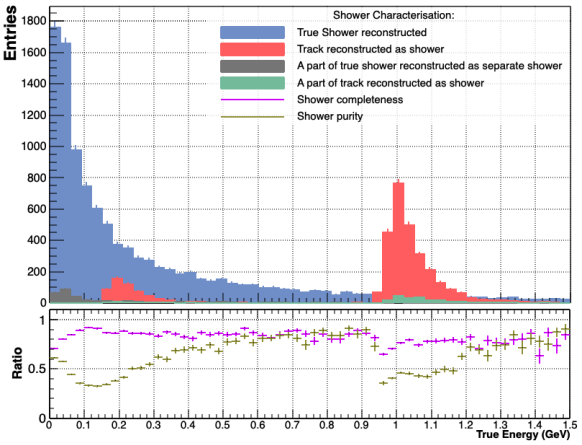

(b) Electron Showers Sample

Figure 5.10: Classification of showers in samples with electrons and photons topologies in the final state. The ratio presented at the bottom of the plots provides an assessment of the reconstruction quality in terms of both competence and purity of the showers.

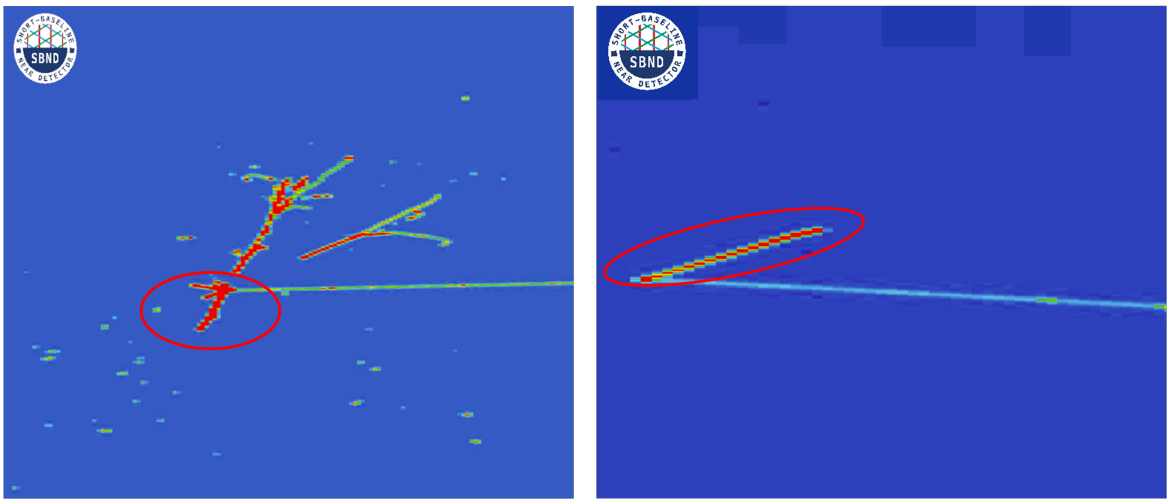

(a) Misclassified proton-track (b) Accurately classified proton-track

Figure 5.11: Event display showcasing accurately and misclassified proton-track.

Figure 5.12 illustrates the classification of clusters identified as track-like particles in both samples. Specifically, Figures 5.12a and 5.12b depict the distribution of track numbers as a function of the true particle energy in GeV for samples containing electrons and photons in the final state, respectively. In both cases, the blue histogram represents true track-like particles that were correctly clustered and classified as tracks during the reconstruction process. Conversely, the red histogram illustrates instances where true electromagnetic showers were mistakenly clustered and classified as tracks. The dark grey histogram represents a collection of hits that were separated from true track-like particles but were still clustered and classified as tracks. Lastly, the green histogram denotes a group of hits originating from true electromagnetic showers that were mistakenly clustered and classified as tracks. Notably, both samples exhibit the misclassification of clusters originating from low-energy electromagnetic showers as tracks due to these particles primarily losing their energy through ionisation [194]. This misclassification arises from the similarities in behaviour between low-energy electromagnetic showers and tracks, presenting challenges in accurately distinguishing and categorising them as showers. Figure 5.13a and Figure 5.13b provide event displays showcasing a misclassified photon shower and an accurately classified photon, respectively.

The ratio plots at the bottom of Figures 5.12a and 5.12b display metrics of purity and completeness, which assess the accuracy and comprehensiveness of clustering the hits corresponding to the respective particles. In both samples, the track-like particles exhibit an overall reconstruction completeness exceeding 85% and a purity exceeding 81%.

The performance evaluation of the track-shower classification in the sample featuring π^0 in the final state indicates that approximately 88% of photon showers were correctly clustered

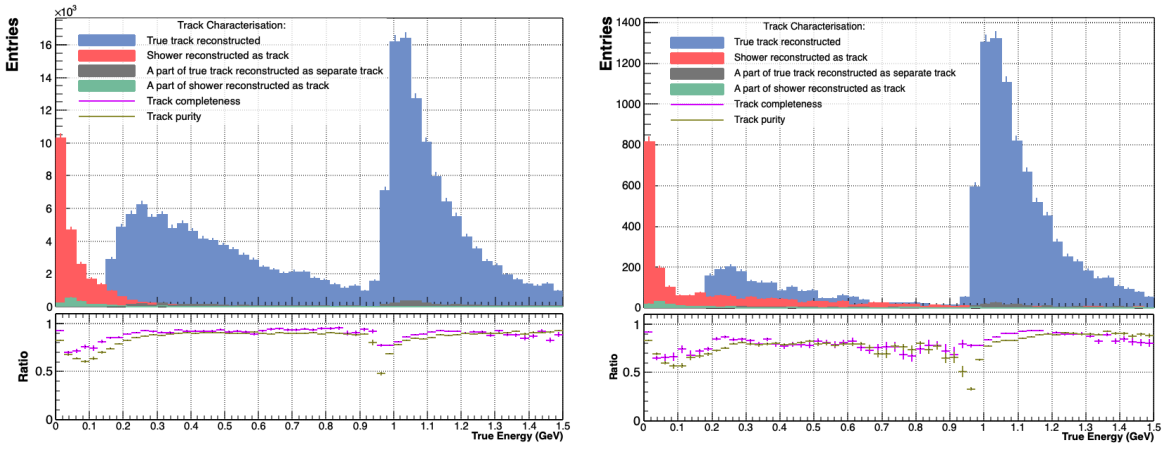

(a) In Photon Sample (b) In Electron Sample

Figure 5.12: Classification of tracks in samples with electrons and photons topologies in the final state. The ratio presented at the bottom of the plots provides an assessment of the reconstruction quality in terms of both competence and purity of the tracks.

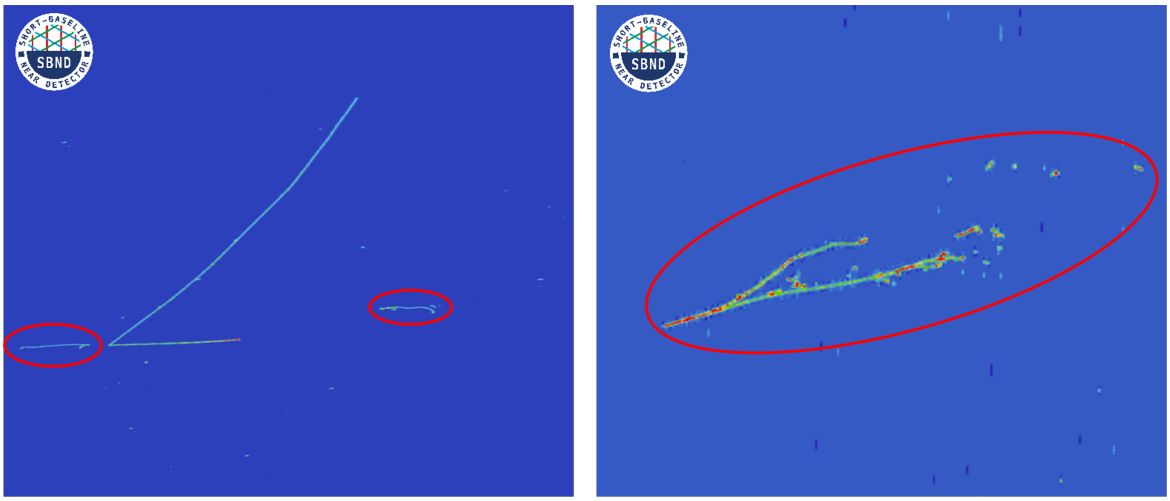

(a) Misclassified photon-shower (b) Accurately classified photon-shower

Figure 5.13: Event display showcasing accurately and misclassified photon-shower.

and classified as showers, while approximately 12% of photon showers were misclassified as tracks. In contrast, around 80.6% of tracks in the sample were accurately classified as tracks, while the remaining tracks were erroneously classified as showers, particularly in the case of protons.

Regarding the classification performance of electron showers in the ν_e *CC* interactions sample, approximately 83% of electron showers were correctly identified and classified as showers, while approximately 76% of track-like particles were correctly classified as

tracks and 24% were misclassified as showers. The main challenges encountered in the track-shower classification revolve around accurately distinguishing low-energy particles and effectively differentiating between tracks and showers.

5.2.3 Neutrino Identification and Reconstruction Performance

As discussed in section 5.2.1, the application of the PandoraCosmic chain effectively eliminates the majority of clearly identifiable cosmic rays, while retaining a notable quantity of ambiguous cosmic ray events that are treated as potential neutrino candidates. These ambiguous cosmic rays are subsequently processed by the PandoraNu algorithms alongside the true neutrino interactions. After the completion of running the PandoraNu algorithms, further attempts can be undertaken to identify cosmic slices using the additional available information by these algorithms.

To evaluate the nature of neutrino candidate slices and distinguish them from cosmic slices, an MVA approach is employed, assigning a "Neutrino Score" to each candidate slice. The Neutrino Score serves as an indicator, with a lower score suggesting a higher likelihood of a cosmic origin, while a higher score suggests a neutrino interaction. The scoring mechanism relies exclusively on topological considerations and without incorporating calorimetric or subsystem information. Various variables are employed to assess the dominance of a single large track, resembling a cosmic slice, versus multiple particles emerging from slice vertex, characteristic of a neutrino interaction. Various variables are employed in this assessment, including the number of "primary" PFOs originating from the interaction vertex, the total number of hits within the slice, the Y-position of the neutrino vertex, the weighted displacement in the Z-direction of space points from the neutrino vertex, the count of space points within a 10 cm sphere centred around the neutrino vertex, the eigenvalues ratio in the sphere indicating the alignment of points, the Y-projection of the longest track direction in the slice, the deflection of space points along the longest track, the fraction of hits belonging to the longest track, and the total number of hits in the longest track. These variables collectively contribute to the Neutrino Score, enabling the identification and distinction of cosmic and neutrino slices based on their respective characteristics.

Given the high neutrino flux in SBND, a considerable fraction of events involves multiple neutrino interactions known as pile-up. Consequently, selecting only the most neutrino-like slice per event would result in the exclusion of actual neutrino interactions and potentially introduce biases. To address this, Pandora is configured to retain all neutrino candidates along with their corresponding "Neutrino Score" and pass them to analysers. This allows for informed decisions to be made once subsystem information becomes available, ensuring a comprehensive evaluation without compromising the identification of neutrino interactions.

Figure 5.14 shows the distributions of the Neutrino Score, as determined by the Pandora MVA, for each candidate slices. The histogram in red represents cosmic slices, while the blue histogram corresponds to all neutrino events. In addition, the green histogram specifically represents ν_μ CC events with a final state topology involving π^0. Notably, there is a distinct separation observed between neutrino and cosmic slices in the Neutrino Score distributions. Also, the performance for events with π^0 topology exhibits better results compared to other ν events. This outcome aligns with expectations since the photon showers generated by the decay of π^0 within neutrino slices possess more discernible topological characteristics that distinguish them from cosmic rays. A cut at 0.4 will reduce the cosmic slices by around half but will reduce the neutrino slice by approximately 2%. A greater amount of cosmic background can be mitigated by employing more stringent cuts; however, this comes at the cost of reducing the neutrino signal. The determination of the optimal threshold relies on the specific analysis requirements. This topic is covered more comprehensively alongside alternative choices in section 7.2. The ratio histograms presented at the bottom show the

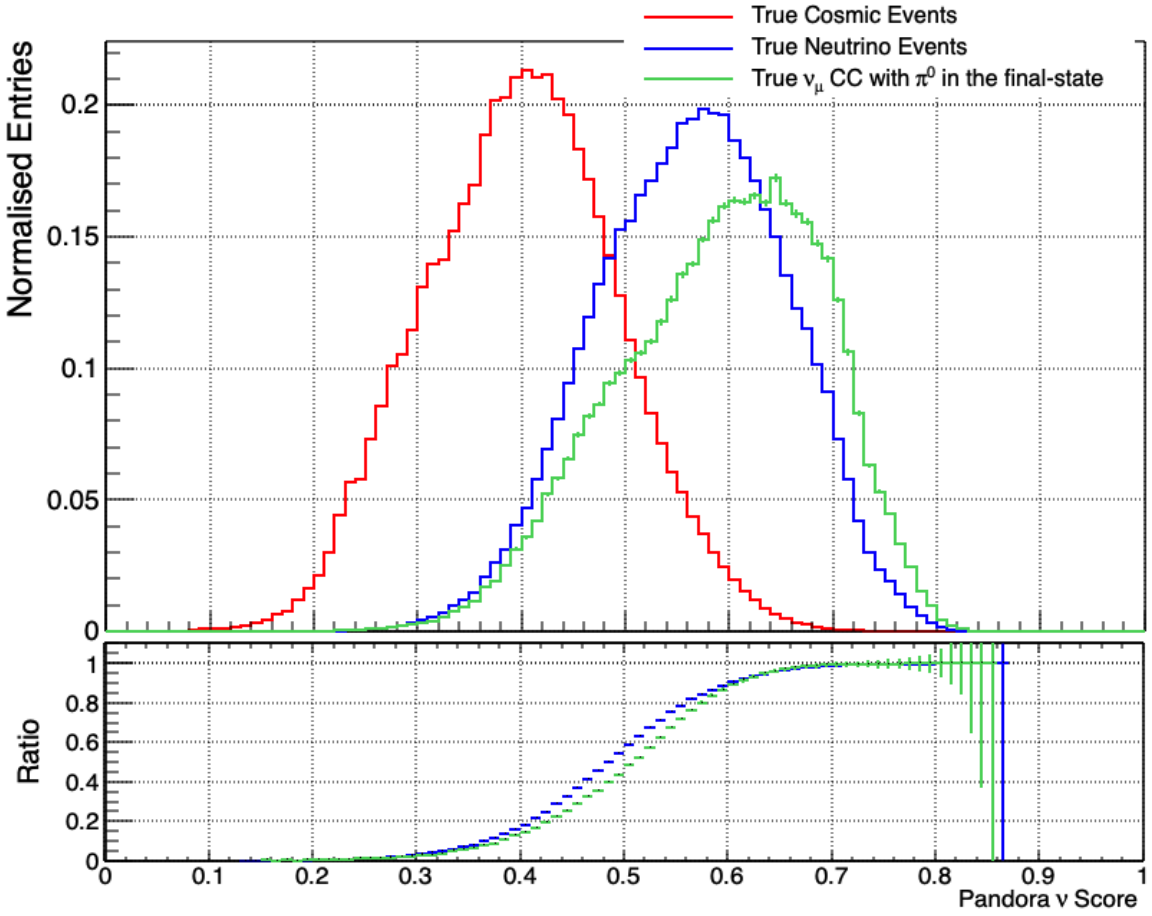

Figure 5.14: Distributions of Pandora neutrino score for neutrino and cosmic rays interactions.

percentage of neutrino slices to cosmic slices with respect to the Neutrino Score distributions. The blue histogram corresponds to all neutrino events slices, while the green represents ν_μ CC events with a final state topology involving π^0.

Overall, the performance of the neutrino events reconstruction process, up to the completion of the Pandora algorithms chain, is shown in Figure 5.15. Figure 5.15a shows the efficiency of reconstruction for GENIE BNB-like ν_μ interactions, which correspond to simulated ν events as expected from the BNB beam. On the other hand, Figure 5.15b displays the reconstruction efficiency for GENIE intrinsic ν_e interactions, exclusively focusing on BNB ν_e events interactions. In both Figures, the left y-axis represents the efficiency, while the right y-axis corresponds to the number of events for the spectrum (indicated by the blue-filled histogram). The x-axis denotes the neutrino energy, measured in GeV units. The blue histogram depicts the reconstructed efficiency, representing the ratio of accurately reconstructed neutrino interactions with both purity and completeness exceeding 50% to the true neutrino events in the BNB ν single interaction dataset, excluding in-time cosmic rays. Conversely, the orange histogram represents the reconstructed efficiency for neutrino interactions in the presence of in-time cosmic rays.

Overall, the reconstruction efficiency for the BNB-like ν_μ single interaction sample is approximately 90%, while for the sample including in-time cosmics, it is around 75%. In intrinsic ν_e interactions, the efficiency is better by about 5% for both with and without in-time cosmics. The reduction in the reconstruction efficiency of the sample with in-time cosmics for both BNB-like ν_μ and intrinsic ν_e interactions is attributed to a decrease in purity and/or completeness. This decrease occurs when the neutrino slice merges with cosmic rays or is divided into multiple slices. Additionally, the reconstruction efficiency is diminished for neutrinos with energy below 300 MeV due to the inherent challenges in reconstructing low-energy neutrinos in LAr experiments, which stem from factors such as reduced particle production.

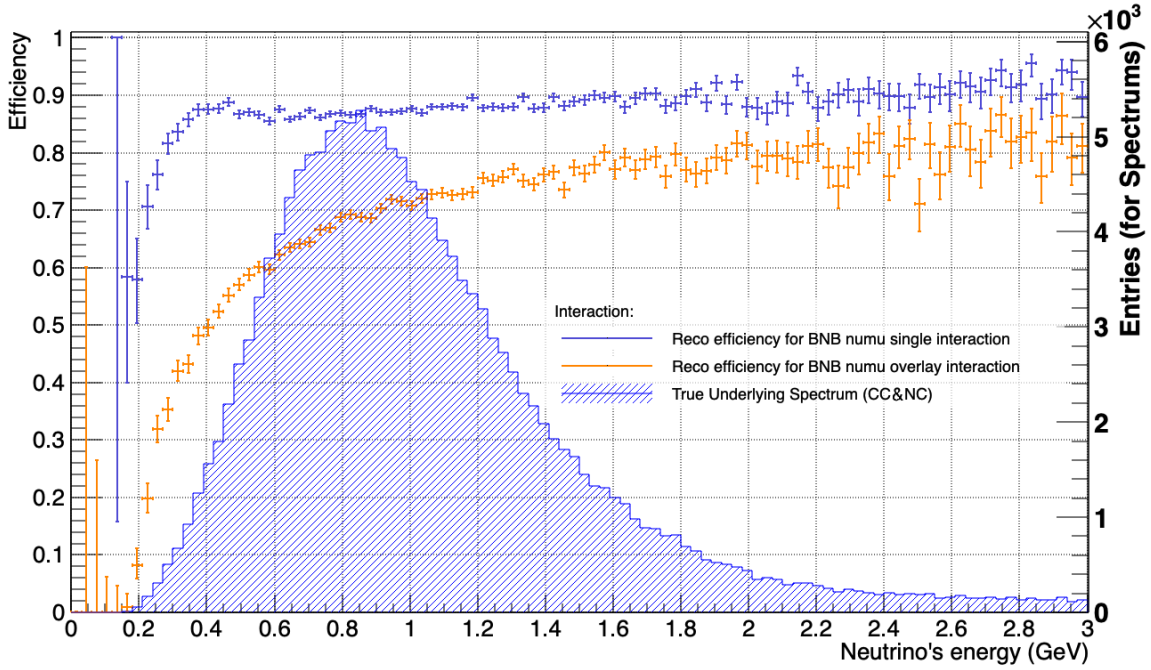

(a) GENIE BNB-like ν_μ interactions

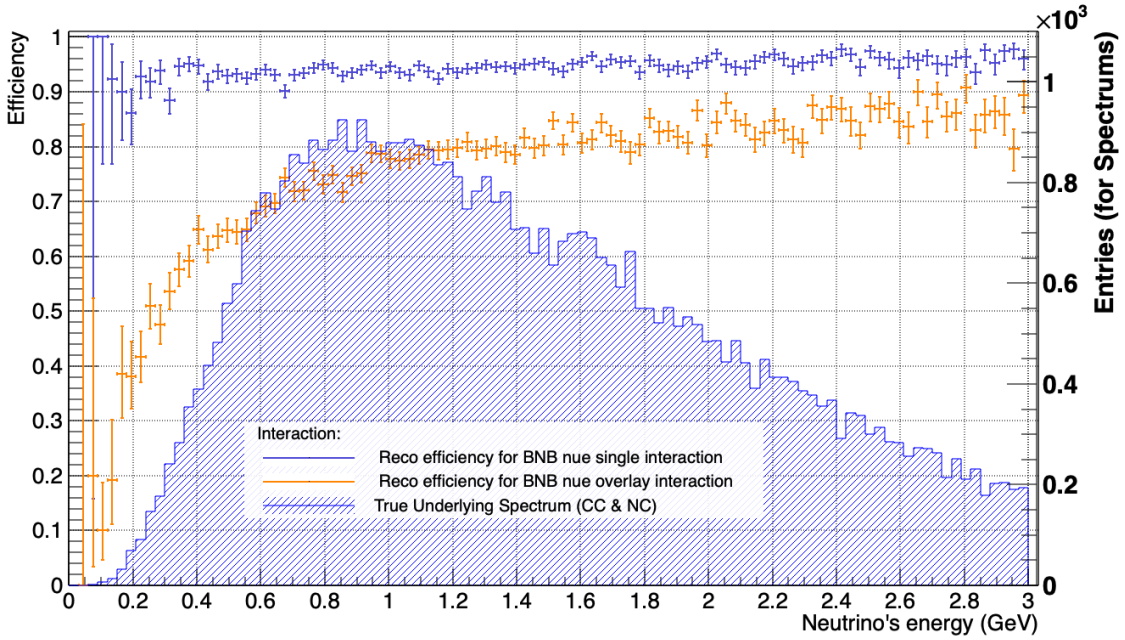

(b) GENIE Intrinsic ν_e interactions

Figure 5.15: Reconstruction performance of neutrino events interactions within SBND detector.

5.3 Summary

The SBND experiment utilises a three-step process for converting raw LArTPC images into analysis-level physics quantities. The process consists of low-level reconstruction, pattern recognition, and high-level reconstruction. Low-level reconstruction involves signal processing, noise filtering, and hit finding to extract meaningful information from the raw data. Pattern recognition transforms the resulting 2D images into sparse 2D hits, clusters, and a hierarchy of 3D particles. High-level reconstruction incorporates calorimetric reconstruction and particle identification to analyse the output of pattern recognition and generate final physics quantities. The effectiveness of these reconstruction steps is evaluated using simulated events and different noise models.

The evaluation of low-level reconstruction plays a critical role in shaping subsequent high-level reconstruction algorithms and analyses, where simulated events are utilised to assess the performance of reconstruction tools. Parameters such as hit efficiency and purity are employed to measure the effectiveness, with a focus on comparing different noise models, including a data-driven noise model based on MicroBooNE data, which provides a more accurate representation of anticipated noise in the SBND detector. The evaluation results demonstrate the effectiveness of low-level reconstruction tools in recovering signals with amplitudes exceeding 20 ADC, although their performance diminishes for signals with lower amplitudes, particularly in the presence of increased noise levels in the data-driven noise model. While the efficiency of reconstruction tools is slightly higher for the data-driven noise samples, the purity of reconstructed hits is significantly reduced compared to the white noise samples. To enhance hit purity in data-driven noise samples, an optimisation study was undertaken for this work to determine the optimal hit-finding threshold using manual adjustment and Bayesian Optimisation methods. The results showcase the effectiveness variation with threshold adjustment and highlight the iterative behaviour of the Bayesian Optimisation algorithm.

The Pandora algorithm is employed in LArTPCs to address the challenges posed by complex and diverse event topologies. Pandora utilises over 100 decoupled algorithms to gradually and robustly reconstruct particles in the detector. It follows two paths: PandoraCosmic for cosmic-ray muons and delta-rays, and PandoraNu for neutrino interactions. The reconstruction process involves clustering, merging clusters across detector gaps, matching clusters across planes, identifying interaction vertices, and classifying clusters as track-like or shower-like. The output of Pandora includes 3D clusters, vertices, space-points, and a hierarchy of particle flows representing the reconstructed event.

Accurate characterisation of PFOs as track-like or shower-like is crucial for further data analysis. The performance of Pandora in characterising PFOs is evaluated using samples

of ν_e CC interactions and ν_μ CC interactions with final state neutral pions. The analysis shows that reconstructed showers align well with true electromagnetic showers, but a fraction of lower-energy showers exhibit misclassification as track-like particles. The evaluation also highlights the misclassification of clusters from low-energy proton-tracks as showers. Challenges arise in distinguishing low-energy tracks and electromagnetic showers accurately.

The Pandora reconstruction process includes an evaluation of neutrino candidate slices and the distinction between cosmic and neutrino slices. PandoraCosmic effectively eliminates identifiable cosmic rays but retains ambiguous cosmic ray events as potential neutrino candidates. An MVA approach assigns a "Neutrino Score" to each candidate slice based on topological considerations. The Neutrino Score enables the identification of cosmic and neutrino slices and helps in avoiding the exclusion of actual neutrino interactions. The distribution of Neutrino Scores shows a clear separation between neutrino and cosmic slices, with better performance observed for ν_μ CC events with a final state involving π^0. A threshold cut at 0.4 decreases cosmic slices by half while minimally affecting neutrino slices. The choice of the optimal threshold depends on specific analysis requirements and can be determined by balancing the reduction of cosmic background with the preservation of the neutrino signal.

The performance of the neutrino event reconstruction process is evaluated in terms of reconstruction efficiency. The efficiency is measured for GENIE BNB-like ν_μ interactions and GENIE intrinsic ν_e interactions. The efficiency is higher for intrinsic ν_e interactions, both with and without in-time cosmic rays, compared to BNB-like ν_μ interactions. The decrease in reconstruction efficiency with in-time cosmics is attributed to decreased purity and/or completeness when neutrino slices merge with cosmic rays or are divided into multiple slices. Challenges in reconstructing low-energy neutrinos also contribute to reduced efficiency for neutrinos below 300 MeV.

Chapter 6

SBND High-Level Track & Shower Reconstruction

Following the Pattern Recognition process detailed in Chapter 5, the subsequent step in the reconstruction process involves characterising the Particle Flow Objects (PFOs) generated. Separate pathways are established for track-like and shower-like PFOs. The primary objective is to extract topological and calorimetric parameters to identify particles and determine their kinematics. This step holds significant importance for any physics measurement since it forms the foundation for downstream Particle Identification (PID) processes, aiding in signal selection and background rejection. Moreover, accurately measuring particle properties is essential for determining the neutrino interaction kinematics, crucial for cross-section and oscillation analyses. The modules discussed in this context are part of the LArSoft framework, which is shared among Liquid Argon Time Projection Chamber (LArTPC) experiments [238].

This chapter begins with Section 6.1 which outlines the track reconstruction process, the calculation of energy loss, and the utilisation of various approaches to accurately estimate particle energy, essential for particle identification and understanding neutrino interactions. The next section, section 6.2, examines and develops the various parameters utilised to characterise showers, including energy, length, and opening angle. A comprehensive discussion of the tools and algorithms employed for these characterisations is presented. The intricacies of separating photon and electron showers are highlighted, emphasising the importance of accurate dE/dx measurements. The chapter ends, covered in Section 6.3, by thoroughly exploring the reconstruction of photon showers from π^0 decay events. It examines leading and sub-leading photon showers, highlighting challenges from misclustering and merging. Distinguishing between photon showers and track-like particles is emphasised, crucial for cross-section measurements linked to π^0 production.

6.1 High-Level Track Reconstruction

After the Pandora pattern recognition software, outlined in Chapter 5, identifies PFOs resembling track-like particles and their corresponding space-points, the track fitting process is performed to reconstruct the trajectory. SBND employs the Pandora Track Creation module [254] to generate 3D tracks, where the resulting track comprises a sequence of smoothed trajectory points, each associated with a specific space-point characterised by refined position and direction. This step is crucial in the reconstruction process since the track direction enables extrapolation to the Cosmic Ray Tagger (CRT), determining the kinematics of neutrino interactions, and extracting calorimetric information from the track.

The track creation algorithm processes a set of 3D space-points associated with a track-like PFO, employing linear regression fits to determine the trajectory. It begins by utilising principal component analysis to find the general direction of the track. The space-points are then ordered along the principal axis in the transverse direction and grouped into segments of the wire pitch width (3 mm). Two 2D sliding fits are conducted on the projected data, each onto orthogonal directions. Each 2D sliding fit is a linear regression performed at each segment in the 2D space, using ten segments before and after as additional fitting points. The track direction is derived from the gradients of these fits, while the gradients and intercepts are used for 3D position reconstruction.

Figure 6.1 shows the deviations in direction and starting position of track-like particles by comparing the reconstructed results with the truth, MC information. In Figure 6.1a, discrepancies in the directions of track-like, muon, proton, and pion particles are presented. It can be seen that over 98% of the reconstructed tracks exhibit alignment in direction with the true particle direction. Additionally, Figure 6.1b demonstrates that the offset between the true and reconstructed starting positions remains within 3 cm. These observations establish a significant concordance between the reconstructed track properties and their true counterparts in terms of both direction and initial position.

As outlined in Chapter 3, LArTPCs are great at charged particle flavour identification and energy determination. Following track reconstruction, a LArSoft module for calorimetric reconstruction calculates the energy loss per unit length (dE/dx) for each track point [255]. This data is utilised in both PID and particle kinematics calculations, which are discussed further in Chapter 7.

The dE/dx is individually calculated for each hit, derived by dividing the charge loss dQ, represented by the signal area, by the corresponding track pitch. The track pitch (dx) signifies the distance the particle traverses within the wire pitch and is determined from the track direction at energy deposition using trajectory points and wire pitch information.

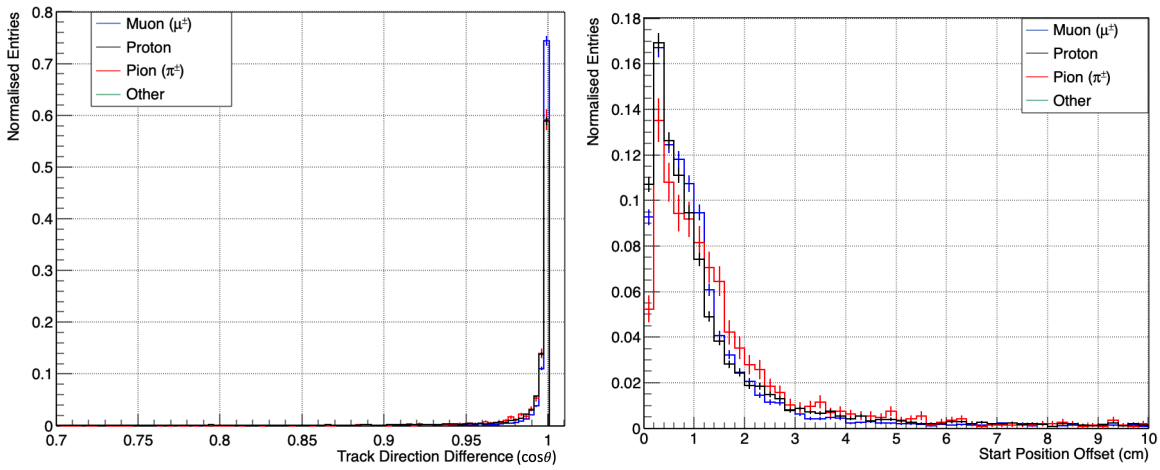

(a) (b)

Figure 6.1: Deviation in direction and start position of track-like particles. Panel (a) illustrates the disparity between the reconstructed direction of track-like PFOs and the true direction of the particles. Panel (b) depicts the disparity in the reconstructed start position compared to the true start position.

The charge loss per unit length dQ/dx is transformed into an electron-based measure using a calorimetric constant. This constant is evaluated by assessing detector responses to MIP muons moving perpendicular to the wires and parallel to the wire planes, while incorporating the most probable dE/dx value (1.9 MeV/cm) for MIP muons in liquid argon.

Upon implementing the calibration constant, a correction for lifetime is introduced to address losses due to impurities, as discussed in Chapter 3. This correction enables the determination of electrons deposited post recombination. Lastly, the modified box model, employing parameters acquired from the Argon Neutrino Test-stand (ArgoNeuT) as outlined in Chapter 3, is used to consider recombination effects and quantify the energy deposition in MeV.

The residual range for each trajectory point is determined by summing the path lengths (dx) from a given point to the track's endpoint. This measurement is essential for analysing the dE/dx distribution along a track, such as identifying Bragg peaks. Additionally, the overall track range, specifically the residual range at its beginning, can be leveraged to estimate track energy using a reference table under the assumption of particle stopping via ionisation [256]. Since the range-energy relationship varies by particle type, multiple hypotheses are considered during energy calculation, with the appropriate one chosen post-PID.

Figure 6.2 presents distributions of the expected dE/dx plotted against residual range for different track-like particles within liquid argon based on SBND simulation. In Figure 6.2, a

notable discriminatory capability is observed between the expectations for track-like protons and those for muon or pion tracks, as illustrated by the respective black and red fitted curves, further details and other PID parameters are discussed in Chapter 7.

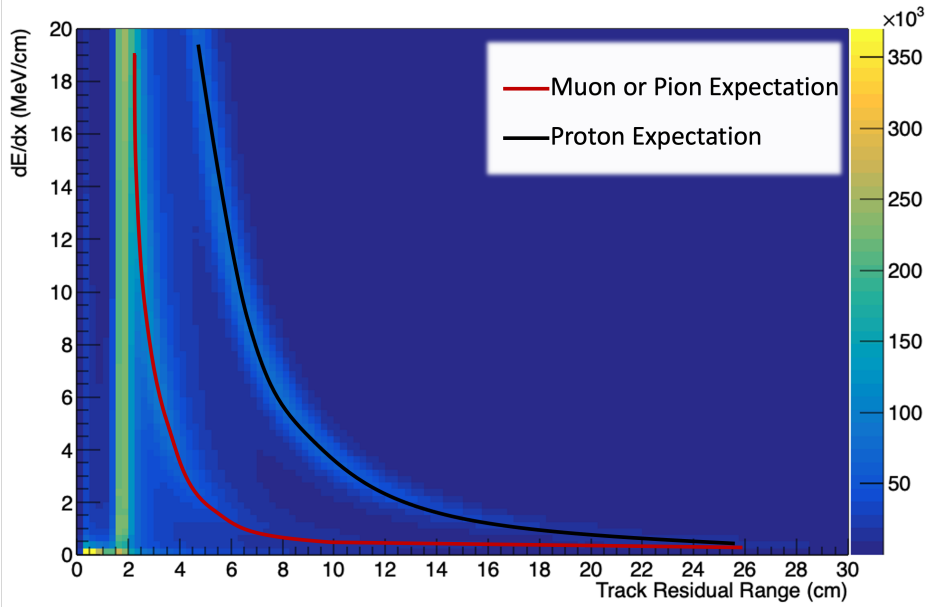

Figure 6.2: Particle Identification via Analysis of dE/dx against Residual Range from SBND simulation.

After completing the dE/dx calculation, the energy reconstruction of track-like particles becomes straightforward by summing up the product of dE/dx and the track pitch at each track point. Alternatively, energy estimation can be achieved through Multiple Coulomb Scattering (MCS) analysis, which is particularly useful for particles leaving the detector, as the range-based and calorimetric approaches are less effective [256]. Similar to the range-based approach, MCS fitting is conducted considering various particle type hypotheses, enabling analysts to select the suitable hypothesis post-PID.

Figure 6.3 shows the reconstructed kinetic energy (KE) spectrum for track-like particles: muons, protons and pions. In Figure 6.3, the reconstructed kinetic energy errors ratio can be seen as a function of reconstructed KE. The observed ratio errors indicate a notable concordance between the reconstructed KE and the true KE of muon tracks exceeding 100 MeV. This alignment similarly holds for proton and pion tracks at the peaks of their respective spectra.

Alongside the assessment of particle kinematics, these alternative energy calculation approaches can serve to verify the consistency of PID, as discussed in Chapter 7. Additionally, the total energy of neutrino events is reconstructed by summing the energies of all particles

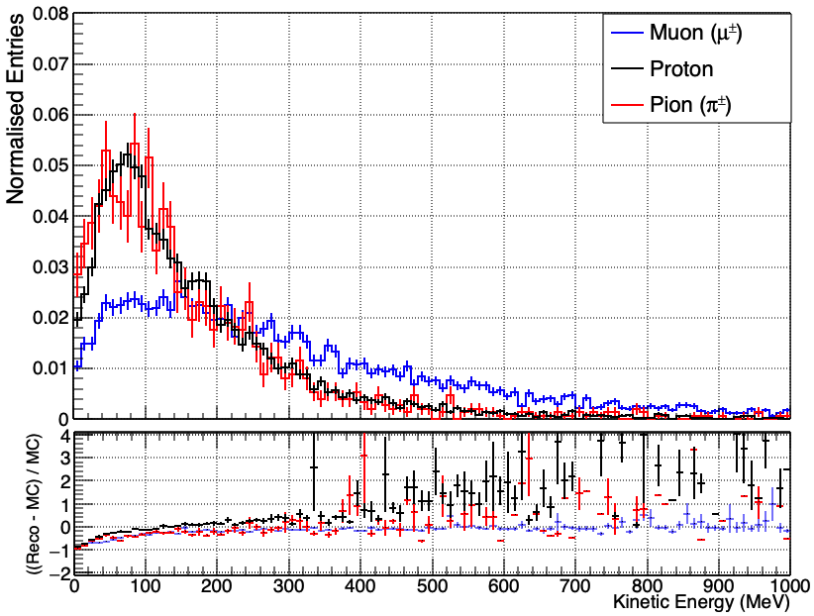

Figure 6.3: Spectrum of reconstructed kinetic energy for track-like particles. The upper plot illustrates the reconstructed kinetic energy as a function of normalised entries, while the lower plot presents the deviation in the reconstruction to the true.

involved in the interaction. In cases of uncomplicated topologies like charge current quasi-elastic scattering, neutrino energy can be reconstructed utilising kinematic principles [138].

In SBND, the Pandora Track Creation module is pivotal for generating accurate 3D tracks, ensuring excellent alignment with true track properties (over 98% for direction and within 3 cm for start positions). Energy estimation via dE/dx and Multiple Coulomb Scattering methods closely matches true particle energies, particularly for muons, protons, and pions exceeding 100 MeV, facilitating precise neutrino event energy reconstruction.

6.2 High-Level Shower Reconstruction

Apart from track reconstruction, shower-like particles undergo a characterisation process subsequent to the pattern recognition's classification into track-like and shower-like particles. However, due to the inherently stochastic nature of electromagnetic shower development, extracting meaningful metrics to describe the shower presents a significant challenge. Despite this challenge, accurately quantifying these characteristics is essential for identifying and measuring showers. In this reconstruction stage, six crucial shower properties are determined: the position and direction of the initial showering particles, dE/dx of the initial track stub of the shower, shower energy, shower length, and shower opening angle.

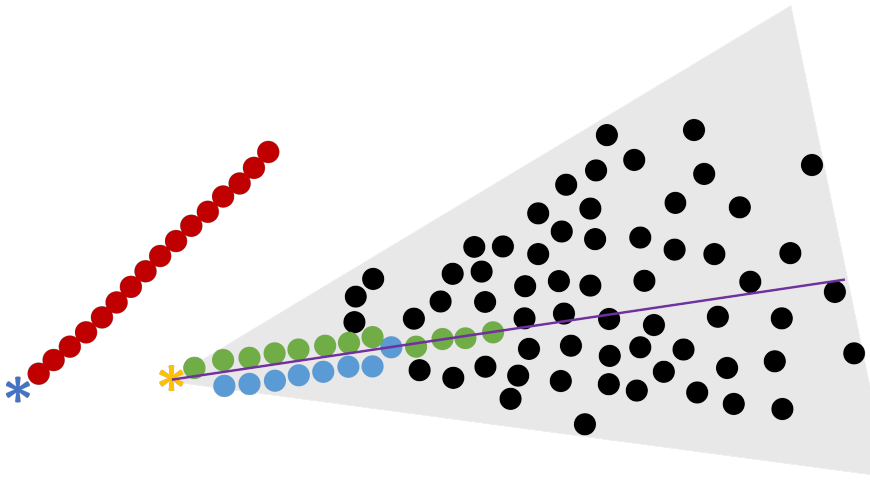

Figure 6.4: Illustration of fundamental reconstructed photon shower characteristics.

Figure 6.4 illustrates the fundamental characteristics of a reconstructed photon shower. The shower start position, depicted by the yellow star, is defined as the initial energy deposition by the showering particle, which is crucial for reconstructing the hierarchy of neutrino events. Measuring the gap between the shower start (illustrated by the yellow star) and the parent interaction vertex (represented by the blue star) is also an imperative indicator for photon showers, commonly referred to as "conversion gaps". The direction of the showering particle (depicted by the purple line) serves as the basis for reconstructing event topologies, such as π^0 invariant mass calculation and differential cross section analyses. The green and blue points illustrate the initial track hits before the start of the showering phenomenon, and these are utilised in the shower dE/dx estimation. The length and opening angle of the shower characterise the dimensions of a conical shape, represented by the shaded grey region in the diagram, which encloses the shower. In the diagram, the red points represent the track-like particle resulting from the parent interaction.

For extracting these parameters within SBND, the Pandora shower creation framework is employed [257]. This framework disassembles the calculation of each characteristic into separate, exchangeable stages processed by art tools [239]. This approach of separating the algorithms allows for quick evaluation and tool advancement, as they can be easily interchanged through configuration file adjustments.

Multiple stages of shower characterisation are inherently interconnected. For instance, the start position contributes to finding the initial track hits, which then contribute to dE/dx calculations. Facilitating information exchange among tools is therefore crucial, accomplished through the ShowerElementHolder within the framework. This holder includes necessary shower characteristics and also allows tools to both access and provide additional

information for subsequent stages. Such an approach enables the examination of interplay between characteristics. For instance, altering only the tool responsible for start position reconstruction and assessing its impact on dE/dx computation.

To evaluate shower reconstruction performance, two vertex samples were generated. These samples encompassed either an electron shower with a charged pion track or photons with a muon track emerging from a common vertex, as illustrated in Figure 6.4. The inclusion of the pion and muon aimed to establish a more neutrino-like pattern for pattern recognition, resulting in improved performance, especially in vertexing, in comparison to single-particle samples. The energy distribution of both the electrons and photons were simulated according to the anticipated distribution. This alignment permitted the comparison of reconstruction metrics unaffected by variations in underlying kinematic distributions. The evaluation and enhancement of the performance of shower characteristic reconstruction using these samples are discussed in the following subsections.

6.2.1 Shower Start Position and Direction

The start position is crucial not only in calculating conversion gaps for photons but also forms the foundational basis for finding the initial track hits and subsequently calculating the dE/dx of showers. The standard method for finding the starting position of showers within PandoraModularShower in SBND is to use the ShowerPFPVertexStartPosition tool, which demonstrates the best performance among the available tools [258]. The PFP start position approach essentially involves selecting the vertex that Pandora assigns to the PFP during the pattern recognition process. This vertex is identified by determining the space point that is closest to the parent particle. Notably, primary showers without a parent particle employ the space point that is nearest to the neutrino vertex, as explained in the Section 5.2.1.

The performance of shower start position reconstruction is shown in Figure 6.5, illustrating the distance between the true and reconstructed shower start positions. From this work it is found that approximately 65% of photon showers and 31% of electron showers exhibit a reconstructed start position within 1 cm of the true start position. Moreover, 77% of photon showers and 52% of electron showers have their start positions reconstructed within 2 cm of the true start position. The better accuracy in reconstructing the start position for photons compared to electrons is anticipated due to the photons travelling a certain distance from the neutrino interaction vertex prior to showering. Consequently, there is less hadronic activity surrounding the shower start, simplifying the assignment of hits to the correct cluster.

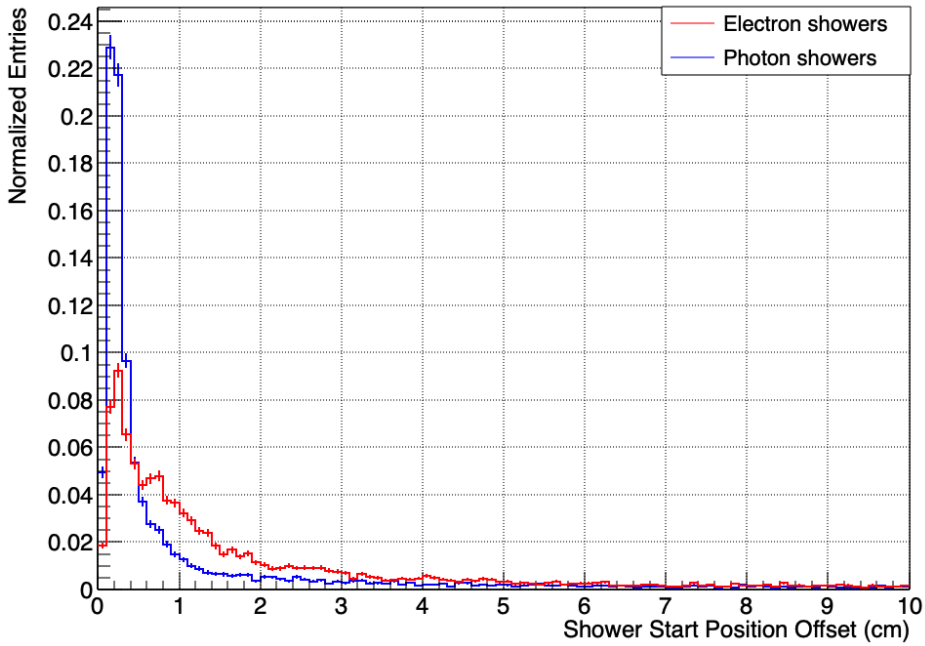

Figure 6.5: Reconstructed shower start position offset from the true position for photon and electron.

Accurately determining the direction of showers is essential for the precise reconstruction of neutrino interaction topologies, including studies such as measuring differential cross sections based on leptonic angles and reconstructing π^0 mass peaks. In the SBND PandoraModularShower framework, the standard approach employed to calculate the shower direction is through the ShowerPCADirection tool, which calculates the direction based on the entire shower [259].

This approach relies on momentum conservation during shower development, assuming a uniform energy distribution along the central axis corresponding to the true direction. This strategy mitigates the effects of misclustering and statistical fluctuations during the initial phase of the shower. However, its effectiveness can be compromised by absent energy or impurities in shower hits, potentially leading to skewed shower directions in cases of incomplete or uncontained showers. Moreover, this method does not address pre-shower development particle scattering or uncontained energy depositions. When computing the shower direction using all hits, a Principal Component Analysis (PCA) is employed; for details, see [260]. In PCA, the shower's axis corresponds to the primary PCA axis, aligning with the axis of maximum point spread. Nonetheless, the PCA is unable to determine whether the shower progresses forward or backward along this axis. Therefore, the shower direction is defined along the primary axis, pointing from the start to the shower centre.

Figure 6.6 presents the difference between the true and reconstructed shower directions for photons and electrons. The shower direction deviation for photons shows a wider distribution, with around 60% deviating more than 10° from the true direction, and approximately 51% for electrons. Both photons and electrons exhibit comparable deviations in shower direction, although photons are more affected due to the reasons mentioned earlier, compounded by their more complicated showering topologies.

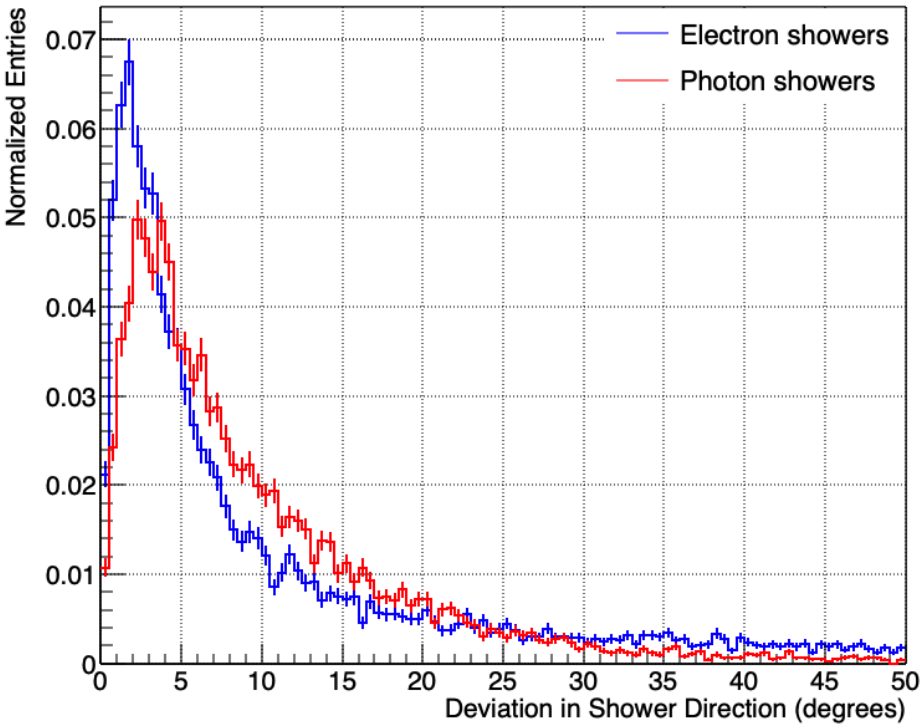

Figure 6.6: Deviation in shower direction for electron and photons.

6.2.2 Shower Initial Track and dE/dx Reconstruction

The hits prior to the shower main particle starts showering hold information regarding the characteristics of the original particle, which becomes obscured once the shower starts propagating, see Figure 6.4. These initial track hits play a critical role in distinguishing between showers induced by electrons and photons through dE/dx analysis. In SBND, the commonly employed approach for the reconstruction of initial track hits is the ShowerIncrementalTrackHitFinder tool [261]. Additionally, a simpler reconstruction tool known as the Shower3DCylinderTrackHitFinder is available [262]. Both of these tools have previously been found to have the best performance compared to other alternatives.

The former algorithm starts by selecting a set of N seed hits in proximity to the vertex, followed by a PCA and calculation of residual distances between hits and the primary axis.

If the mean residual exceeds a specific threshold, the hit with the highest residual is excluded. This process continues until the average residual falls below the threshold. Subsequently, hits located farther from the vertex are assessed to determine whether their inclusion would result in an increase or decrease in the average residual; only hits that result in a decrease are added. This sequence continues until three consecutive hits are rejected. This procedure aids in eliminating erroneous hits from the initial track, thereby preventing the extension of the track into the main bulk of the shower.

The second method, the simplest approach, for determining the initial track hits involves creating a cylinder around the shower starting point, utilising the previously determined start position and direction. This approach heavily depends on the accuracy of clustering around the shower start to ensure correct hit assignment, given that all hits within the cylinder are taken into account.

Defining the truth for initial track hits is somewhat ambiguous due to the difficulty in reliably determining the point at which the shower can be classified as fully developed. Consequently, the evaluation of initial track hit finding performance relies on the dE/dx metric.

Studying the dE/dx of the initial track at the start of the shower offers a robust means of distinguishing between electrons and photons that undergo pair production. For an electron, the dE/dx aligns with that of a single MIP, whereas a photon undergoing pair production resulting in an e^+ e^- pair corresponds to two MIPs, as detailed in Chapter 3. Following the identification of initial track hits through the previously discussed methods, the calculation of dE/dx becomes feasible.

This computation process closely resembles the approach outlined in Section 6.1 for determining the dE/dx of tracks. It entails firstly calculating the effective pitch (dx), followed by the conversion of charge (dQ/dx) into energy (dE/dx). While each tool employs this fundamental method, there are subtleties concerning the specifics of this calculation. In SBND, the ShowerTrajPointdEdx tool is utilised, leveraging the sliding fit conducted on the initial track hits to establish a direction for each hit [263]. Other tools can be used, such as the ShowerUnidirectiondEdx tool, which calculates the effective pitch using the overall shower direction, as defined by the algorithms in Section 6.2.1. The former approach allows for more accurate pitch calculations, thereby enhancing the precision of dE/dx estimation and is, therefore, employed for the subsequent studies.

Figure 6.7 shows the dE/dx distribution for the two employed methods in reconstructing initial track hits for both photon and electron showers. The Figure shows the anticipated singular peak for electrons corresponds to a single Minimum Ionising Particle (MIP) peak at 1.8 MeV/cm, as well as both the single (1.8 MeV/cm) and double MIP (4.5 MeV/cm)

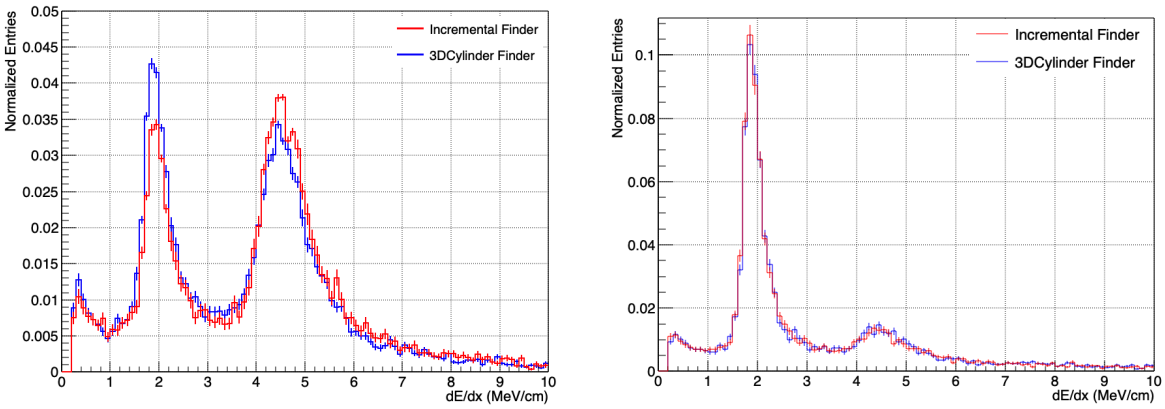

(a) Photon Showers

(b) Electron Showers

Figure 6.7: Comparing dE/dx for various track hit finding approaches for photon showers on the left and electron showers on the right.

peaks for photons [264]. The Incremental tool provides a more distinct profile to the dE/dx in comparison to the 3DCylinder hit finder for photons, with 64% having a dE/dx above 3 MeV/cm compared to 58% for 3DCylinder. In the case of electron showers, both tools exhibit comparable performance, although the Incremental hit finder demonstrates slightly superior performance, outperforming the other tool by approximately 1%. Overall, the incremental tool has the highest separation capability for both samples, resulting in the selection of 65% of photon showers and a rejection of 68% of electron showers when applying a cut at 3 MeV. This enhanced separation capability will directly influence selection efficiency and background rejection, as discussed in Chapter 7. Notably, the difference between the two methods is relatively minor for the electron sample, in contrast to the photon samples, which is the central focus of this thesis.

The dE/dx distribution shown in Figure 6.7 originates from the shower best-plane, defined as the plane with the highest hit count. This parameter is one of the shower reconstruction metrics and provides the most accurate estimation of dE/dx values compared to the other planes.This is illustrated in Figure 6.8 which shows a comparison of dEdx distribution between different planes. Therefore, the incremental track hit finder tool and the shower best plane are used for the calculation of dE/dx in the subsequent studies.

In order to enhance the performance of the initial track hits finder and achieve an improved estimation of dE/dx, thereby enhancing the separation between electron and photon showers, a study was undertaken to assess potential areas for improvement and identify any existing failure modes. The first step involved providing truth-based initial track hits to the ShowerTrajPointdEdx tool to calculate the dE/dx using the cheating tool.

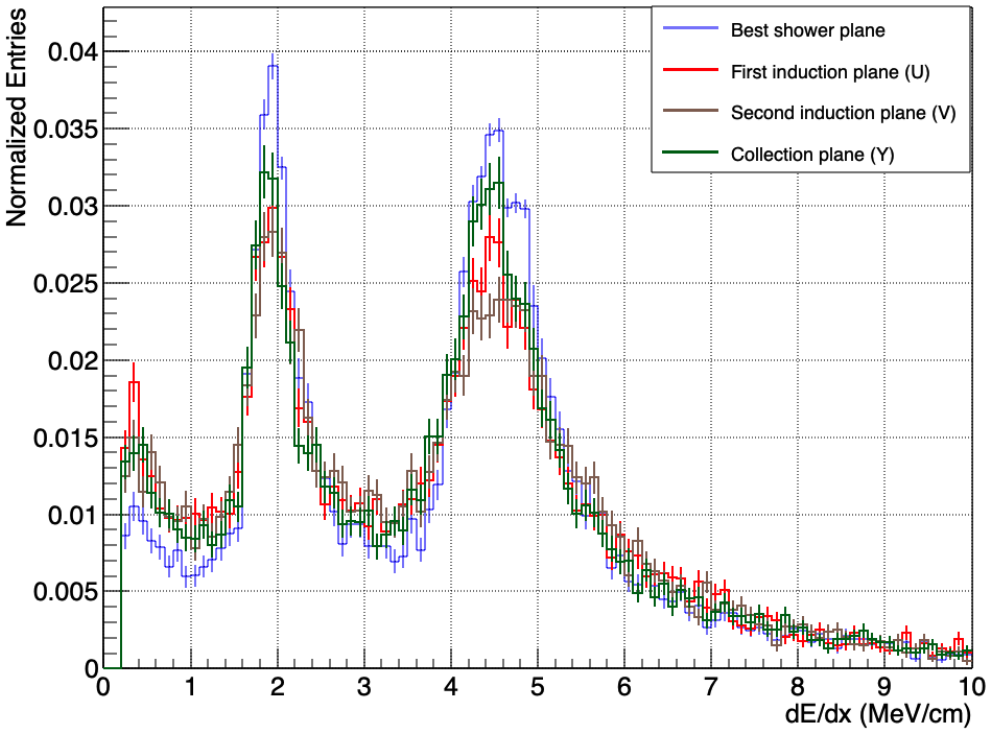

Figure 6.8: Comparison between the dE/dx distribution for different planes where the initial track hit is reconstructed using the 3DCylinder hit finder tool.

Figure 6.9 shows a comparison between the cheated and incremental initial track hit finders as a function of the dE/dx distribution. For electron showers, a discrepancy of approximately 5% is observed between the two tools at the single MIP peak, indicating a potential improvement of around 5% through the accurate reconstruction of the initial track

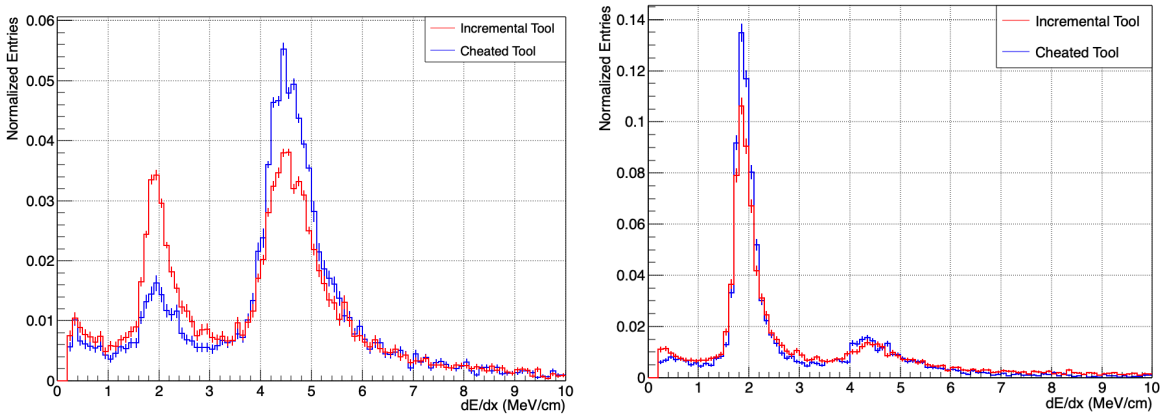

(a) Photon Showers

(b) Electron Showers

Figure 6.9: Comparing dE/dx for incremental and cheated track hit finding approaches for photon showers on the left and electron showers on the right.

hits. On the other hand, a possible enhancement of approximately 20% can be achieved, given the noticeable shift from the single MIP peak to the double MIP peak.

Following the evaluation of potential enhancements, the subsequent step involves an assessment of the failure modes in the reconstruction of initial track hits. This is accomplished through an event display model to examine instances where the track hit reconstruction tools exhibit deficiencies. Figure 6.10 shows two event displays for photon showers with well-reconstructed initial track hits on the left and poorly-reconstructed initial track hits on the right. The x-axis represents the wire ID, while the y-axis corresponds to time in tick units.

In Figure 6.10, the presence of inadequately reconstructed initial track hits can be attributed to instances where the algorithm selects a limited number of hits. In contrast, in the well-reconstructed event shown on the left, the incremental tool halts at the appropriate point. After analysing numerous event displays for both electron and photon samples, a range of recurrent failure modes was identified. Common failures associated with the initial track hit finder tools include the tool's inability to stop at the intended end of the initial track, and/or the tool assigns only a limited number of hits to the initial track. Additional frequent failure modes encompass inaccurate reconstruction of the shower start position and/or merging of shower hits with hits from other particles.

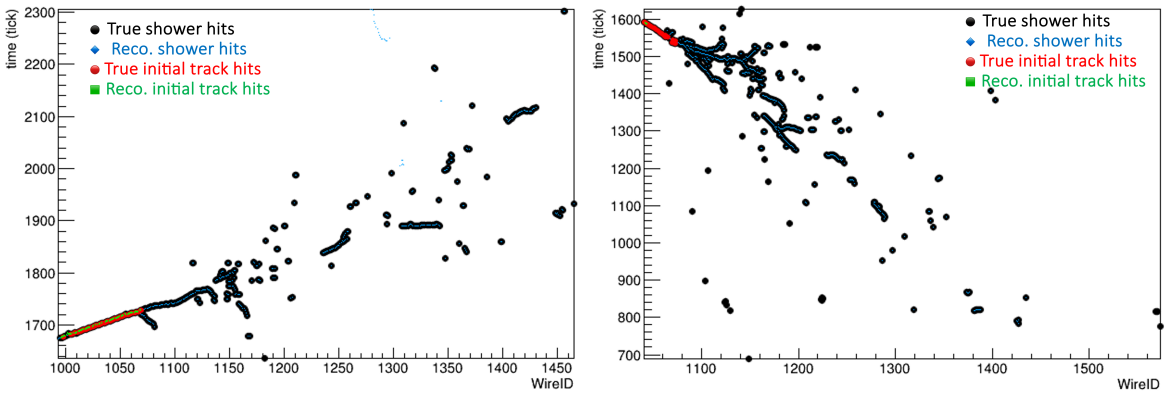

(a) (b)

Figure 6.10: Event display of events for photon showers with well (on the left) and poorly (on the right) reconstructed initial track hits.

In order to mitigate the failure modes associated with initial track reconstruction, adjustments were made to fine-tune the incremental and 3DCylinder tools to achieve improved performance. The tuning of both tools was conducted through Bayesian Optimisation methods, details in Section 5.1.3, utilising the Separation parameters from the TMVA toolkit to evaluate the dE/dx-based separation between electron and photon showers [250, 265]. The separation $\langle S^2 \rangle$ parameter is defined as:

$$\langle S^2 \rangle = \frac{1}{2} \int \frac{(\hat{y}_S(y) - \hat{y}_B(y))^2}{\hat{y}_S(y) + \hat{y}_B(y)} dy \tag{6.1}$$

where $\hat{y}_S$ and $\hat{y}_B$ represent the Probability Density Functions (PDFs) of the variable y for the signal and background, respectively. The separation is at a minimum when the signal and background shapes are identical and reaches a maximum value of one when there is no overlap between the shapes.

Figure 6.11 presents a comparative analysis of the incremental tool's performance before and after tuning for both photon (left) and electron (right) showers, with respect to the distribution of dE/dx. The tuned version of the incremental tool exhibits improved performance compared to the untuned version, resulting in an enhancement of photon-electron separation by approximately 6% with a cut placed at 3 MeV. For photon showers, there is an improvement of around 5% for showers with dE/dx values above 3 MeV, while for electron showers, there is a 1% increase in the calculation of dE/dx below 3 MeV.

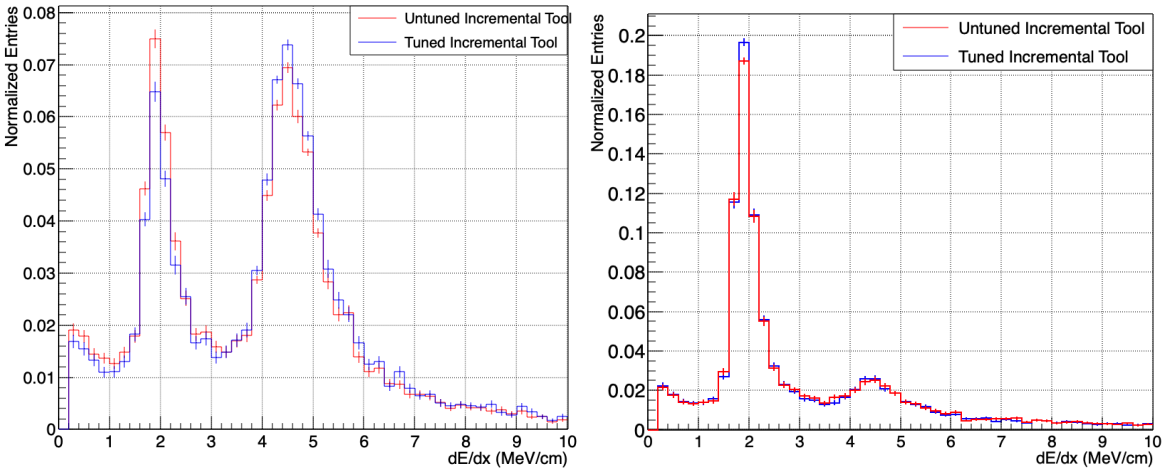

(a) Photon Showers (b) Electron Showers

Figure 6.11: The dE/dx distribution for tuned incremental tools for photon showers on the left and electron showers on the right.

Another failure mode was identified while analysing the event displays, related to the selection of the shower best plane based on the count of shower hits. In Figure 6.12, the left-side display shows the reconstructed best plane, revealing a concentration of hits on a limited number of wires but with varying timestamps, resulting in potential inaccuracies in the initial track hit reconstruction. Conversely, the event display on the right presents the same photon shower on a different plane, demonstrating it as a promising candidate for the best plane selection. Therefore, the definition for the shower best plane was changed to be

the plane where shower hits are distributed across a wider range of wire-IDs rather than the plane with the highest hit count.

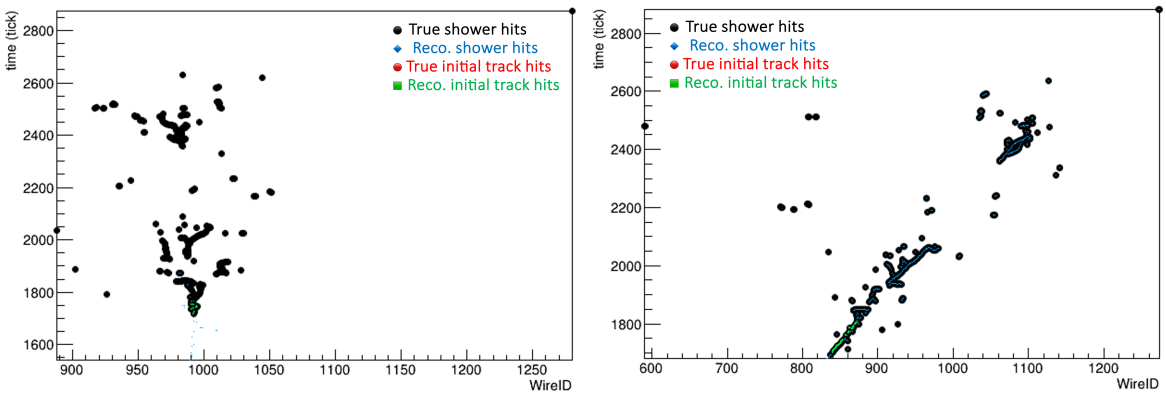

(a) (b)

Figure 6.12: Event display showing failure mode of photon shower best plane. The reconstructed best plane is displayed on the left, while the expected best plane on the right.

Figure 6.13 shows the performance comparison of the tuned incremental tool before and after redefining the shower best plane for photon (left) and electron (right) showers in terms of the dE/dx distribution. The tuned incremental tool with the new definition demonstrates enhanced performance, leading to about a 4% increase in photon-electron separation with a 3 MeV cut. Photon showers demonstrate around a 4% improvement in dE/dx values above 3 MeV, while electron showers show no change. However, a slight enhancement is observed in estimating dE/dx for showers below 1 MeV in both photon and electron samples.

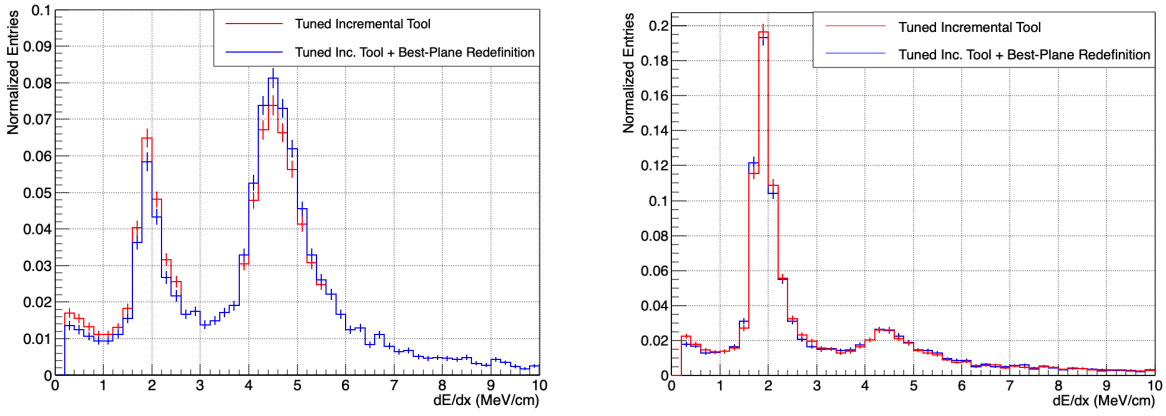

(a) Shower Photon (b) Shower Electron

Figure 6.13: Comparing dE/dx for tuned incremental tool with old and new best plane definitions for photon and electron showers.

Overall, the photon-electron shower discrimination using dE/dx, with a 3 MeV cut, has been improved by approximately 10%. Alternative tools, such as the hybrid track hit finder combining Incremental and 3DCylinder methods, were explored, but due to limited performance or testing, they were excluded. Instead, the tuned incremental tool with the redefined best plane was chosen.

6.2.3 Shower Energy

Unlike energy reconstruction for track-like particles, the complex nature of showers makes calculating the pitch for every hit impractical. As a result, summing dE/dx, as discussed in section 6.1, is not viable. Instead, a direct conversion of charge to energy is employed, assuming a linear correlation.

First, the collected charge is converted into the count of electrons captured on the wires, utilising the discussed calorimetry constants. Then, the electrons number on the wire is correlated with the electrons deposited, accounting for factors such as electron lifetime and recombination using a constant factor of 0.64, established from Monte Carlo (MC) analyses. Eventually, by multiplying this number of electrons by the energy required to ionise an argon atom (W_{ion} = 23.6 eV), the deposited energy is yielded [200].

Figure 6.14 shows photon showers reconstructed energy versus true shower energy, as well as the reconstruction errors ratio shown at the bottom. Additionally, the representation of the expected fit is shown by the red line, while the black line represents a constrained linear fit passing through the origin. As evident from the histogram, a minor discrepancy between the data fit and the expected fit is noticeable, primarily attributed to high-energy showers. Various factors, including potential clustering of the shower into multiple components and the occurrence of uncontained showers, could contribute to this variation by leading to the loss of hits and subsequent inaccuracies in reconstructed energy. However, in the lower energy range below 300 MeV, where photon showers are more concentrated, the distinction between true and reconstructed shower energy is found to be minimal. Overall, for energies above 100 MeV, the reconstructed shower energy closely approximates the true shower energy, as evidenced by the reconstruction error ratio converging towards zero.

6.2.4 Shower Length and Opening Angle

The last parameters derived through the process of shower reconstruction are the shower length and opening angle, as shown in the diagram in Figure 6.4. These parameters play a crucial role in describing the topological configuration of the shower and offer a means of distinguishing genuine showers from incorrectly identified tracks, as discussed in Chapter 7.

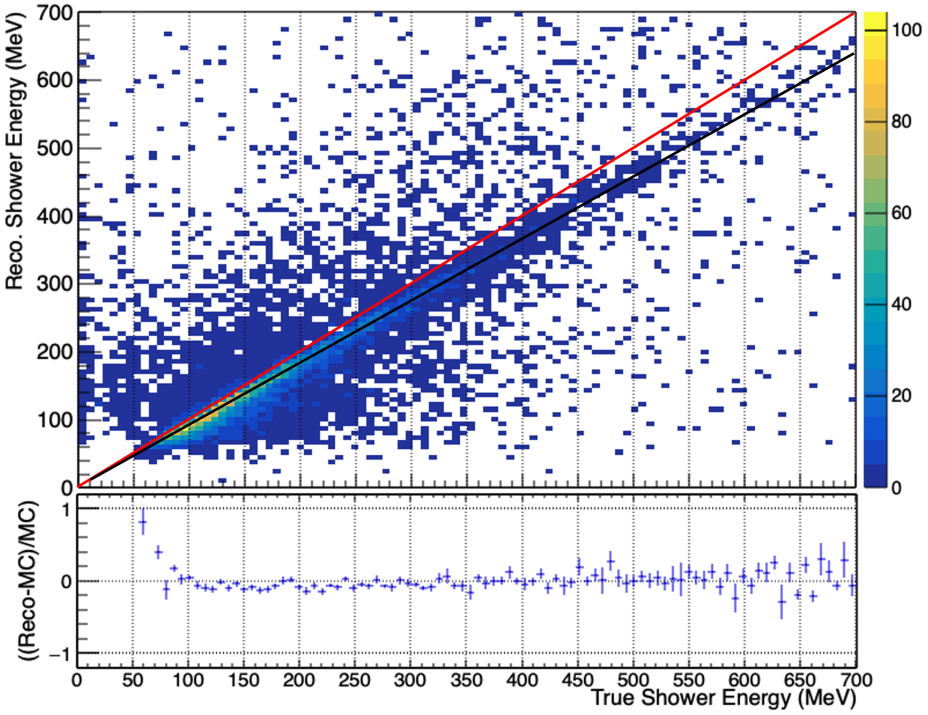

Figure 6.14: Photon shower reconstructed energy versus true shower energy, with reconstruction errors ratio shown at the bottom. In the 2D histogram, representation of expectation fit is given by red line and the constrained linear fit passing through the origin by the black line. The reconstruction of energies below 100 MeV indicates instances of mis-reconstruction of the shower.

These two variables, the length and opening angle, are interconnected, with the opening angle of a shower defined as:

$$\theta_{\text{Open}} = \tan^{-1}\left(\frac{\text{Shower Width}}{\text{Shower Length}}\right) \tag{6.2}$$

The shower's width and length are determined using the same approaches, utilising the dispersion of points along both the longitudinal and transverse axes from the shower centre. Yet, defining the length and width of a shower encounters ambiguity due to the absence of a definitive endpoint. Calculating the length can involve using the farthest point from the shower as its endpoint or establishing a characteristic length that encompasses the main portion of the shower.

In SBND, these parameters are computed through various approaches, but the chosen method involves using percentiles derived from the distribution of the spread, as executed through the ShowerLengthPercentile tool [266]. This method establishes the length and width within a specific percentile (typically the 90th) of all hits situated relative to the shower

centre. This approach is designed to mitigate the influence of anomalous energy depositions distant from the shower's centre, which could potentially distort calculations relying on average distances.

Given the inherent uncertainties mentioned earlier, the absence of a definitive definition for true shower length or opening angle prevents a direct comparison with reconstructed quantities, as done in previous sections. Nonetheless, Figure 6.15 shows the length and opening angle distributions for both photon and electron showers. In general, both types of showers display similar distribution shapes, with electrons exhibiting a peak at shorter lengths due to factors such as misclustering and containment.

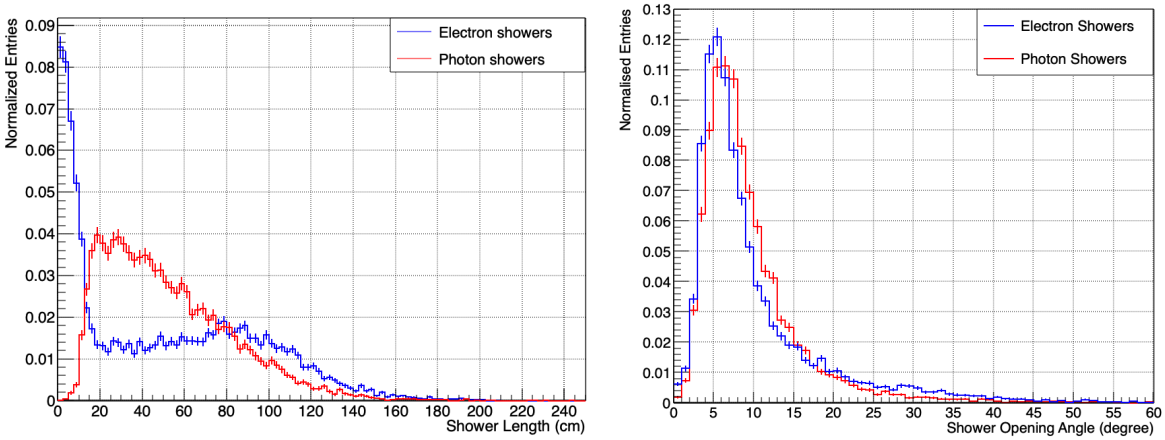

(a) Shower Length

(b) Shower Opening Angle

Figure 6.15: Comparing reconstructed shower length (left) and opening angle (right) for photon and electron showers.

In the shower reconstruction process for particles, several crucial characteristics are determined, including the position and direction of the initial showering particles, dE/dx, shower energy, shower length, and opening angle. These parameters play vital roles in identifying and measuring showers, such as photons and electrons. Various tools and methods are employed to achieve accurate reconstructions, with a focus on improving the separation between electron and photon showers based on their dE/dx values. Notably, improvements in dE/dx separation between photons and electrons have been achieved through tuning tools and redefining the shower best plane, leading to a 10% enhancement in discrimination. Furthermore, the reconstruction of shower energy closely approximates true values, particularly for energies above 100 MeV. Lastly, shower length and opening angle are calculated using percentiles to describe shower topology, aiding in distinguishing genuine showers from misidentified tracks.

6.3 π^o Reconstruction Performance

The accurate reconstruction of π^0 parameters is crucial for studying cross-section measurements related to π^0 production, which heavily relies on accurately reconstructing the leading and sub-leading photons originating from the decay of π^0. Therefore, understanding the performance of shower reconstruction by considering both photon showers within each event instead of treating them separately, as was done in the previous section, is essential for both the selection and reconstruction of π^0 properties. To achieve this objective, a sample comprising 10,000 events of filtered ν_μ CC π^0 production was generated.

Reconstructing both the leading and sub-leading photon showers from π^0 faces significant challenges, primarily attributed to misclustering, potentially resulting in their misidentification as track-like signatures. Accomplishing this task presents challenges, as showers with energies relevant to π^0 frequently exhibit characteristics resembling scattered track-like segments, as seen in Figure 5.13. Additionally, distinguishing energy depositions originating from photon showers versus those resulting from track-like particles, notably protons, presents considerable issues, as discussed in Section 5.2.2.

Figure 6.16 shows characterisation of π^0 photon showers based on the number of showers per event. In scenarios where only one shower is reconstructed, either the leading or sub-leading photon shower is successfully reconstructed and appropriately clustered as a shower,

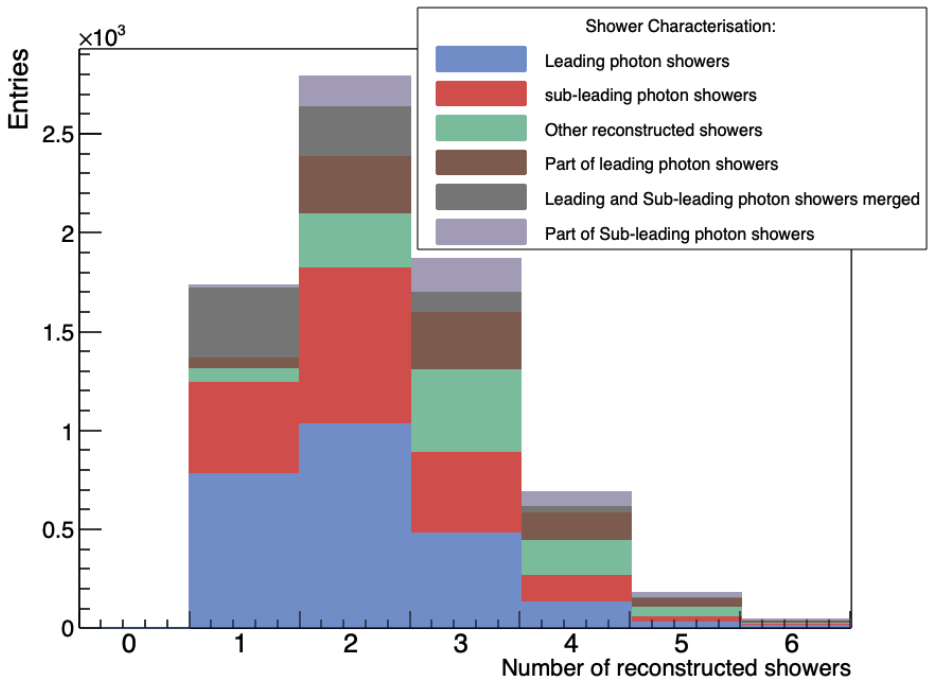

Figure 6.16: Characterisation of π^0 photon showers based on the number of showers per event.

while the other may be inaccurately misclustered as a track-like particle. Additionally, a considerable percentage of leading and sub-leading showers exhibit merging. In cases of events with multiple showers, especially three or more showers, a notable proportion of these showers correspond to track-like particles.

Figure 6.17 shows the characterisation as a function of the reconstructed shower opening angle. The upper plot displays reconstructed showers categorised by true interaction types, while the lower plot illustrates completeness, purity, and the percentage of merged leading and sub-leading photon showers. As can be seen, the probability of both leading and sub-leading photon showers being merged is high for showers with an opening angle higher than 10 degrees. Importantly, the purity and completeness of shower reconstruction exceed 80%, where purity is defined as the ratio of true hits within reconstructed showers to the total number of reconstructed shower hits, and completeness is the ratio of true hits within reconstructed showers to the true hits of the showering particle.

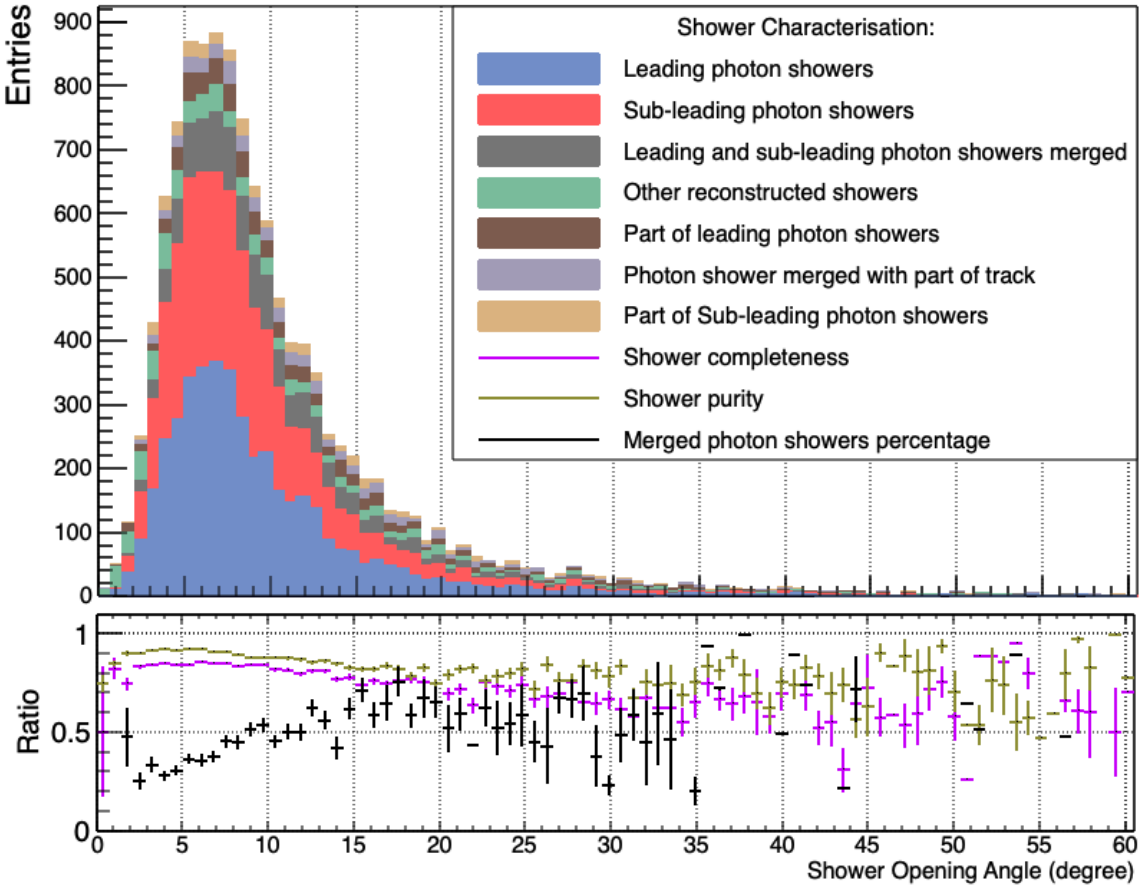

Figure 6.17: Characterisation of π^0 photon showers as a function of shower opening angle.

A summary of shower characterisation based on the percentage of showers reconstructed from π^0 decay events is shown in Figure 6.18. In π^0 decay events, photon showers originating from π^0 are clustered as showers 78% of the time, while they are misclustered as track-like. Among these misclustered showers, 41% correspond to the leading photon showers and 36% to the sub-leading photon showers. Additionally, a fraction of 23% of reconstructed showers involves cases where the leading and sub-leading showers are clustered together as a single shower. The merging of showers is primarily attributed to two factors: the small angle between the two photon showers and the misreconstruction of the shower starting position. Overall, the inclusion of these misclustered showers is taken into account during the selection of π^0 events. This is discussed further in Chapter 7.

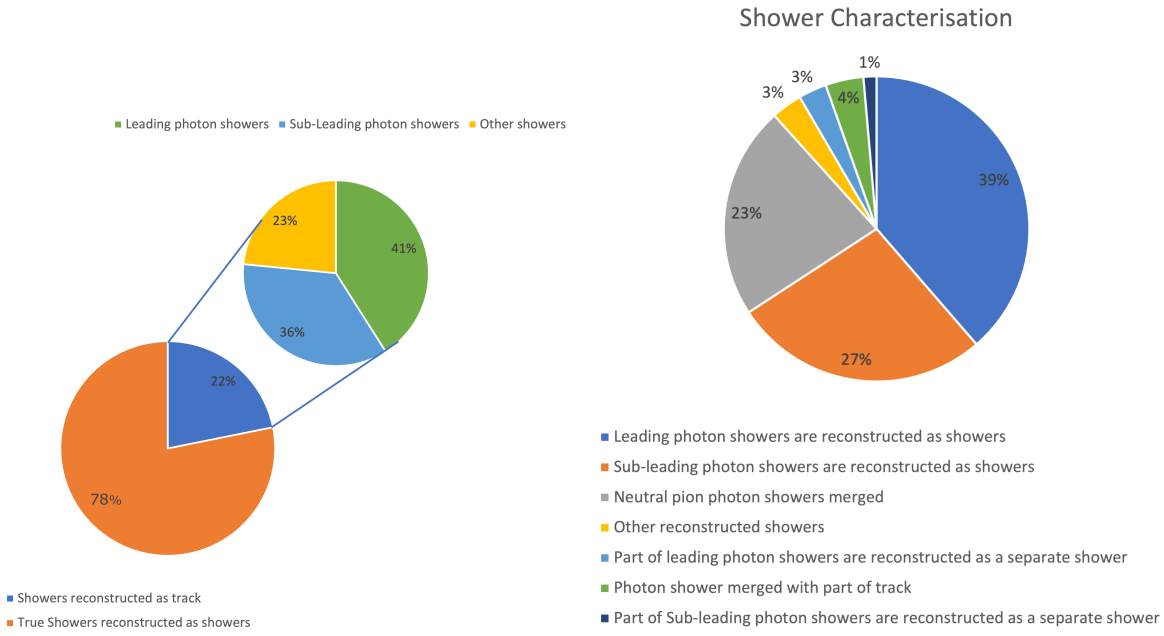

Figure 6.18: Characterisation of reconstructed π^0 photon showers in events

The estimation of π^0 energy reconstruction is influenced by factors such as the number of reconstructed showers and the misclustering of track-like and shower-like particles, both of which need to be taken into consideration. Figure 6.19 shows the relationship between reconstructed and true energies for π^0 events, with the reconstructed π^0 energy calculated by summing the energies of the reconstructed photon showers. For single reconstructed showers, the corresponding shower is utilised for reconstructing the π^0 energy, while in cases with more than two reconstructed showers, only the showers with the highest energies are employed. However, this approach might introduce bias in the π^0 momentum distribution. The red line represents the expected fit depicting the relationship between the reconstructed

and true π^0 energies. Overall, the reconstructed energy demonstrates comparability to the true energy, exhibiting a minor deviation in relation to the expected fit. The notable discrepancy in low reconstructed energy primarily attributed to scenarios where only one shower is reconstructed, with approximately 68% of such cases experiencing a misclassification of the second photon shower as track-like. Moreover, the relationship between the reconstructed π^0 energy and its corresponding true energy is depicted as a ratio in the lower panel of Figure 6.19.

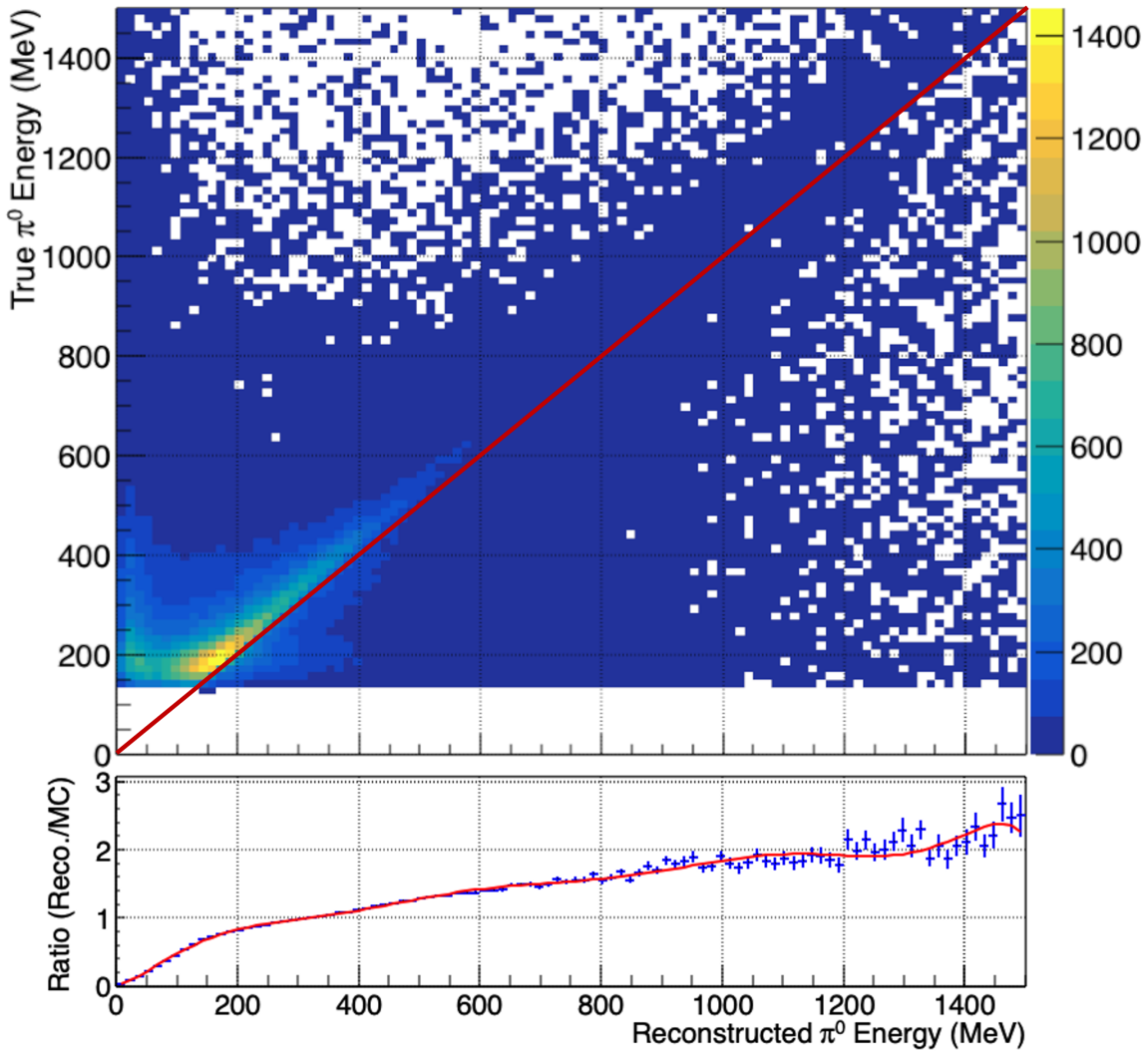

Figure 6.19: Reconstructed versus true energy for π^0. The estimated energy of the reconstructed π^0 is calculated by summing the energies of the reconstructed photon showers.

The disparity between the true and reconstructed π^0 energy can be mitigated through the application of a correction factor to account for the energy loss. Figure 6.20 shows the discrepancy between true and reconstructed π^0 energy both before and after the application of

a correction factor derived from the fitting presented in the Figure 6.19, the corrected energy is obtained by dividing the reconstructed energy by 0.87. The distribution of differences in true and reconstructed π^0 energies indicates a shift towards zero in the peak.

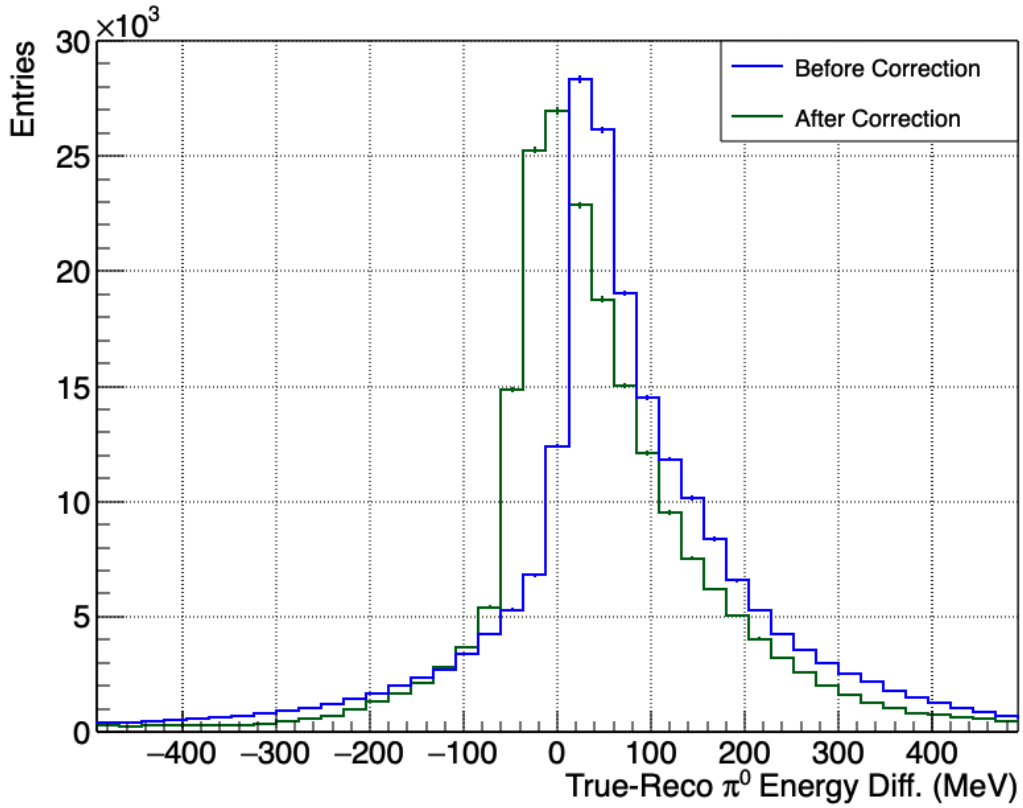

Figure 6.20: Reconstructed versus true energy for π^0. The estimated energy of the reconstructed π^0 is calculated by summing the energies of the reconstructed photon showers.

The estimation of the diphoton invariant mass encompasses the reconstruction of two or more showers, considering primarily those showers exhibiting the highest energies, as anticipated with respect to the π^0 mass. The resulting distribution of invariant mass is depicted in Figure 6.21, exhibiting a mean value of 123 MeV/c^2. The mass is derived using the decay characteristics of the two γ showers, employing the formula:

$$M_{\gamma\gamma} = \sqrt{2E_1E_2(1-\cos\theta)} \tag{6.3}$$

where E_1 and E_2 represent the energies attributed to the two photons, here used the two showers with the highest energy, while θ signifies the reconstructed angle between them, determined using the reconstructed direction of the showers.

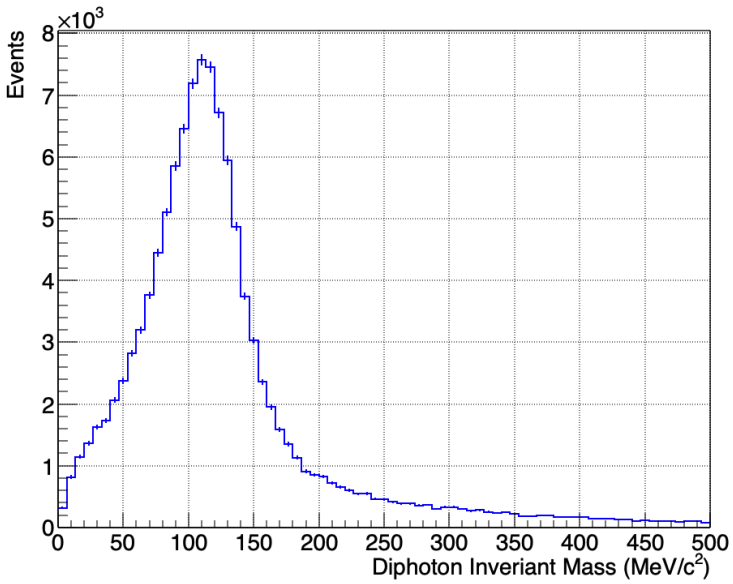

Figure 6.21: The calculated invariant mass of the pair of photons associated to the decay of the π^0 particle.

Reconstructing π^0 parameters is critical for cross-section measurements related to π^0 production. Challenges arise when reconstructing both leading and sub-leading photon showers due to misclustering and distinguishing them from track-like particles. In π^0 decay events, photon showers from π^0 are clustered correctly 78% of the time, but they are misclustered as track-like or merged in other cases. However, the inclusion of these misclustered showers is considered during π^0 event selection, and correction factors are applied to mitigate discrepancies in π^0 energy reconstruction. Additionally, the diphoton invariant mass, calculated from the energies and angles of the two highest-energy photon showers, yields a mean value of 123 MeV/c2 for π^0 mass estimation.

6.4 Summary

Presented here was an overview of the high-level reconstruction of both track-like and shower-like particles within the SBND experiment, starting with track reconstruction. For track reconstruction, the Pandora pattern recognition software plays a crucial role in detecting potential tracks and their associated space-points. The track reconstruction process entails generating 3D tracks from identified patterns, enabling extrapolation for CRT, neutrino interaction kinematics, and extraction of calorimetric information. This is accomplished through PCA and linear regression fits to determine track directions and reconstruct trajectory

points. The efficacy of track module in generating accurate 3D tracks is highlighted through the close alignment between reconstructed and true track properties.

Shower reconstruction is challenging due to stochastic nature of electromagnetic shower development. Six crucial shower properties were determined: initial position and direction, dE/dx of the initial track stub, shower energy, length, and opening angle. Various tools are utilised to characterise showers, and the evaluation of their performance using simulated samples is presented by assessing their effectiveness.

The performance of photon-electron shower discrimination through dE/dx analysis is improved by tuning the tools for initial track hit reconstruction, redefining the shower best plane, and refining the separation parameters. These led to an enhancement in the separation between the electron and photon showers by 10%. Additionally, the reconstructed shower energy is compared to the true energy, showing good agreement except for high-energy showers where complexities like clustering and containment come into play.

Accurate reconstruction of π^0 parameters is vital for cross-section measurements involving π^0 production, but this poses challenges in distinguishing leading and sub-leading photon showers due to misclustering and confusion with track-like particles. While 78% of photon showers from π^0 decay are correctly clustered, misclustering or merging occurs in other cases. These misclustered showers are considered during π^0 event selection and correction factors are applied to improve π^0 energy reconstruction, as will be discussed in next chapter.

Chapter 7

Selecting CC π^0 Production Events

For the Short-Baseline Near Detector (SBND) to perform precise physics measurements, a rigorous selection process is crucial. This selection serves two primary objectives: to reject backgrounds and to ensure the reliability of the chosen signal. This work focuses on identifying ν_μ and $\overline{\nu}_\mu$ Charged Current (CC) π^0 production interactions, building on the advancements in reconstruction detailed in Chapter 5 and Chapter 6, with the objective of studying ν_μ CC π^0 production cross section. This process involves reconstructing a neutral pion candidate for precise measurement of interaction kinematics, alongside the rejection of cosmic and neutrino-induced background events. The selection criteria were primarily optimised to maximise the purity times efficiency of the sample, although there were exceptions where cuts were applied to ensure signal integrity rather than solely focusing on background rejection.

First, the objectives of the selection process are discussed in Section 7.1, establishing the specific signal criteria under consideration for this selection. This section provides an overview of the reconstruction process, examining aspects such as efficiency losses and the potential backgrounds. Section 7.2 presents an outline of pre-selection process, along with an examination of the remaining signal and background components. Following, Section 7.3 focuses on cosmic background mitigation and incorporates the capabilities of the Cosmic Ray Tagger (CRT), Photon Detection System (PDS), and Time Projection Chamber (TPC) subsystems. Section 7.4 delves into the identification of muons based on reconstructed track topology, which is indicative of ν NC backgrounds. The selection of the photon showers that result from the signal interactions is discussed in Section 7.5. Lastly, an application of energy cuts on reconstructed π^0 energy, along with an analysis of the remaining backgrounds resulting from the combined effects of all the cuts are presented in Section 7.6.

In summary, the described selection process effectively mitigate a significant portion of background events while successfully identifying numerous signal ν_μ and $\overline{\nu}_\mu$ CC π^0 production interactions. This selected sample serves as the foundation for the subsequent cross section study detailed in Chapter 8

7.1 Signal Definition

The process of selection begins by identifying the target signal for selection, namely ν_μ and $\overline{\nu}_\mu$ CC π^0 production interactions occurring within the defined Fiducial Volume (FV),as detailed in Section 7.2, of the SBND detector. To be concise, and considering the $\overline{\nu}_\mu$ interactions account for only 5.86% of overall (anti)neutrino events while sharing identical topological final states, the combined ν_μ and $\overline{\nu}_\mu$ will be simply denoted as ν_μ. Every neutrino interaction results in energy deposition within the SBND detector and is excluded from the signal definition, including the interactions that fail the FV cuts, labelled as "Other ν", all of which are classified as background.

Based on this defined signal criterion, there are a total of 481,117 simulated signal interactions, compared to backgrounds of 23,623 simulated ν_e interactions, along with 2.49 and 1.14 million ν_μ simulated CC and NC interactions, respectively. These figures are based on a Protons On Target (POT) exposure of 6.6×10^{20}, representing three years of data collection within the SBND experiment. Additionally, there are 9.63 million simulated dirt interactions— neutrinos interacting outside the defined FV— to be taken into account as part of the background, with a notable fraction of these interactions potentially not resulting in any energy deposition within the detector.

The selection depends on the "events" as defined by the detector triggers, as detailed in Chapter 4, and the "slices" produced by Pandora algorithms, as explained in Section 5.2.1, with each aiming to encompass energy depositions within the TPC attributed to a single neutrino interaction or primary cosmic ray source. Some cuts discard entire events due to a lack of association with a single slice, like cutting CRT data not linked to a specific slice. The remaining slices are subjected to a sequence of criteria, either based on reconstructed data within the slice or by correlating the slice with activity in detector subsystems like the PDS.

Based on this it is found that there are a total of 473,464 reconstructed slices associated with the $\nu_\mu CC\pi^0$ production signal interactions, indicating an efficiency decrease of around 1%. Likewise, ν_e and ν_μ CC interactions experience corresponding reductions of 4.2% and 16.8% to 22,627 and 2.07 million, respectively. The dirt and NC interactions undergo reductions of 78% and 70%, resulting in 2.12 million and 344,364 slices respectively. Finally, the cosmic-induced slices total 62 million, significantly surpassing the count of all neutrino interactions. These include out-of-time cosmics that overlay with neutrino interactions and in-time cosmics that trigger the detector. The considerable cosmic ray rate associated with a surface-level detector creates a notably challenging scenario for reconstruction and selection, primarily due to the low inherent signal-to-background ratio.

7.2 Pre-Selection Criteria

The pre-selection stage is the first step in the selection process and is intended to eliminate candidates that are incompatible with subsequent selection and analysis stages, such as cosmic slices and neutrino slices lacking both a shower and a muon track. A muon candidate is required within a given slice through fundamental track criteria, incorporating a containment criterion to ensure that the majority of shower hits are contained within the FV of the detector. Excluding these slices ensures the suitability of the remaining slices and eliminates numerous potential backgrounds, enabling later selection stages to focus more on removing the remaining background.

The pre-selection starts by excluding slices failing Pandora's clear cosmic removal; these slices lack essential data products, including a reconstructed interaction vertex, as they are reconstructed as cosmic rays rather than neutrino interactions. Demanding that the reconstructed vertex resides within a defined FV achieves both purpose of rejecting cosmic and dirt backgrounds, while also ensuring the quality of shower reconstruction. Lastly, a necessary condition entails the presence of a viable photon candidate shower, ensuring its complete containment within the detector, alongside the necessity for a muon track within the FV of the detector. Absence of such a shower results in a failure to satisfy the signal definition. Details of the pre-selection are as follows:

7.2.1 Clear Cosmic Removal

As a surface detector, most of the reconstructed slices originate from cosmic rays, an estimated 62 million cosmic slices, while neutrino interactions amount to 6 million for an exposure of 6.6×10^{20} POT. To mitigate this, all slices marked as "clear cosmic" by Pandora are discarded, as detailed in Section 5.2.1. This procedure targets slices that are topologically incompatible with neutrinos, such as tracks traversing the detector walls from start to end, or slices located outside the primary drift window, thus precluding entry into the TPC within the beam spill window.

This applied criterion effectively eliminated 79.4% of cosmic background slices, yet it resulted in the removal of approximately 1.2% of the ν_μ CC π^0 signal and comparable reductions in background neutrino interactions. This step assures that the remaining slices are exclusively reconstructed as neutrino interactions rather than cosmic rays, thereby guaranteeing the presence of a reconstructed vertex in each slice, as required by subsequent criteria.

7.2.2 Detector Fiducial Volume Cut

Following the removal of all slices identified as clear cosmic by Pandora, a Fiducial Volume (FV) cut is used to discard slices with interaction vertices near the detector walls. This primarily aims to eliminate cosmic rays and dirt neutrino interactions entering through the walls. Moreover, this cut guarantees that photon showers from signal interactions primarily deposit their energy within the TPC. This is crucial due to the current energy calculation approach, which sums all energy depositions within the detector, leading to insufficient energy resolution for uncontained showers.

The reconstructed neutrino vertex distribution for the remaining slices post clear cosmic removal is shown in Figure 7.1, with the orange dashed lines marking the detector edges. Each distribution is normalised for clarity and comparison of shapes, given the prevalence of cosmic backgrounds at this initial selection stage. Dirt neutrino interaction slices generally enter through all detector walls, predominantly from the face of the detector along the beam

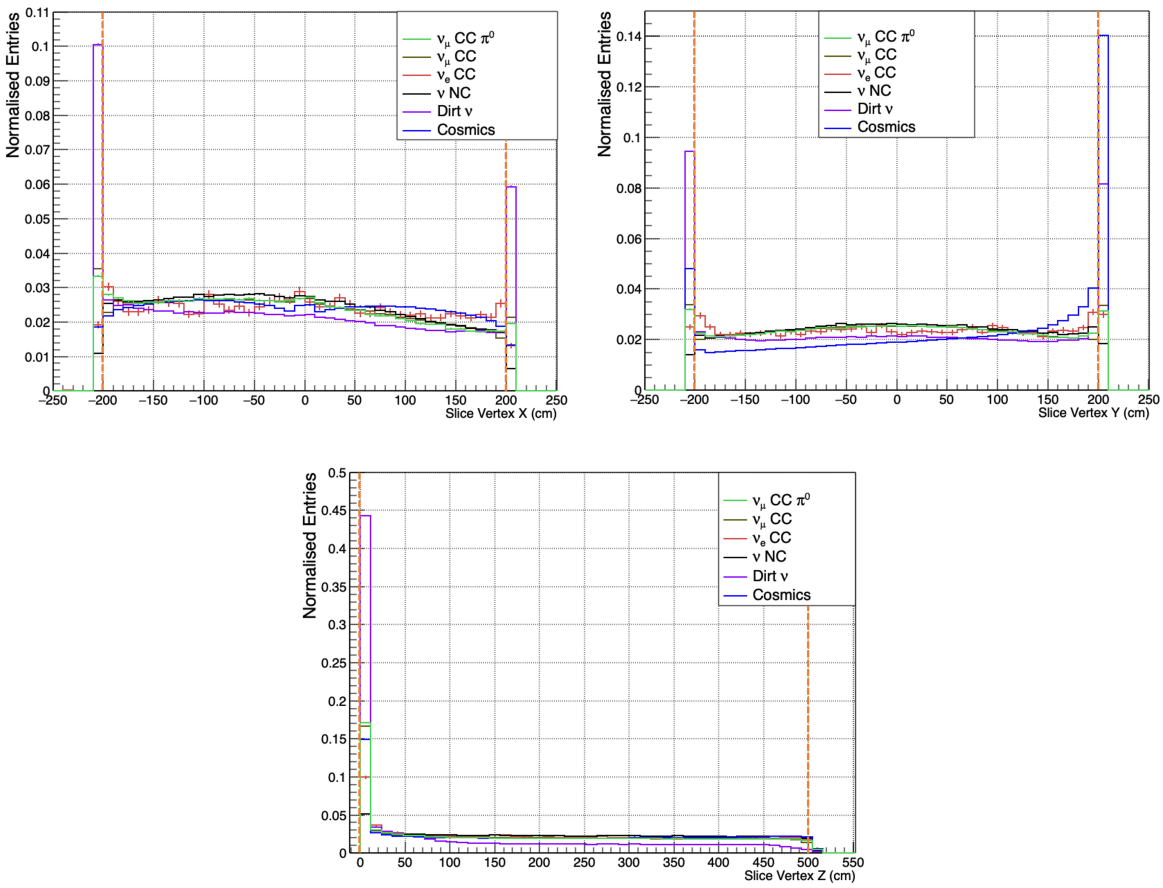

Figure 7.1: Reconstructed slice vertex position used for FV cut, with detector boundaries indicated by orange dashed lines.

direction as expected, as seen in the plot displaying slices vertex z. On the other hand, cosmic ray slices primarily access the detector through its upper face (high Y), with notable occurrences of reconstructed vertices at the lower face (low Y) and upstream face (low Z). Upstream and bottom face vertices largely result from residual through-going cosmic rays, where Pandora assigns the vertex to the upstream end of the slice.

The FV was established through an overlap analysis of the normalised dirt background and ν_μ CC π^0 signal distributions, as summarised in Table 7.1. A 15 cm cut is employed across all sides of the detector to mitigate dirt and cosmic backgrounds, especially at the upstream face in the beam direction (low Z) and the top side of the detector (high Y), while also ensuring the containment of low-energy hadronic activity. Additionally, to enable unimpeded reconstruction around the vertex and ensure that the 3 cm initial track for shower dE/dx calculations remains unaffected by the dead region at the cathode (X = 0), a 5 cm buffer is employed.

Coordinate	Minimum (cm)	Maximum (cm)
|X|	5	185
Y	-185	185
Z	15	485

Table 7.1: Fiducial Volume (FV) containment criteria for slice vertex position.

Upon the application of the FV cut, roughly 87% of dirt interactions have been excluded, along with approximately 66% of the cosmic ray interactions that remain post the clear cosmic removal. In contrast, this cut results in the removal of 44% of other ν_μ CC interactions, along with approximately 40% and 53% removal rates for ν NC and ν_e CC interactions, respectively. However, only 51% of the identified signal (ν_μ CC π^0) successfully meets this criteria, effectively leading to the rejection of the majority of uncontained events.

Figure 7.2 shows the spectrum of signal and multi-backgrounds based on true ν energy after the FV cut. The selection purity and efficiency plots are presented on the ratio plane, where selection purity represents the ratio of signal events to background per bin, and selection efficiency signifies the ratio of selected signal events to true contained signal events per bin. As neutrino interactions are not subject to specific constraints, the majority of backgrounds originate from other ν CC and NC interactions, as well as the residual dirt ν interactions. These factors will be addressed and mitigated through the imposition of restrictions on reconstructed tracks and showers.

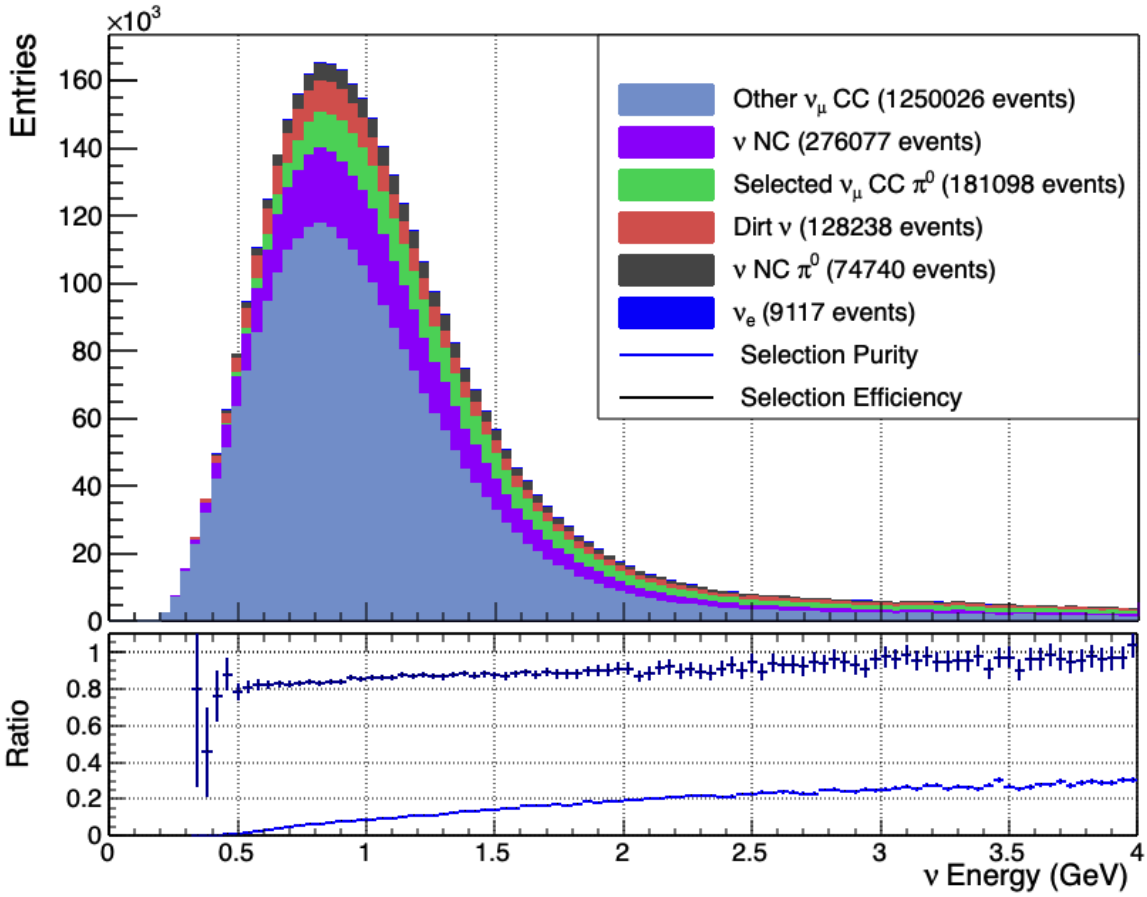

Figure 7.2: Spectrum of signal and backgrounds based on true ν energy after FV cut.

7.2.3 Reconstructed Track and Shower Criteria

In order to mitigate the events lacking a reconstruction topology consistent with the signal expectation, fundamental criteria are applied to the reconstructed tracks and showers. Firstly, a cut is applied based on the number of reconstructed showers, ensuring the presence of a reconstructed shower within the given slice, resulting in a substantial reduction of other ν_μ CC slices. Subsequently, a requirement is applied to the reconstructed tracks employing χ^2 hypothesis for muon hypotheses, wherein χ^2 hypothesis assesses the energy loss profile, dE/dx versus residual range, by comparing it against a set of templates corresponding to various particle hypotheses. Additionally, a restriction is imposed on the track length to guarantee the containment of the showers and their associated energy. In summary:

- **Reconstructed Showers:** At least one reconstructed shower present within the slice.
- **MIP Hypothesis:** The track is required to be aligned with the MIP hypothesis ($\chi^2_\mu <$ 30).

- **Track Length:** Either the longest track in a given slice is contained, or the track length is at least 100 cm.

Applying these selection criteria resulted in the removal of 63% of cosmic ray slices and 82% of dirt interaction slices that remained following the application of the FV cut. Additionally, 67% of other ν_μ CC interactions and 57% of ν NC interactions, including 17% of ν NC π^0 slices, are removed. However, the signal, namely ν_μ CC π^0 production interactions, experiences an approximate reduction of 23%, primarily attributed to the containment cut.

Figure 7.3 presents the distribution of true ν energy for the signal and multi-backgrounds after all the pre-selection cuts. The lower plots display the signal purity and efficiency, with corresponding average values of approximately 60% and 18%, respectively. Observably, the predominant source of background arises from neutrino interactions, including other ν_μ CC events and ν NC interactions.

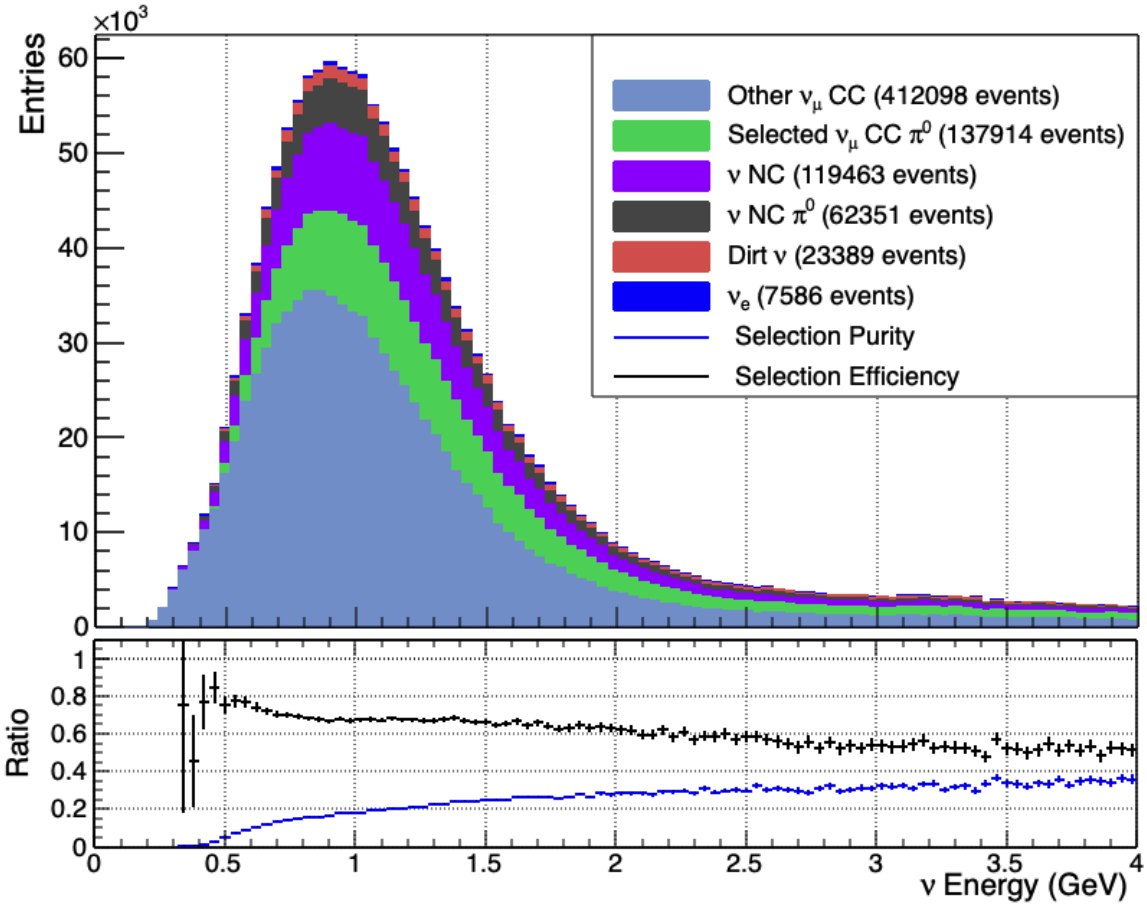

Figure 7.3: Spectrum of signal and backgrounds based on true ν energy after pre-selection cut.

Overall, the initial selection process resulted in a substantial reduction of 75% and 74% in the backgrounds associated with other ν_μ CC and ν NC interactions, respectively. This reduction can be attributed mainly to the absence of showers in these types of interactions. Moreover, the cosmic background has undergone a significant decrease of 98%, whereby each of the pre-selection cuts contributed to the rejection of segments of this background. Other ν interactions, and dirt interaction, were notably decreased by approximately 97%, mostly due to the FV criteria. However, ν_μ CC π^0 signal slices were also reduced by 58%, primarily attributable to the effects of both the FV and track containment cuts.

Although significant background reduction has been achieved, the sample remains largely dominated by background, with the ν_μ CC π^0 signal accounting for just 6.8% of the remaining slices. The primary background results from cosmic ray slices, representing 65.5% of the total selected slices, which remain significant even after pre-selection cuts, see Figure 7.3. The other background consists of ν_μ CC, comprising 20.3% of the sample, while ν NC interactions contribute around 6%. The remaining 1.5% comprises other neutrino interactions, predominantly dirt ν interaction slices.

7.3 Cosmic Background Rejection

Given that the pre-selection cuts leave cosmic as the dominant background which represents 65.5% of the total selected slices, dedicated measures are necessary to significantly reduce the cosmic background. All the remaining cosmic slices after pre-selection cuts, including the clear cosmic removal, are reconstructed under the assumption that they emerged from neutrino interactions and share the same pre-selection slice topologies. Candidate slices can be subjected to cuts aimed at mitigating the predominant cosmic ray background, and these cuts are categorised as timing cuts and topological cuts. The former approach employs the timing resolution of the detector subsystems to distinguish between events coinciding with the beam spill, known as in-time, and those occurring beyond this time window, termed out-of-time. Any out-of-time occurrences are attributed to cosmic sources and consequently rejected. The second approach focuses on analysing TPC activity to distinguish between topologies characteristic of neutrino events and those of cosmic events, employing the Slice ID Multi Variate Analysis (MVA) as discussed in Chapter 5.

Liquid Argon Time Projection Chambers (LArTPCs) typically exhibit inadequate timing resolution due to electron drift times, such as the 1.25 ms drift time in SBND. The TPC timing alone is less dependable due to ambiguity between early-time, distant drift events and later-time, closer-to-anode events. Furthermore, if a slice is tagged, the time resolution is primarily influenced by the cold electronics' 0.5 μs readout frequency, comparable to the 1.6

μs beam spill width [1]. Thus, TPC timing is not employed to differentiate between in-time and out-of-time slices. In comparison, the PDS and CRT subsystems can achieve timing resolution at the nanosecond scale [1]. Therefore, by correlating TPC slices with the relevant subsystem activity, cosmic backgrounds entering the TPC outside the beam window can be eliminated. The process of applying these cuts is outlined as follows:

7.3.1 PDS Cosmic Rejection

As a charged particle traverses a LArTPC, it generates both ionised electrons and scintillation light, the latter of which can be collected, as detailed in Section 3.2. SBND incorporates a thorough Photon Detection System (PDS) for capturing this light, discussed in Section 4.3.3. With its nanosecond-level timing resolution, the PDS can identify events occurring outside the beam spill time [1].

Through the process of flash matching, the alignment of charge and light centres enables the correlation of TPC and PDS activities, leading to the rejection of out-of-time slices. Utilising the PDS positioned in the Y-Z plane behind the anode enables the calculation of the Y and Z coordinates of the flash by averaging the PE-weighted positions of the individual photon detectors.

Two methods can be used to determine the drift position (X) of the flash: utilising the flash spread and the coated/uncoated ratio. The distance from the anode affects the spreading of light; therefore, the X position can be approximated by the overall spread of light detected by the PDS. SBND incorporates both coated Photo-Multiplier Tubes (PMTs) collecting Vacuum Ultra-Violet (VUV) scintillation light directly, as well as uncoated PMTs capturing light reflected from cathode-mounted foils, as detailed in Section 4.3.3. The ratio of direct to reflected light detection varies with the X position of an interaction, favouring more reflected light for interactions nearer to the cathode than the anode. Therefore, the X position is estimated by considering the relative ratio of direct and reflected light, accounting for the quantity of each PMT type. These two approaches are then combined to yield a refined X position estimate.

The match quality is evaluated by comparing the charge and light centres. This score is calculated as the sum of the absolute differences between the flash and charge coordinates in each dimension, divided by the expected spreads for each dimension. The expected spreads (σ) are obtained from simulation and take into account the varying precision in each coordinate. A lower score signifies improved alignment, while a higher score indicates poorer alignment. Improbable matches, like those between light and charge in opposite TPCs, are assigned a -5 score and discarded in this analysis. However, this method can only distinguish

between in-time and out-of-time activity, so it cannot eliminate in-time cosmic rays because their light emission coincides with the beam spill window.

The score distribution of flash matching, as defined previously, is shown in Figure 7.4, which includes both in-time and out-of-time cosmic events. The negative peaks mainly consist of cosmic slices within a TPC volume lacking flashes occurring during the beam spill period. Neutrino slice scores peak at the anticipated value of around 3, indicating an appropriate estimation of the expected score spreads. The scores above six, predominantly observed, correspond to out-of-time cosmic events with poor alignment to the in-time light.

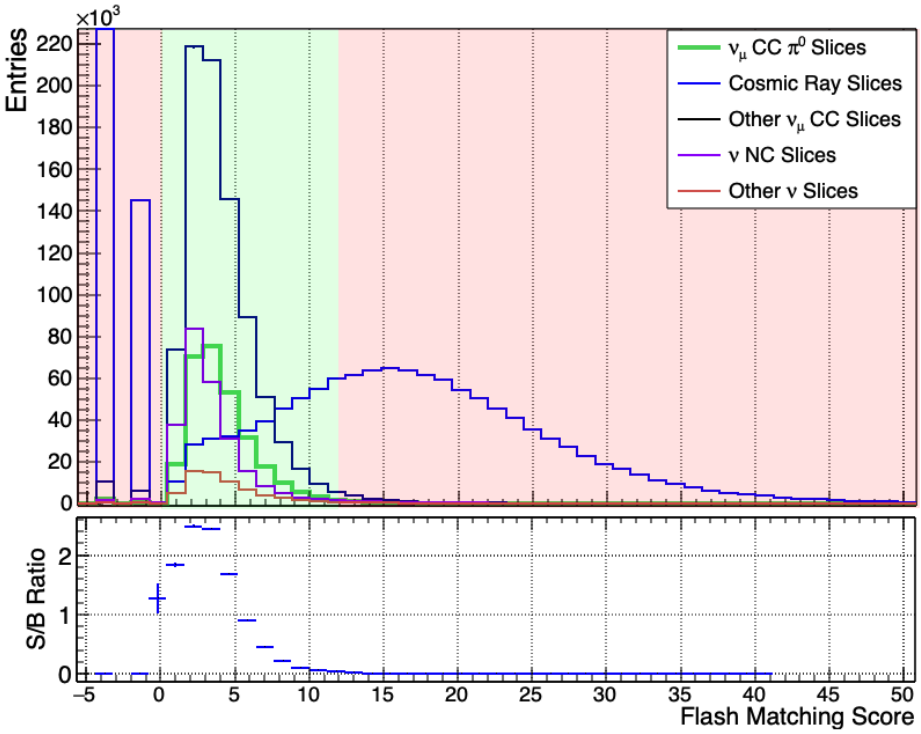

Figure 7.4: Score distribution of flash matching between in-time light and TPC slices. The negative score is assigned to matches that are incompatible, while lower scores, positive values, indicate stronger alignment between the light and charge signals. The plot at the bottom displays the signal-to-cosmic background ratio.

Demanding a score within the range of 0 to 12 (green shading) resulted in the rejection of 72.4% of cosmic slices while affecting only 2.4% of the ν_μ CC π^0 signal. There is also an approximate reduction of 4.0% for other ν_μ CC and ν NC backgrounds. Other ν backgrounds show an approximate 10% decrease, with 6.8% for dirt interactions and 3.1% for ν_e slices. This approach stands out as the most potent cosmic rejection technique within SBND, highlighting the significance of the timing information provided by the PDS.

7.3.2 Pandora Neutrino Score

Based on the TPC reconstructed information, distinguishing cosmic rays from neutrino interactions is possible due to their distinct characteristics: cosmic rays often exhibit a single long track along with delta rays, while neutrino interactions involve multiple particles emerging from a common vertex. To enhance clear cosmic ray removal performed by Pandora, an MVA is employed to compute a "Neutrino Score" for every slice. This score quantifies the degree of neutrino-likeness in a slice by utilising topological variables detailed in Section 5.2.1. The application of this MVA further decreases the cosmic ray slices, exclusively using TPC information without utilising the other detector subsystems.

Figure 7.5 shows the Pandora ν score distribution, where higher values correspond to a more neutrino-like interaction. Notably, there is a distinct separation between neutrino and cosmic slices within the distributions. Introducing a cut at 0.46 (separating green from red areas on the plot) results in a 57.4% reduction in cosmic slices, while impacting less than 3% of signal neutrino interactions. Additionally, this cut resulted in a reduction of approximately 15% in dirt neutrino interactions and around 13.5% in other neutrino backgrounds, including 6.2% for ν NC slices, 5% for other ν_μ CC interactions, and 2.25% for ν_e.

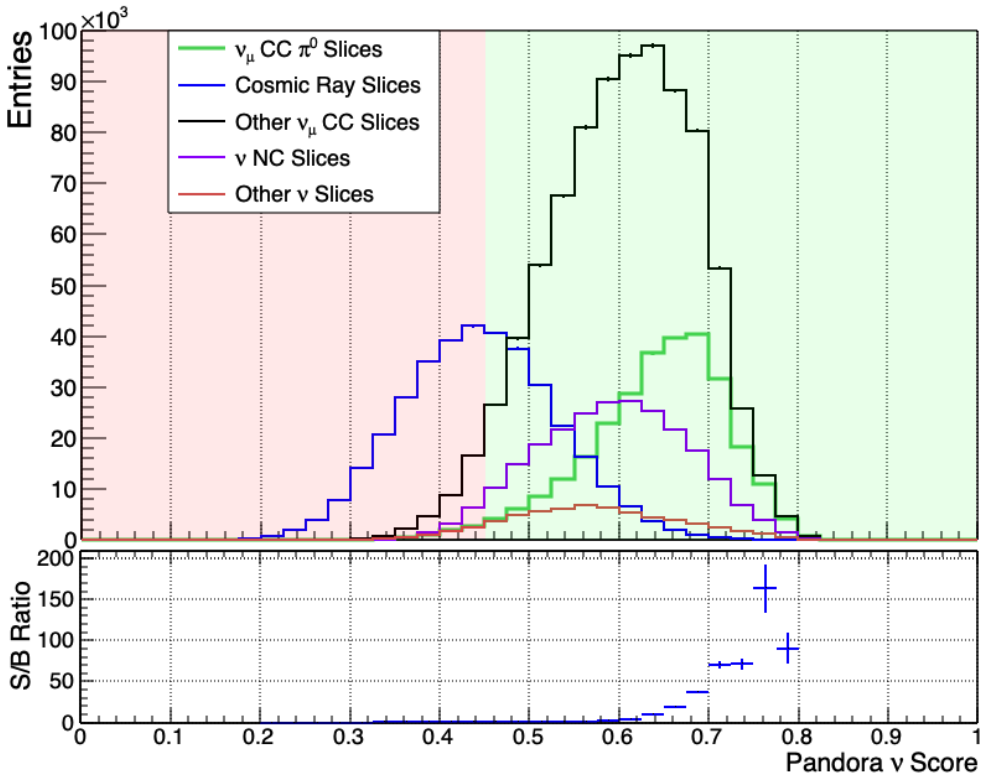

Figure 7.5: Pandora ν score distribution indicating the degree of neutrino-like characteristics in a given slice. The plot at the bottom displays the signal-to-cosmic background ratio.

7.3.3 CRUMBS Cosmic Rejection

The CRUMBS tool leverages the complementary information from different subsystems by combining their inputs into a BDT score, credit to H. Lay. Incorporating the information from both the TPC and PDS subsystems as utilised in previous methods, the present approach also integrates the matching information between TPC tracks and CRTs. By amalgamating these inputs, a BDT score comparable to the Pandora ν score can be generated.

The distribution of CRUMBS scores after applying Pandora ν score cut is shown in Figure 7.6, where higher scores correlate with interactions that exhibit a stronger resemblance to neutrino-like behaviour. The distributions distinctly differentiate between cosmic slices and neutrino slices, and notably, ν_μ CC π^0 interactions generally possess slightly higher scores than NC interactions. Implementing a cautious cut at -0.1 results in a reduction of cosmic slices by around 65.8% in cosmic slices while affecting fewer than 1% of signal interactions. Furthermore, this measure results in a 7.2% decrease in dirt neutrino interactions and a 3.7% reduction in NC interactions.

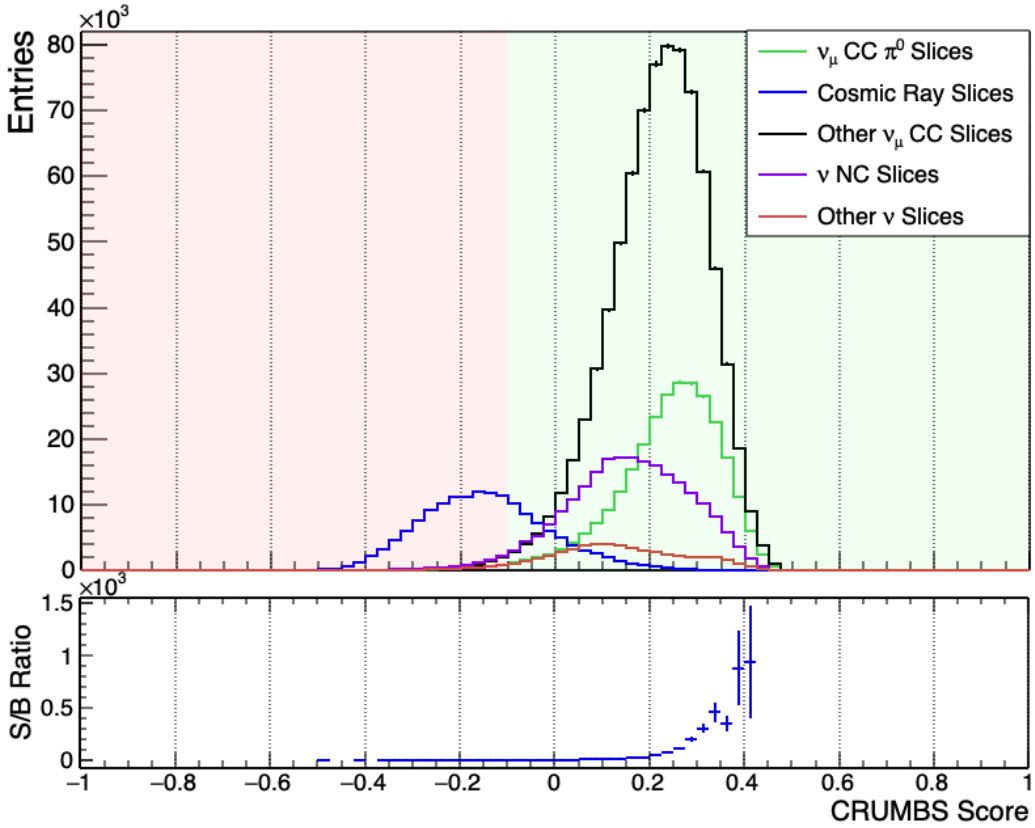

Figure 7.6: CRUMBS score distribution reflecting neutrino-like characteristics in respective slices. The ratio between the signal and cosmic background is displayed in the lower plot.

7.3.4 Combined Cosmic Removal Effectiveness

Overall, following the implementation of the rejection criteria derived from the three methodologies discussed in this section, there is a significant reduction of 98.1% in the number of cosmic ray slices that remained after the pre-selection step, effectively reducing their count from 1.33×10^6 slices to 24,867 slices. Taking into account the rejection achieved by the pre-selection, the overall cosmic rejection rate reaches 99.95%. The cosmic ray slices that remain are now outnumbered by the ν_μ CC π^0 production signal. The cosmic ray slices constitute approximately 3.9% of the total selected slices, a significant decrease from the pre-selection phase where they accounted for about 50% of the overall slices. Additionally, the other ν_μ CC, ν NC, and other ν backgrounds experience reductions of 9.0%, 13.3% and 32.0%, respectively, while they still make up 78.6% of the selected slices, as shown in Figure 7.7. Conversely, these cuts lead to the removal of only 6.2% of the targeted signal, yielding 129,296 remaining candidates, which accounts for 20.2% of the total slices retained after the cuts applied.

The distribution of true neutrino energy for the signal candidates corresponding to the remaining slices with neutrino interaction backgrounds is shown in Figure 7.7, highlighting the dominant backgrounds as the other ν_μ CC and NC backgrounds, with 374,814 and 103,537 candidates, respectively. The lower portion of the figure displays the purity and efficiency of the signal, indicating an average selection purity of approximately 20% and an efficiency of around 75%.

7.4 CC ν_μ Events Selection

Upon implementing the cosmic ray removal criteria, only a minor fraction of approximately 4% of the initially selected slices remained, while the dirt neutrino interactions constituted only 2.6% of the remaining slices. The predominant residual background for the ν_μ CC π^0 arises from other ν_μ CC and ν NC interactions, accounting for 58% and 16%, respectively, of the remaining slices. Both NC and ν_e interactions can be distinguished by the presence of a muon track. Additionally, these track-based criteria are independent of the cuts applied to select photon showers, providing an additional approach to mitigate this specific background.

The subsequent step in the selection involves identifying neutrino interactions that generate muons from the primary vertex. The primary challenges arise from NC interactions involving charged pions or protons that can resemble muon tracks at momenta exceeding a few 100 MeV. This selection can be achieved by applying criteria to topological and calorimetric parameters, a process known as Particle Identification (PID), to classify a track as a muon, pion, or proton. Moreover, additional cuts are applied using parameters derived

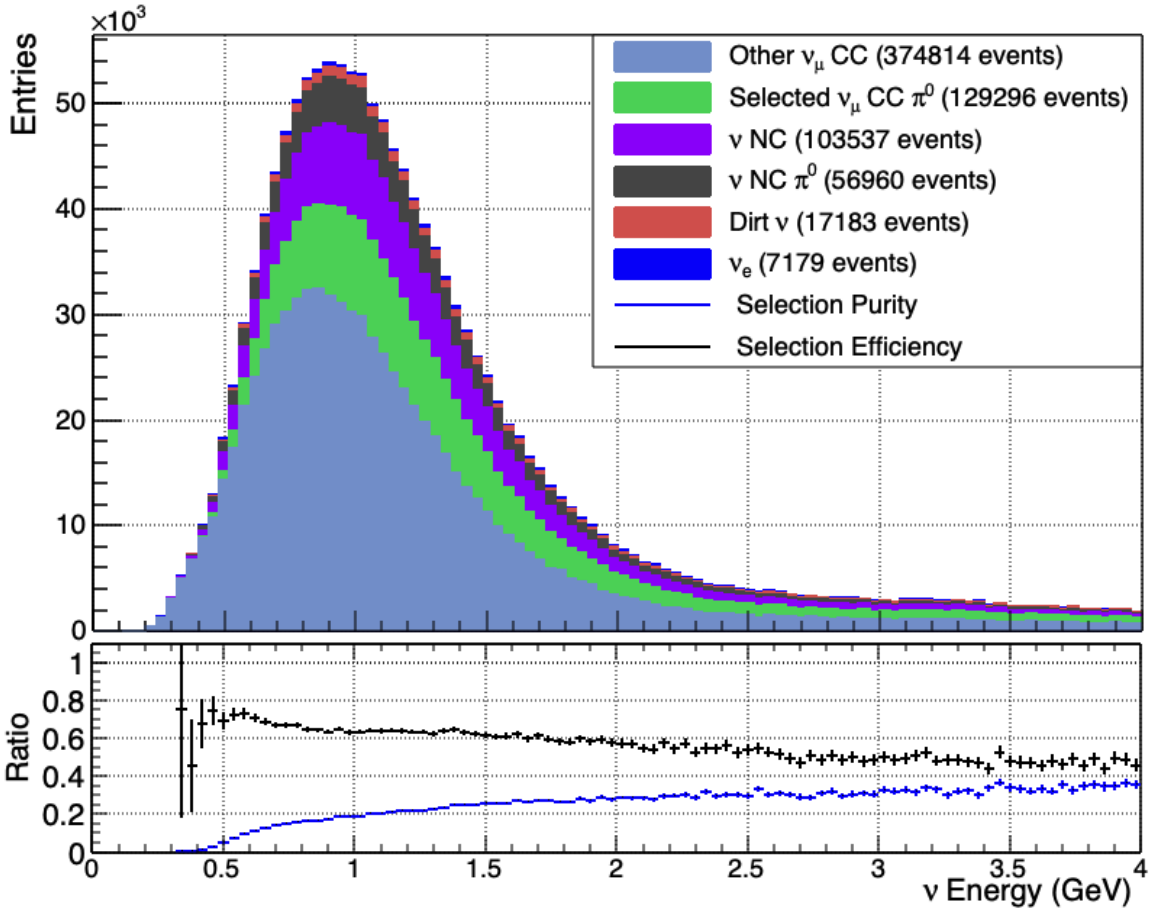

Figure 7.7: Energy spectrum of signal and backgrounds based on true neutrino energy after cosmic rejection criterion.

from a Boosted Decision Tree (BDT) model that integrates both topological and calorimetric variables. Based on the reconstructed track topology, the parameters exhibiting the most pronounced discrimination between the background and signal are selected, and then appropriate cuts are applied and optimised to achieve the most effective separation performance.

Figure 7.8 shows signal and background in selected slices in relation to the number of reconstructed tracks. As observed, the background contributions from cosmic, dirt, and NC interactions exhibit higher rates when only one or two tracks are reconstructed, with a notable increase when only one track is reconstructed. Therefore, these backgrounds, especially those originating from NC interactions, can be substantially mitigated by exclusively selecting slices in which a muon track is reconstructed. This is discussed in the following sub-sections:

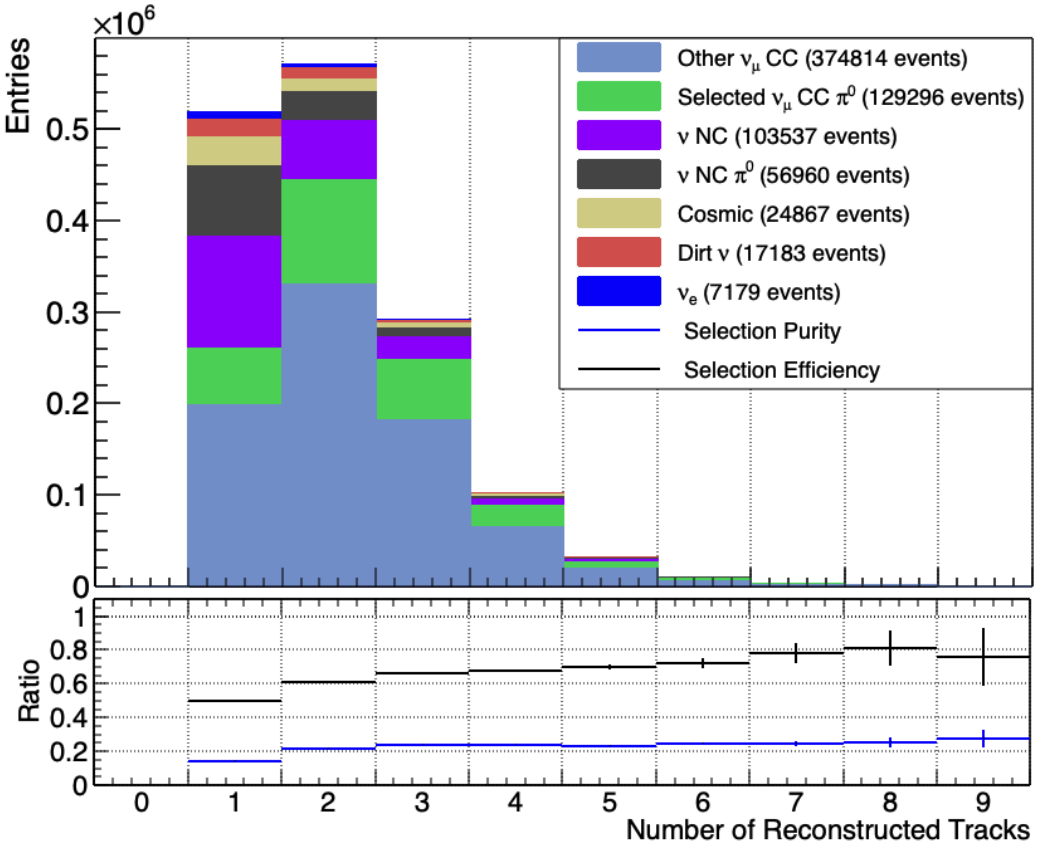

Figure 7.8: Signal and backgrounds in selected slices as a function of the number of reconstructed tracks.

7.4.1 Single Reconstructed Track Scenario

In the case of a single reconstructed track, various selection cuts are implemented to identify slices that are most likely to contain a track originating from a muon. After evaluating the PID parameters, only those with the most effective power of separation are selected and optimised to achieve the best muon track-like selection.The first selection parameters include cuts based on χ^2 PID hypotheses, discussed in Section 7.2.3.

Figure 7.9 shows distributions of χ^2 calculated for the muon, proton and pion hypotheses and PIDA score that used in the selection criteria. In addition, Figure 7.9d shows the distribution of χ^2 pida scores for the muon, proton, and pion. In this context, the particle identification variable, PIDA, is defined as the mean value of A_i computed across all space points along the track, with A_i represented as [199]:

$$A_i = (dE/dx)_{calo,i}\, R_i^{0.42} \tag{7.1}$$

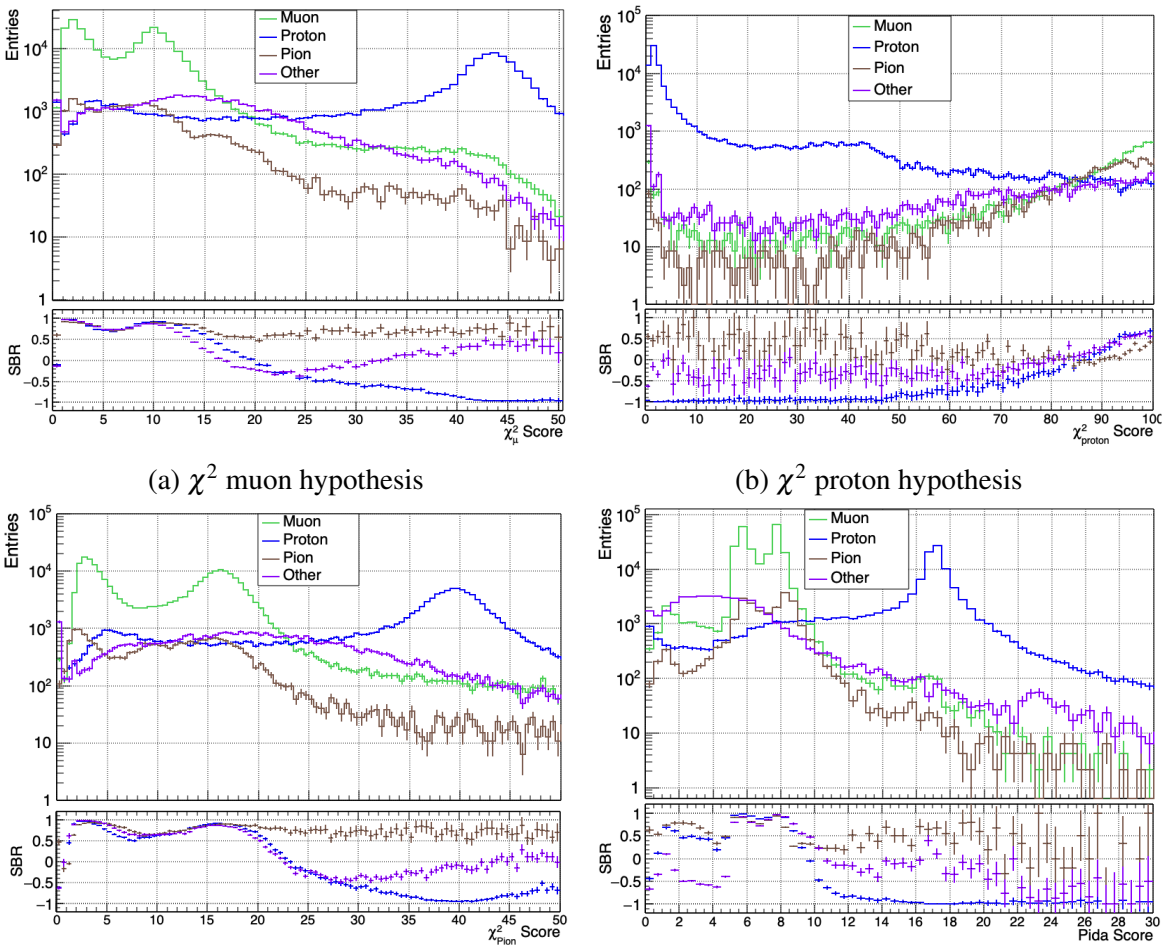

(a) χ^2 muon hypothesis

(b) χ^2 proton hypothesis

(c) χ^2 pion hypothesis

(d) PIDA score

Figure 7.9: Distributions of χ^2 calculated for the energy loss profile of reconstructed tracks compared with the muon, proton and pion hypotheses and PIDA score. The x-axis on the plots is presented as a logarithmic axis. The Signal-to-Background Ratio (SBR) is calculated with muon tracks identified as signal and other track-like particles as categorised as background, including those misclassified tracks, labelled as Other, as detailed in Section 5.2.2.

Figure 7.9 demonstrates a clear separation between muon tracks and other track-like particles. However, to minimise the risk of signal loss, an additional set of cuts based on parameters from a BDT model is applied. This multi-classification technique, known as Dazzle, comprises individual BDTs for each of the intended output classifications, including muon, proton, pion, and other. Each BDT assigns a score to indicate the degree of compatibility between an input track and the specific hypothesis. For example, the muon BDT assigns a score to evaluate how closely a given track resembles a muon. These BDTs are trained simultaneously and standardised so that the total scores across all hypotheses equal one. Therefore, each score can be interpreted as the probability of the corresponding hypothesis.

Figure 7.10 shows the BDT scores for the muon, proton, pion, and other hypotheses, with each line corresponding to a specific particle type. Notably, muons exhibit the most significant separation from protons compared to other particles, as indicated by their low scores under the proton hypothesis. This outcome aligns with expectations since protons are the most distinguishable in terms of calorimetric and topological characteristics, as observed in the χ^2 PID (see Section 6.1). Muons and pions display some separation but also a degree of overlap, which is anticipated, especially for stopping pions that closely resemble muons.

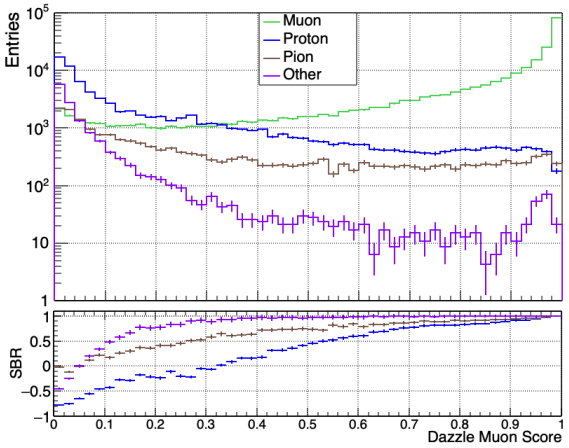

(a) Muon hypothesis

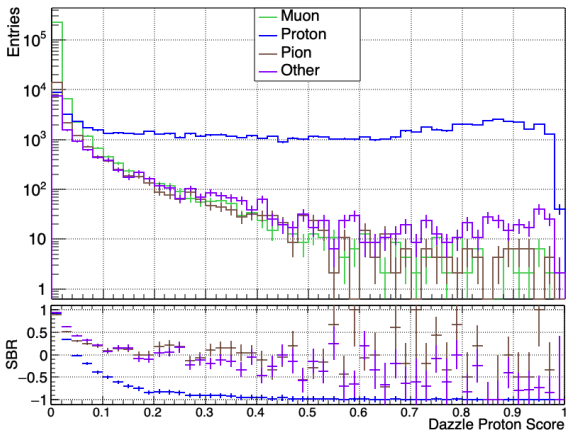

(b) Proton hypothesis

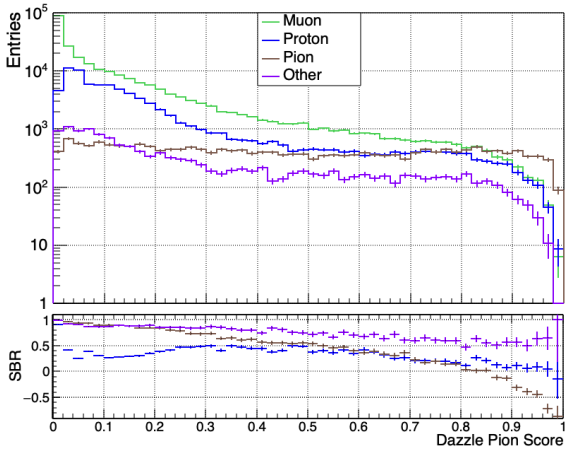

(c) Pion hypothesis

Figure 7.10: Distributions of Dazzle Track PID BDT scores for the muon, proton and pion hypotheses. The x-axis on the plots is presented as a logarithmic axis. The Signal-to-Background Ratio (SBR) is calculated with muon tracks identified as signal and other track-like particles as categorised as background, including those misclassified tracks, labelled as Other, as detailed in Section 5.2.2.

Other tracks, primarily misclassified photons and electrons, demonstrate reasonable separation from the other hypotheses.

The parameters derived from both χ^2 PID and Dazzle Track PID were optimised using the separation parameter calculated by Equation 6.1 to achieve the best performance in selecting slices with the highest likelihood of containing reconstructed muon tracks. Table 7.2 shows a summary of track selection criteria in the case of a single reconstructed track. In this scenario, given the presence of a single track, the tracks meeting all these criteria will be selected, while the remaining tracks will be excluded.

PID Hypotheses	Minimum Score	Maximum Score
χ^2_μ	0	25
χ^2_{proton}	80	/
PIDA	4	11
Dazzle muon	0.8	1
Dazzle proton	0	0.04
Dazzle pion	0	0.3

Table 7.2: Summary of track selection criteria in the case of only one reconstructed track.

Figure 7.11 shows the slices with single reconstructed tracks, categorised by their true topology, for the signal and background distributions before and after the application of the selection cuts. Implementing these cuts results in the removal of 28.1% of NC interactions, 30.0% of ν_e CC interactions, and 11.0% of dirt interactions. Moreover, cosmic slices and other ν_μ interactions are reduced by approximately 5.0%. Nonetheless, these cuts resulted in the rejection of approximately 6.0% of signal slices while increasing the signal account to 2% of the total selected slices, with the main backgrounds originating from other ν_μ CC interactions and from ν NC and cosmic interactions.

7.4.2 Two Reconstructed Tracks Scenario

Utilising the same approaches introduced in the previous subsection, several selection criteria were applied to slices containing two reconstructed tracks. In this scenario, the longest track within a slice is designated as the muon candidate, and selection cuts are subsequently applied to it. This assumption can be corroborated by examining the true simulated particle that corresponds to this longest track in truth. Figure 7.12 illustrates the length of the longest track, categorised by the true particle to which the track was associated for each interaction type. It can be observed that the longest track is matched to a muon in 83.8% of slices, while

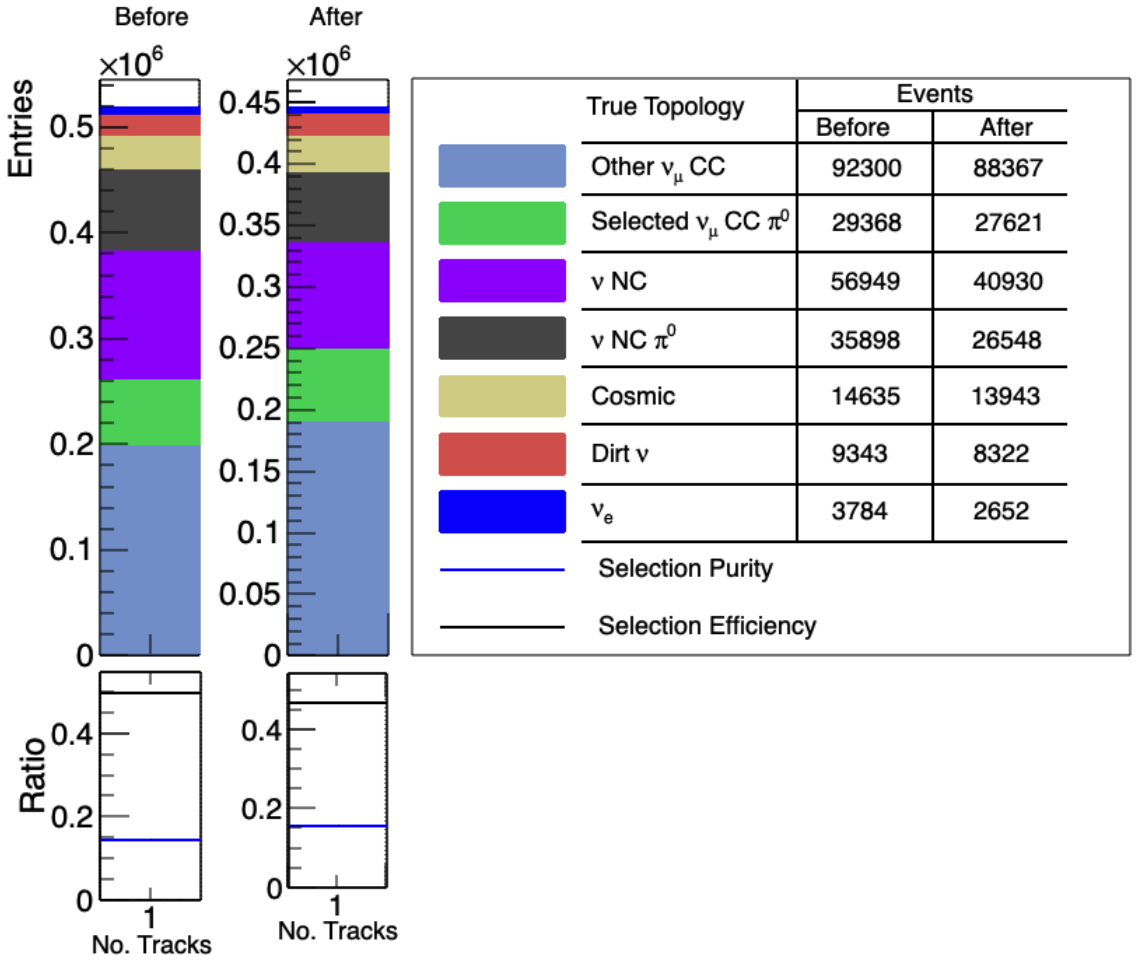

Figure 7.11: Signal and backgrounds in selected slices with single reconstructed track before (left) and after (right) applying selection cuts.

the remaining cases are predominantly associated with protons (9.8%) and pions (4.4%), which are associated with shorter track lengths.

Table 7.3 provides a comprehensive overview of the cuts used for track selection when two tracks are reconstructed. In this scenario, the slice with the longest tracks that satisfy all of these criteria will be selected, whereas those not meeting these requirements will be discarded.

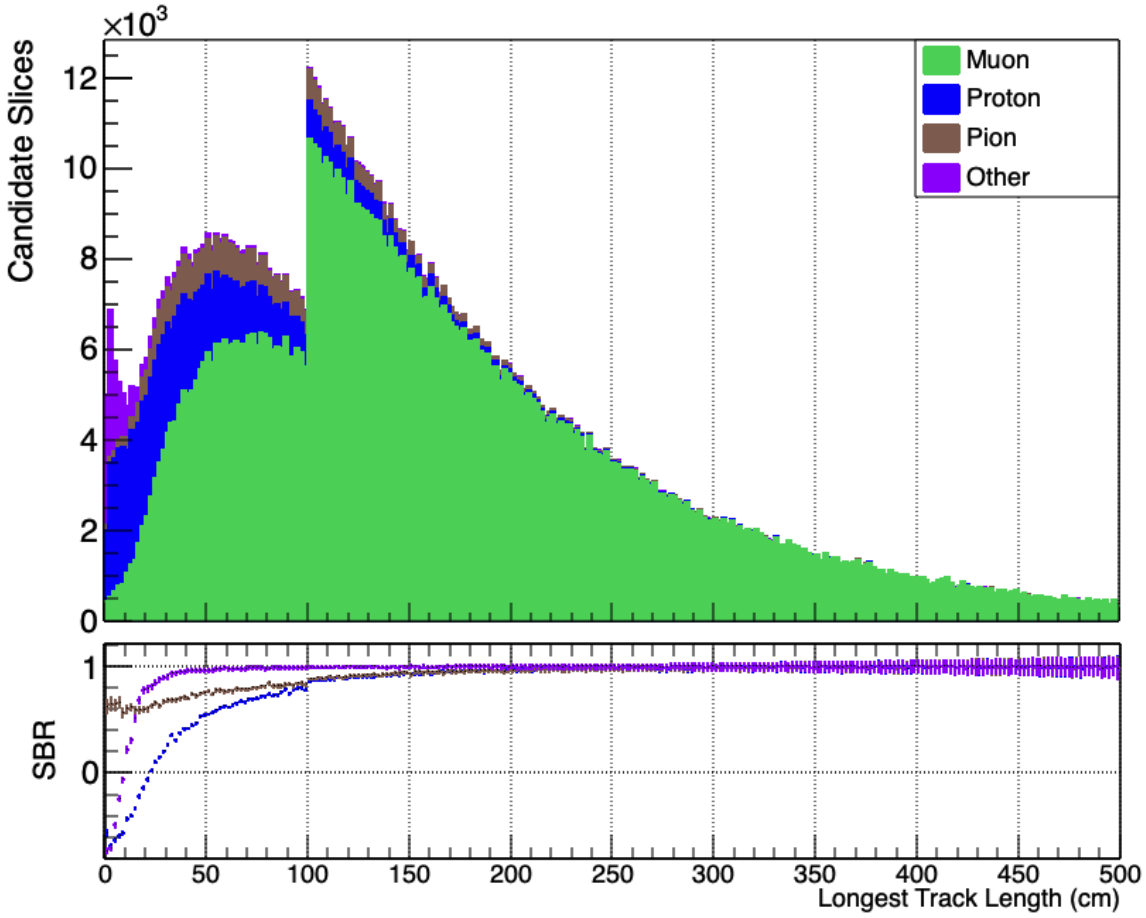

Figure 7.12: Distribution of the longest track length for ν_μ CC interactions after cosmic rejection cuts. Each histogram is stacked and divided based on the true particle that corresponds to the track. The sharp peak at 100 cm is due to the requirement that the longest track with a length below 100 cm must be contained.

Scenarios →	Two Reconstructed Tracks		Three or Higher Reconstructed Tracks	
PID Par. ↓	Min. Score	Max. Score	Min. Score	Max. Score
χ^2_μ	0	20	0	20
χ^2_{proton}	70	250	70	270
χ^2_{pion}	0	25	0	25
PIDA	0	10	0	10
Dazzle muon	0.8	1	0.7	1
Dazzle proton	0	0.15	0	0.15

Table 7.3: Summary of track selection criteria in the case of two or three and higher reconstructed tracks.

After the application of these criteria to the longest track within each slice, approximately 8% of the background has been rejected, as shown in Figure 7.13. This including 26.7% of NC slices, 27.4% of ν_e slices and around 7% of cosmic and dirt slices. On the other hand, the signal is reduced by around 5.2%, accounting for 21.5% of the remaining slices. The proportion of background rejected is relatively lower in this scenario compared to the case of a single reconstructed track, primarily because of the increased likelihood of at least one track originating from $\pi^\pm$ interactions, which are challenging to distinguish from muon tracks.

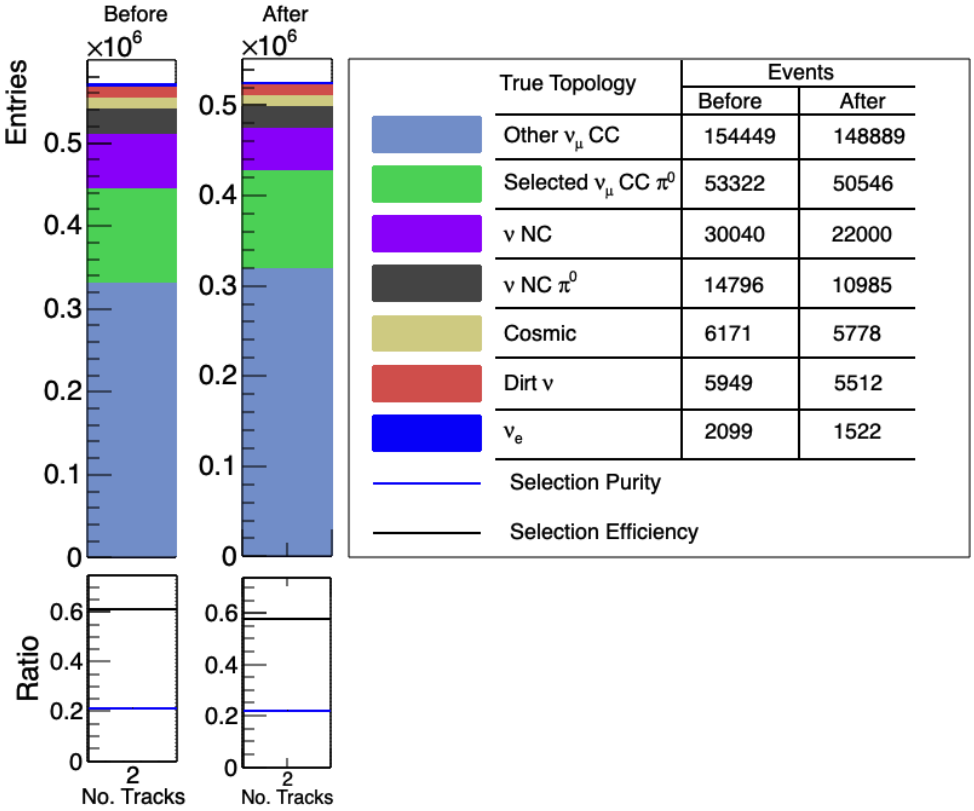

Figure 7.13: Signal and backgrounds in selected slices with two reconstructed tracks before (left) and after (right) applying selection criteria.

7.4.3 Slices with Three or More Reconstructed Tracks

In this scenario, the same parameters as those used in the case of two reconstructed tracks were employed, with optimisations carried out to achieve the best selection performance. Table 7.3 summarises the track selection criteria for scenarios with reconstructed tracks. The selection prioritises slices with the longest tracks meeting these criteria, while discarding other slices.

These cuts led to a 5.4% reduction in background, thereby decreasing the background contribution to 76.2% of the remaining slices. The primary contributor to the background remains other ν_μ CC interactions, which decreased by 3.5% after applying these criteria. However, the NC interactions reduced by 21.9%, ν_e interactions by 22.5%, and cosmic and dirt interactions by approximately 7%. In contrast, the signal slices decreased by approximately 4%, comprising 23.8% of the remaining slices.

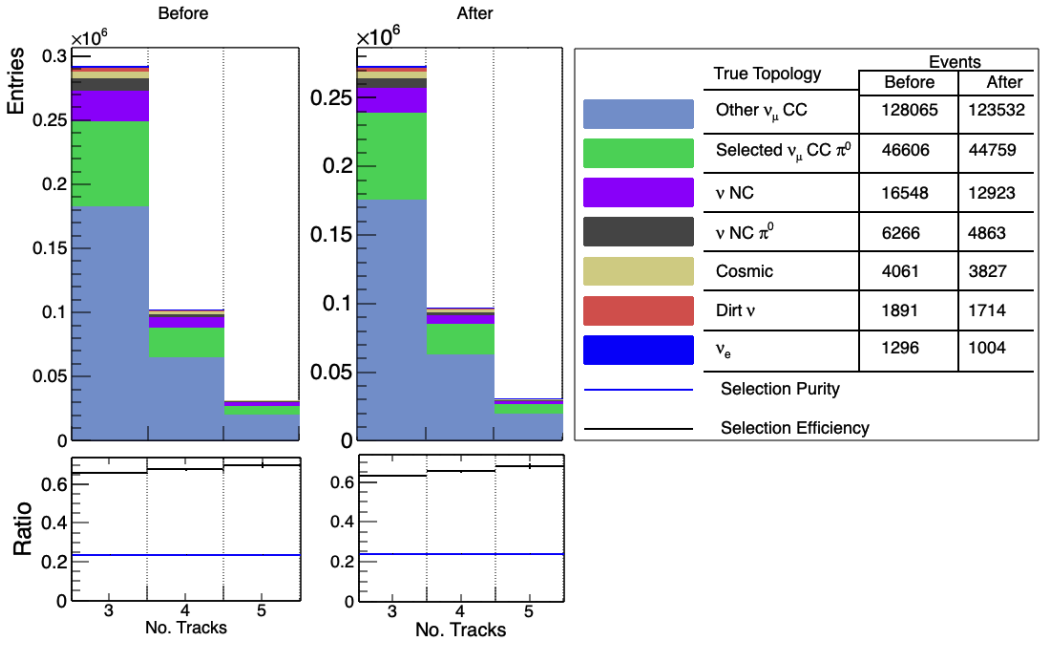

Figure 7.14: Signal and backgrounds in selected slices with three or higher reconstructed tracks before (left) and after (right) applying selection criteria.

7.4.4 Summary

Overall, selecting slices containing muon tracks resulted in a reduction of background by approximately 10%. The most substantial reductions in background were observed in ν NC interaction slices, with a reduction of 26.7%, and in ν_e interaction slices, with a reduction of 27.8%, as intended by introducing these criteria. Additionally, the number of cosmic ray slices decreased by 5.3% and ν dirt slices reduced by 9.5%. Conversely, the slices associated with ν_μ CC π^0 production decreased approximately 5%, resulting in it representing 20.3% of the total selected slices.

Figure 7.15 shows the distribution of selected slices categorised by their true interaction type in relation to true neutrino energy. The predominant background within the selected slices originates from other ν_μ interactions, accounting for 59.7%, which is expected given

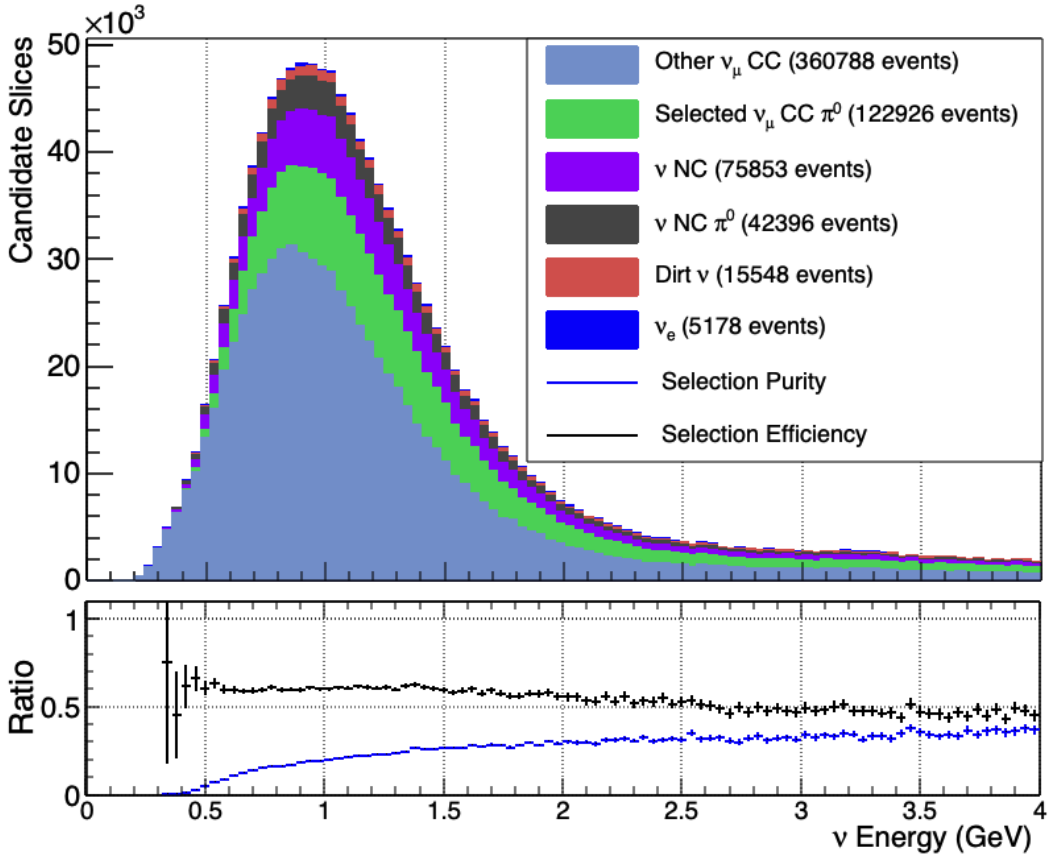

Figure 7.15: Signal and background energy spectrum after muon track selection.

the focus up to this stage has been on selecting slices with a higher likelihood of containing muon tracks while applying basic restrictions on showers. Additionally, the second most significant background in the selected slices arises from ν NC interactions, making up 12.5% of the total selected slices, despite a one-third reduction in the last stage. This is likely due to the presence of pion tracks in the remaining slices from ν NC interactions, which poses challenges in distinguishing them from muon tracks. The backgrounds from cosmic and dirt slices account for only 3.8% and 2.5% of the total selected slices, respectively.

7.5 π^0 Event Selection

After applying selection criteria to identify slices with a high likelihood of containing muon tracks, the next step is to select slices with π^0 production, which can be accomplished by choosing slices with a high probability of containing one or more photon showers. Identifying photons are crucial, not only for selecting ν_μ CC π^0 production interactions but also for

accurately measuring the interaction properties. This capability is essential for effectively reducing remaining backgrounds, especially those arising from other ν_μ CC interactions.

The pre-selection process ensures that all remaining slices contain a candidate photon shower thus a set of cuts can be applied. The selection process is accomplished by applying criteria to reconstructed topological and calorimetric parameters, as well as utilising a BDT model referred to as Razzle, which incorporates both topological and calorimetric variables. Similarly to the muon track selection, parameters with the highest discriminatory power between background and signal are identified based on the reconstructed shower topology. Subsequently, cuts are applied to these parameters, and optimised to achieve the highest separation performance. This is outlined in the following sub-section:

7.5.1 Slices with One Reconstructed Shower

Given that the predominant source of background originates from other ν_μ CC interactions, and ν_e slices accounting less than 1% of the total selected slices, as shown in Figure 7.15, the primary objective is to effectively mitigate showers arising from inaccurately classified track-like particles, as discussed in Section 5.2.2. This is accomplished through a two-fold approach: first, by applying traditional selection criteria based on reconstructed parameters that describe shower properties, as discussed in Section 6.2; and second, by employing a multi-classification BDT model to categorise each shower as either an photon, electron, or other.

Figure 7.16 presents examples of the reconstructed shower parameters that exhibit the highest discriminatory power when considering single shower reconstruction. Figure 7.16a shows a comparison between shower conversion gaps among the three categories, defined as the gap between the vertex of Pandora-identified neutrino interaction and the shower start position. Additionally, shower density, which is calculated as the ratio of shower energy to the square of shower length, addresses energy-length correlations presented in Figure 7.16b. The dE/dx and length characteristics of the photon, electron, and other showers are illustrated in Figure 7.16c and Figure 7.16d. Observing the Signal-to-Background ratio (SBR) presented on the ratio plane within each plot, these parameters can be employed to discriminate against showers with a low likelihood of being photon showers, especially those originating from incorrectly classified tracks.

To enhance the performance of the selection criteria, Razzle Shower PIDs based on the BDT model were employed. These PIDs assign scores signifying the level of agreement between an input shower and a given hypothesis. Figure 7.17 shows distributions of Razzle Shower PID BDT scores for the photon, electron, and other hypotheses. These plots

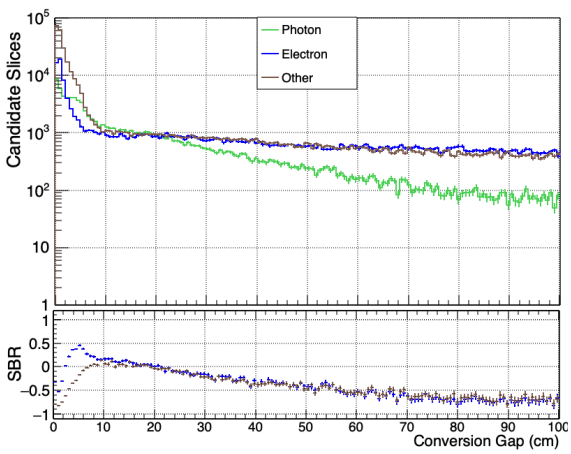

(a) Showers conversion gap

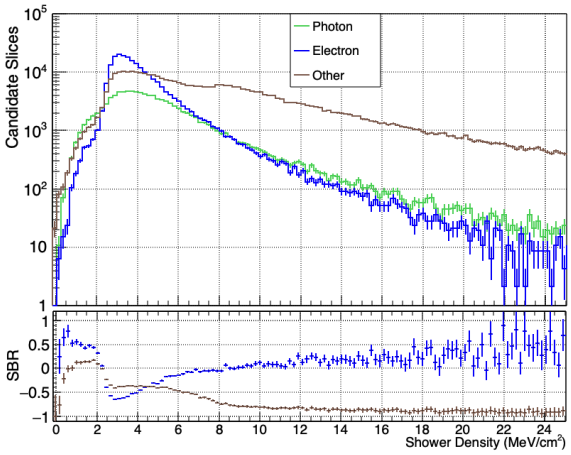

(b) Showers density

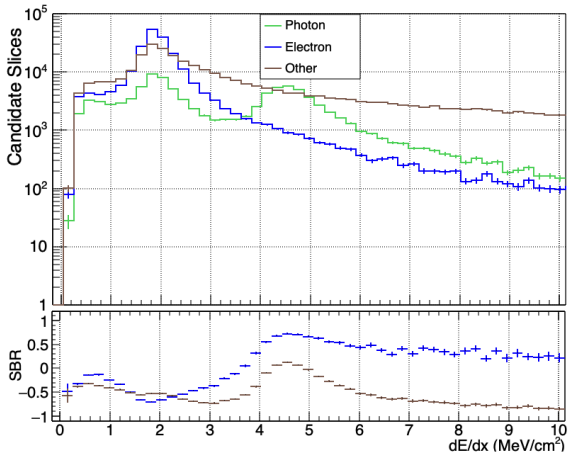

(c) Showers best-plane dE/dx

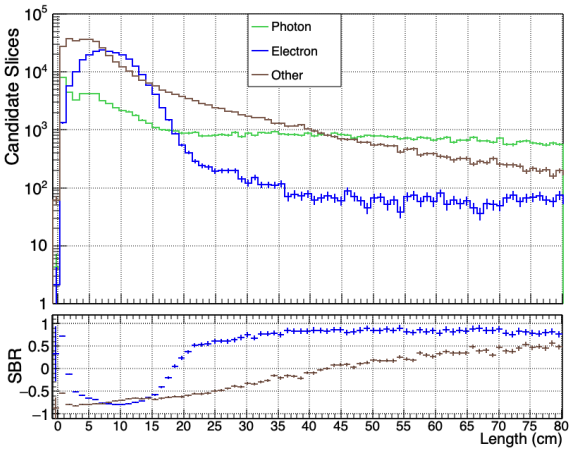

(d) Shower length

Figure 7.16: Illustrations of reconstructed shower parameters demonstrating discriminatory capability among photon, electron, and other shower categories. The x-axis on the plots is presented as a logarithmic axis.

demonstrate that applying selection criteria based on these hypotheses leads to a significant rejection of background showers originating from sources other than photons.

The parameters obtained from both approaches were optimised using the same approach outlined in Section 7.4, aiming for better performance in selecting slices with the highest probability of containing reconstructed photon showers. Table 7.4 shows a summary of shower selection cuts used in the single reconstructed shower scenario. In this case, given the presence of a single shower, the showers meeting all these criteria will be selected, while the remaining showers will be rejected.

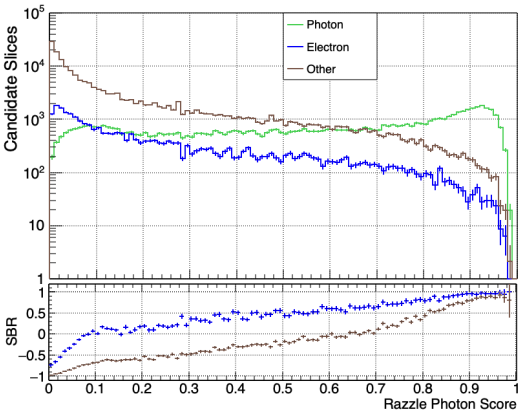

(a) Photon hypothesis

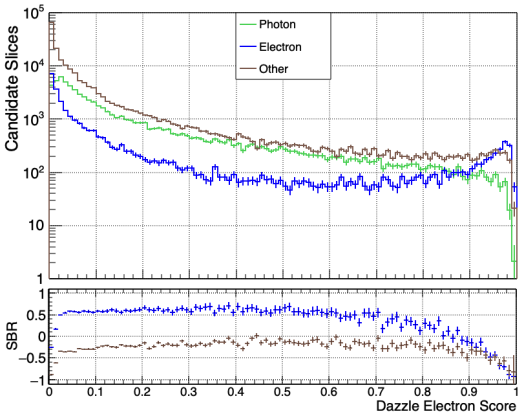

(b) Electron hypothesis

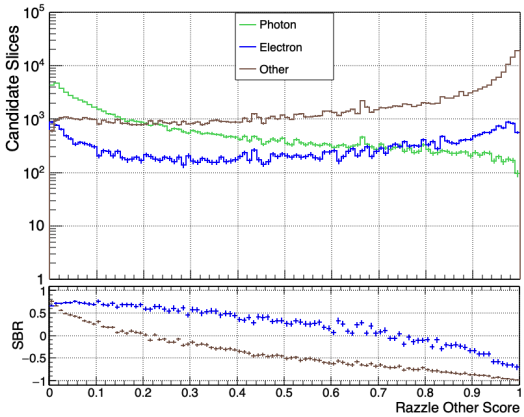

(c) Other hypothesis

Figure 7.17: Distributions of Razzle Shower PID BDT scores for the photon, electron and other hypotheses. The x-axis on the plots is presented as a logarithmic axis.

Shower PID	Minimum Value	Maximum Value
Conversion Gap [cm]	0	50
Density [MeV/cm]	0	15
Shower dE/dx (best-plane) [MeV/cm]	1.5	8
Length [cm]	3	/
Initial Track Width [cm]	0.5	30
Number of Hits (best-plane)	10	/
Razzle Photon Hypothesis (score)	0.5	1
Razzle Electron Hypothesis (score)	0	0.6
Razzle Other Hypothesis (score)	0	0.4

Table 7.4: Single reconstructed shower selection criteria.

After implementing the cuts listed in Table 7.4, the number of background slices decreased by 96.6%, leaving background slices accounting for 47% of the total slice count. Figure 7.18 shows the signal and backgrounds categorised by their true topology in the selected slices both prior and after the application of the selection criteria, in cases where only one shower has been reconstructed. Observably, the selected slices predominantly consist of ν_μ CC π^0 production events, accounting for approximately 64.0% of the total. However, after these cuts applied, the signal reduced by 52.8%.

Additionally, the second significant background comes from NC interactions, representing about 10% of the total selected slices. The majority of these interactions arise from ν NC π^0 production, accounting for 73.4% of these slices, which generate two photon showers. Furthermore, another notable source of background is attributed to NC interactions, accounting for approximately 10.2% of the total selected slices. A substantial majority of these NC interactions, specifically 73.4%, are attributed to ν NC π^0 production, resulting in the generation of two photon showers with hadron tracks. The remaining backgrounds, including ν_e, dirt, and cosmic events, collectively account for 6.4% of the total selected slices, with cosmic-induced slices constituting the predominant majority.

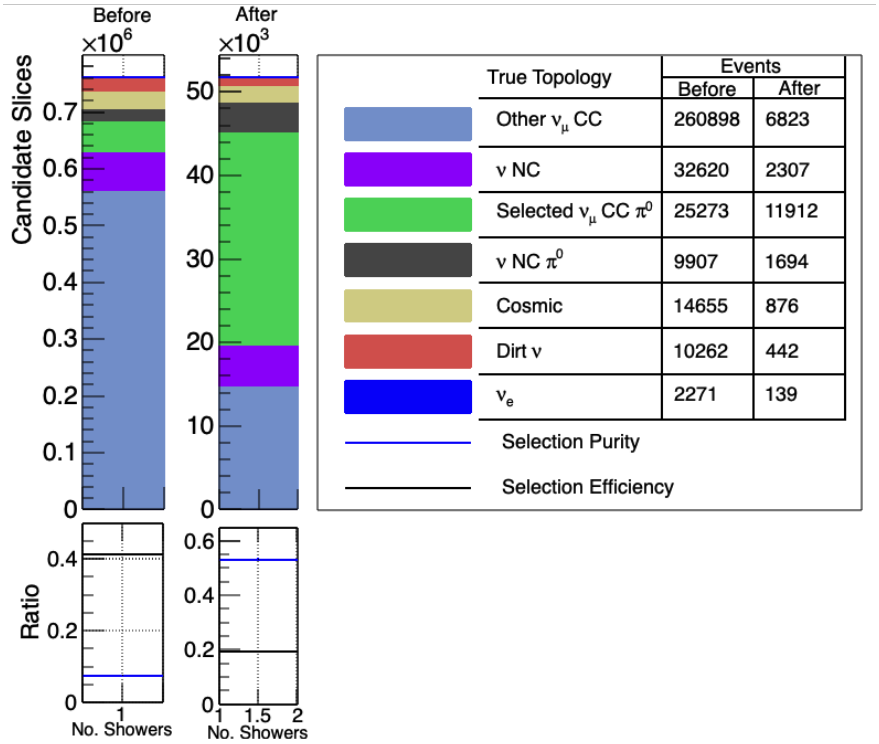

Figure 7.18: Distribution of signal and backgrounds in selected slices with single reconstructed shower before (left) and after (right) applying shower selection cuts.

7.5.2 Slices with Two Reconstructed Showers

In this case, as each slice contains two reconstructed showers, a slice will be selected if at least one of the showers exhibits a high probability of being a photon shower; otherwise, the slice is rejected. Showers meeting the selection criteria are considered as photon showers. A summary of these selection criteria can be found in Table 7.5.

Shower PID	Minimum Value	Maximum Value
Conversion Gap [cm]	0	70
Density [MeV/cm]	1	12
Shower dE/dx (best-plane) [MeV/cm]	1.5	8
Initial Track Width [cm]	0.2	30
Razzle Photon Hypothesis (score)	0.2	1
Razzle Electron Hypothesis (score)	0	0.5
Razzle Other Hypothesis (score)	0	0.8

Table 7.5: Two reconstructed showers selection criteria.

Upon applying these selection criteria in this scenario, the background is significantly reduced, by approximately 85.6%, and constitutes only 33% of the total selected slices after the cuts, as shown in Figure 7.19. The predominant sources of the remaining background

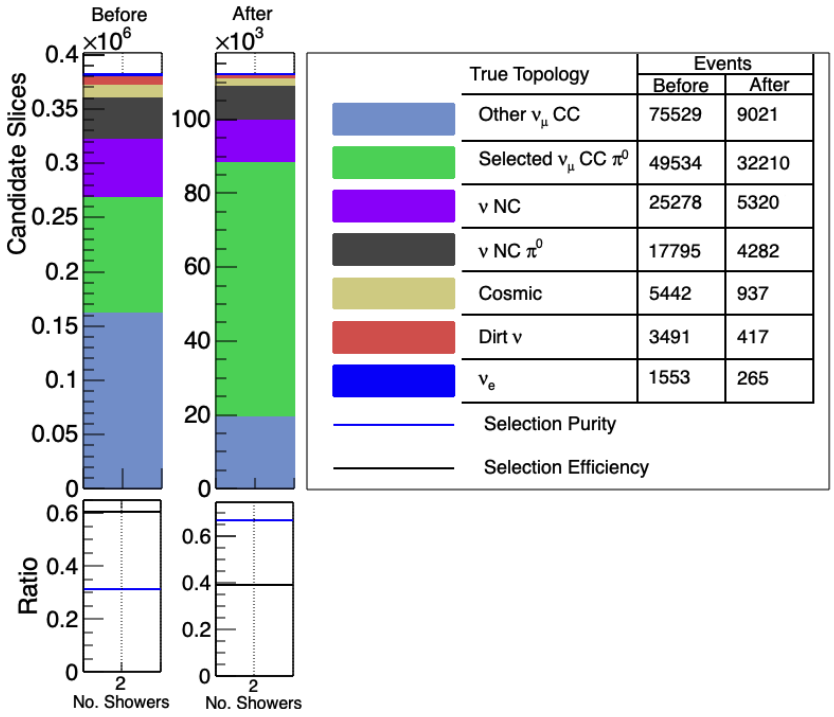

Figure 7.19: Distribution of signal and backgrounds in selected slices with two reconstructed showers before (left) and after (right) applying shower selection cuts.

are other ν_μ CC interactions, accounting for approximately 18.7% of the remaining slices. Additionally, 11% of the background is attributed to NC interactions, with the vast majority of these arising from ν NC π^0 production interactions, constituting around 80.4%. The contributions from cosmic, dirt, and ν_e interactions collectively account for only 3.3% of the selected slices.

7.5.3 Slices with Three or More Reconstructed Showers

Like the case where two showers are reconstructed per slice, a slice is chosen if at least one of the showers demonstrates a high likelihood of being a photon shower. Slices containing showers that satisfy the selection criteria summarised in Table 7.5 are selected.

Shower PID	Minimum Value	Maximum Value
Conversion Gap [cm]	2	70
Shower dE/dx (best-plane) [MeV/cm]	1.5	8
Initial Track Width [cm]	0.15	30
Razzle Photon Hypothesis (score)	0.1	1
Razzle Electron Hypothesis (score)	0	0.5
Razzle Other Hypothesis (score)	0	0.85

Table 7.6: Three or higher reconstructed showers selection criteria.

Following the implementation of these selection cuts, the background was reduced by roughly 76%, resulting in the signal accounting for approximately 68.5% of the total selected slices, as seen in Figure 7.20. The bulk of the remaining background is primarily attributed to other ν_μ CC slices, constituting approximately 15.8% of the 31.4% of remaining slices, with an additional 11.2% originating from ν NC interactions, largely induced from ν NC π^0 interactions. The combined contributions of cosmic, dirt, and ν_e interactions make up just 4.3% of the selected slices.

7.5.4 Summary

In summary, the process of selecting signal events, as defined in Section 7.1, based on shower reconstruction information resulted in an enhancement of the selected slices by approximately 44.1% with an associated efficiency of 56.0%. The most significant reduction in background was observed in other ν_μ CC interactions slices with a decrease of 94.0%, as intended by introducing these cuts. Furthermore, the number of NC slices decreased by approximately 84.6%, resulting in their contribution being 10.9% of the total selected slices. Overall, the

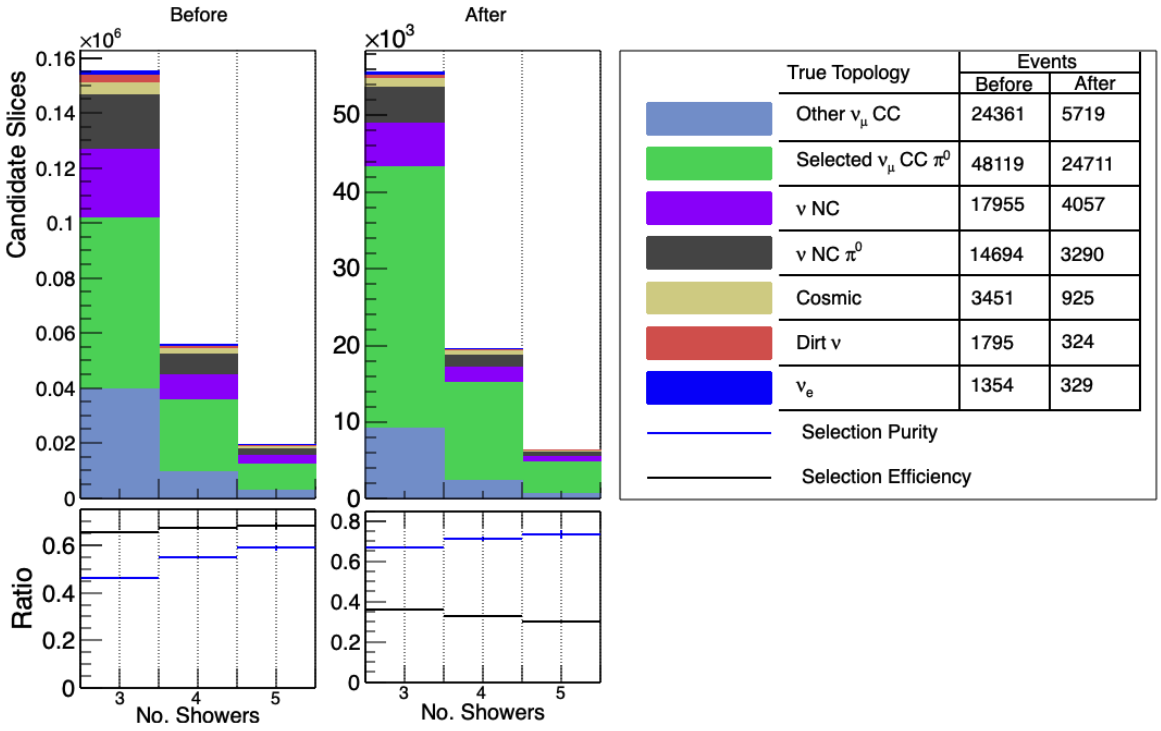

Figure 7.20: Distribution of signal and backgrounds in selected slices with three or higher reconstructed showers before (left) and after (right) applying shower selection cuts.

background was substantially reduced by approximately 92.1%, resulting in the background constituting around 35.5% of the selected slices.

Figure 7.21 shows the distribution of selected slices categorised by their true interaction type in relation to true neutrino energy. The primary background within the selected slices mainly originates from other ν_μ interactions, constituting 20.2% of the total selected slices. Moreover, the second most prominent source of background can be attributed to ν NC π^0 production interactions, posing a challenge in their discrimination from the signal due to their generation of two photon showers, contributing to 8.6% of the overall selected slices. The backgrounds from cosmic and dirt slices account for only 2.5% and 1.1% of the total selected slices, respectively.

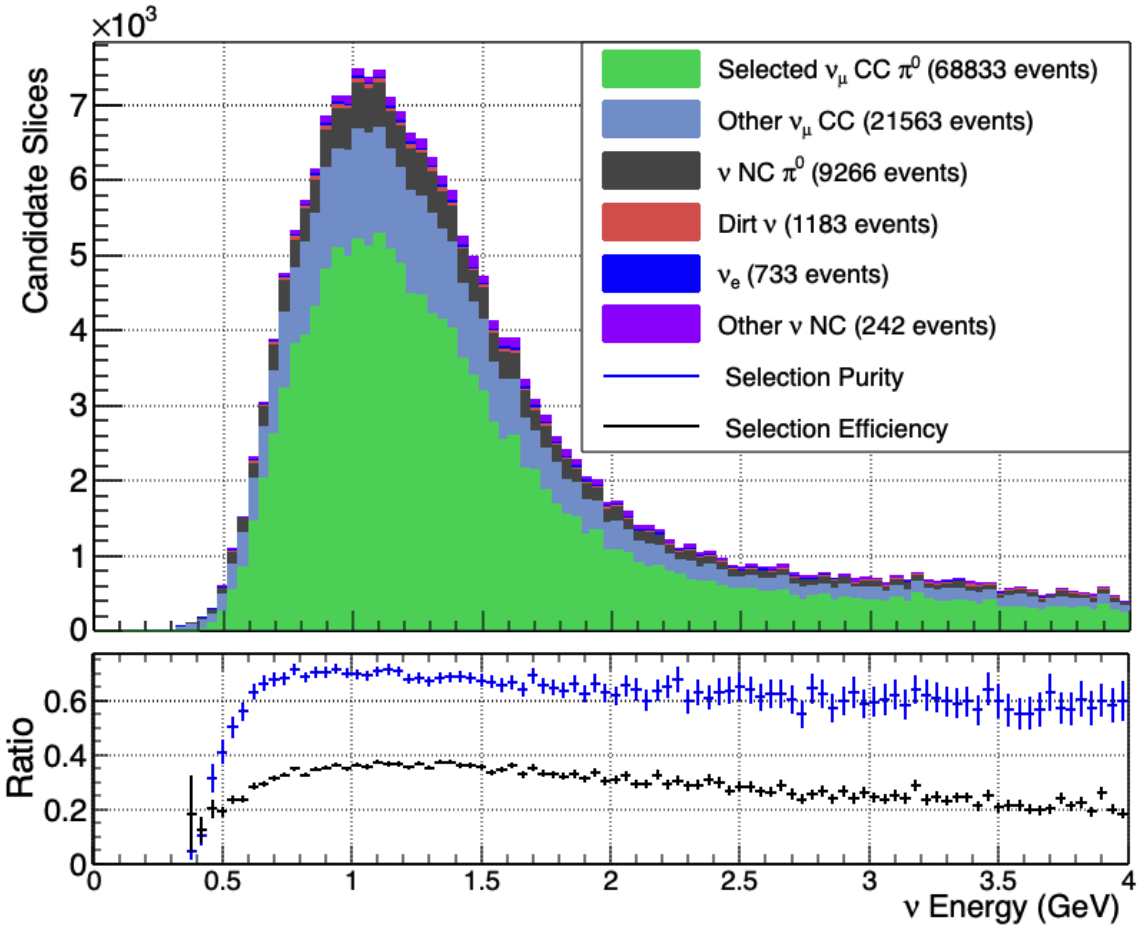

Figure 7.21: Signal and background energy spectrum after π^0 slices selection based on shower reconstruction.

7.6 Final Selection Results

Accurately reconstructing π^0 parameters is essential for studying cross-section measurements related to π^0 production, which relies on precisely reconstructing the leading and sub-leading photon showers from π^0 decay. Therefore, to ensure the validity of the selected signal, the remaining slices that have passed all previous selection criteria are subjected to a final cut based on the reconstructed π^0 energy, as discussed in Section 6.3. This is achieved by applying a cut on the reconstructed shower energy; if there is one reconstructed shower, it must deposit more than 100 MeV, and in the case of two or more reconstructed showers, the sum of the energies of the two showers with the highest energy must be greater than 100 MeV.

Figure 7.22 shows the distribution of reconstructed π^0 energy and invariant mass broken down by true interaction types after applying shower energy selection cuts. Upon implement-

ing this cut, the signal decreased by approximately 8.5%, but it led to an increased purity of the selected slices, reaching 71.0%, while maintaining the quality of the remaining slices. In contrast, backgrounds originating from cosmic, dirt, and other ν_μ CC interactions experienced reductions of 53.6%, 70.1%, and 37.3%, respectively, with a decrease of approximately 15.0% observed in ν NC interactions.

Figure 7.22 illustrates the distribution of reconstructed invariant masses, calculated as described in Section 6.3, for the final selected signal slices. A distinct peak is observed around 123±6 MeV/c^2, closely aligning with the true π^0 mass of approximately 135 MeV/c^2. Additionally, Figure 7.22a shows the distribution of reconstructed π^0 energies for these slices prior to the corrections discussed in Section 6.3, with a discernible cutoff evident at 100 MeV. The purity and efficiency of the selected signal slices are depicted in the ratio plane in both figures.

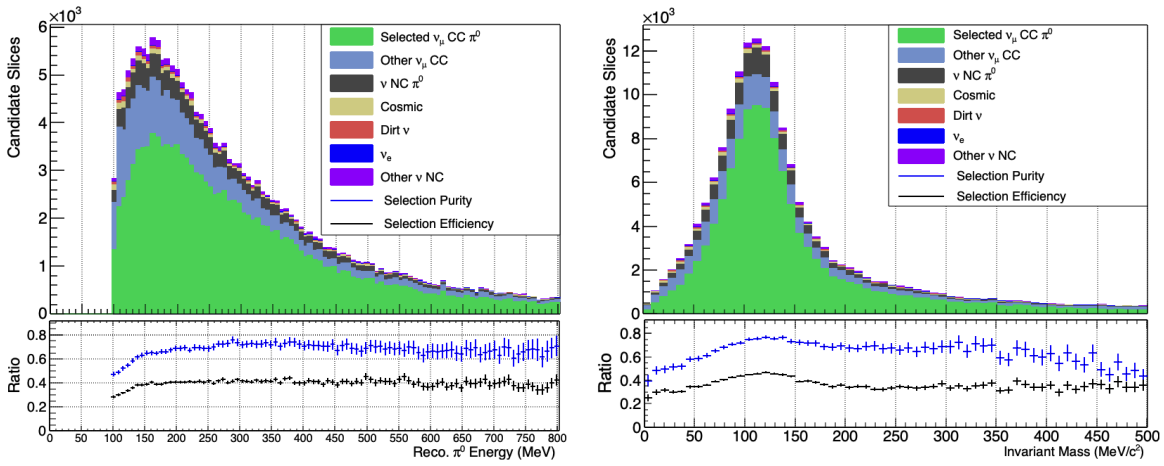

(a) (b)

Figure 7.22: Distribution of reconstructed π^0 energy (a) and invariant mass (b) segmented by true interaction types after applying shower energy selection cuts.

Comparisons of reconstructed versus true energy for π^0, before and after corrections, are shown in Figure 7.23. Figure 7.23a displays the reconstructed energy before applying the correction, along with the expected fit represented by the red line. A noticeable deviation between the reconstructed and true π^0 energy can be seen. However, this deviation is significantly reduced after applying the correction, as shown in Figure 7.23b.

Table 7.7 summarises the purity and efficiency of signal slice selection, as well as the accounted backgrounds within the total slices for each stage of the selection. The final purity of the chosen slices stands at approximately 70.94%, signifying a substantial improvement over the 0.53% at the start of the selection process. On the other hand, the signal efficiency experienced a reduction from 94.0% to 37.1%. This reduction in efficiency can be attributed

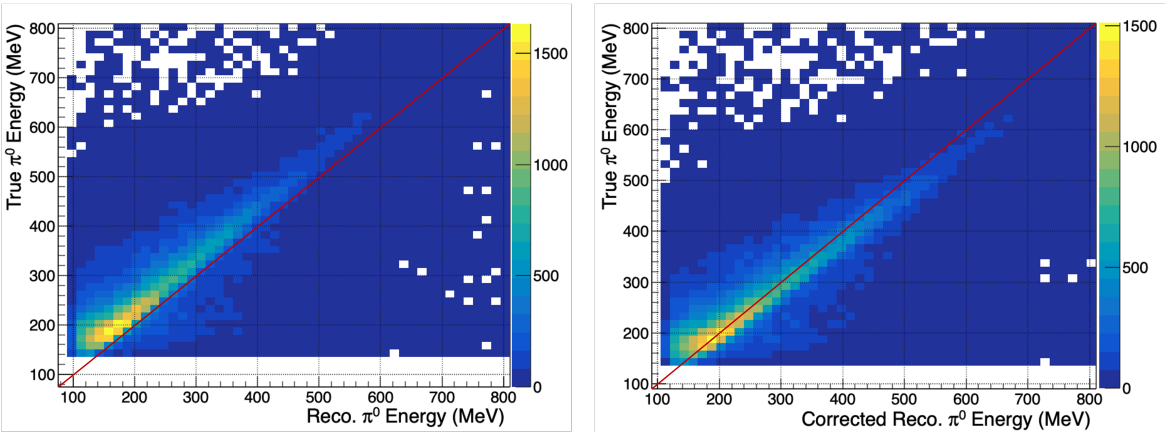

(a) (b)

Figure 7.23: Comparison of reconstructed versus true energy for π^0 before and after correction.

to the FV cuts, which resulted in a decrease of 23.7%, and the subsequent π^0 selection based on reconstructed shower cuts, which further decreased efficiency by 21.9%.

True Type →	$\nu_\mu CC\ \pi^0$		*Other* ν_μ	ν NC	*Other* ν	Cosmics
Cut Type ↓	Purity	Efficiency	Accounted in the selected slices			
Reconstruction	0.53	94.08	95.01	50.04	33.53	-
Pre-Selection	6.79	70.36	20.29	5.88	1.15	65.50
Cosmic Rejection	19.68	66.28	57.06	15.76	2.61	3.78
μ Selection	20.35	62.52	59.74	12.56	2.57	3.89
π^0 Selection	64.49	40.6	20.20	10.94	1.10	2.65
Final Selection	70.94	37.11	15.23	11.20	0.39	1.42

Table 7.7: Purity and efficiency of signal selection with background fraction in total slices.

7.7 Summary

Although the ν_μ CC π^0 production signal accounts for just around 5% of the expected ν interactions within the SBND, the final selected sample achieves a purity of 70.9%, primarily due to the rejection of nearly all cosmic-induced backgrounds. Backgrounds from other ν_μ CC and NC interactions have been significantly reduced by 99.1% and 97.8%, respectively, while maintaining a signal efficiency of 37.1%. These selected events can now be employed for conducting a ν_μ CC π^0 production cross section study, as will be detailed in the upcoming chapter.

Chapter 8

$\nu_\mu + \overline{\nu}_\mu$ CC π^0 Production Cross Section Analysis

The primary objective of this thesis is to evaluate the capability of the Short-Baseline Near Detector (SBND) to perform a measurement of the $\nu_\mu + \overline{\nu}_\mu$ Charged Current (CC) π^0 production cross section. This chapter serves as the conclusion of the efforts detailed in the previous chapters, which involve the reconstruction and selection of these interactions.

First, Section 8.1 provides an overview of the analysis procedure, including details about the simulated input data used in the analysis. Also, this section introduces the mathematical framework for calculating the cross section, outlining the parameters involved in the process. Section 8.2 presents the integration of the Booster Neutrino Beam (BNB) flux for both ν_μ and $\overline{\nu}_\mu$ within the designated Fiducial Volume (FV), as defined in Chapter 7. discussion of the signal and background parameters of the cross section is presented in Section 8.4, followed by an exploration of the efficiency parameters in Section 8.5. Section 8.6 then delves into a discussion of the systematic uncertainties, elucidating the techniques employed, the formalism applied, and the various sources of uncertainty incorporated into the final measurement. Finally, Section 8.7 presents the actual simulated measurement of the cross section, through each stage of the procedure.

8.1 Introduction

Since there is no data yet available from SBND, Monte Carlo (MC) simulation has been employed to generate "fake data", allowing for the simulated measurement of a cross section and the evaluation of associated uncertainties. This simulated dataset comprised two separate samples: BNB and In-time Cosmics samples. The BNB sample contains all neutrino interactions, including dirt interactions, from the Booster Neutrino Beam (BNB) overlaid with cosmics simulated through CORSIKA, as discussed in Section 4.4. This sample consists of 3,560,488 events, corresponding to an exposure of $3.084\,15 \times 10^{20}$ POT, Proton On Target, representing 46.7% of the anticipated event rate over three years of SBND operation.

In the second sample, CORSIKA simulated cosmic events were generated without the presence of neutrino interactions to replicate events that would typically be triggered by in-time cosmic interactions. This sample consists of 417,245 events, which align with 37,475,00 beam spills or equivalent to an exposure of 1.87×10^{20} POT, assuming a standard beam spill intensity of 5×10^{12} POT.

The samples were re-scaled to match the anticipated exposure of 6.6×10^{20} POT, which is equivalent to the expected rate over three years of SBND operation, while appropriately scaling the statistical errors. The BNB sample was used for modelling signal reconstruction and selection processes while the in-time cosmic sample was used to evaluate the extent of background contributions within the final selected sample.

The observed rate of neutrino interactions within a detector, determined by the incoming neutrino flux, cross section, and the number of nuclear targets in the detector, can be represented as follows:

$$N = \Phi \cdot \sigma \cdot n_t \tag{8.1}$$

where N represents the observed interaction rate, Φ the incoming neutrino flux, σ signifies the cross section, and n_t the number of nuclear targets in the detector.

Ideally, if a detector could accurately reconstruct the energy of neutrino, it would be possible to express the cross section measurement in terms of neutrino energy, thereby removing flux dependencies from the observed rate. On the other hand, challenges such as Final State Interactions (FSI), nuclear effects, and limitations in detector capabilities result in imperfect reconstruction and selection processes. Considering the imperfections in these processes, the observed event rate, N, can be expressed as follows:

$$N = \Phi \cdot \sigma \cdot n_t \cdot \varepsilon + N_B \tag{8.2}$$

where Φ and σ represents the integrated flux and cross section, respectively, and n_t the number of target nucleons, ε the signal selection efficiency, and N_B for selected background events. The efficiency, ε is defined as the the ratio of the true number of selected signal events to the total true expected signal events, a quantity that must be estimated through simulations.

To calculate the integrated cross section based on these events, Equation 8.2 can be reformulated to derive Equation 8.3:

$$\sigma = \frac{N - N_B}{\varepsilon \cdot \Phi \cdot n_t} \tag{8.3}$$

The rate, as directly observed by the detector, is predominantly subject to statistical uncertainty resulting from the likelihood of obtaining similar results with repeated measurements. However, the expected background, N_B is influenced by both flux and cross section models, while Φ depends on the flux model. ε is estimated through simulation thus its dependence also extends to the flux and cross section models since it integrates across kinematic variables. Various aspects of these models can similarly impact rate predictions, rendering the interplay among these factors highly complex.

8.2 BNB Integrated Flux

The BNB sample contains neutrino events originating from both the ν_μ and $\overline{\nu}_\mu$ fluxes. These fluxes are estimated through MC simulation, as outlined in Chapter 4, with each flux calculated individually and presented as the number of neutrinos per square centimetre and scaled to the expected 6.6×10^{20} [187]. The total flux passing through the Fiducial Volume (FV) as defined in Section 7.2.2 is illustrated in Figure 8.1, separated for ν_μ and $\overline{\nu}_\mu$. This highlights the predominance of ν_μ (in Blue) over $\overline{\nu}_\mu$ (in red), as outlined in Chapter 4. The integrated flux can be calculated by integrating over the ν_μ and $\overline{\nu}_\mu$ fluxes and scaled to the expected 6.6×10^{20} POT, as shown in Figure 8.1, using:

$$\Phi = POT \cdot \int_{E_{Low}}^{E_{High}} \Phi_E dE \tag{8.4}$$

where Φ_E represents the flux at a specific energy level, with E_{High} being defined as the energy where the flux spectra are integrated up to its peak. The maximum energy in the flux utilised is 5 GeV, which significantly exceeds the energies of the highest selected events and remains several MeV above the point where the flux effectively becomes negligible. E_{Low} is set at the minimum value within the simulated flux range, 0 MeV. Within this energy range, 0 to 5 GeV, the count of ν_μ and $\overline{\nu}_\mu$ times POT per cm^2 in the BNB beam is calculated as follows:

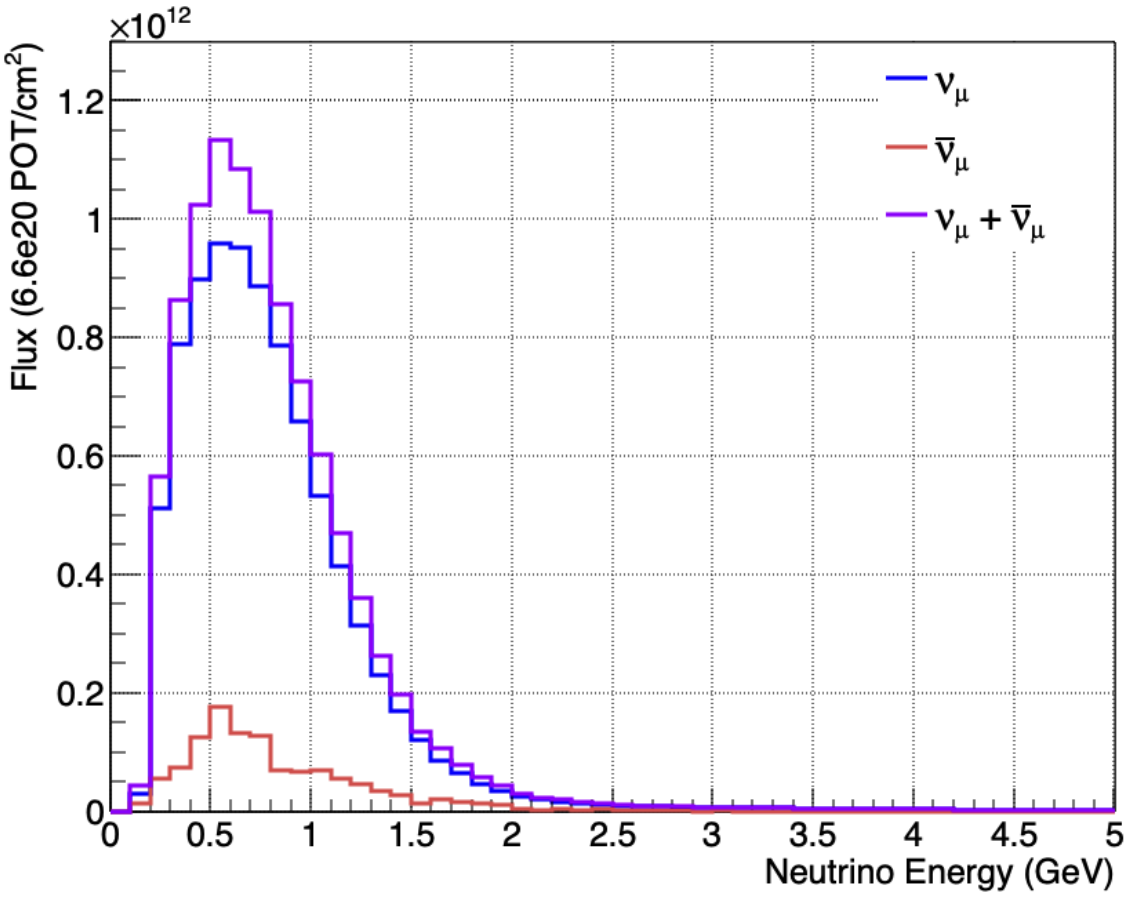

Figure 8.1: Estimation of ν_μ (in Blue) and $\overline{\nu}_\mu$ (in Red) and their combination (in Violet) flux at the front face of SBND FV based on the true neutrino energy.

$$\begin{aligned} \Phi_{\nu_\mu} &= 8.66033 \times 10^{12} cm^{-2} \ (for \ \ 6.6 \times 10^{20} \ POT), \\ \Phi_{\overline{\nu}_\mu} &= 1.15464 \times 10^{12} cm^{-2} \ (for \ \ 6.6 \times 10^{20} \ POT). \end{aligned} \tag{8.5}$$

Hence, the total integrated flux from both fluxes is $\Phi_{\nu_\mu+\overline{\nu}_\mu} = 9.81497 \times 10^{12} \ cm^{-2}$, corresponding to the expected exposure of 6.6×10^{20} POT. An overall normalisation uncertainty related to this integrated flux will arise because of systematic uncertainties in the flux prediction, which will be elaborated upon in Section 8.6.

8.3 Number of Target Nucleons

The determination of the count of target nucleons takes into consideration the dimensions of the detector as the material interacting with incoming particles. The assumption is made

that the whole detector volume is composed solely of argon nuclei, and the average density is considered representative of the entire FV. The number of the target nucleons, n_t can be calculated using standard approach:

$$n_t = \frac{N_{Ar} \cdot M_{det}}{M_{Ar}} = \frac{N_{Ar} \cdot V_{det} \cdot \rho_{Ar} \cdot N_A}{m_{mol}} \tag{8.6}$$

where N_{Ar} is the number of nucleons within an argon nucleus, V_{det} is the Fiducial Volume (FV) of the detector, which is defined in Section 7.2.2, ρ_{Ar} is the density of liquid argon, N_A is Avogadro number, and m_{mol} signifies the number of grams per mole of argon. The parameters required for computing the quantity of target nucleons can be found in Table 8.1.

Parameter.	Value
N_{Ar}	40.0
V_{det}	6.2604×10^7 cm^3
ρ_{Ar}	1.40 g/cm^3 [267]
N_A	6.022×10^{23} molecule/mol
m_{mol}	39.95 g/mol

Table 8.1: List of Parameters Utilised for Target Nucleon Count Calculation.

Hence, the complete count of target nucleons is determined using Equation 8.7:

$$n_t = \frac{40.0 \times 6.2604 \times 10^7 \times 1.40 \times 6.022 \times 10^{23}}{39.95} = 5.28 \times 10^{31}. \tag{8.7}$$

The accuracy of the target nucleon count can be subject to uncertainties arising from a limited understanding of the actual detector mass. Specifically, the Space Charge Effect (SCE), discussed in Section 3.3, affects ionised electrons by shifting or delaying their arrival at the anode plane. This effect can reduce the effective detector volume, potentially leading to inaccurate estimations of the true mass. While the current simulation corrects for this effect, potential flaws in the correction process can introduce residual uncertainties. As of the time of writing, only the nominal SCE is included in the simulation, and systematic variations are not available, which means this uncertainty is not considered in this study.

8.4 Signal and Background

The input value in the numerator of the cross section formula corresponds to the count of signal events identified in the sample. This count is calculated by subtracting the estimated number of background events, N_B, from the total number of selected events, N. The background events can be categorised into two distinct groups: on-beam and off-beam. The former refers to events linked to neutrino beam activity, such as ν Neutral Current (NC), other ν_μ Charged Current (CC), ν_e, and dirt events. In contrast, off-beam backgrounds include events unrelated to the neutrino beam, specifically cosmic backgrounds.

Off-beam Backgrounds can be assessed by collecting data when the beam is not active, eliminating systematic errors related to background modelling and detector performance, resulting in off-beam backgrounds having only statistical uncertainties. Conversely, on-beam backgrounds cannot be isolated from the signal in a similar way, requiring the use of MC simulations or side-bands to predict their expected rate, with this analysis focusing solely on the former. Thus, modelling these backgrounds introduces associated systematic uncertainties.

Apart from Poissonian uncertainty related to selected background interactions, there is an extra uncertainly because of limited statistics. This stems from the understanding of the actual count of backgrounds being constrained by the finite number of background interactions that are represented, whether through simulation or by using anti-coincidence data for on-beam and off-beam cases. Typically, this uncertainty is mitigated by generating a substantially larger number of backgrounds than anticipated from the data, thereby decreasing this error when combined with the Poissonian uncertainty.

In the process of cross-section computation, it is imperative to ascertain the selected signal. This is achieved through subtraction of background events from the overall count of selected events, as described in Equation 8.3. The estimation of the absolute expected background count is conducted through a detailed analysis of the selection process employing the MC sample, as discussed in Chapter 7.

A detailed breakdown of the selected events, as discussed in Chapter 7, categorised by their true types and scaled to the on-beam POT of 6.6×10^{20} POT, is provided in Table 8.2. The accounting of each type within the total selected events is provided in the 'Percentage' column of Table 8.2. The incorporation of statistically calculated Poissonian uncertainties for each individual component, is presented in the last column.

Component		Events Selected	Percentage (%)	Stat. Error (Events)
Signal (ν_μ CC π^0)		139023	67.16	236.17
Background	Other ν_μ CC	37896.8	18.30	217.63
	ν NC	22959.8	11.08	244.07
	ν_e	1352.46	0.65	363.74
	Dirt	1688.44	0.81	229.51
	Cosmic	4070.23	1.96	292.70
Total		206990	100	237.404

Table 8.2: Breakdown by true type of signal and background counts normalised to the on-beam POT of 6.6×10^{20} POT, the details of which are discussed in Chapter 6.

8.5 Efficiency

The efficiency, as ε, is determined by comparing the count of correctly identified events to the total number of true signal events within the sample, is presented as a function of reconstructed π^0 energy in Figure 7.22a. Table 8.3 presents the counts for both ν_μ and $\overline{\nu}_\mu$ CC π^0 events, both in terms of those that were correctly identified (selected) and the overall total.

Int. Type	Selected Events	True Events	Efficiency
ν_μ CC π^0	122668	310970	39.44%
$\overline{\nu}_\mu$ CC π^0	16355	41460	39.44%
ν_μ and $\overline{\nu}_\mu$ CC π^0	139023	352430	39.44%

Table 8.3: Number of selected signal and true signal events for an exposure of 6.6×10^{20} POT.

The Statistical uncertainty related to the efficiency depends on the total count of true events and can be computed using:

$$\sigma_\varepsilon = \left(\frac{1}{\sqrt{N_s}} \cdot \sqrt{\varepsilon \cdot (1-\varepsilon)} \right) \tag{8.8}$$

where N_s represents the true signal events number and ε the efficiency.

Conducting this calculation results in an efficiency uncertainty of $\sigma_\varepsilon = 0.082\%$, resulting in an efficiency of $39.44\% \pm 0.082\%$, which is negligible in comparison to the other statistical and systematic uncertainty as discussed in the next section.

8.6 Systematic Uncertainties

To assess systematic uncertainties in a physics measurement, multiple samples can be simulated, each with a specific parameter adjusted within its uncertainty range. These samples help identify any variations or distortions in the measurement across different parameter settings. However, simulating and reconstructing many events for each parameter variation is computationally costly. Hence, an approach called "re-weighting" assigns event weights based on adjusted parameters, efficiently recovering the desired distribution and reducing computational costs [3].

Reweighting leverages the characteristics of Monte Carlo generators, as outlined in Section 4.4, where events are randomly generated and retained based on a calculated probability using the cross section model. Each event is assigned a weight corresponding to its likelihood of occurring. When model parameters are adjusted, event probabilities change, allowing for weight modifications without the need to generate new events [268]. The reweighting process commences with an initial physics parameter P and converts it into a modified form, denoted as P', as defined in Equation 8.9:

$$P \to P' = P\left(1 + x_p \frac{\delta P}{P}\right) \tag{8.9}$$

where the standard deviation of parameter P is represented as δP, and x_p indicated the number of standard deviations by which the parameter is shifted. When $x_p = 0$, it signifies the original unweighted parameter.

In the context of neutrino interactions, the cross section σ_p determines the interaction likelihood. Consequently, a weight is assigned to a neutrino interaction to reflect its increased or decreased likelihood of occurring due to a modification of x_p applied to the input parameter P. Applying this weight to all simulated neutrino interactions allows for the generation of an event distribution as if it were produced with the specified input parameter adjustment, assuming the sample has adequate statistics and covers the relevant phase space.

The influence of a specific uncertainty on an experiment measurement can be evaluated by multiple "universes" are generated by randomly varying an input parameter according to a unit Gaussian distribution (with $\mu = 1$, $\sigma = 1$). Weights are calculated for each neutrino in

every universe, and the variations and potential biases in the physics measurement across these universes quantify the impact of the parameters on the measurement.

When multiple systematic parameters are adjusted, their combined effect can be assessed by multiplying the weights is each universe, effectively adding their uncertainties in quadrature. This approach enables a thorough assessment of systematic parameter impacts without the computational burden of multiple sample simulations. Yet, systematic parameter adjustment might not always translate directly to probabilities, as mentioned earlier. In specific cases, such as hadronic scattering within the nucleus, reweighting can still be employed, affecting the Mean Free Path (MFP) [3].

Unlike the cross sections, the MEP does not directly represent the interaction probability. The interaction probability, P, for hadrons within the nucleus is determined from MEP and the distance they need to traverse to exit the nucleus. Thus, the calculation of the weight assigned to a neutrino interaction depends on if the hadron interacts or remains intact in the nominal simulation.

Reweighting might not be possible in other cases, and rerunning the simulation and reconstruction becomes necessary. For instance, when simulating detector effects like wire noise, it might be possible but challenging to assess whether a specific energy deposition will be reconstructed as a hit. Even if individual hit weights can be determined, the impact of removing a single hit on reconstruction stages, as discussed in Chapter 5 and 6, cannot be analytically calculated. Hence, for each systematic variation, downstream reconstruction still necessitates running, incurring substantial computational cost.

The evaluation of uncertainty effects can be performed using a covariance matrix, which is constructed using a set of observations N, as defined:

$$V_{ij} = \frac{1}{U}\sum_{n}^{U}(N_i^n - N_i^{CV})(N_j^n - N_j^{CV}) \tag{8.10}$$

This matrix captures the typical deviation between values in bins i and j from the Central Value (CV) across U universes, labelled as n. The diagonal terms indicate the variance in each bin and are subsequently utilised to calculate the errors ($\sigma_i = \sqrt{V_{ii}}$). This presumes that the CV, obtained as the mean across the universes, aligns with the nominal value employed in simulations, which is typically accurate. However, for flux uncertainties, as discussed later in this section, this alignment does not hold. Therefore, the total error matrix E_{ij} can be broken down into distinct bias and resolution matrices, with the resolution matrix representing the standard covariance matrix.

$$E_{ij} = V_{ij}^{Bias} + V_{ij}^{Resolution} \tag{8.11}$$

where V_{ij}^{Bias} signify the deviation from the nominal value and the CV and given as:

$$V_{ij}^{Bias} = (N_i^{Nom} - N_i^{CV})(N_j^{Nom} - N_j^{CV}) \tag{8.12}$$

and $V_{ij}^{Resolution}$ represents the variation around the CV across the universes, as outlined in Equation 8.13:

$$V_{ij}^{Resolution} = \frac{1}{U}\sum_{n}^{U}(N_i^n - N_i^{CV})(N_j^n - N_j^{CV}) \tag{8.13}$$

The overall error matrix is calculated by combining the individual covariance matrices from various sources, effectively summing up the errors in a quadrature:

$$E_{ij} = E_{ij}^{Flux} + E_{ij}^{Genie} + E_{ij}^{Stat} + ... \tag{8.14}$$

Additionally, a fractional covariance matrix can be used to assist in visualising uncertainties, depicting the proportional error in each bin, facilitating comparisons between bins with varying numbers of entries:

$$V_{ij}^{Fraction} = \frac{V_{ij}}{N_i^{Nom}\, N_j^{Nom}} \tag{8.15}$$

Three main sources of systematic errors impact SBND measurements: detector, flux, and interaction. Reweighting techniques from MiniBooNE and GENIE can assess flux and interaction systematics [233, 3]. However, detector systematics, which cannot be reweighted, require separate simulations, as discussed above, which SBND currently lacks the resources to conduct. Additionally, the SBND simulation chain has yet to incorporate the latest detector simulation models from other LArTPCs, making a production campaign difficult to justify. As a result, the simulated cross section measurement undertaken in this work excludes detector systematics but should be considered in future work. Details of the flux and interaction systematics are covered in the following sub-sections.

8.6.1 Flux Systematic

Utilising the identical neutrino beam as other experiments like MiniBooNE and MicroBooNE offers advantages, including extensive studies on the neutrino flux and its associated uncertainties [233, 269]. MicroBooNE reported various factors contributing to the overall flux uncertainty, which were reassessed for the SBND flux. Table 8.4 provides an overview of

the parameters subjected to variation during flux reweighting; the reweighting effect on the selected events is presented Appendix A, including:

- Horn Magnetic Field: Magnetic field uncertainties in the horn affect charged particle focusing from the target. These uncertainties include the horn current and induced surface "skin current" on the target are modelled.
- Hadronic Interactions: Interactions of hadrons in the target, whether elastic or inelastic, before exiting can impact both kinematics and neutrino production numbers. These interaction cross sections uncertainties influence the neutrino flux prediction.
- POT: Toroid measurements of delivered protons have a 2% calibration uncertainty affecting the flux normalisation.

Parameter	Method	σP/P (Plot)
Horn Current	FU	$\pm$1kA (FIG A.1a)
Skin Current	FU	On/Off (FIG A.1b)
σ_{π^+}	CSV	[269] (FIG A.1c)
σ_{π^-}	CSV	[269] (FIG A.1d)
σ_{K^+}	FS	[269] (FIG A.2a)
σ_{K^-}	N	$\pm$100% (FIG A.2b)
σ_{K^0}	SW	[269] (FIG A.2c)
σ^{π}_{Tot}	FU	$\pm$11.9 mb (FIG A.2d)
σ^{π}_{QE}	FU	$\pm$11.2 mb (FIG A.2e)
σ^{π}_{Ine}	FU	$\pm$10 mb (FIG A.2f)
σ^{n}_{Tot}	FU	$\pm$15 mb (FIG A.3a)
σ^{n}_{QE}	FU	$\pm$20 mb (FIG A.3b)
σ^{n}_{Ine}	FU	$\pm$5 mb (FIG A.3c)
POT	N	2% [233]

Table 8.4: Systematic uncertainties in BNB Flux Simulation.

The initial approach to establish simulated the flux model parameters often influenced subsequent reweighting methods, as following:

- Flux Unisim (FU): Physics parameters is modified in different universes by applying Gaussian distributions or single values at $\pm 1\sigma$, followed by recalculating event weights.

- Central Spline Variation (CSV): Central value predictions is compared to varied spline fits of smeared pion cross section data, generating interaction weights based on the parent particle of the neutrino.

- Feynman Scaling (FS): Extrapolation of kaon cross section measurements into data-sparse regions via FS. Coefficients in the scaling is adjusted within correlated uncertainties, resulting in new weights.

- Sanford-Wang (SW): Smeared parameters from the SW fit to data is used to generate event weights be fitting the parameters to E910 and KEK data [233].

- Normalisation (N): A normalisation uncertainty is applied and propagated to event weights

Figure 8.2 shows the impact of uncertainties on the predicted $\nu_\mu + \overline{\nu}_\mu$. It contrasts the nominal flux prediction (in red) devoid of uncertainties with the flux prediction generated from a thousand systematic universes (in blue), wherein all parameters are subjected to random variations. The CV is shown in blue, with errors indicating the standard deviation across the universes, computed using a covariance matrix. At the ratio plane, the fractional uncertainty through the universes, known as resolution, is depicted by the blue line.

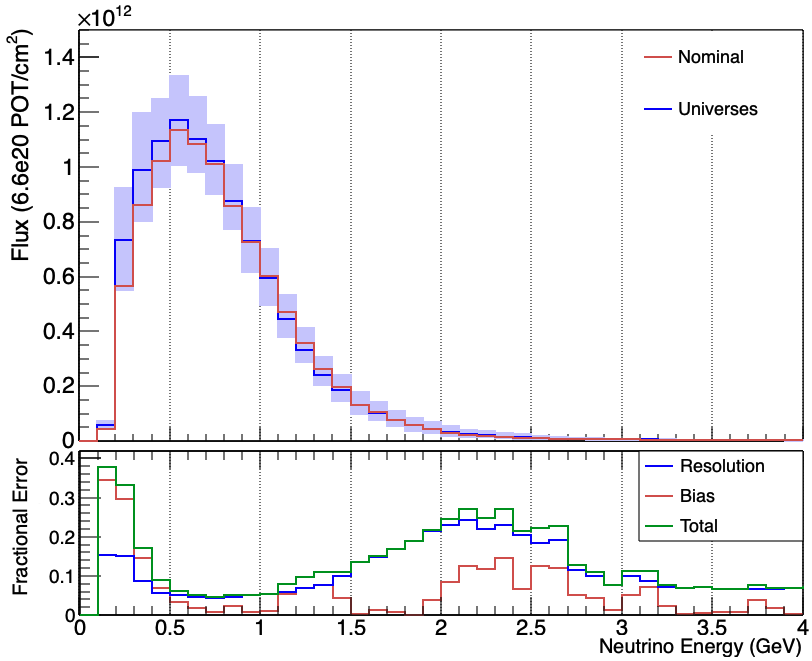

Figure 8.2: Predicted ν_μ and $\overline{\nu}_\mu$ flux in SBND FV, nominal (Red) vs. reweighted universes (Blue), with fractional uncertainty shown at the bottom.

Normally, the nominal simulation and CV of the universes should align, as observed at high energy. Nevertheless, variations arise due to disparities between the SW parameterisation employed in the nominal flux and the fitted splines in the universes, leading to notable distinctions, particularly in the uncertainty associated with π^+ [233]. Therefore, a second bias term (Red) is included in the uncertainties, which is combined in quadrature with the resolution to obtain the total systematic uncertainty (Green).

The effect of this uncertainty on SBND predicted event rate is shown in Figure 8.3. The signal definition, requiring the selected photon showers energies above 100 MeV (as discussed in Chapter 7), minimises the bias effect concentrated at low neutrino energy. As a result, the event rate is primarily influenced by the resolution, with the largest impact at high energy. The total flux uncertainty on the event rate is 9.7%, with contribution of 4.8% from bias and 8.5% from resolution terms.

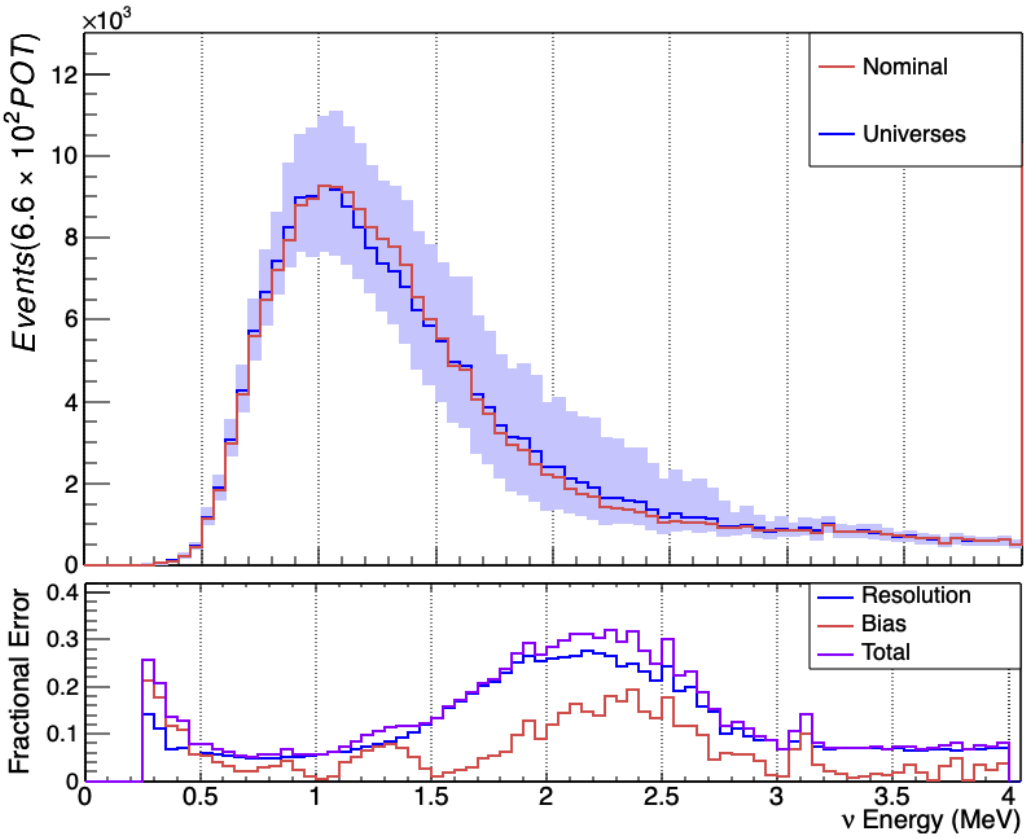

Figure 8.3: The distribution of selected events with flux systematic errors, including fractional uncertainty across universes shown below, split into resolution and bias, added in quadrature for the total.

These flux systematic uncertainties similarly impact the integrated flux used for cross-section calculation. Figure 8.4 shows the distribution of integrated flux through a one

thousand universes in blue, while the red line represents the nominal prediction. The difference between the SW parameterisation employed in the nominal simulation and the splines utilised in the universes is evident in the histogram centre offset from the red line. This bias has been incorporated into the overall systematic uncertainty in the total flux, as previously discussed, which amounts to 9.7%.

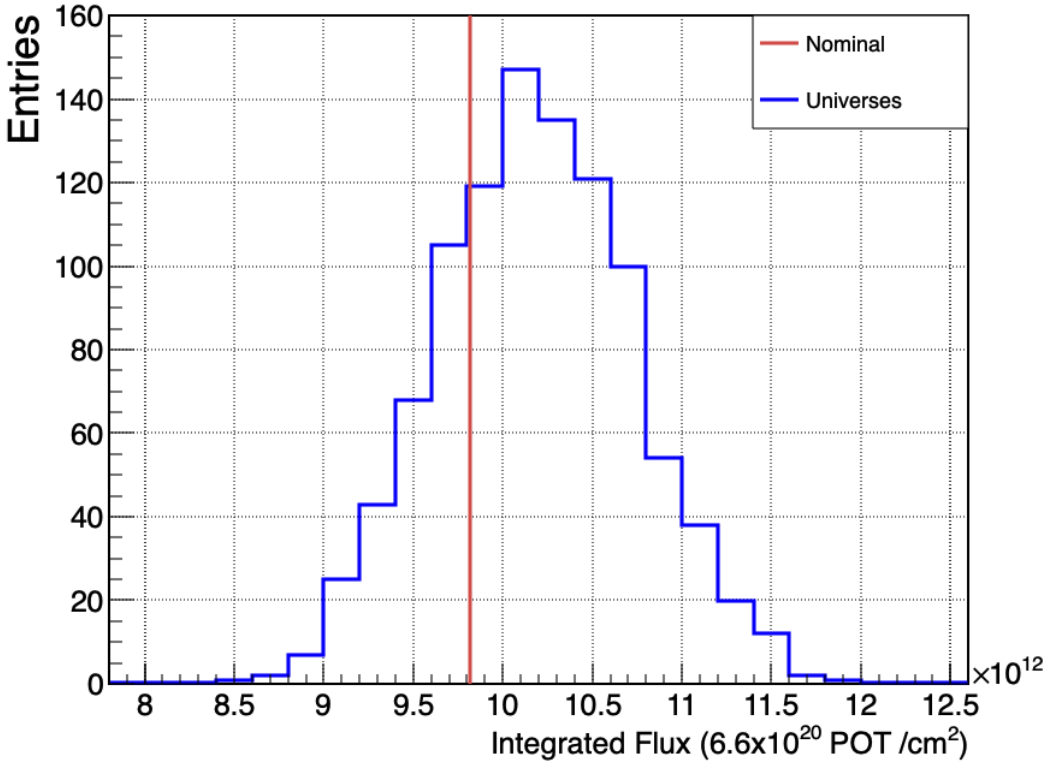

Figure 8.4: Total Flux in SBND fiducial volume for nominal (Red) versus reweighted universes (Blue) for 6.6×10^{20} POT.

8.6.2 Interaction Systematic

Much like the flux simulation, the GENIE generator offers a set of adjustable parameters and a framework for reweighting these parameters [3]. The systematic uncertainties of interaction employed can be found in Appendix B.1.

The impact of interaction systematics on event rates is shown in Figure 8.5. In contrast to flux uncertainties, the bias between the nominal and CV simulations is insignificant, with uncertainties primarily driven by the resolution term. These uncertainties are negligible at low energy but remain significant throughout the rest of energy range, higher than 600 MeV.

The integrated rate uncertainty is 11.9%, with a minor 2.0% from bias and the remaining from resolution (11.8%).

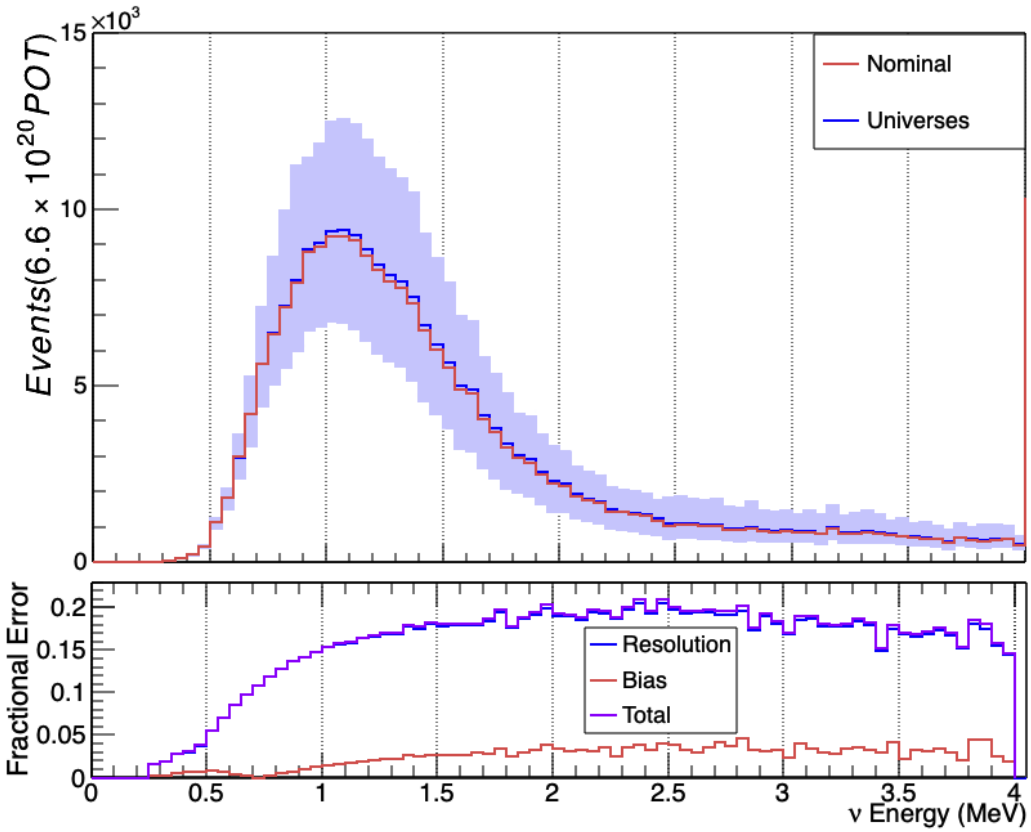

Figure 8.5: The distribution of selected events with genie systematic errors, including fractional uncertainty across universes shown below, split into resolution and bias, added in quadrature for the total.

Finite simulation statistics can introduce uncertainty in efficiency and background estimations due to Poissonian limitations. To minimise this, experiments often simulate a much larger number of events than expected in the data, surpassing data statistical uncertainties. However, due to production constraints, this analysis uses a fraction of the total expected events compared to the final target. Measuring the finite statistics impact would reflect the current uncertainty sample, not the ultimate one SBND will have with data. Therefore, this uncertainty was not considered in this analysis due to its limited utility.

Table 8.5 shows the total uncertainty associated with the integrated cross section. Interaction related uncertainties are the most influential among the various sources of systematics, primarily attributed to axial mass for CC resonance production. However, the flux related systematics also make a notable contribution, mainly through the normalisation uncertainty.

In contrast, the statistical uncertainty in the integrated rate is minimal compared to the systematic uncertainties.

Source	Uncertainty
Interaction	11.97%
Flux	9.79%
POT	2.0%
Total Systematic	15.59%
Statistical	0.16%
Total Uncertainty	15.59%

Table 8.5: Contributions to integrated cross section errors, both systematic and statistical.

Figure 8.6 presents the impact of the total systematic uncertainty on the purity and efficiency of the selected events. As observed in the fractional error plane, the total systematic uncertainty is primarily concentrated at low neutrino energies, specifically below 500 MeV, and is primarily attributable to the resolution factor, affecting both the purity and efficiency of selected events. However, at higher energies, purity is more significantly influenced by systemic uncertainties in comparison to efficiency, where the impact of these uncertainties is negligible.

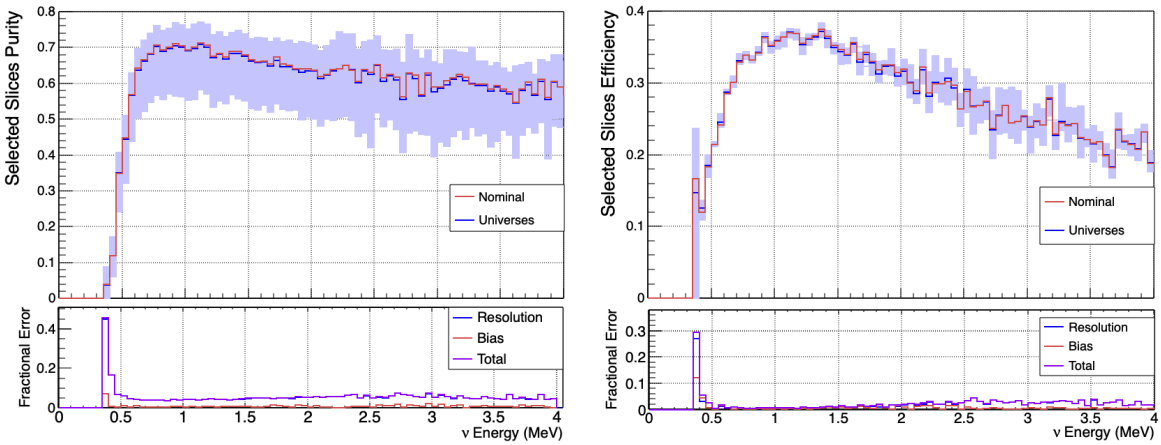

(a) (b)

Figure 8.6: The purity and efficiency of the selected events with total systematic uncertainties, including the fraction error throughout universes shown below, split into resolution and bias, added in quadrature for the total.

Overall, both systematic and statistical uncertainties exert an influence on the selected signal and, consequently, the calculation of the cross-section measurement. Approximately 99%, as indicated in Table 8.5, of these uncertainties are attributed to the systematic component. This impact is particularly pronounced for neutrinos with low energy, as illustrated in Figure 8.6.

8.7 Cross Section Calculation

Incorporating the components established in the previous sections, a prediction of the integrated cross section of ν_μ and $\overline{\nu}_\mu$ CC π^0 production can be calculated. This section includes cross section projections utilising exclusively MC signal events based on true information from the generator, as well as the observed cross section derived from simulated reconstructed data.

Utilising Equation 8.3, the cross section extracted by GENIE for the charged-current π^0 channel on argon, under ideal conditions where $\varepsilon = 1$, $N_B = 0$, and $N = N_S$, can be expressed as:

$$\begin{aligned} \sigma^{True}_{CC\pi^0} = \frac{N - N_B}{\varepsilon \cdot \Phi \cdot n_t} &= \frac{352420 - 0}{1 \times 9.81 \times 10^{12} \times 5.28 \times 10^{31}} \\ &= (6.8 \pm 0.001) \times 10^{-40} \ \frac{cm^2}{nucleon} \end{aligned} \tag{8.16}$$

The statistical uncertainty associated with $\sigma^{True}_{CC\pi^0}$ is directly related to the uncertainty in the count of signal events. The cross section based on the reconstructed parameters can be calculated in a similar manner as follows:

$$\begin{aligned} \sigma^{Reco}_{CC\pi^0} = \frac{N - N_B}{\varepsilon \cdot \Phi \cdot n_t} &= \frac{352420 - 67967}{0.394 \times 9.81 \times 10^{12} \times 5.28 \times 10^{31}} \\ &= (6.81 \pm 1.07) \times 10^{-40} \ \frac{cm^2}{nucleon} \end{aligned} \tag{8.17}$$

The statistical uncertainty associated with $\sigma^{Reco.}_{CC\pi^0}$ arises from both systematic and statistical uncertainties, as detailed in Table 8.5. The result are within statistical uncertainty of the true calculated cross section above. Comparing the central values of the MC^{True} and fake data cross sections reveals difference of approximately 0.14%, demonstrating that there is no obvious bias due to the analysis.

8.8 Summary

The procedure for deriving the integrated cross section analysis of ν_μ $\overline{\nu}_\mu$ CC π^0 production has been presented. This analysis represents a step towards calculating the differential cross section, which can be achieved by applying folded and unfolded approaches to establish the relationship between observed and true quantities. This study incorporates both statistical and systematic uncertainties, resulting in uncertainties of 0.16% and 15.59%, respectively, contributing to a total uncertainty of 15.59% for the integrated measurement. Detector systematics are not included in this analysis due to their unavailability at the time of writing. Comparative evaluations between the true MC cross section (MC^{True}) and the reconstructed MC cross section ($MC^{Reco.}$) derived from the nominal GENIEv3 model demonstrate good agreement. Future improvements in reconstruction and selection, as well as in-situ constraints on flux and backgrounds, can further increase the achieved discriminating power.

Chapter 9

Development of LArPixel Charge Readout

As mentioned in Chapter 4, the Short-Baseline Near Detector (SBND) aims to test new liquid argon readout techniques for DUNE. SBND, a wire-based LArTPC prototype for the Deep Underground Neutrino Experiment (DUNE) far detector, raises concerns about near detector pile-up. With an estimated 0.2 interactions/tonne/spill 574 m downstream of the 2 MW beam, simultaneous events could create wire readout ambiguities. To address this, pixelated readouts with extra degrees of freedom are being explored and tested at the University of Sheffield's liquid argon research test stand.

This chapter presents an evaluation of the Sheffield LAr test stand, a cryogenic system used to test the performance of the LArPixel charge readout system. The test stand comprises four main systems, including the LAr dewar, purification system, condenser system, and detection system. The evaluation was conducted on individual systems, subgroups, and groups to ensure that they functioned as intended. Specifically, we assessed the components within the LAr dewar, conducted leak tests, evaluated external CRTs, tested the pixel-readout equipment and connection up to the pixel board, and performed a successful argon recirculation test. Based on engineering studies, we determined that a two to three weeks long run is achievable to evaluate the pixel readout system. This chapter provides a summary of our findings and the overall performance of the Sheffield LAr test stand.

9.1 The Sheffield LAr Test Stand for Pixel Development

The Sheffield LAr test stand for pixel development, or LArPixels test stand, comprises a sealed cryogenic vessel in which test pixel planes can be mounted in both liquid and gaseous argon. A key feature is the provision of continuous recirculation of argon through a filtration system to remove oxygen and water impurities in the gas phase. The cryogenic system

was designed by Brookhaven National Laboratory (BNL) [270] and consists of four main sub-systems: liquid argon (LAr) dewar, purification system, condenser system and detection system. These systems are described in detail in the following sections and shown in a schematic diagram and a photograph in Figure 9.1 and Figure 9.2, respectively.

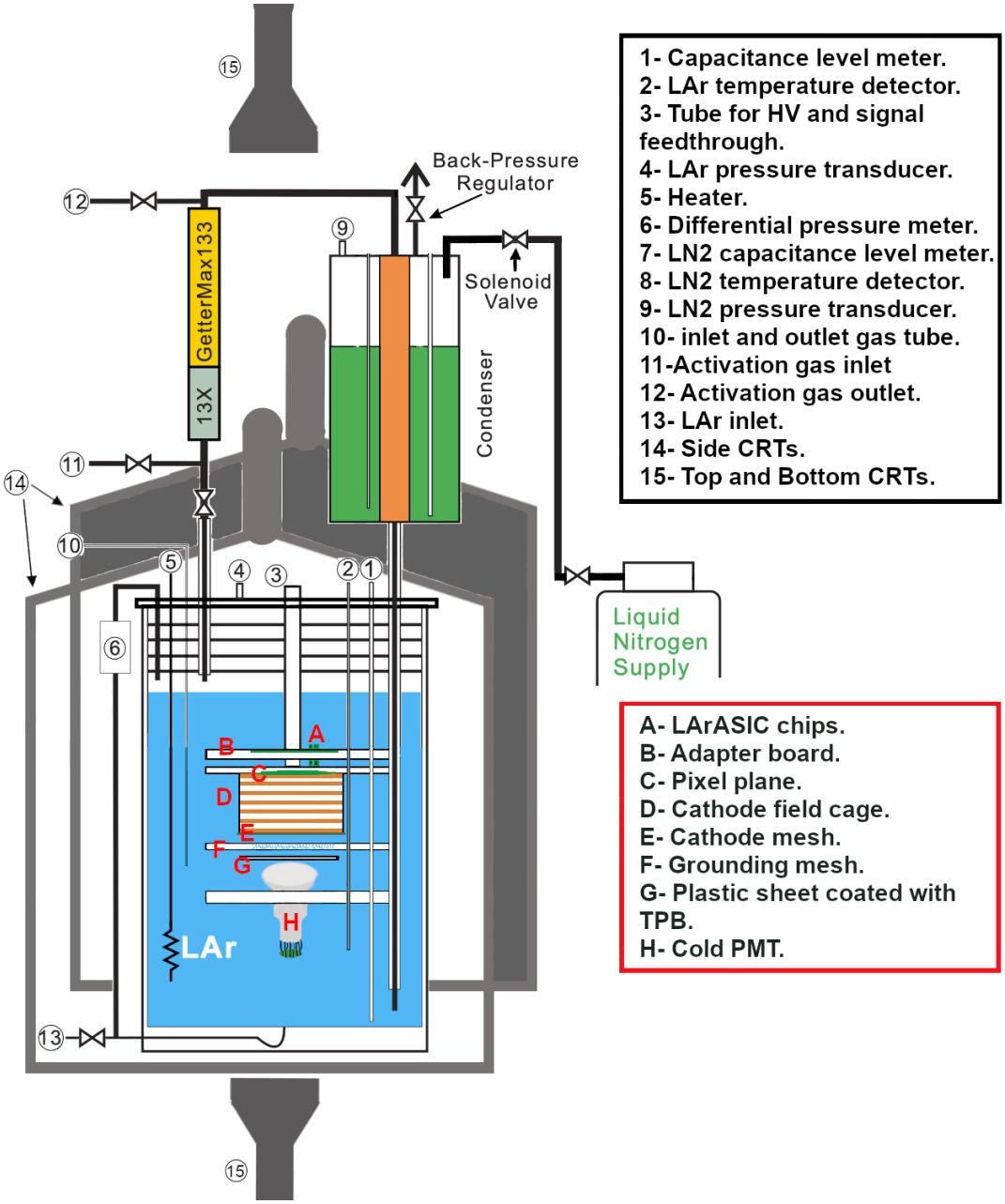

Figure 9.1: Schematic of the Sheffield LArPixel. The numerical and alphabetical labels indicate the rig system components and pixels readout equipment, respectively.

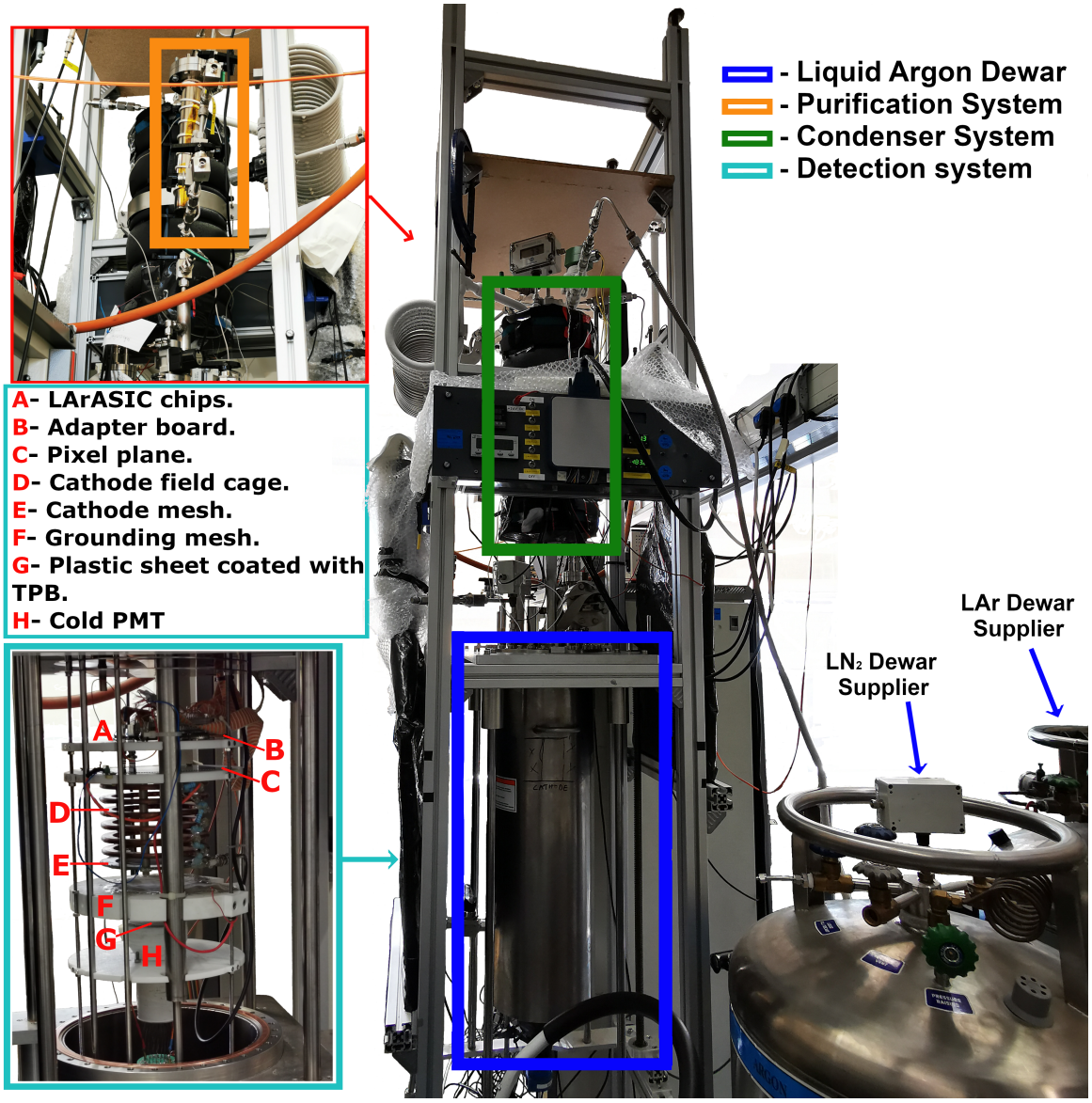

Figure 9.2: Photograph of the Sheffield LArPixels rig showing the subsystems. The alphabetical labels indicate the pixels readout equipment. The photograph shows the front of the rig, the back can be seen in the picture at the top left in the red frame. The photograph shows the four sub-systems; LAr dewar (in the dark blue box), the condenser system (in the green box), the purification system (in the light blue box, top left), and the detection system (in the light blue frame).

9.1.1 LAr Dewar

The LAr vessel is made from stainless steel (SS) and is double-walled and vacuum-jacketed to minimise heat loss. The dewar has a cylindrical shape with an ellipsoidal bottom and an inner diameter and depth of approximately 24 cm and 59.9 cm, respectively. The dewar can be filled with a total of 27.6 L of liquid argon if empty and around 22.1 L with the pixel-readout equipment.

An inlet valve at the bottom of the vessel is used to fill the low-temperature detector medium – in this case, liquid argon – and measure the hydrostatic pressure at the bottom. The dewar hosts the detector medium, pixel readout equipment and supporting sensors and tools installed from the top; see Figure 9.1 and Figure 9.2. At the top, there are five stainless steel baffle plates to significantly reduce the heat transfer between the top flange and the LAr through radiation and GAr convection. These plates are around 1 mm thick and spaced approximately 1 cm apart with several feed-throughs for pipes and electronics.

As can be seen from Figure 9.1 and Figure 9.2, temperature and pressure sensors and controls are installed from the top through the baffle plates to keep the LAr dewar in its optimal working condition. The temperature in the vessel is detected using a PT-100 RTD, a resistance temperature sensor with ± 0.01°C accuracy [271], and the temperature can be increased by the heater if needed. Similarly, the pressure is measured using an Omega PX-209 transducer sensor with approximately 0.25% precision [272]. The LAr level is monitored by utilising a differential pressure transducer type "GP:50 216" to gauge the pressure difference between the top and bottom of the vessel [273]. The dewar is designed to withstand up to 30 psia (around 2 atm), and two relief pressure valves ensure the dewar pressure is below this value. However, in ideal working conditions, the pressure should be maintained below 20 psia so the closed-loop argon recirculation is not affected. The argon closed-loop process is summarised in Figure 9.3, where the arrows' colours show an estimation of argon temperature.

The LAr dewar aims to keep the detector system at its typical conditions by controlling the temperature and the pressure inside the vessel. The dewar is not entirely thermally isolated from the outside environment temperature. Hence, once the vessel is filled with liquid argon, the LAr gains heat from the vessel walls and boil-off, producing argon gas. The argon gas flows through a vacuum-jacketed pipe linking the LAr dewar, installed below the baffle plates in the dewar, with the purification system. The gas is purified in the purification system (see section 9.1.2) and flows to the condenser system to be liquefied and returned to the LAr dewar.

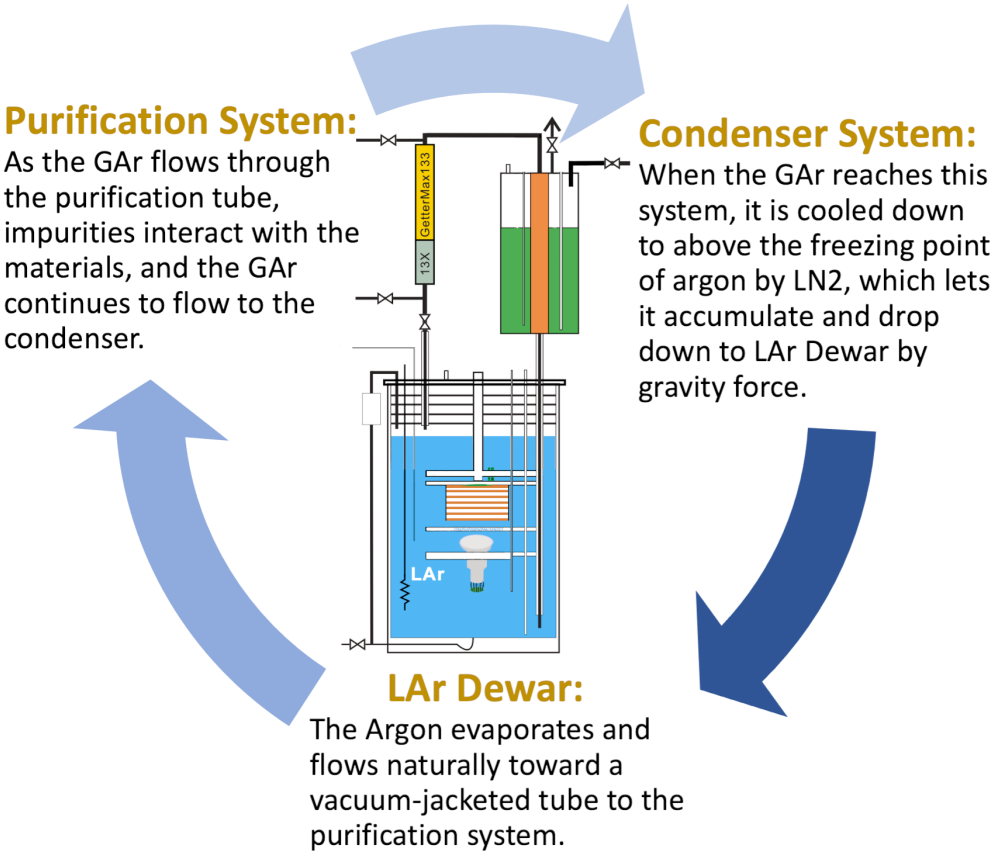

Figure 9.3: Schematic diagram of the close argon recirculation loop. The arrows' colours show an estimation of argon temperature.

9.1.2 Purification System

As can be seen from Figures 9.1 and 9.2, the purification system is connected to the LAr dewar from the bottom and the condenser system from the top, so the argon gas flows naturally. The system is a tube made from 304 stainless steel with dimensions of 33 cm and 5 cm in length and diameter, respectively. As seen in Figure 9.4, the tube is closed by a ConFlat (CF) flange and connected to a variable area flow meter [274] that measures the discharge rate of liquids and gases, which is connected to the gas outlet valve.

The tube is filled with around 33% of 13X molecular sieve, which consists of 8–14 mesh beads weighing approximately 1 kg. The rest is filled with GetterMax-133 copper catalyst 3×3 mm tablets with a total weight of up to 3 kg [275]. The mesh beads are located at the bottom of the tube and are designed to remove water molecules through selective adsorption. In contrast, the GetterMax-133 is placed on top of the mesh beads to remove the oxygen

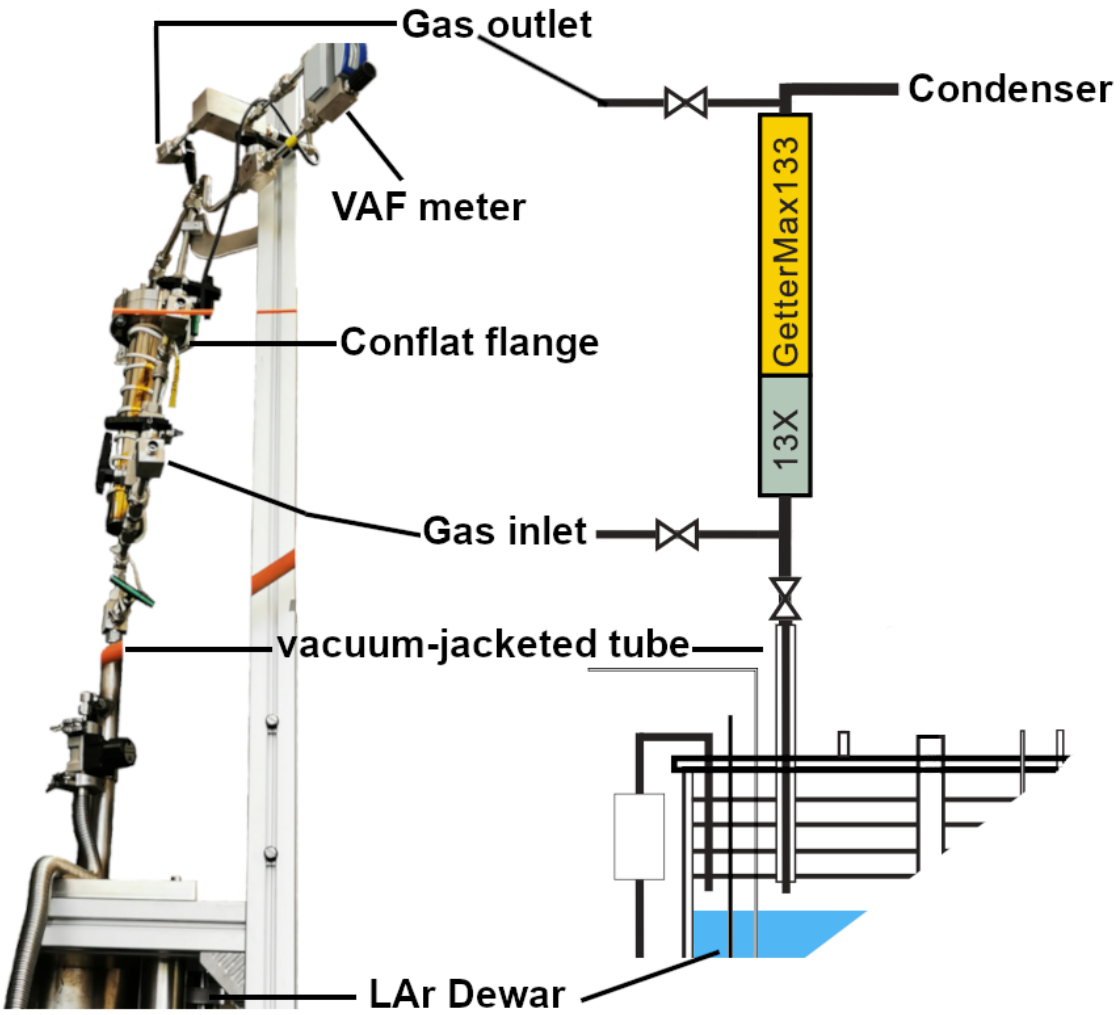

Figure 9.4: The purification system photograph and diagram are shown on the left and right, respectively. In the image, a coiled heating cable can be seen wrapped around the purification tube.

impurities, which undergo oxidation with the copper [275]. The efficiency of the purification system drops significantly as impurities build up on the active materials with time. By then, restoration of the materials is needed. The regeneration process is explained in detail in Section 9.2.

As mentioned before and depicts in Figure 9.3, GAr passes through the vacuum-jacketed tube from the LAr dewar to the purification system. Once purified, it is cooled down to its liquid state in the condenser and returned to the LAr dewar.

9.1.3 Condenser System

The condenser system has a simple design. It is formed of 304 stainless steel as seen from the diagram in Figure 9.1. The condenser is cylindrically shaped with a 15 cm diameter and a 47 cm length. It can hold up to 7.6 L of liquid nitrogen. The condenser is covered with 2.5 cm-thick engineered foams, AFArmaFlex Class O [276], to provide thermal insulation and minimise the heat loss. However, it is not 100% isolated from the outer environment. There is heat transfer between GAr and LN_2, so a continuous liquid nitrogen supply is required. Therefore, an LN_2 supply is connected to the inlet tube at the top of the dewar, which is linked to a cryogenic solenoid valve to control the filling.

Pressure and temperature sensors, the same models as those in the LAr dewar described in Section 9.1.1, are installed from the top of the LN_2 vessel. A back-pressure regulator releases the build-up pressure at the top, where it is connected to a spiral tube that heats the nitrogen gas before discharge. This vessel is designed to withstand up to 60 psia (around 4 atm); however, the standard operating pressure should be between 30 and 40 psia. Lower pressure is not recommended as it will reduce the LN_2 more quickly and increase the system's cost.

As mentioned previously, the condenser is linked to the purification system from the top and passes to the LAr dewar via an inner coaxial pipe 5.08 cm in diameter. This tube is filled with coarse copper wool, which improves and accelerates the heat transfer. After the argon gas is purified and gains heat, it flows to the condenser, where it cools but remains above argon's freezing point. Then, the liquid argon droplets accumulate and fall down the tube to the LAr dewar; the argon recirculation process is summarised in the diagram shown in Figure 9.3.

9.1.4 Detection System

The detection system has two main subsystems: Cosmic Ray Tagging (CRT) and LArTPC detector (Pixel Readout). The CRT subsystems include a cold PMT installed inside the LAr dewar to detect the scintillation light (Vacuum Ultra-Violet (VUV)) emitted during cosmic-ray interaction with liquid argon. Also, four CRT paddles are placed outside of the LAr dewar, two at the sides, one at the top, and one at the bottom, as shown Figure 9.1 and 9.2. These CRTs trigger the muons crossing the detector's main volume. Figure 9.5 shows the CRT subsystems' distance from the medial of the active detector volume and the direction of the side CRTs' paddles. The CRT subsystems' output signals are passed to a Keysight data acquisition system (DAQ) U5309A [277] via coaxial cables for readout and a CAEN N417 discriminator [278] via BNC cables for triggering.

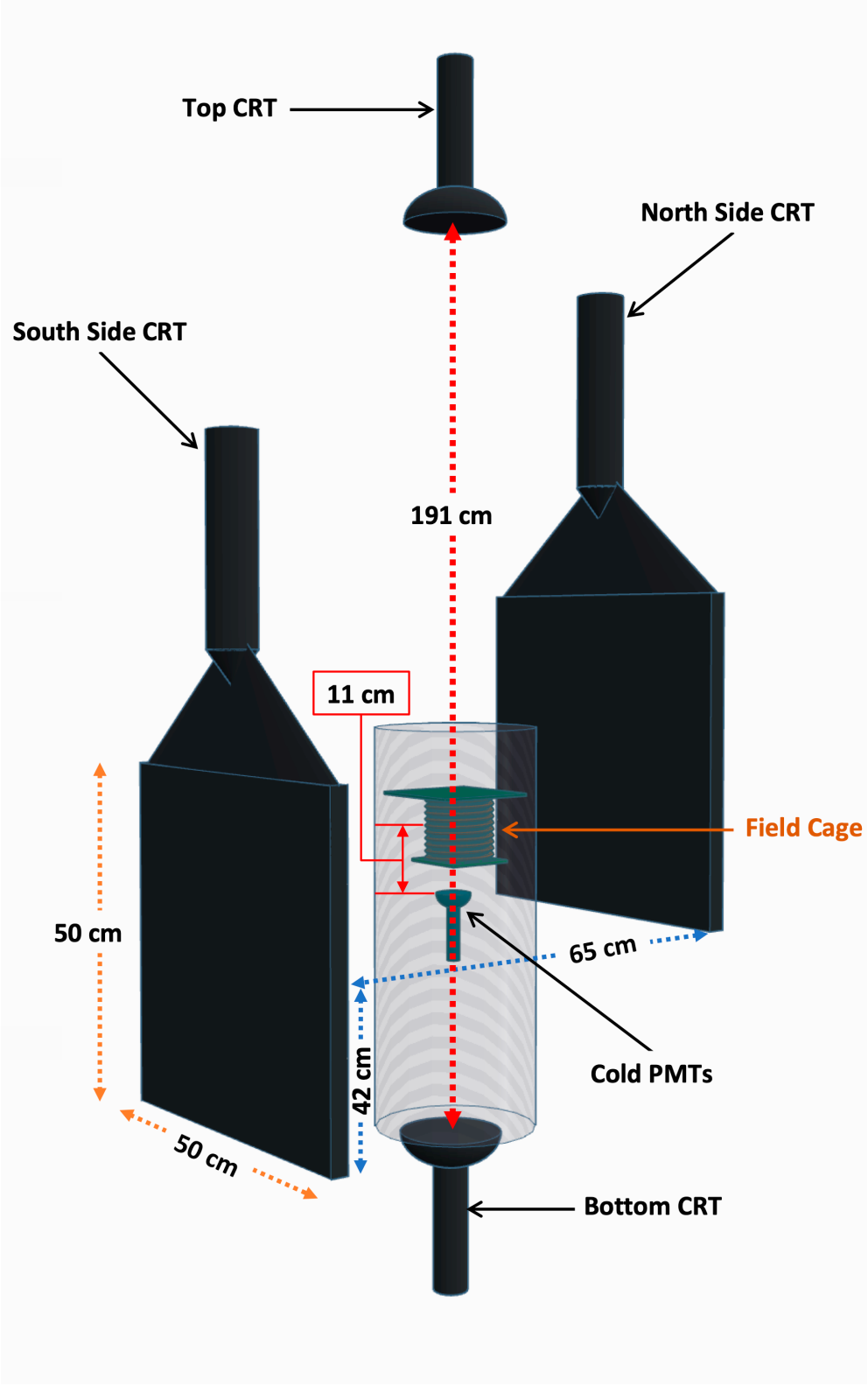

Figure 9.5: A diagram shows the CRT subsystems position to medial of the active detector volume (centre of the field cage).

Internal CRT (Cold PMT)

The cold PMT is a photomultiplier tube type Hamamatsu R11065 76 mm [279] designed to work in the low-temperature cryostat down to -186 °C. The objective of the cold PMT is to trigger the cosmic muon interaction with GAr and LAr within the LAr dewar. The cold PMT is installed in the LAr dewar below the grounding mesh facing the pixels' plane, and the distance between them is 16 cm, as shown in Figure 9.1 and Figure 9.2. The field of the cold PMT is protected from the cathode field by installing a secondary grounded mesh between the PMT and the cathode (see Figure 9.6). Additionally, a plastic sheet coated with TPB is placed under the secondary grounded mesh to shift the argon-invisible scintillation light for detection by cold PMT. The PMT receives 1700 V from a CAEN V6521 power supplier [280]. A summary of the cold PMT's operating parameters can be found in Table 9.1 [279, 281, 282].

PMT Type → / Parameters ↓		Cold PMT	Vertical CRTs	Sides CRTs
Spectral response range	Short (nm)	200	300	280
	Long (nm)	650	650	650
	Peak (nm)	420	390	∼400
Anode to Cathode Voltage	Average (V)	1500	1350	2000
	Max (V)	1750	1850	2300
	HV Polarity	Negative	Positive	Positive
Anode Current (mA)		0.1	1.0	/
Gain Typl.		$5.0x10^6$	/	$5.0x10^6$
Max. Dark Current (nA)		100	125	2
Time Response (ns)	Rise Time	5.5	20	2
	Transit Time	46	110	3
Operating temperature	Max. (°C)	L.T. only	60	60
	Min. (°C)	-186	-5	-5

Table 9.1: A table of main operational parameters for CRTs system [10][12][13].

External CRTs

The external CRT system is built up using two vertical PMTs and two horizontal PMTs and installed outside the LAr dewar, as Figure 9.5 shows. The vertical PMTs, called top and bottom PMT, are placed at the nearest possible position to the LAr dewar to align with the cold PMT to detect vertical muons crossing the active detector volumes, ensuring a charge deposition on the pixel readout regardless of LAr purity. The horizontal side CRTs are installed on the north and south side of the LAr dewar (Figure 9.5). The north side CRT is

higher than the other by around 42 cm to allow only cosmic muons with an angle of less than 52° with respect to the pixel readout to pass through the paddles. This prevents the drift time in pixel from being higher than 2 μs, which is the shaping time of the LArASIC amplifier, and thus also precluding saturation. Saturation occurs when charge builds up on a capacitor in the ASIC circuit caused by a large charge deposition near the pixel board.

The top and bottom CRTs have mini paddles attached to PMTs type EMI 9791KB [281] using BC-630 silicone optical grease, which has an excellent light transmission with low evaporation and bleeding at room temperature [283]. Each paddle is made from four pieces of scintillator plastic with dimensions of 5 cm $\times$ 5 cm $\times$ 2.5 cm and joined using the silicone grease to make a paddle with an area of 10×10 cm^2. The distance between the top CRT and the middle of the active volume of the detector is around 136 cm and about 186 cm to the bottom CRT, making the distance between the centre of the detector and the bottom CRT approximately 50 cm (see Figure 9.5).

The side CRTs have bigger paddles connected to PMTs type electron tubes 9954KB [282] via the same grease. These paddles have a 50 cm length, a 50 cm width and a 2.5 cm thickness. The side CRTs are placed on the north and south sides of the LAr dewar, and they are 32.5 cm away from the centre of the TPC detector.

The CRTs are wrapped with black tape to shield the scintillator medium (paddles) and the PMTs against environmental light to reducing the noise to a minimum. Therefore, triggering cosmic muon events that are most likely to cause a charge deposition in the active volume of the TPC detector, the pixel readout system.

LArTPC Detector

The LArTPC detector in the Sheffield rig is based on liquid argon time projection chambers (LArTPCs) technology. However, unlike regular LArTPCs detector experiments, which use wired readout channels, in the Sheffield rig, a pixel readout technology is used. The LArTPC detector in the Sheffield rig uses the same principle as the usual LArTPC detector, where the ionisation electrons caused by a charged particle interaction with an argon atom are drifted by the high-voltage cathode to the anode to be collected. In the standard setup, the anode consists of one or more induction planes to centralise the drifted electrons towards the collection plane. On the other hand, in this system, the anode is an eight-layer printed circuit board (PCB) with regions of interests (ROIs) to centralise the drifted electrons to be collected in pixels, which will be described in detail later (see pixel plane (D) subsection). An image of the Sheffield LArTPC detector can be seen in Figure 9.6 in which letters label the main detector components described as follows:

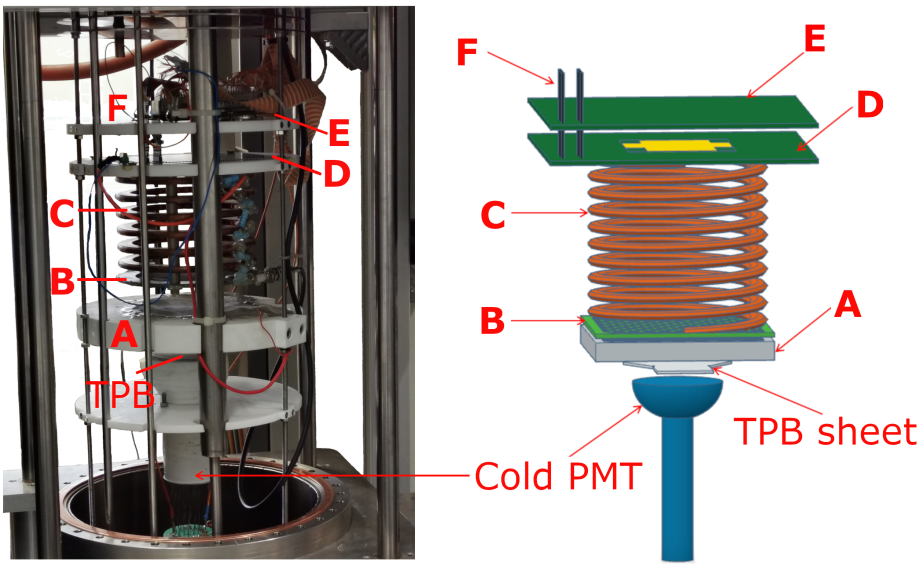

Figure 9.6: An image and a diagram of the LArTPC detector system; the alphabetical labels are: A) Grounding mesh, B) Cathode mesh, C) Cathode field cage, D) Pixel plane, E) adaptor board, F) Two LArASIC chips, Plastic sheet coated with TPB, and Cold PMT.

Grounding mesh (A)

The grounding mesh is designed to protect the cold PMT from sparks that can be generated while supplying the cathode with high voltage. The mesh is created from wires, so it does not interfere with scintillation light and allows it to pass through. The mesh is connected to the ground and placed under the cathode mesh, labelled as A in Figure 9.6.

Cathode mesh (B)

The cathode is a wire mesh that lets scintillation light pass and is installed directly under the field cage, labelled as B in Figure 9.6. The cathode mesh is disk-shaped, with a 10 cm diameter placed 10 cm below the pixel plane (which makes the drift region in the detector about 10 cm) and an active detector size of 0.79 L. Using CAEN V6521 [280], a negative voltage is fed to the cathode via SHV wires inside and outside the LAr dewar through the feedthrough tube. The cathode's stability has been successfully tested in air, argon gas and liquid argon up to 5 kV, as will be explained further in section 9.2.3.

Field cage (C)

The TPC field cage is built up using six equally spaced 6.35 mm-thick copper rings, with approximately 1.67 cm between the rings, and linked by a 56 MΩ resistor. Figure 9.6 shows an image of the field cage, labelled as C.

Pixel plane (D)

The pixel plane is located at the top of the TPC field cage (labelled D in Figure 9.6), where ionisation electrons are drifted vertically from the cathode to the pixel plane, with a 10 cm drift region and 10 cm diameter. The pixel plane (anode) is a PCB-based pixelated readout system with a total of 1008 pixel channels designed by the University of Bern [216, 284, 285]. These pixels are split into 286×6 squares called ROIs, and each ROI surrounding the pixels has an induction grid to concentrate the readout charge onto the pixels [216]. Hence, the induction grid is biased and supplied with voltage via the field cage through a 56 MΩ resistor. Figure 9.7 shows the pixels distributed in a 10 cm area on the pixel plane, and each pixel is formed of a 0.9 mm diameter point with a 2.54 mm pitch. Multiplexing limits the number of readout channels, which would otherwise be excessive if every pixel had its own. The multiplexing decreases the required channels from $N \times N$ to a more manageable $2N$. Hence, all pixels with the same relative position in each ROI are connected to one DAQ channel; for example, all the pixels in the upper left corners of all ROIs share the same DAQ channel. Therefore, the DAQ channels are reduced to 64 channels (36 channels for pixels and 28 channels for ROIs). To identify the charge-detected pixel, a collecting pixel channel's signal is coupled with the signal induced on an ROI channel.

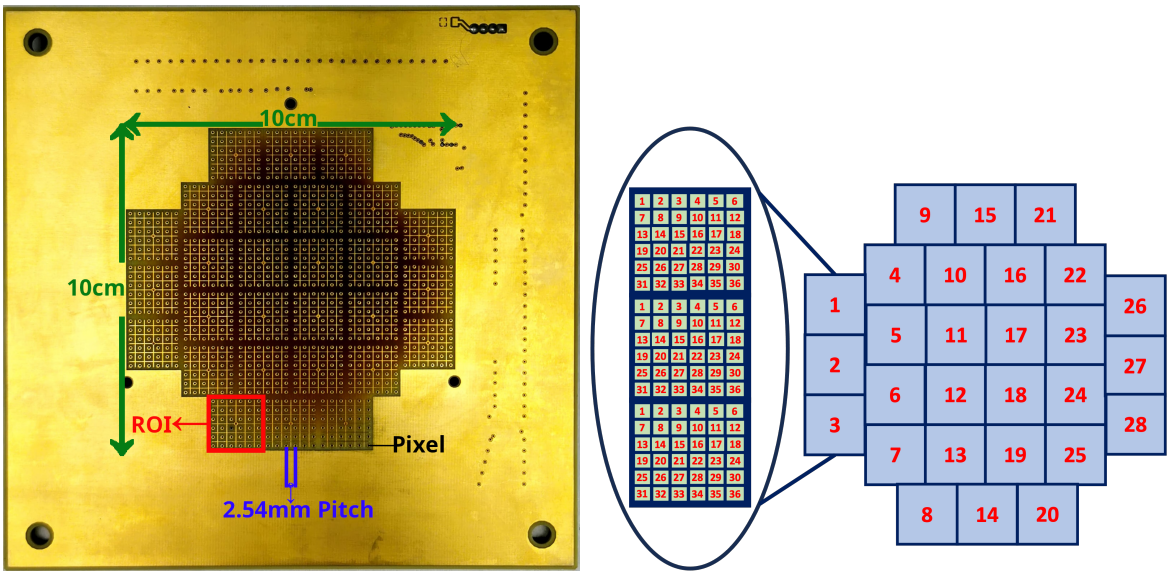

(a) (b)

Figure 9.7: On the left is a picture of the anode pixel plane with a pixel area of 10 cm × 10 cm, displaying one of the ROIs in red, the pitch distance in blue, and the pixel in black. On the right, a diagram of ROI DAQ readout channels is shown, along with examples of Pixel DAQ readout channels.

Adaptor board (E) and LArASIC chips (F)

Figure 9.6 shows the adaptor board and LArASIC7 [286] chips that are fixed above the pixel plane, labelled as E and F, respectively. A diagram of the rig's electronic chain is shown in Figure 9.8. Once a signal is detected on the pixel board, it is sent to one of the two chips to be amplified and shaped. The settings of the LArASIC7 shaping time and gain can be modified with an Arduino Nano [287], which transmits a bit-wise signal to the ASIC via ribbon wires. The system is intended to operate with a 2 μs shaping time and 25 mVfc gain for the LArASIC7. The signal is then transmitted to an adaptor board, which transmits the channels to a feedthrough using Kapton ribbon wires. then two ribbon wires send the pixel signals to the V1740-64 Channels CAEN DAQ [288]. To allow for testing provision is made for test pulses to be passed from the Arduino to the LArASIC7. Details of this and other tests performed to confirm the pixel planes functionality are reported in the next section (see Sec 9.2.3).

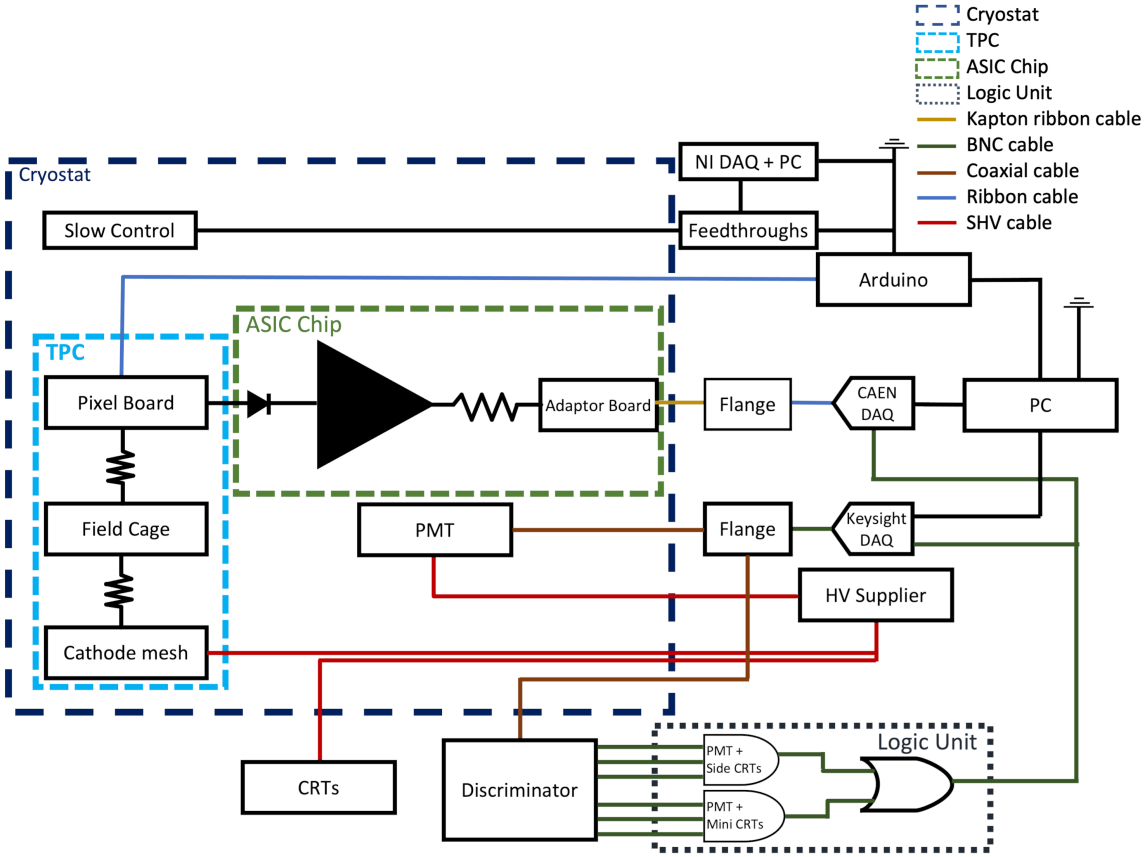

Figure 9.8: A diagram of the Sheffield rig's electronic chain.

9.2 Engineering Studies of the Test Stand Systems

In order to prepare the rig for a long run of two to three weeks, it is vital that all components are tested. Described here are details of the tests conducted on individual system components, groups and subgroups. Firstly, covered in sections from sec. 9.1.1 to sec. 9.2.3, the cold PMT, cathode and pixel readout were examined individually to ensure full performance before closing LAr dewar. Then, the LAr dewar was closed, and a leak test was completed to ensure the leak rate should be lower than 0.2 mbar per day, covered in section 9.2.4. Finally, the external CRTs and the argon recirculation systems were examined and reported in section 9.2.5 and section 9.2.6, respectively.

9.2.1 Cold PMT

As described in Section 9.1.4, the internal cold PMT is vital for triggering of the pixel readout. Also, mention that the cold PMT is designed for cryogenic use with liquid argon and has a special internal cathode design with a photoemissive surface of Bialkali with 25% quantum efficiency (QE), 85 mA/W radiant sensitivity, 90 μA/lm cathode sensitivity, and 10 cathode blue sensitivity index.

The cold PMT was tested to confirm it was fully functional before being installed in LAr dewar. To guarantee complete isolation from the light in the outside environment, the PMT was placed in a box that had been darkened from the inside. Firstly, the high-voltage (HV) operation stability of the PMT was tested by gradually applying negative HV from the CAEN-V6521 supplier –30 V at a time until reaching the recommended operating voltage of 1700 V. The PMT was then left with this voltage applied for approximately 30 minutes to observe any change in the current. This procedure was followed several times, whenever the operating conditions of the PMT changed, such as when the PMT was moved.

Figure 9.9 shows example results of these tests. At the top, a graph shows the change in current as a function of voltage supplied to the cold PMT. At the bottom a graph of resistance versus the HV applied on the PMT. It can be seen that current(μA) and resistance (MΩ) are plotted against voltage (V) in three different environments; in the dark box (Blue), inside the LAr dewar filled with air (Brown) and in LAr dewar filled argon gas (Green). The current was stable in the three working environments, and there was a slight variation between 1600 V and 1700 V. However, there is a fluctuation in the resistance by about 0.2 MΩ, which is considered negligible compared with the average resistance (36.5 MΩ). Next, a scintillator plastic with an alpha source from Am-241 was attached to the PMT to assess the output signal of the PMT using an MSO-3054 mixed signal oscilloscope [289]. After that, the PMT was coupled with sodium iodide crystals to calibrate the PMT using a Cs-137 gamma

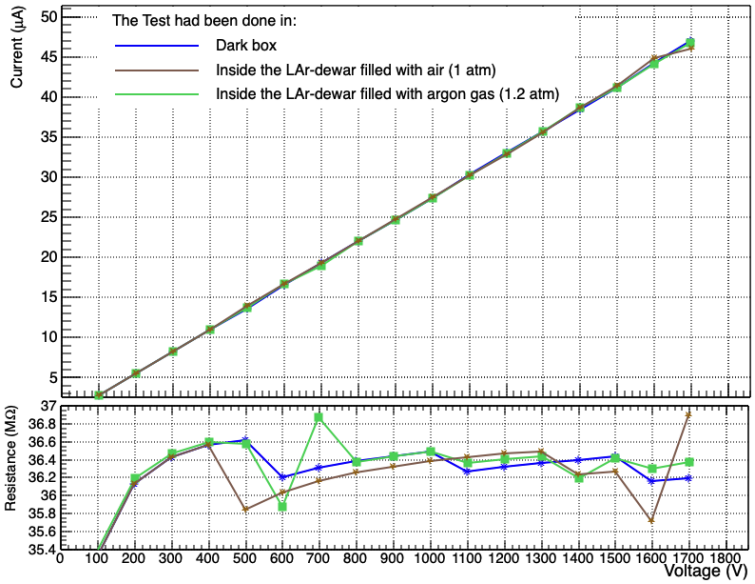

Figure 9.9: The top graph shows the change in current as a function of voltage supplied to the cold PMT. At the bottom, a graph of resistance versus the HV applied on the PMT.

source emitter before being installed in the LAr dewar (credit to D. Barker and E. Tyley). Figure 9.10 shows an example of these tests' results along with the calibration results. On the left is a picture of the output signal from the cold PMT when attached to a scintillator plastic with Am-241, alpha emitter. The fluctuation in the spectrum is due to Am-241 emitting different alpha energies. On the right, the calibration result of the cold PMT using Cs-137. A clear gamma spectrum of Cs-137, Compton peak, Compton edge and photo-peak, can be seen on the right plot. The cold PMT was found to be operating satisfactorily following these tests.

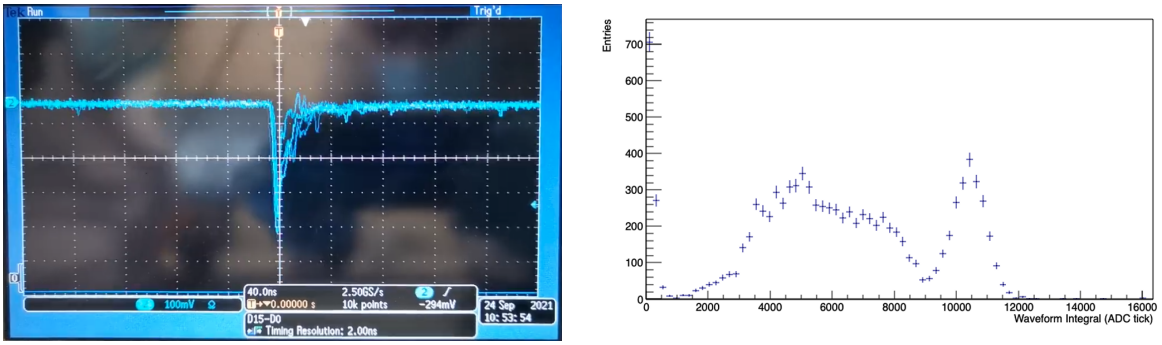

(a) Testing the cold PMT with Am-241 (b) Calibration the cold PMT with Cs-137 source

Figure 9.10: The output signal from the cold PMT, when attached to a scintillator plastic with Am-241, alpha emitter, is shown on the left. On the right, the calibration result of the cold PMT using Cs-137, a tick in the DAQ is 1 ns, credit to D. Barker and E. Tyley.

9.2.2 Cathode High Voltage Tests

As described above (see Section 9.1.4), the cathode is there to provide a drift electric field across the TPC. The cathode was tested when the dewar was filled with air and gaseous argon after the cold PMT was successfully tested and installed in the LAr dewar. The examination was conducted using the CAEN-V6521 HV supply (see Figure 9.8), the voltage being slowly raised to a maximum of 4.5 kV. For the test in air the target voltage was reached successfully and safely without problems. For the test in gaseous argon the HV was found to break down at 2.5 kV. There are various possibilities for this behaviour, including the gas pressure within the dewar, the gas's purity, the system design, and most likely, the HV supply, as a spark in the dewar will draw more current than the supply limit. An example of the cathode mesh current (μA) and resistance (MΩ) as a function of the voltage applied is shown in Figure 9.11. It can be seen that the current was stable in the two working environments. However, the resistance in air starts at 560 MΩ, then decline until reach 2500 V, and then remains constant up to 4.5 kV, whereas for GAr, the resistance is constant primarily until breakdown at 2.5 kV.

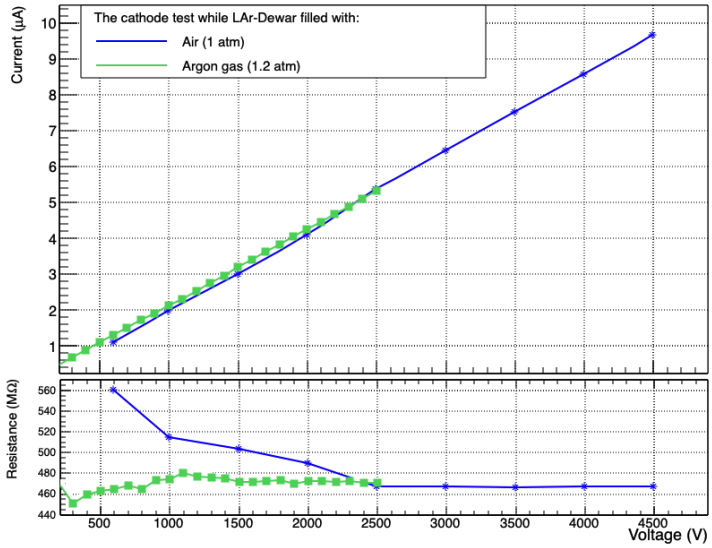

Figure 9.11: The change in current as a function of voltage supplied to the cathode is shown in top graph. At the bottom, a graph of resistance versus the high voltage applied on the cathode mesh. Current(μA) and resistance ($M\Omega$) are plotted against voltage (V) in two environments; inside the LAr dewar filled with air (Blue) and filled with GAr (Green).

The desired cathode HV (4.5 kV) while the LAr dewar filled with gaseous argon was achieved by changing the cathode HV supply, iseg NHQ 238L [290], which has a 1 mA current limit, and increase the GAr pressure to 2.5 atm. Following these tests, it was determined that the cathode functioned properly.

9.2.3 Pixel Readout Tests

To examine the connection of the pixel readout chain, a square test pulse was delivered from the Arduino to the LArASIC7. A successful test result would verify the functionality of the pixel readout equipment and the connection to the LArASIC chips. An example can be seen in Figure 9.12. As expected, a negative peak at 2000 tick on pixel channel two and at the same time on ROI 1 can be seen in the Figure 9.12. This was seen in all pixel and ROI channels.

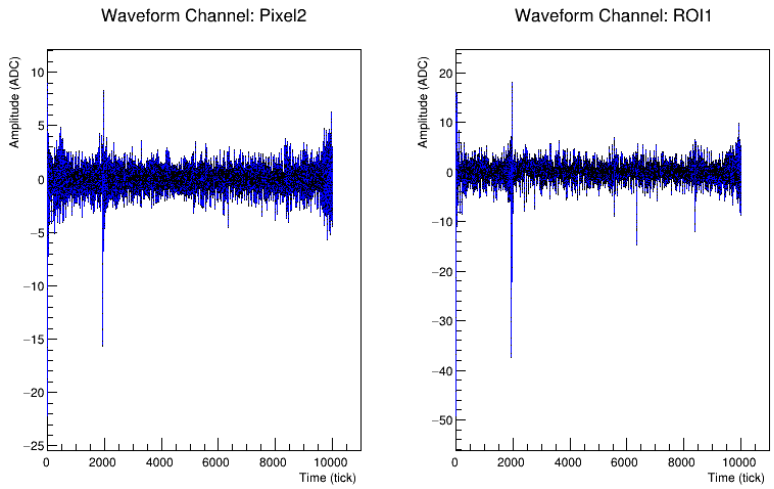

Figure 9.12: An example of a test pulse sent from Arduino to the LArASIC7 chips which shows the channel from Pixel2 and ROI1.

The testing revealed that all channels responded as predicted to test pulses. However, note that this does not guarantee full operational functionality of the pixels, for example that they successfully collect charge deposited in the target gas. This is best determined using particle interactions in the complete detector set-up (see section 10.3).

9.2.4 LAr Dewar Leak Tests

After successfully conducting the tests of the main TPC detector components, internal PMT and Pixel readout covered above, and closing the LAr dewar, the next step was to conduct a full system leak check. This is required to confirm that the detection medium, liquid argon, is isolated from the outer environment. The leak test is performed by pumping down the LAr dewar to the lowest value possible, which might take days, and then, with the pump switched off, recording the pressure every 15 min. This test ensures that the pressure, temperature, argon purity and argon level do not degrade in long term operation. As shown in Figure 9.13, this test was done multiple times to get the lowest value of the leak rate per day. If the leak value was unacceptable, helium was used to determine the location of the leak.

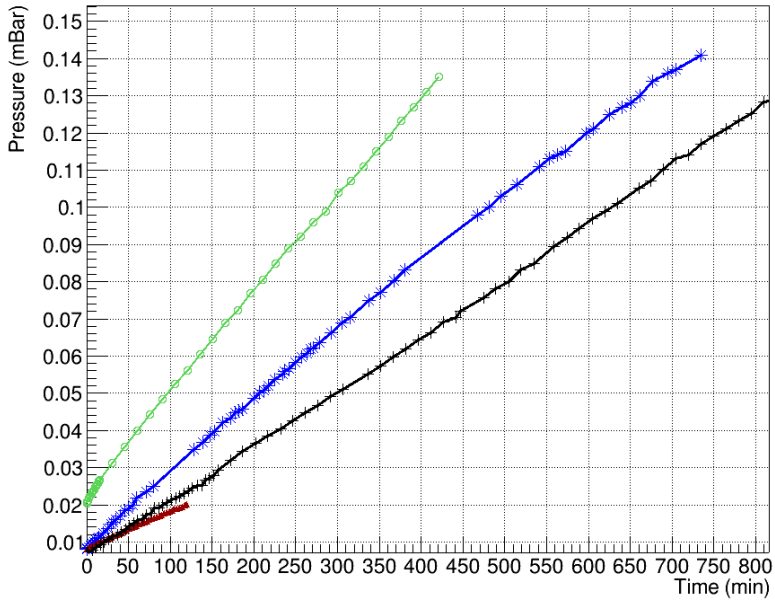

Figure 9.13: Examples of leak test carried out on the LAr dewar, each colour represent a test for a few hours.

The leak test process did indeed reveal several sources of gas leak. Each of these was successfully corrected, for instance, a poor seal in one of the feedthrough flanges. The final leak rate obtained was typically 0.14 mbar/day. Ideally, a lower rate should be obtainable in the future, but this was deemed acceptable for the current preliminary pixel tests.

9.2.5 CRTs Tests

The four CRTs were calibrated and tested by triggering off cosmic ray muon interactions. Figure 9.14a and 9.14b show plots of the time difference (ns) between the CRTs versus the number of events, where the blue vertical line represents the time difference per event from data and the red line represents a Gaussian fit to the data. Figure 9.14a illustrate that the offset between the side CRT signals was around 28 ns. On the other hand, Figure 9.14b indicates that the offset of the CRTs with mini paddles showed a smaller time difference between signals, approximately 0.5 ns. Multiple factors, such as the length of the BNC cables, could affect the offset between the CRTs' signals. Figure 9.14c show the peak height (ADC) spectrum for Far (North) and Bench (south) side CRTs, as seen Figure 9.5. Also, Figure 9.14d show the spectrum for the top and bottom CRTs.

It was established that the offset between the sets of CRTs, particularly between the side CRTs, around 28 ns, is negligible and does not effect the pixel readout tests and may be adjusted in the software module. Therefore, it was determined that the CRTs functioned as expected, and no more testing was necessary.

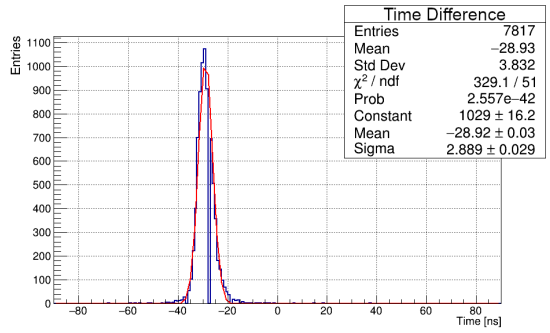

(a) Far and bench side CRTs

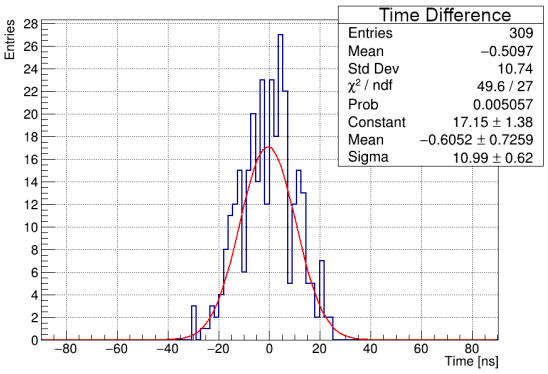

(b) Top and bottom CRTs

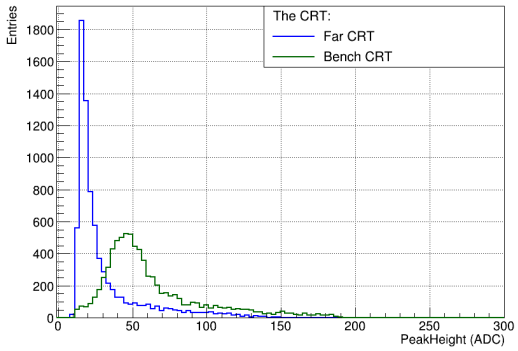

(c) Far and Bench side CRTs

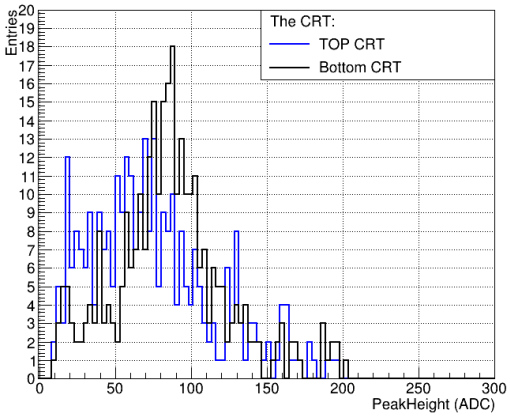

(d) Top and Bottom CRTs

Figure 9.14: Plots showing the response of the CRTs to several cosmic ray incidents. At the top, the time difference between; a) far and bench side CRTs and b) top and bottom CRTs. At the bottom, the CRTs response spectrum as peak height in (ADC) for c) far and bench side CRTs and d) top and bottom CRTs.

9.2.6 Argon Recirculation Tests

After completion of the detector system tests, attention was turned to examination of the argon recirculation involving LAr dewar, the purification system and the condenser system, see Figure 9.3. This process was aimed to test the argon gas flow by operating all systems together and observing the change in LAr and LN_2 pressure and temperature as well as LAr level. The first step was to close all valves from and to the LAr dewar and manually fill the dewar with liquid argon to approximately 80%. Next, the condenser system was manually filled with liquid nitrogen, and the valves between the LAr dewar, purification system and condenser system were opened. Finally, after the systems operated stably, an automatic system was used to fill the condenser system, and the system's stats were monitored. An

example of a one-day run is presented in Figure 9.15, the LAr and LN^2 levels, pressures and temperatures are shown at the top, middle and bottom, respectively. As can be seen in Figure 9.15, the LAr level, pressure and temperature are steady from the start of the run at 0 min until the end at around 550 min. However, there is a slight fluctuation in the LAr pressure due to the change in LN^2 pressure as the condenser is refilled. The change in LAr level that can be seen is due to malfunction of the LAr level detector when there is a rapid change in the pressure, which happen for a few seconds at the beginning of LN^2 refilling. Also, the fluctuation in LN^2 pressure is during the refilling process. Figure 9.15 at the top also shows the change in LN^2 level between 60% and 90%, as the system is designed to be refilled automatically when the LN^2 level reaches 60% and stops at 90%.

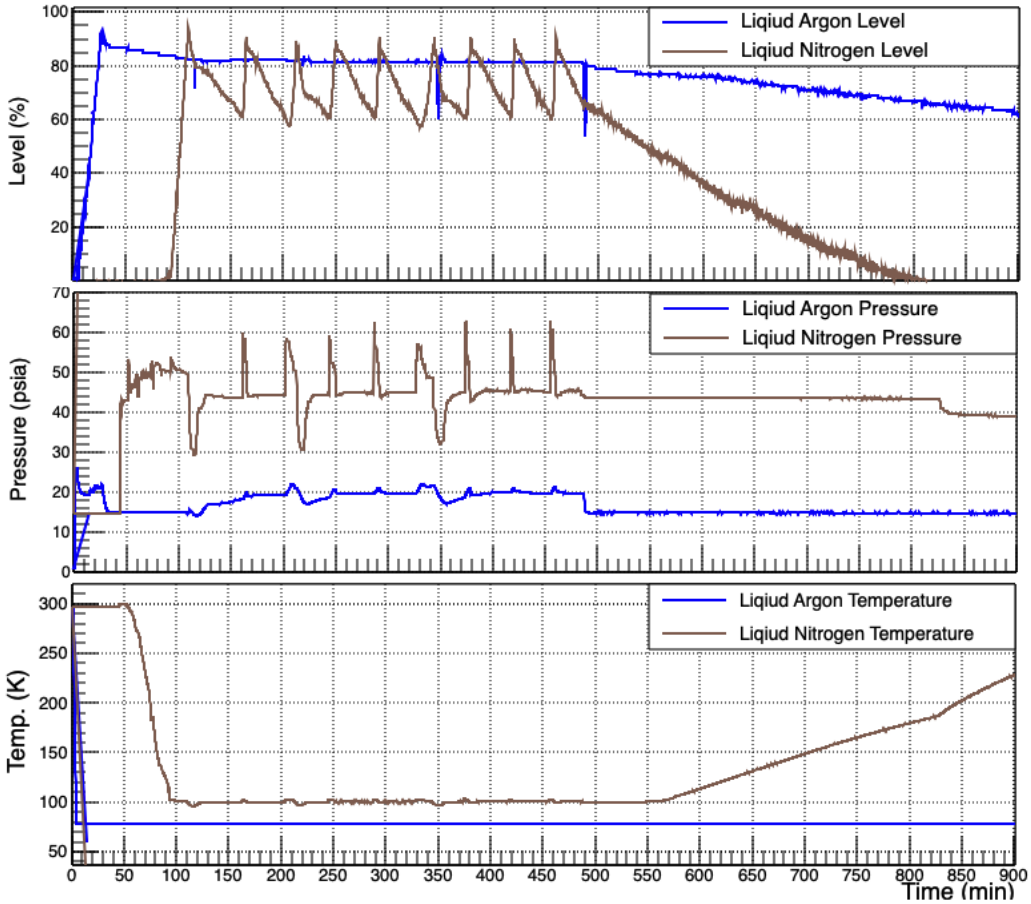

Figure 9.15: An example of metrics measured during the recirculation test. The graph shows a few hours of the test. The top graph shows the level of LAr inside the LAr dewar and the liquid nitrogen level in the condenser. The pressure within the LAr dewar and the condenser system is shown in the middle. At the bottom, the temperature of the condenser and LAr dewar.

The test was successful, and the Sheffield rig systems operated in stable condition for a few hours without issues. Hence, the Sheffield test stand was determined to be ready for the long run, as reported in the next chapter.

9.3 Experiment Operation Procedures

The Sheffield test stand's standard operating procedures can be summarised in a few steps, explained in more detail in [291]. Once a functional electronic and detector system has been installed and tested successfully, these steps must be taken since a malfunction during the operations can lead to the need to restart all operational procedures from the beginning.

Firstly, after completing the internal and external detection systems tests described earlier, the system must pass a helium leak test to prevent air from entering the LAr dewar and contaminating the liquid. Hence, the LAr dewar must be repeatedly pumped with argon gas and carefully purged to remove air; four cycles will sufficiently lower the air content.

Next, the purification system must be reactivated by having argon gas mixed with 2% hydrogen passed through it to ensure functionality. The reactivation is completed once the output gas flow does not contain water, which is measured via a dew-point sensor that can monitor water content in argon gas between 0–1000 parts per million (ppm).

Next, close the valves connecting the systems to start cooling the LAr dewar for LAr filling. This process begins by connecting an external LAr dewar and opening the valve between them to let argon gas flow to the vessel. Slowly reduce the vessel temperature to avoid causing thermal shock to the LAr-dewar's detector systems and equipment. Figure 9.16 which shows the argon and nitrogen temperature (K) versus the pressure (bar on the left and psig on the right) in gas and liquid phases. Depending on the temperature and pressure requirements, various cooling speeds can be achieved by manually adjusting the flow from the supplier. When the vessel temperature is lowered to the boiling point of argon, the liquid will start to fill it. Once the LAr dewar has been filled, the LN_2 vessel should then be filled to enable purification and recirculation. After that, the LN_2's pressure must be adjusted via the system's back-pressure regulator to balance the system's thermodynamics, as seen in Figure 9.16, and reduce the consumption of LN_2.

In a normal long operation, the LN_2 vessel is continuously refilled while being discharged from the back pressure regulator. The refilling speed is directly related to the amount of heat loss in the system. Additional insulation would result in a slower release of nitrogen, reducing the rate of nitrogen escaping into the atmosphere. In a normal operation, a continuous LN_2 supply is needed, usually 200 L per day.

Finally, after ending the run, the system is warmed by first closing the purification system to prevent the oxygen and moisture from entering. Then, the argon and nitrogen vessels can be directly vented to the atmosphere, which will take a few hours, as seen in Figure 9.15.

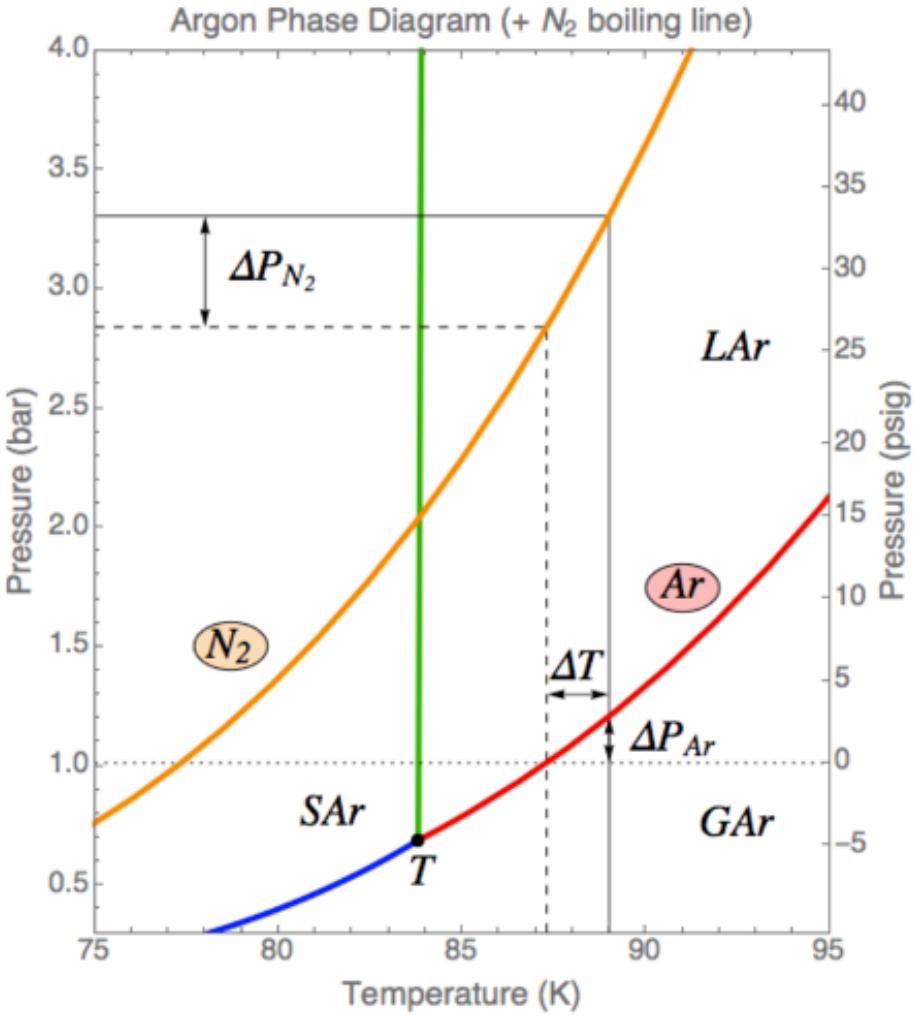

Figure 9.16: Argon phase diagram with the N_2 boiling line superposed [270]. The orange line represents the boiling line for the nitrogen and the red line for the argon. The ideal operating condition for the Sheffield test stand near the vertical green line for both LAr and LN_2.

9.4 Summary

The Sheffield LAr test stand is a cryogenic system with a recirculation system in which argon is continuously filtered to remove oxygen and water impurities, a summary of this process can be seen in Figure 9.3. The test stand consists of four main systems; LAr dewar, purification system, condenser system and detection system. The systems were evaluated as individuals, subgroups and groups to confirm they functioned as intended. Firstly, the components within the LAr dewar were assessed, and it was determined that they function properly; no further tests were required. After the LAr dewar was sealed, several leak tests were conducted, and the final leak rate was found to be 0.14 mbar/day, which was considered adequate. The external CRTs were then evaluated and verified to operate as intended. Also, the pixel-readout equipment and connection up to the pixel board were tested by sending a test pulse, and the signal was observed on the pixel and ROI channels, indicating that they work as designed. Finally, a successful argon recirculation test was done, and the Sheffield systems ran in stable condition for several hours without incident. According to the engineering studies of the Sheffield test stand systems, a two to three weeks long run is achievable to evaluate the pixel readout system.

Chapter 10

Evaluation of Sheffield LArPixel Charge Readout in LAr

In Chapter 9, the Sheffield LAr test stand was introduced, which is a cryogenic system that employs a recirculation system to continuously filter argon and eliminate impurities. The four primary components of the test stand, namely LAr dewar, purification system, condenser system, and detection system, were thoroughly examined at various levels to ensure their optimal functioning. The evaluation of LAr dewar components, external CRTs, and pixel-readout equipment was emphasised, and the successful performance of the system was demonstrated during an argon recirculation test.

Building on the previous chapter, this chapter presents the outcomes derived from an extensive two-week operational evaluation of the test stand, with a particular focus on the performance of the pixel readout system through the observation of charge deposition on the pixel board. Section 10.1 reports on the system operation and performance for the 343 hours of running using liquid argon. The three-step processing procedure used for data obtained from the CRT system is discussed in Section 10.2. Section 10.3 presents the noise filtering and hit-finding algorithms employed to analyse the pixel readout data, along with the 2D and 3D event displays used to observe charge deposition on the pixel plane using external triggers from the CRT system. Finally, Section 10.4 provides a summary of the experimental results regarding the functional evaluation of the entire system, including the LArPixel charge readout.

10.1 System Operation and Performance

In order to thoroughly evaluate the functionality and performance of both the system and the LArPixel charge readout, a rigorous assessment was conducted through a 343-hour (20,576 minutes) run employing liquid argon. During this 14-day period of operation at the Sheffield

test stand, a total of 12,214 events were triggered, utilising 60 L of 99.999% pure LAr, carefully mixed to contain less than 2 vpm of oxygen, 1 vpm of moisture, and 6 vpm of nitrogen impurities, as well as 2.8 kL of nitrogen [292]. Subsequently, this section will provide a comprehensive account of the Sheffield test stand's operation and performance during this extended runtime.

10.1.1 Operation of the Cryogenic System

The work discussed in this section pertains to a two-week run started on 27th July 2022, commenced following the integration of the test stand, as described in Chapter 9. Critical to understanding operation of the cryogenics, as described in Chapter 9.1.1, is to monitor the LAr level and pressure, ensuring strict adherence to operational limits. These parameters are shown in Figure 10.1a and 10.1b respectively for the full 343 hours of the run.

Figure 10.1a shows the variations in the levels of LAr and LN_2 in the system over the course of 343 hours of operation, and as can be seen, the LAr level was steady. However, on the fifth day, there was a minor decrease of approximately 10% in the LAr level. This decline was deemed insignificant since all LArTPC detector equipment (as seen in Figure 9.6) remained submerged in liquid argon, allowing the run to continue. The reduction in LAr level resulted from an increase in pressure due to a rise in LAr temperature. This increase in temperature was caused by a malfunction in the LN_2 dewar supply, leading to a decrease in the LN_2 level to approximately 30%. The malfunction occurred because the LN_2 supply pressure fell below the required threshold of two bars, necessary for supplying the condenser with LN_2.

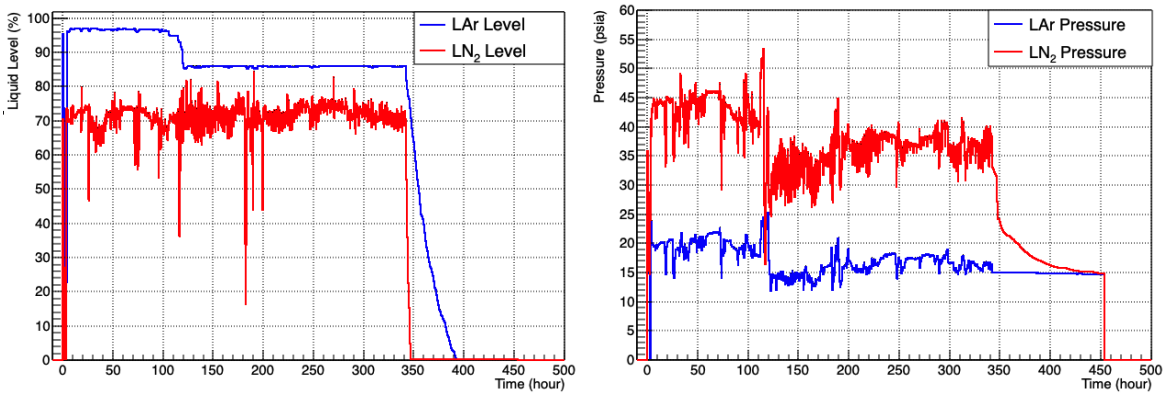

(a) LAr and LN_2 levels

(b) LAr and LN_2 pressures

Figure 10.1: The levels and pressures of LAr and LN_2 during 343 hours operation of the Sheffield test stand.

To ensure the stability of the cryogenic system, a two-person shift protocol was implemented for continuous monitoring and pressure adjustment as needed. After the fifth day, there were a few minor fluctuations in LN_2 levels and one significant decrease to less than 20%, primarily due to an LN_2 shortage. Nevertheless, these fluctuations were effectively managed, preventing any decline in LAr levels. Figure 10.1b shows the pressure levels in the LAr dewar and condenser, and as can be seen, the pressure fluctuated within the normal operating range, as outlined in Section 9.2.6.

Overall, regardless of the fall in LAr level, by around 10% on the fifth day of running, the LAr level remained stable throughout the run. The pressure variations observed in the LAr dewar and condenser remained within acceptable standard limits, thereby averting any potential shutdown due to malfunction.

10.1.2 System Heat Load

In addition to understanding the general operational parameters of liquid levels and pressure, comprehending the heat loads is also crucial in the effective operation of the test stand. Figure 10.2 depicts the temperature of liquid argon and nitrogen over 343 hours. The temperature in the LAr dewar was roughly 80 K and remained constant throughout the 14 days. However, as stated previously, due to the fault and the LN_2 shortage, the liquid nitrogen temperature rose a few times. However, this did not affect the temperature of the LAr dewar.

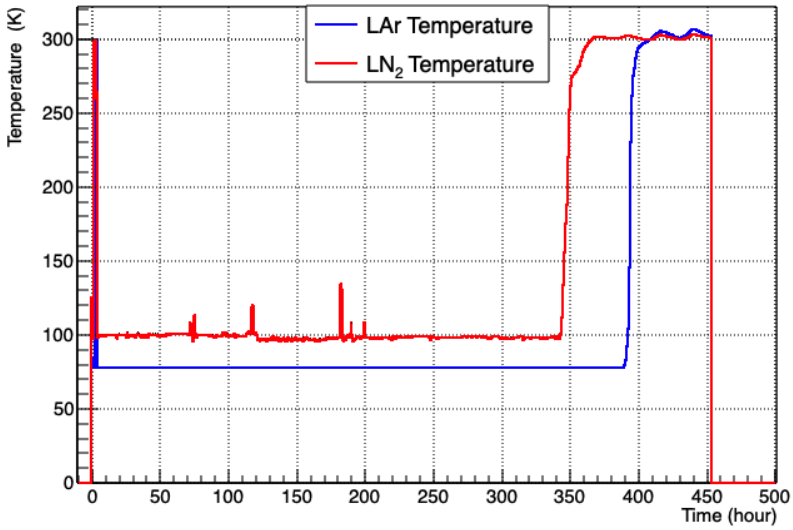

Figure 10.2: The temperature in the LAr dewar and condenser during 343 hours. The red and blue lines represent the LN_2 and LAr temperature, respectively. As can be seen, the temperature was stable with a few rises in LN_2 temperature.

The temperature and pressure in the LAr dewar were managed very well during the test run time. Hence, the triggering and recording of the cosmic muons continued from the beginning to the end of the test, with a total of 12,214 events were recorded.

10.1.3 Data Collection and Triggering

Data collection for the run proceeded using the electronics and DAQ set-up as described in Chapter 9.1.4 and illustrated in Figure 9.8. Events were triggered when cosmic particles met the triggering condition while passing through the detector, which occurred in two ways: either if there were signals on both side CRTs with the cold PMT or if there were hits on the top and bottom CRTs with the cold PMT. Hence, the events from CRTs and pixels were recorded if these conditions were fulfilled. The CRTs triggering parameters in the discriminator were set to values shown in Table 10.1. These parameters were set after studies were conducted to effectively detect cosmic muons.

CRTs	Threshold		Output Width (WDT) (ns)
	Polarity	Level (mV)	
Cold PMT	Positive	128	80
North Side CRT	Negative	123.0	500
South Side CRT	Negative	110.8	500
Top CRT	Negative	32	80
Bottom CRT	Negative	32	80

Table 10.1: A table of the primary discriminator parameters for CRTs system.

10.1.4 Cathode Breakdowns in Liquid Argon

The objective was to operate the cathode in the LArTPC detector at 3 kV, which given the length of the drift region, was deemed sufficient to drift the vast majority of the ionisation electrons to the pixel board without issues. However, as described in Section 9.2.2, the cathode voltage broke at 2.5 kV while the LAr dewar was filled with GAr. The cause was believed to have been the generated sparks, and the issue was solved by changing the HV supply and increasing the GAr pressure. Similarly, the cathode HV started to break down at 2.3 kV in LAr, but the cause this time was believed to have been GAr bubbles within the drift region as well as the potential impurities in the LAr. Nevertheless, the progressive enhancement of liquid argon (LAr) purity over time is believed to have played a substantial role in mitigating cathode HV breakdown. This improvement resulted in the achievement of the desired HV levels after 270 hours of operation, as voltage levels were incrementally increased. As shown in Figure 10.3, the cathode HV increased by approximately 200 V steps

every 100 hours, and as the LAr purity improved after 270 hours of operation, the HV was raised in a single step to the intended voltage. Thus, though a few ionisation electrons were lost at low cathode voltages, all 343 operational hours' worth of data are considered valid. However, the cathode voltage has been factored into the 3D reconstruction, as discussed in Section 10.3.4.

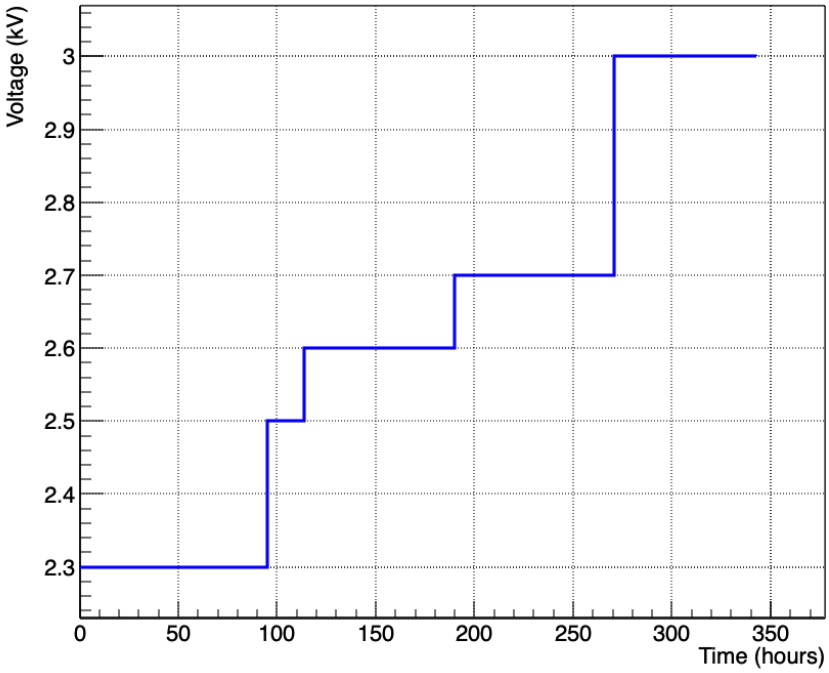

Figure 10.3: Summary of the high voltage of the LArTPC cathode during 343 operational hours.

10.2 CRT Data Analysis

As mentioned earlier, the total number of events detected after 343 hours of running the experiment were 12,214, and Table 10.2 summarises the number of daily events that were triggered. The average number of events detected daily was around 850 events, and on the first day, fewer events were detected because the run lasted less than 12 hours.

CRT data analysis is crucial to pixel event selection and data analysis as well as studying the purity of argon using the cold PMT events. Once the CRT data was acquired and stored in a ".dat" file using Keysight data DAQ [277], the analysis was done in three steps: decoding into a ROOT [293] data format, noise filtering and, event selection. Section 10.2 describes this process as follows.

Date	Days	Number of events
27/07/2022	1	381
28/07/2022	2	843
29/07/2022	3	1000
30/07/2022	4	1100
31/07/2022	5	1000
01/08/2022	6	1000
02/08/2022	7	630
03/08/2022	8	501
04/08/2022	9	600
05/08/2022	10	487
06/08/2022	11	600
07/08/2022	12	808
08/08/2022	13	958
09/08/2022	14	1541
10/08/2022	15	765
Total	12214 Events	

Table 10.2: A daily summary of events triggered by the CRTs.

10.2.1 CRTs Data Decoding

Each DAQ channels data was decoded into ROOT format after data collection using the Keysight decoding module [294]; credit to D. Barker for repurposing the module (see Section 9.1.4. The decoder rewrites the data recorded by Keysight DAQ to a ROOT file along with finding the pulse and the baseline and integral of the waveform. First, the baseline of the waveform is estimated by averaging the ADC of the waveform. Then, a basic pulse height algorithm is used to locate the peak of the waveform. Next, the width of the pulse is determined using an iterative process that calculates the mean of five ticks (5 ns, 1 tick = 1 ns in the DAQ) from the pulse's peak until the average falls below three times the RMS of the noise, which is derived from the standard deviation of a Gaussian fit to the distribution. Finally, the area under the waveform between the peak and stopping points is calculated and stored in a ROOT file; for details see [295] [285].

Figure 10.4 shows an example of an event waveform after decoding. The plot on the left of Figure 10.4 presents the waveforms of an event triggered by the horizontal CRTs, while the plot on the right displays an event detected by the vertical CRTs. Figure 10.4a displays four waveforms, namely the cold PMT waveform shown in green, the logic channel waveform in purple, the north side CRT waveform in black, and the south side CRT waveform in blue. In Figure 10.4b, triggered by different CRTs, the top CRT waveform is represented by black and the bottom CRT waveform by blue. As both graphs show, the waveforms on the time

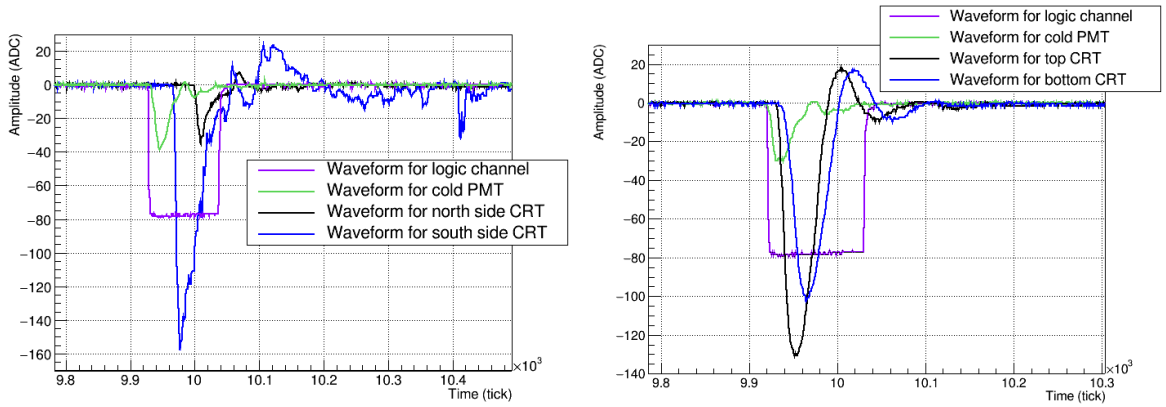

(a) Detected by Horizontal CRTs

(b) Detected by Vertical CRTs

Figure 10.4: An example of an event waveform triggered via side and vertical CRTs. On the right and left, respectively, is a waveform for an event detected by the side (horizontal) CRTs and the vertical CRTs with the cold PMT. The time, measured in ticks, is represented on the x-axis, while the y-axis represents the distribution of the waveform in ADC units.

axis are largely overlapping, with a minor temporal discrepancy between the channels, as section 9.2.5 describes, while remaining within the limits of the logic channel. Also, the waveforms recorded by the cold PMT and external CRTs exhibit low levels of noise, enabling clear visibility of the peaks. Contrastingly, the side CRTs, particularly the south side CRT, manifest relatively higher noise levels. Nevertheless, despite these challenges, the outcomes of the initial CRT test demonstrate the system's satisfactory functionality. Noteworthy is the achievement of the complete CRT triggering setup for the first time, with the internal PMT successfully operating within the LAr.

10.2.2 Noise Filtering

Noise filtering is critical in many studies using CRT data, including event selection and studying the purity of LAr using a cold PMT. In response to this challenge, two methods have been tested with the aim of reducing noise levels within the CRTs of the Sheffield test stand. The first step in reducing noise was to analyse the frequency of the noise in the waveform using Fast Fourier Transform (FFT) [296], an algorithm used to transform time-domain signals into their corresponding frequency-domain representation. FFT is based on the idea that any signal can be depicted as a sum of sinusoidal waves of different frequencies; hence, the concept is to identify the frequencies present in a signal and analyse them. The FFT algorithm used to analyse CRT signals is based on a ROOT interface class for FFTs [297]. Figure 10.5 shows the FFT waveform for an example cold PMT signal before applying and after noise filtering algorithms.

Two types of noise filtering were used to reduce the noise from the CRTs waveforms: one based on a frequency cut and the other on a threshold cut. These filters are as follows:

Filter-1 [298]: After applying the FFT algorithm [299] to the CRT's waveforms and analysing the frequencies, a band-pass filter-based algorithm is applied to remove the noise frequencies. This filter allows a specific range of frequencies, known as the passband, to pass through while attenuating or removing frequencies outside of the passband. The band-pass filter was used to isolate a specific frequency range of interest while removing unwanted frequencies between 2×10^3 Hz and 18×10^3 Hz.

Filter-2 [300]: The second filter was based on a threshold cut and a smoothing function applied to the waveform to reduce the noise. First, a threshold cut was applied to remove any peaks in the CRT's waveforms with an amplitude of less than 3 ADC. Then, a smoothing function was implemented to eliminate the random noise without a specific frequency.

Figure 10.5 depicts the FFT waveform for the cold PMT signal before applying noise filtering algorithms, represented by the brown line, and the waveforms after applying Filter-1 and Filter-2, depicted by the blue and green lines, respectively. The signal frequency was

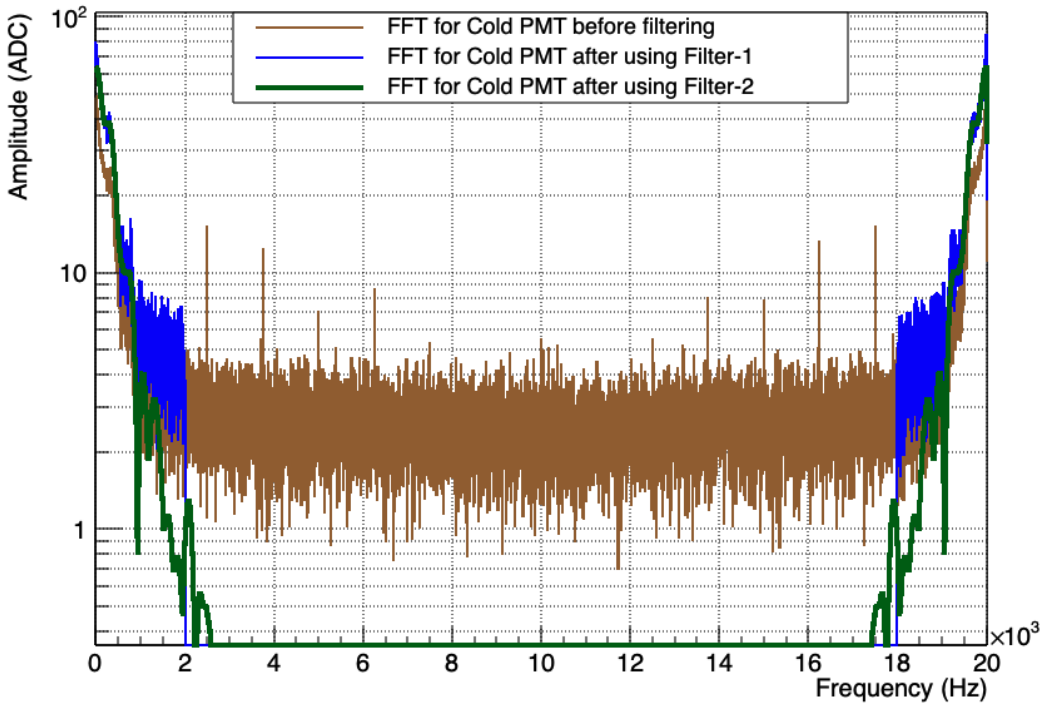

Figure 10.5: An FFT comparison of the Cold PMT signal before and after noise filtering. The x-axis represents frequency in Hz, and the logarithmic y-axis represents the amplitude of frequencies in ADC. The FFT of the cold PMT signal prior to applying noise filtering algorithms is shown in brown, whereas blue and green correspond to the FFTs of the waveforms following noise filtering with Filter-1 and Filter-2, respectively.

estimated to be below 2×10^3 Hz and higher than 18×10^3 Hz, so the frequencies between these have been cut using Filter-1. The difference before and after applying Filter-1, brown and blue lines, can be seen in Figure 10.5. In addition, the waveform after applying the second filter, Filter-2, is shown by the green line, and most of the noise was removed, as seen in the difference between the three waveforms.

Figure 10.6 shows an example of the cold PMT signal waveform before and after using filters. The figure displays a selected segment of the waveform, spanning approximately 0.45 ns out of 20 μs, which includes the highest peak. Additionally, a zoomed section on the noise can be seen within the figure, and the differences in the noise levels between the three steps can be observed. The first filter reduced the noise level, but applying the second filter reduced the noise to below detectable levels on this scale.

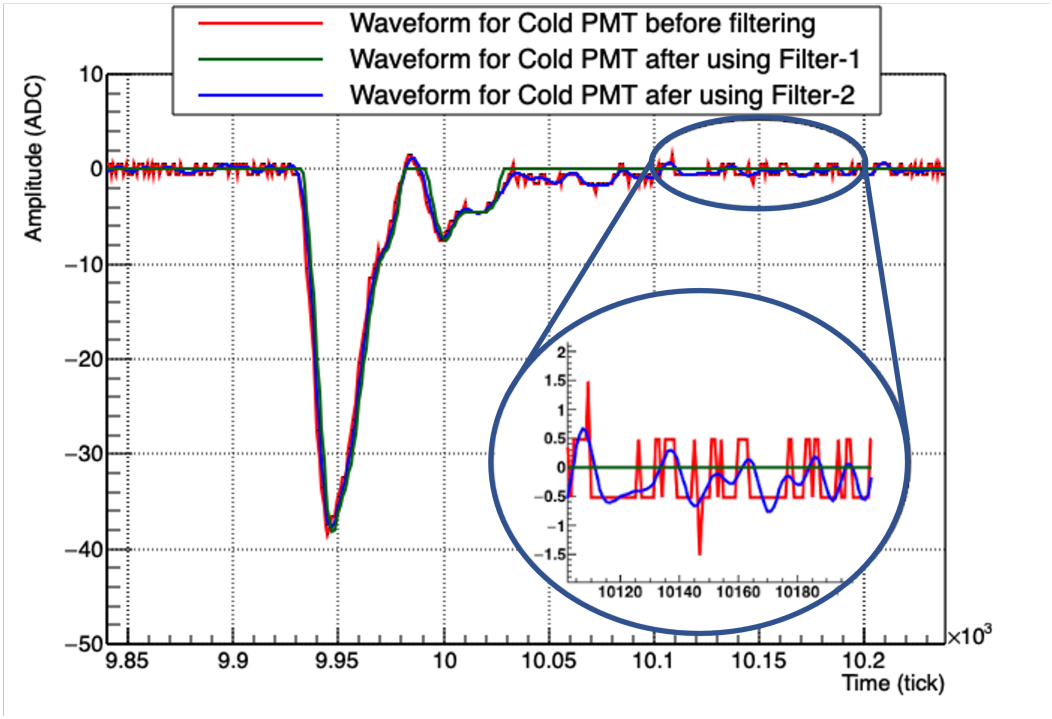

Figure 10.6: A comparison of the waveform of a cold PMT signal before and after noise filtering. A zoomed section of the waveform is displayed in the bottom-right corner. A comparison of two types of filters is shown; Filter-1 (Green) and Filter-2 (Blue).

Figure 10.7 presents the signal segment of a waveform acquired from the cold PMT before and after noise filtering for one of the events detected. The figure shows two distinct peaks: the first is a sharp and narrow peak, while the second is a broader and longer peak, typically referred to as the fast and slow components of the scintillation light. The fast component is produced by the promptly recombining the ionisation electrons with the argon atoms, and its decay time is typically between 6 and 7 ns [301]. The slow component, on

the other hand, is produced by the delayed recombination of the ionisation electrons with impurities in the liquid argon, and it typically has a decay time of around 1.5 μs [301]. The two peaks in the cold PMT signal arise because the cold PMT is sensitive to both the fast and slow components of the scintillation light. As depicted in Figure 10.7, applying both filters has a minor effect on the peak of the fast component, but it effectively clears the noise from the peak shape, leading to a more accurate measurement of the peak characteristics. On the other hand, applying only Filter-1 to the waveform before applying Filter-2 is more efficient in removing noise from the slow component peak, as the edges of the peak, which might lead to an inaccurate representation of the slow component peak, were cut by Filter-2's threshold-based filtering.

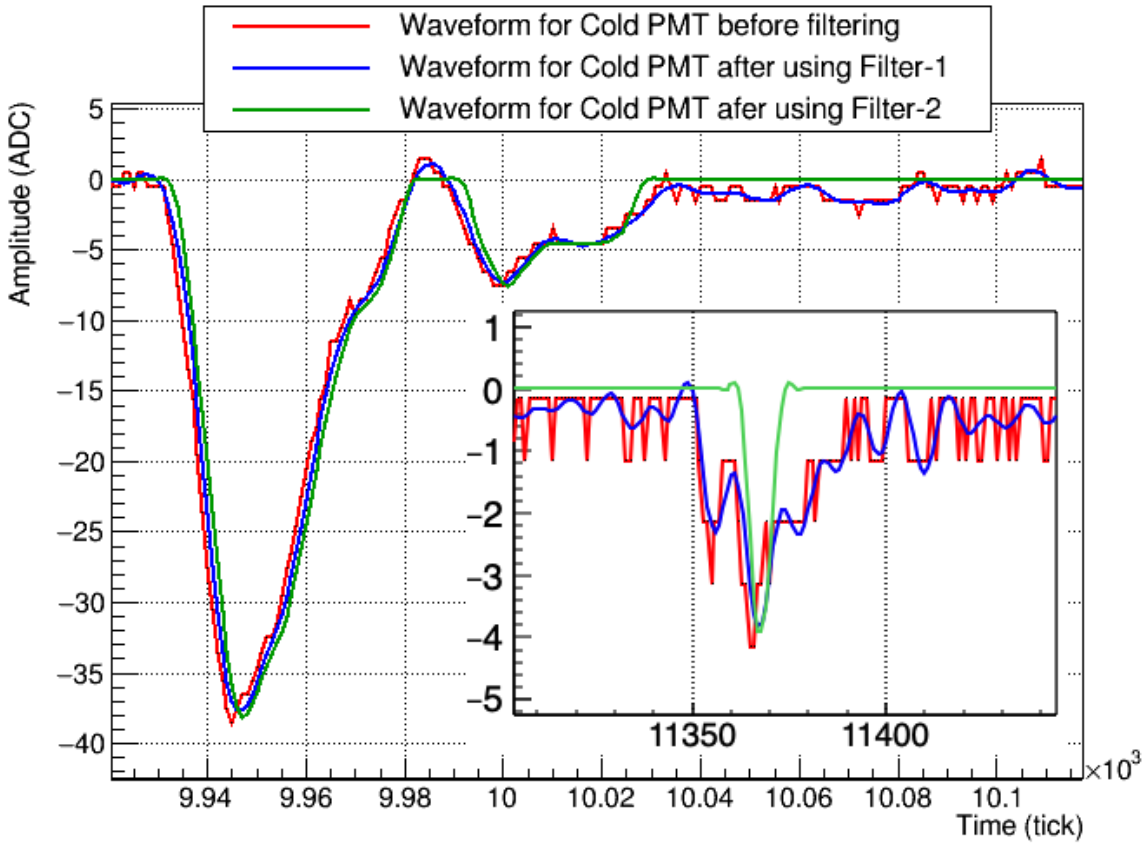

Figure 10.7: Cold PMT signal segment before and after noise filtering.

10.2.3 CRT Event Selection

The event selection process aims to remove noise events and identify the events most likely to result in charge deposition on the pixels. For the selection process, the data sample was used after applying both filters while disregarding the impact on the slow component peak.

The initial step was to discard events not triggered by the cold PMT with the side CRTs or vertical CRTs, as well as events with a time difference between CRT signals that exceeded the expected range. Subsequently, the CRT data was classified into two categories based on their triggering CRTs, namely horizontal and vertical events, depending on whether they were detected by the side or vertical CRTs, respectively. After that, a threshold cut of 10 ADC on the cold PMT signal peak was used to eliminate events less likely to have a deposition on the pixel board. Figure 10.8 shows the peak height distribution of cold PMT signals for events triggered by side and vertical CRTs. The red dashed line indicates the threshold cut located at 10 ADC, the peak heights below this have been removed.

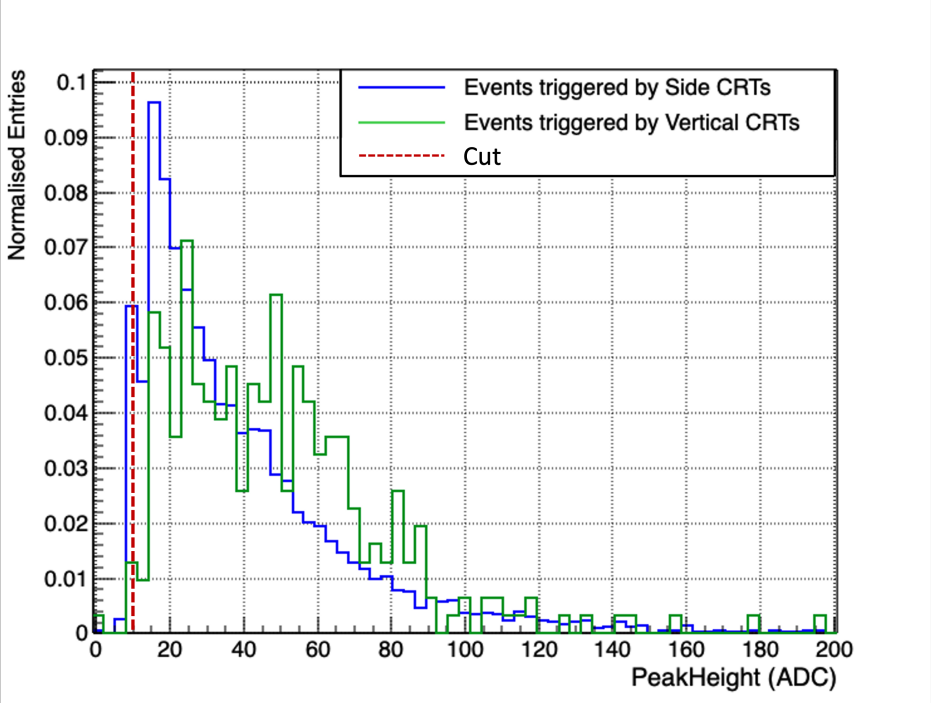

Figure 10.8: Peak height spectrum of cold PMT signal for events triggered by side and vertical CRTs. The distribution for events triggered by side CRTs is shown in blue, while the one for vertical CRTs is shown in green. The red dashed line indicates the threshold cut placed at 10 ADC, resulting in the removal of events with peak heights below this value.

After applying the selection criteria, a total of 7,788 out of 12,214 events were retained for pixel event selection. These events were divided into two categories, horizontal comprising 7,483 events and vertical comprising 305 events.

10.3 Pixel Data Reconstruction and Analysis

The pixel readout system, as previously discussed in section 9.1.4, comprises a total of 1008 pixel channels that are organised into 64 DAQ channels. Of the 64 channels, 36 are allocated to pixels while the remaining 28 are dedicated to ROIs. Pixel events are collected from these channels using either the software trigger or external trigger methods. The software trigger [302] is based on a threshold of 2.7 ADC, so an event will be recorded if one channel has a peak higher than 2.7 ADC from the baseline. The external trigger [303] is based on the CRT triggering system, where an event is recorded only if triggered by the cold PMT with side or vertical CRTs. The external code is based on the software trigger code that was edited to accept an external triggering from the CRT logic channel. The objective of this run was to observe a charge deposition on the pixel plane, so the external trigger was used. Following the event acquisition, the 64 DAQ channels were stored in a ".dat" file by Pixel DAQ [288]. The data was processed in four principal stages: decoding into a ROOT data format, noise filtering, hit finding and matching, and 3D reconstruction.

10.3.1 Pixel Data Decoding

Following a similar principle to the decoding of CRT data, the Pixel decoder [304] facilitates converting the collected data into a ROOT format; D. Barker is credited for writing the module. The decoder module is designed to parse binary DAQ files and generates a ROOT file containing event objects filled with event numbers, time stamps in nanoseconds, and channel objects. The channel object for each event contains the channel ID, channel numbers, number of ADC recorded, waveform baseline, and waveforms for all 64 channels. The waveform baseline is calculated by fitting a Gaussian fit around the ADC. An example of an event waveform from Pixels and ROIs triggered by the CRTs is shown in Figure 10.9. The Pixel-9 (blue) and ROI-13 (green) waveforms are displayed on the right and left, respectively, in the Figure 10.9. The graph shows a peak at approximately 2,550 ticks in the pixel-9 and similarly in ROI-13, indicating that there is a charge deposition on Pixel-9 in ROI-13.

Figure 10.9 demonstrates that the ROI channels exhibit a higher susceptibility to noise, with levels exceeding 3 ADC. Contrastingly, the pixel channels display a relatively lesser degree of noise in this event, although noise filtering techniques remain crucial. Therefore, for decoding the pixel data, the next stage involves removing noise events and applying waveform cleaning techniques to enhance the accuracy of hit finding and matching.

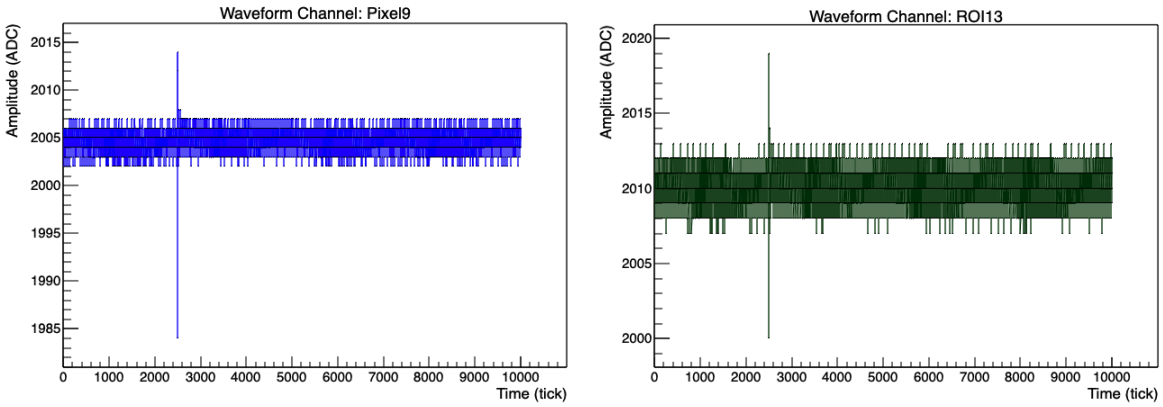

Figure 10.9: An example of an event waveform for pixel-9 and ROI-13 triggered by the CRTs. The graph on the right shows a signal on pixel-9, whereas the plot on the left displays the same signal on the ROI-13. The y-axis indicates the waveform amplitude in ADC, while the x-axis represents time in units of ticks (1 tick equals 16 ns in the PixelDAQ).

10.3.2 Noise Filtering

To assess the potential of the system, a pixel readout noise analysis study was conducted, with the RMS of the noise from the system serving as the evaluation metric. Data were collected using the software trigger, and for each event, a Gaussian fit was applied around the baseline of each pixel/ROI to calculate the RMS. Subsequently, a second Gaussian fit was performed, with entries outside 5σ removed from the first fit mean (where σ represents the standard deviation of the first Gaussian fit). The noise RMS was obtained by taking the standard deviation of the Gaussian from the second fit. Finally, the noise RMS was converted into electrons (ENC/e^-) by leveraging the shaping time of the LArASIC.

The RMS of the noise in the air was found to be 2.27$\pm$0.38 ADC for the pixels and 3.7$\pm$0.3 ADC for the ROIs, where 1 ADC = 121.89 e^-. In addition, the average RMS of the noise in LAr was calculated as 1.55$\pm$0.11 ADC and 1.54$\pm$0.19 ADC for the pixels and ROIs, respectively. Figure 10.10 illustrates the average RMS noise variation in LAr over time and channel number. In Figure 10.10a, the mean RMS noise for pixels at the top (blue) and ROIs at the bottom (green) are depicted over a duration of approximately 325 operational hours. The average noise level in the pixel channels was around 1.55 ADC with a few increased peaks noticeable around 225 hours, as seen in the top graph. Similarly, the mean noise level in the ROI channels was about 1.54 ADC, equivalent to 187 e^-, with reduction peaks occurring around 125 to 210 hours. As shown in Figure 10.10b, some channels had higher RMS noise, especially pixel-12, pixel-17 and ROI channels greater than 14, where the pixel

channels (channel numbers 0 to 35) are represented by the blue line and ROI channels the remaining (36 to 64) are the green line.

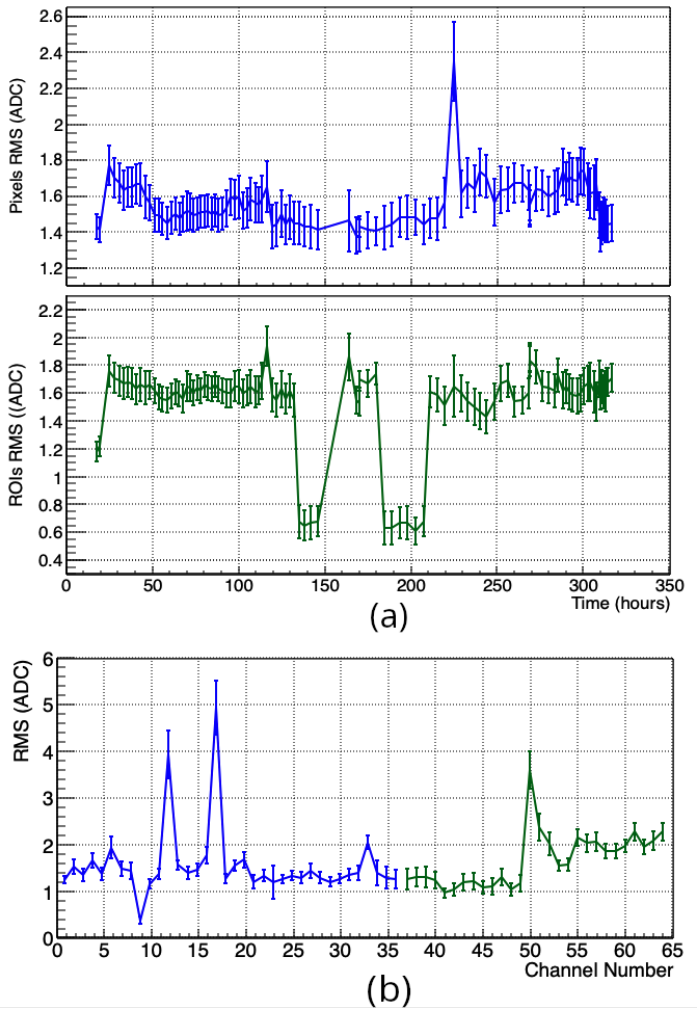

Figure 10.10: The average RMS noise on the pixel and ROI versus time (b) and channel number (a). The graphs in (a) show the average RMS noise as a function of time in hours for the pixels at the top and the ROIs at the bottom the RMS noise average. Also, the plot in (b) depicts the mean RMS noise on pixels and ROIs, with the first 36 channels representing pixel channels and the remaining channels corresponding to the ROI channels. The errors in the plots represent the standard deviation of the RMS values computed for each event.

The initial stage in the process of hit identification involves minimising the noise present in the channel waveforms to the greatest extent possible. Before analysing the noise characteristics of the waveforms, noise events were precluded from the dataset. An event was deemed to be a noise event if its timing deviated from the triggering time of the CRTs systems, or the event's RMS noise level surpassed 10 ADC.

An module [305] was developed to compare pixel events timing to the triggering timestamp from the selected CRT events, as described in section 10.2.3, to eliminate the noise events from the dataset. After implementing noise event filtering, a total of 1,313 events were rejected, including 1,109 events triggered by the side CRTs and 204 by vertical CRTs. Table 10.3 summarises the selected events up to the current stage.

Stage	Event triggered by	
	Side CRTs	Vertical CRTs
Total Events Recorded	12214	
CRTs Selection	7788	
CRTs Classification	7483	305
Pixel Noise Event Rejection	6374	101

Table 10.3: A summary of events selected up to the current stage.

Before applying the noise filter to the raw data, the noise characteristics were examined of all pixel-readout DAQ channels (pixel and ROI channels). Figure 10.11 shows unfiltered raw data for an event from pixel readout channels, where pixel channels are presented on the left plot, while the ROI channels are on the right plot. As depicted in Figure 10.11, the noise displays a significant level of correlation across all channels, especially pixel-17 and ROI-14.

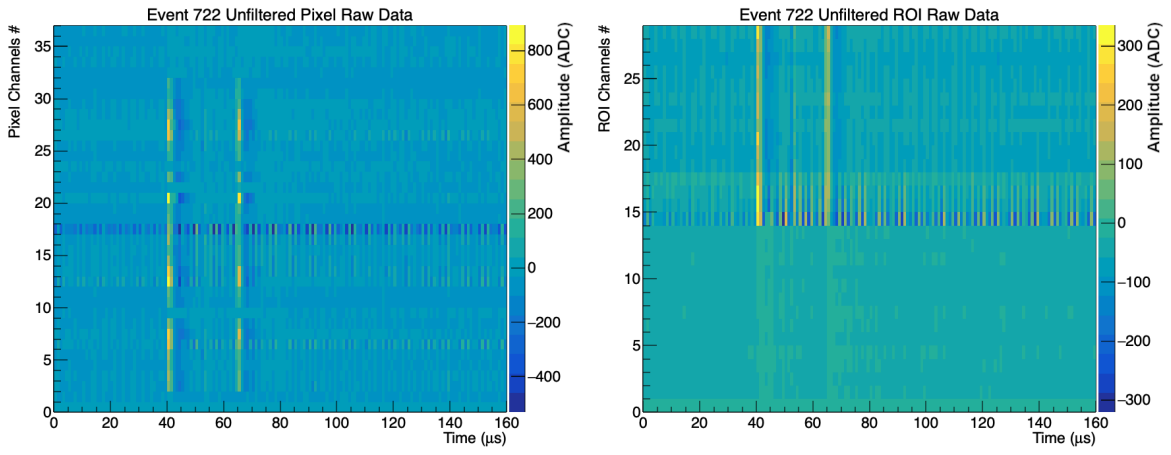

Figure 10.11: Unfiltered raw-data of a typical event from pixel readout. The pixel and ROI channels data for an event are respectively presented on the left and right plots. The colour scale is adjusted to accentuate charge signals in both pixels and ROI channels.

The noise frequencies in the pixel readout channels were analysed using an FFT module, as was done for the CRT data. The grounding was believed to be responsible for the majority of the noise; thus, a study was conducted to mitigate the grounding noise using the FFT algorithm. Three sets of data, each comprising one thousand events triggered by the CRT system, were used to check the grounding noise level. These events were collected while an external grounding cable was unconnected to the system or connected at two different locations. Figure 10.12 compares the noise frequency levels obtained with the different grounding methods. The second position for the external grounding cable had the best outcomes, which was used for this run. As depicted in the figure, two noise frequencies exhibit an amplitude exceeding 700 e^-, likely because the LAr dewar was filled with air during the grounding noise test, this test was conducted prior to running with LAr. The identified noise frequencies were also observed during the LAr run but exhibited a lower amplitude, along with other noise frequencies. Therefore, a low-pass filter was employed to eliminate the noise from the pixel-readout channels before hit finding.

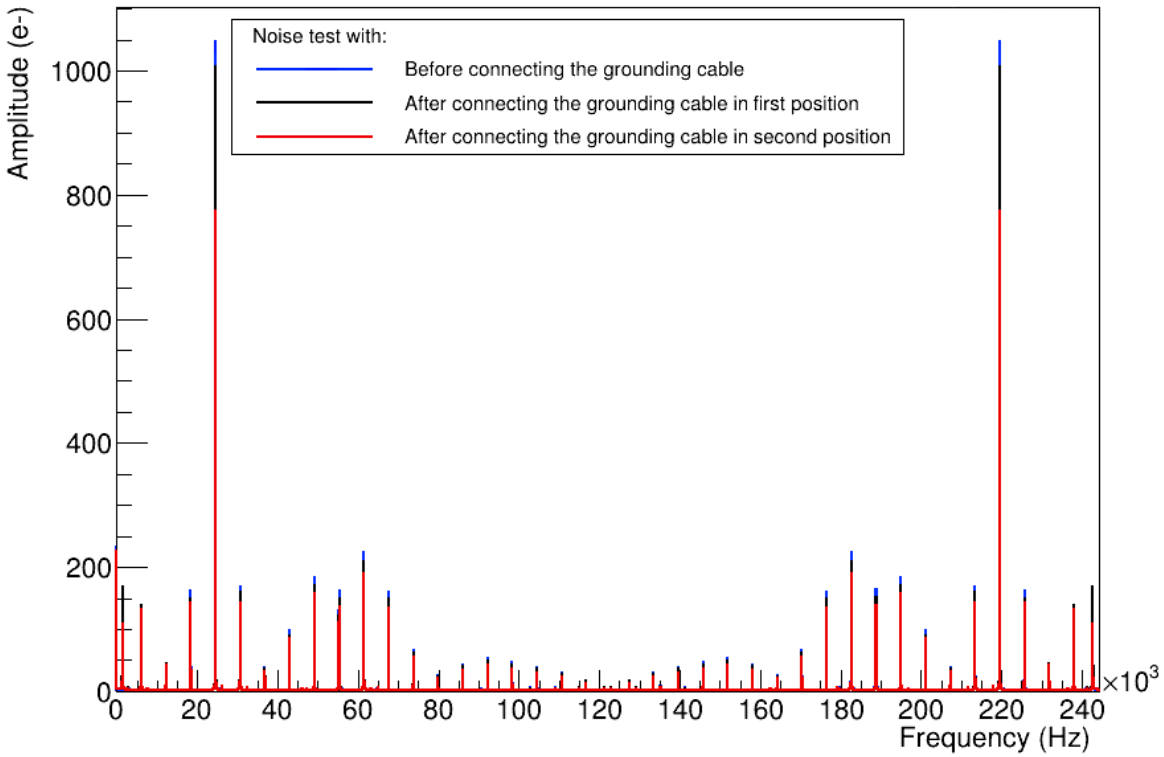

Figure 10.12: Comparison of pixel readout via FFT analysis at various grounding procedures.

Similar to the approach used for the CRTs data, a noise reduction algorithm based on low-pass filtering was employed to eliminate unwanted noise frequencies. This noise reduction was employed after the FFT algorithm was applied to the pixel and ROI channels'

waveforms to analyse noise frequencies. The low-pass filter allows low-frequency signals to pass through while attenuating or removing high-frequency signals. It removes high-frequency noise from a signal while preserving its low-frequency components. The noise filtering module used in this study is based on a low-pass filter with a threshold of 10 ADC. Peaks in the pixel readout waveforms with amplitudes below the threshold or frequencies higher than 4×10^5 Hz are removed. Figure 10.13 depicts filtered raw data of an event from a pixel readout, corresponding to the same event presented in Figure 10.9 and Figure 10.11. Figure 10.13a shows the pixel-9 (blue) and ROI-13 (green) filtered waveforms on the right and left, respectively. Figure 10.13b shows the filtered raw data from the pixel and ROI channels for an event on the right and left, respectively, and the colour scale represents the charge signals.

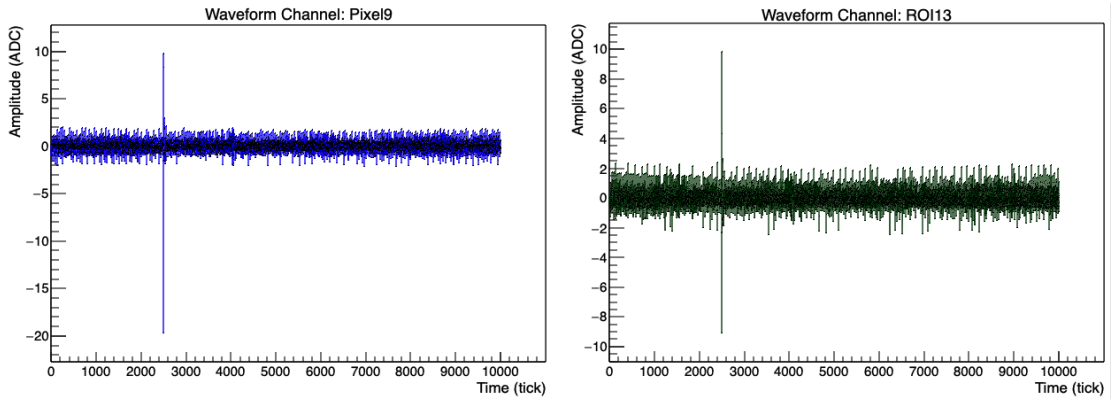

(a)

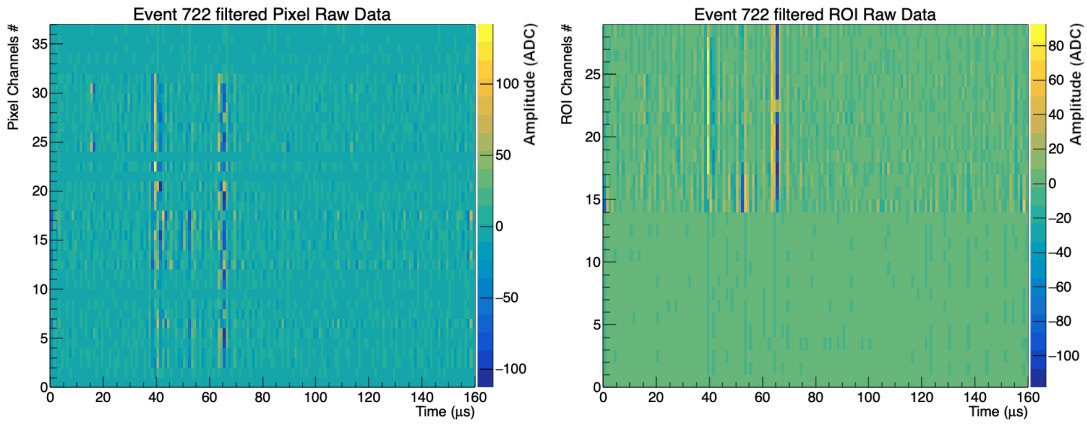

(b)

Figure 10.13: Filtered raw-data of a typical event from pixel readout (the same event as in Figure 10.9 and Figure 10.11). a) Filtered waveform for pixel-9 and ROI-13 triggered by the CRTs depicted on the right and left plots, respectively. b) Filtered raw-data of a typical event from pixel and ROI channels, as displayed on the right and left plots, respectively.

As shown in Figure 10.13a, the application of the filter significantly reduced noise in the waveforms of pixel-9 and ROI-13. Additionally, Figure 10.13b illustrates that noise reduction was substantial across all pixel and ROI channels. It was previously mentioned that the channels pixel-17 and ROI-14 were most affected by noise. However, after applying the filter, noise levels in these channels were significantly reduced, rendering them indistinguishable from other channels. Following the reduction of noise from the pixel and ROI channels waveforms, the next step was to identify the signal peaks in both pixel and ROI channels and match them to reconstruct the events.

10.3.3 Hit Finding and Matching

Upon the successful reduction of noise in the pixel and ROI channels waveforms, the next crucial step was to apply a hit-finding algorithm to identify the signal peaks in the pixel readout channels. This step is fundamental in analysing data from the LArPixel charge readout system. At this stage, a basic hit-finding algorithm was used to locate the signal peaks, which involves segmenting the waveform into time slices of 100 ticks and then iterating through each slice. If the amplitude exceeded five times the RMS value, the peak was identified as a signal peak and saved. This process was repeated for all waveforms obtained from both pixel and ROI channels of an event, and potential signal peaks were saved for each channel. Figure 10.14 depicts an instance of a hit found on pixel (top) and ROI (bottom) channels.

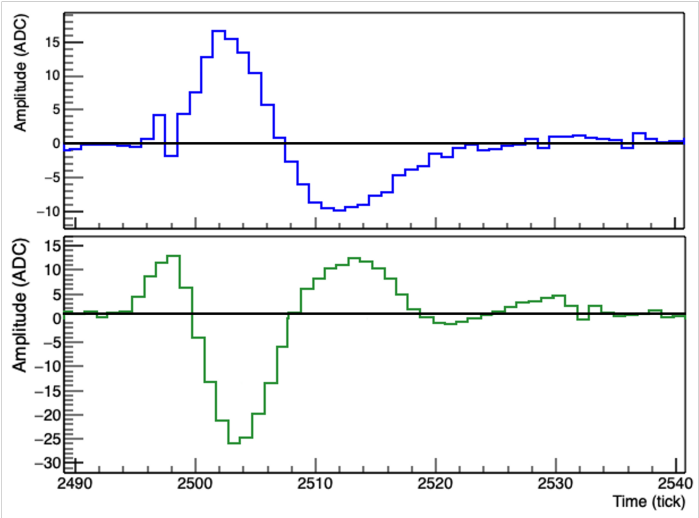

Figure 10.14: Typical MIP event pulse shapes for a single pixel (top) and ROI (bottom) hits.

After identifying potential signal peaks within the waveforms of both pixel and ROI channels, a matching algorithm was used to identify the corresponding peaks between the

two channels. The objective of matching the peaks in the pixel and ROI channels was to associate the pixels with their corresponding ROIs and eliminate any noise peaks that did not have a matching peak in either pixel or ROI channels. The matching process involved comparing the timing of the pixel peaks to those of the ROI peaks. An ROI peak may be matched with multiple pixel peaks, but each pixel peak can only be matched with one ROI peak. An example of a hit from a pixel (top) matched to a hit from an ROI (bottom) is shown in Figure 10.14.

Per the information reconstructed from the hit finding and matching algorithms, a two-dimensional (2D) event display module was developed. The first step involved creating a mapping system to designate the pixel and ROI channels according to their unique channel IDs. After matching the pluses of the pixels pluses and the ROIs, their channel IDs were compared to the mapping system to locate the hits on the pixel board. The mapping system and 2D event display were evaluated by conducting a test on a fake event, as illustrated in Figure 10.15a. Figure 10.15b shows a 2D event display of the same event from in previous figures. The event display illustrates that several hits with varying energy levels, up to 50 ADC amplitude, were deposited on the pixel board. No discernible track of a single particle can be observed, as multiple track-like particles may have deposited energy in the LAr detector during the detection window. A total of 10,000 tick waveforms were recorded for each pixel and ROI channel, corresponding to a time of 160 μs or a distance of approximately 20 cm at an electric field strength of 300 (V/cm). Hence, three-dimensional (3D) reconstruction was essential for understanding to understand the events detected by the LAr detector.

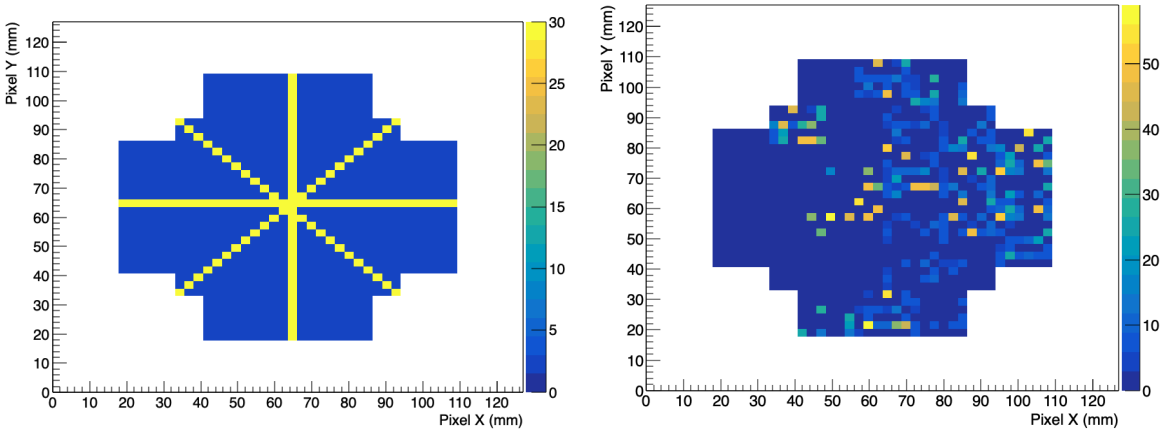

(a) (b)

Figure 10.15: (a) A two-dimensional event display with fake data. (b) A two-dimensional event display showing the energy deposited by a typical event in the LArPixels detector. The colour scale represents the amplitude of the hits in ADC.

10.3.4 3D Reconstruction

In order to gain a comprehensive understanding of the phenomena taking place within the LAr detector, it was imperative to perform a 3D reconstruction incorporating time information. The first step was to transform the time coordinate into a spatial coordinate, which is directly proportional to the strength of the drifting field. In LAr detectors, achieving this conversion was a multifaceted process that necessitated considering of several factors, including the electric field strength, the temperature of the liquid argon, and the detector geometry. The conversion is based on the fundamental principle that the time required for a particle to drift through the LAr is proportional to the distance travelled, which is determined by the speed at which it drifts towards the anode. A study was conducted to estimate the drift velocity in the LAr detector based on data points from references [306, 307] [308].

Figure 10.16 shows the electron drift velocities (cm/10^{-5} s) as a function of electric field strength (V/cm). The data points were fitted with a polynomial of degree two to estimate the drift velocity, as depicted in Figure 10.16. Following the estimation of the drift velocity via the regression equation, the distance travelled by the ionisation electrons was calculated by multiplying the drift velocity by the elapsed time.

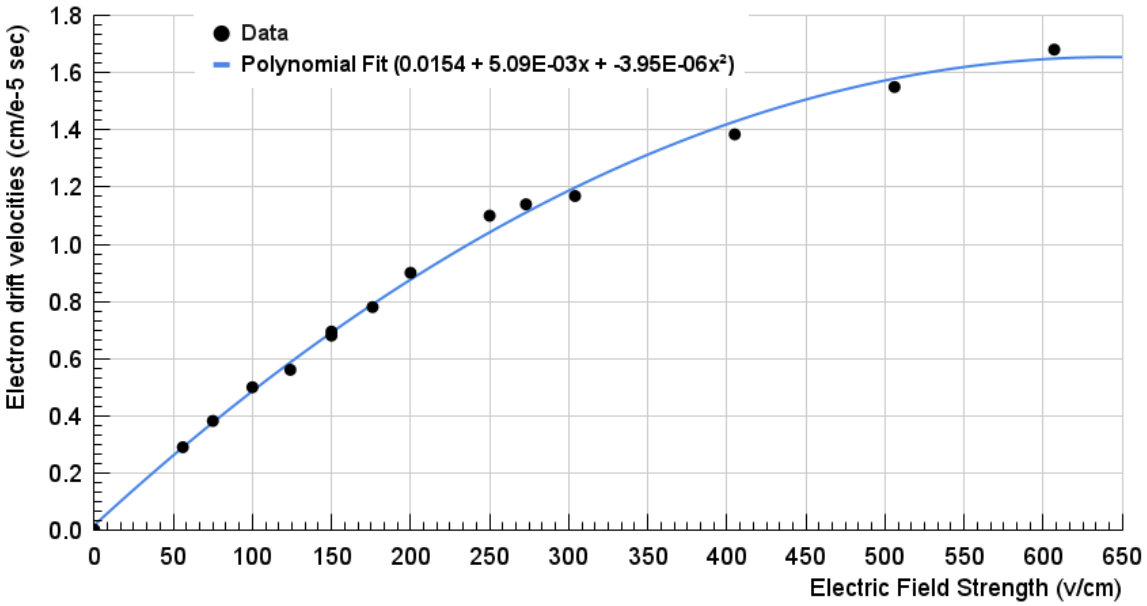

Figure 10.16: Electron drift velocities versus drift field strength.

A 3D event display was developed after transforming the time coordinate to the space coordinate. Figure 10.17 shows a 3D event display of the same event as in Figure 10.15b. As depicted in the event display, it is possible to identify two distinct track-like events, one at approximately 40 mm and the other at 63 mm. The two tracks shown have several hits with a various energies deposited, as shown by the colour scale.

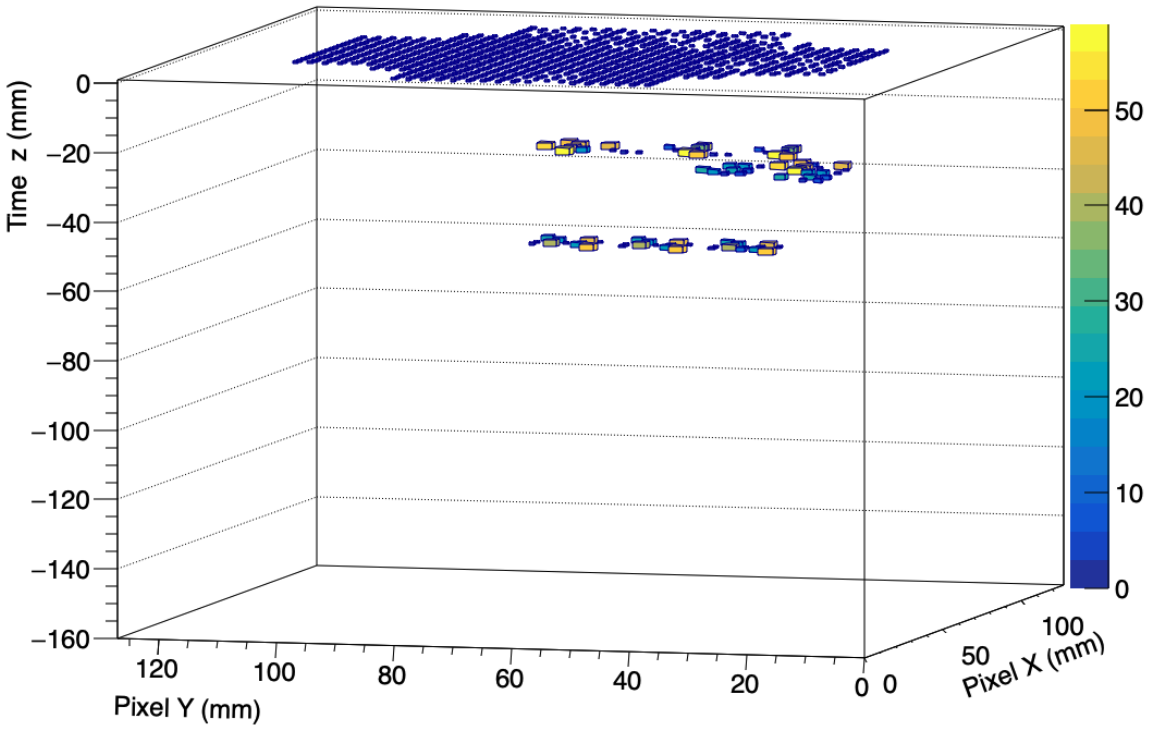

Figure 10.17: A 3D event display showing the energy deposited by a typical event in the LArPixels detector. The colour scale represents the amplitude of the hits in ADC.

From Figure 10.15b and Figure 10.17, it can be concluded that a charge deposition on the pixel plane was observed using the external triggers from the CRT system. Advanced algorithms for hit finding and noise filtering are under development for further analysis.

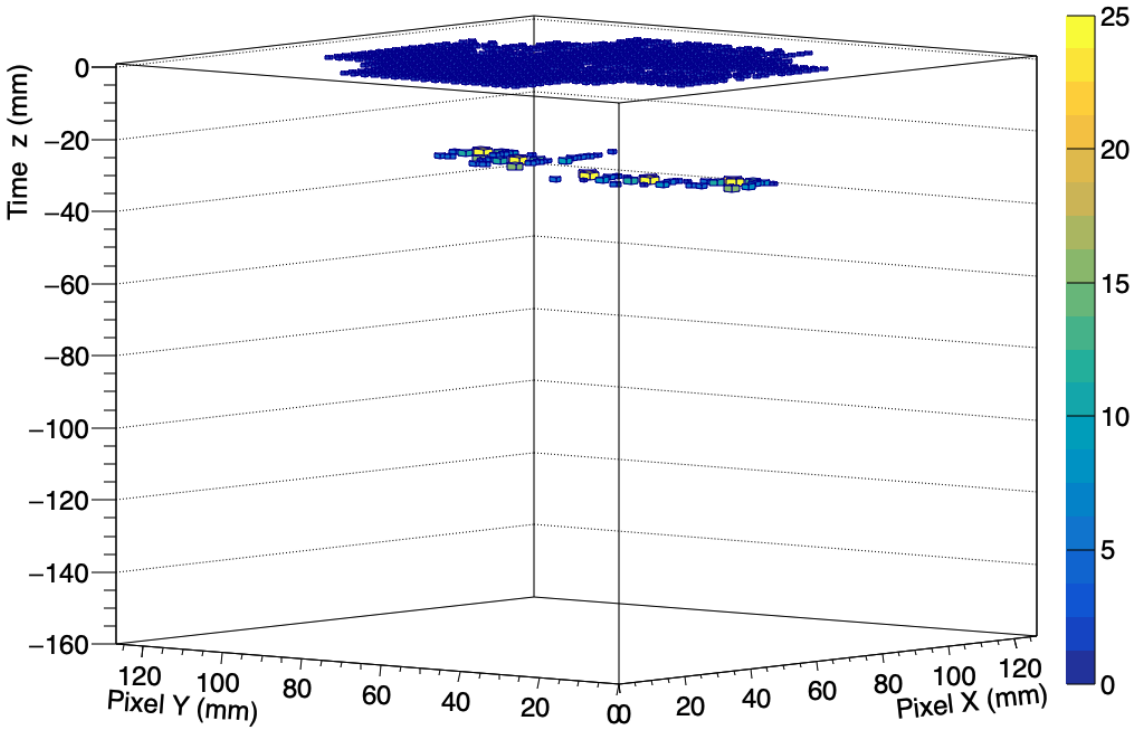

Figure 10.18: Another 3D event display showing the energy deposited by a typical event in the LArPixels detector. The colour scale represents the amplitude of the hits in ADC.

10.4 Summary

A 343 hour test was conducted to evaluate the performance of a LArPixel charge readout system. During the 14-day test, a total of 12,214 events were triggered, with an average of around 850 events per day. The Sheffield LAr test stand exhibited stability and performed as expected. The LAr level remained stable, with only a slight decrease observed on the fifth day, and the temperature and pressure within the LAr dewar were well-regulated, with only minor fluctuations during LN_2 refilling.

The data during this period were collected using the CRT system as a ".dat" file which was decoded afterwards for analysis. The data obtained from the CRT system underwent a three-step processing procedure, which involved conversion into the ROOT data format, noise filtering, and event selection. After decoding the CRTs data, two types of noise filtering were used to reduce the noise from the CRTs waveforms: one based on Frequency cut and the other on threshold cut. Subsequently, a selection criterion was implemented, resulting

in 7,788 events being retained for pixel event selection. These events were categorised into horizontal and vertical groups based on their triggering.

After decoding the pixel readout data, the events that did not correspond to the selected events from the CRT data were excluded from further analysis. Subsequently, a noise reduction algorithm based on low-pass filtering was used to eradicate unwanted noise frequencies from pixel readout data. Then, the next step was to identify the signal peaks in both pixel and ROI channels and match them to reconstruct the events. Finally, after transforming the time coordinate to the space coordinate, a 3D event display was developed, allowing for the observation of charge deposition on the pixel plane using external triggers from the CRT system.

The results of the experiment showed that the system and the LArPixel charge readout are functional and perform well. The noise filtering and hit-finding algorithms proved effective in reducing noise and detecting the hits in the waveforms, as is evident from the 2D and 3D event displays that clearly indicate the charge deposition on the pixel board. Advanced algorithms are presently being developed for hit finding and noise filtering, to facilitate more comprehensive analysis. Furthermore, additional track information, including energy deposition and angular distribution, is being studied by another PhD student.

Chapter 11

Conclusion

This thesis marks the inaugural evaluation of the Short-Baseline Near Detector (SBND) capabilities to conduct a $\nu_\mu + \overline{\nu}_\mu$ Charged Current (CC) π^0 production exclusive cross section analysis. This measurement holds significant importance for advancing the modelling of neutrino-nucleus interactions, thereby unlocking the potential for future experiments, especially those employing Liquid Argon Time Projection Chambers (LArTPCs). Given its close proximity to the neutrino beam source, SBND aims to amass the highest number of neutrino interactions among all LArTPCs. This extraordinary statistical depth not only yields remarkably low statistical uncertainties but also empowers SBND to explore rare phenomena and exclusive channels.

Assessment and enhancements in the three-level reconstruction process have been presented, discussed in Chapter 5 and 6, aiming to improve the capacity of SBND to conduct this measurement. The assessment of low-level reconstruction tools highlighted their effectiveness in recovering signals with amplitudes exceeding 20 ADC but revealed reduced performance for lower amplitude signals, particularly in the presence of increased noise levels from the data-driven model. While reconstruction efficiency was slightly higher for data-driven noise samples, it significantly compromised the purity of reconstructed hits. Efforts to enhance hit purity through threshold optimisation were explored, demonstrating the improvement of effectiveness with threshold adjustments. Additionally, the performance of photon-electron shower discrimination through dE/dx analysis is improved by tuning the tools for initial track hit reconstruction, redefining the shower best plane, and refining the separation parameters. These led to an enhancement in the separation between the electron and photon showers by 10%. Moreover, the reconstructed shower energy is compared to the true energy, showing good agreement except for high-energy showers where complexities like clustering and containment come into play. Expanding on the enhancements, the shower reconstruction establishes a robust basis for subsequent selections and analyses.

A selection process has been designed to select the $\nu_\mu + \overline{\nu}_\mu$ CC π^0 production signal while effectively eliminating the overwhelming cosmogenic and neutrino-induced background, as detailed in Chapter 7. Despite the initial low purity of the signal, it has been substantially enhanced by removing over 99.997% of cosmic-ray and 98.45% of neutrino-induced backgrounds. This results in a final purity of 67.16% while preserving the efficiency of 39.44%. This enhances the selected sample purity and guarantees the containment of the selected events, thus improving their energy resolution.

Next, extending the discussion on reconstruction and selection mentioned earlier, Chapter 8 assessed SBND capability to measure the $\nu_\mu + \overline{\nu}_\mu$ CC π^0 production exclusive cross section. Since real data were unavailable, the cross section was computed using simulated data, employing GENIEv3 as the interaction model. The primary source of uncertainty in the integrated cross section was found to be the underlying interaction model, primarily due to discrepancies between the nominal value and reweighted universes, contributing 11.97% to the total 15.59% error. Additional uncertainty arose from the flux (9.79%), while statistical uncertainties made a minor 0.16% contribution.

Additional research and development endeavours were presented in Chapter 9, including the establishment of a liquid argon test stand at the University of Sheffield. This test stand was aimed to assess novel electronic readout systems for upcoming liquid argon experiments, with an initial emphasis on evaluating a 3D pixelated readout for the near detector of the Deep Underground Neutrino Experiment (DUNE). The University of Sheffield test stand featured a LArTPC with sub-detectors, designed and tested for this purpose. The systems underwent evaluation at the individual, subgroup, and group levels to ensure their intended functionality. Firstly, an assessment of the components within the LAr dewar confirmed their proper operation, requiring no further tests. Subsequently, after the LAr dewar was sealed, multiple leak tests were conducted, resulting in a final leak rate of 0.14 mbar/day, deemed satisfactory. External CRTs were then scrutinised and found to perform as intended. Additionally, the pixel-readout equipment and connections up to the pixel board were tested through the transmission of a test pulse, which yielded signals on both the pixel and ROI channels, affirming their functionality as designed. Lastly, a successful argon recirculation test was conducted, during which the Sheffield systems operated stably for several hours without any issues. Engineering studies of the Sheffield test stand systems indicate the feasibility of running evaluations of the pixel readout system over a period of two to three weeks.

Finally, during a 343-hour test of a LArPixel charge readout system, 12,214 events were triggered over 14 days, averaging around 850 events daily. The Sheffield LAr test stand demonstrated stability, with minor fluctuations in LAr level, temperature, and pressure.

The CRT data was analysed using a three-step process: conversion to ROOT format, noise filtering using frequency and threshold cuts, and event selection, resulting in 7,788 events being retained for pixel event selection. These were categorised as horizontal and vertical groups based on triggering. Non-matching pixel readout events were excluded, and a low-pass filtering noise reduction method was applied. Next, signal peaks in both pixel and ROI channels were identified and matched to reconstruct events. The time coordinate was transformed into a space coordinate, creating a 3D event display for charge deposition observation using CRT triggers. Results showed the system and LArPixel charge readout worked well. The noise filtering and hit-finding algorithms proved effective in reducing noise and detecting the hits in the waveforms, as is evident from the 2D and 3D event displays that clearly indicate the charge deposition on the pixel board. Advanced algorithms for hit finding and noise reduction are under development to enhance analysis.

References

[1] R. Acciarri et al. A Proposal for a Three Detector Short-Baseline Neutrino Oscillation Program in the Fermilab Booster Neutrino Beam, 2015.

[2] BNL. Liquid argon properties (tables and calculators). https://lar.bnl.gov/properties/#refs. Accessed: 17-07-2023.

[3] C. Andreopoulos, C. Barry, S. Dytman, H. Gallagher, T. Golan, R. Hatcher, G. Perdue, and J. Yarba. The GENIE Neutrino Monte Carlo Generator: Physics and User Manual, 2015.

[4] C. Ellis and W. Wooster. The average energy of disintegration of radium E. *Proceedings of the Royal Society of London. Series A, Containing Papers of a Mathematical and Physical Character*, 117:109–123, 12 1927.

[5] P. Hernández. Neutrino Physics. *CERN Yellow Reports*, 5:85–85, 12 2016.

[6] Laurie M. Brown. The idea of the neutrino. *Physics Today*, 31(9):23–28, 09 1978.

[7] E. Fermi. Versuch einer Theorie der β-Strahlen. I. *Zeitschrift für Physik*, 88:161–177, 3 1934.

[8] C. Cowan, F. Reines, F. Harrison, H. Kruse, and A. McGuire. Detection of the free neutrino: A confirmation. *Science*, 124:103–104, 7 1956.

[9] S. Neddermeyer and C. Anderson. Note on the Nature of Cosmic-Ray Particles. *Phys. Rev.*, 51:884–886, May 1937.

[10] B. Pontecorvo. Electron and Muon Neutrinos. *Zh. Eksp. Teor. Fiz.*, 37:1751–1757, 1959.

[11] G. Danby, J-M. Gaillard, K. Goulianos, L. M. Lederman, N. Mistry, M. Schwartz, and J. Steinberger. Observation of High-Energy Neutrino Reactions and the Existence of Two Kinds of Neutrinos. *Phys. Rev. Lett.*, 9:36–44, Jul 1962.

[12] L. Perl et al. Evidence for Anomalous Lepton Production in $e^+ - e^-$ Annihilation. *Phys. Rev. Lett.*, 35:1489–1492, 1975.

[13] D. DeCamp et al. Determination of the number of light neutrino species. *Physics Letters B*, 231(4):519–529, 1989.

[14] O. Adriani et al. Determination of the number of light neutrino species. *Physics Letters B*, 292(3):463–471, 1992.

[15] K. Kodama et al. Observation of tau neutrino interactions. *Physics Letters B*, 504(3):218–224, 2001.

[16] J. Formaggio and G. Zeller. From eV to EeV: Neutrino cross sections across energy scales. *Rev. Mod. Phys.*, 84:1307–1341, Sep 2012.

[17] V. Dadykin et al. Detection of a Rare Event on 23 February 1987 by the Neutrino Radiation Detector Under Mont Blanc. *JETP Lett.*, 45:593–595, 1987.

[18] K. Hirata et al. Observation in the Kamiokande-II detector of the neutrino burst from supernova SN1987A. *Phys. Rev. D*, 38:448–458, Jul 1988.

[19] H. Bethe. Energy Production in Stars. *Phys. Rev.*, 55:434–456, Mar 1939.

[20] R. Davis, D. Harmer, and K. Hoffman. Search for Neutrinos from the Sun. *Phys. Rev. Lett.*, 20:1205–1209, May 1968.

[21] Pontecorvo, B. Inverse beta processes and nonconservation of lepton charge. *Zh. Eksp. Teor. Fiz.*, 34:247, 1957.

[22] Pontecorvo, B. Neutrino Experiments and the Problem of Conservation of Leptonic Charge. *Zh. Eksp. Teor. Fiz.*, 53:1717–1725, 1967.

[23] Maki, Z. and Nakagawa, M. and Sakata, S. Remarks on the unified model of elementary particles. *Prog. Theor. Phys.*, 28:870–880, 1962.

[24] M. Peskin and D. Schroeder. *An introduction to quantum field theory*. Westview Press, Colorado, U.S., 1995.

[25] T. Haines et al. Calculation of Atmospheric Neutrino-Induced Backgrounds in a Nucleon-Decay Search. *Phys. Rev. Lett.*, 57:1986–1989, Oct 1986.

[26] Y. Fukuda et al. Evidence for Oscillation of Atmospheric Neutrinos. *Phys. Rev. Lett.*, 81:1562–1567, Aug 1998.

[27] Q. Ahmad et al. Measurement of the Rate of $\nu_e + d \rightarrow p + p + e^-$ Interactions Produced by ^8B Solar Neutrinos at the Sudbury Neutrino Observatory. *Phys. Rev. Lett.*, 87:071301, Jul 2001.

[28] F. Suekane. *Neutrino Oscillations*, volume 898. Springer Japan, 2015.

[29] J. Bahcall. Solar Neutrino Cross Sections and Nuclear Beta Decay. *Phys. Rev.*, 135:B137–B146, Jul 1964.

[30] K. Hirata et al. Observation of ^{8}B solar neutrinos in the Kamiokande-II detector. *Phys. Rev. Lett.*, 63:16–19, Jul 1989.

[31] K. Hirata et al. Results from one thousand days of real-time, directional solar-neutrino data. *Phys. Rev. Lett.*, 65:1297–1300, Sep 1990.

[32] P. Anselmann et al. Solar neutrinos observed by GALLEX at Gran Sasso. *Physics Letters B*, 285(4):376–389, 1992.

[33] M. Cribier et al. Results of the whole GALLEX experiment. *Nuclear Physics B - Proceedings Supplements*, 70(1):284–291, 1999. Proceedings of the Fifth International Workshop on topics in Astroparticle and Underground Physics.

[34] A. Abazov et al. Search for neutrinos from the Sun using the reaction ^{71}Ga(ν_e,e^-)^{71}Ge. *Phys. Rev. Lett.*, 67:3332–3335, Dec 1991.

[35] J. Abdurashitov et al. Solar neutrino flux measurements by the Soviet-American gallium experiment (SAGE) for half the 22-year solar cycle. *Journal of Experimental and Theoretical Physics*, 95:181–193, 8 2002.

[36] J. Bahcall, F. Calaprice, A. McDonald, and Y. Totsuka. Solar Neutrino Experiments: The Next Generation. *Physics Today*, 49(7):30–36, 07 1996.

[37] T. Gaisser and M. Honda. FLUX OF ATMOSPHERIC NEUTRINOS. *Annual Review of Nuclear and Particle Science*, 52(1):153–199, 2002.

[38] T. Haines et al. Calculation of Atmospheric Neutrino-Induced Backgrounds in a Nucleon-Decay Search. *Phys. Rev. Lett.*, 57:1986–1989, Oct 1986.

[39] K. Hirata et al. Experimental study of the atmospheric neutrino flux. *Physics Letters B*, 205(2):416–420, 1988.

[40] K. Hirata et al. Observation of a small atmospheric ν_μ/ν_e ratio in Kamiokande. *Physics Letters B*, 280(1):146–152, 1992.

[41] et al. R. Becker-Szendy. Electron- and muon-neutrino content of the atmospheric flux. *Phys. Rev. D*, 46:3720–3724, Nov 1992.

[42] Edward Tyley. *Reconstructing and Selecting Electron Neutrino and Anti-Neutrino Interactions on Argon in the Short-Baseline Near Detector*. PhD thesis, The University of Sheffield, 2 2023.

[43] S. Bilenky, J. Hošek, and S. Petcov. On the oscillations of neutrinos with Dirac and Majorana masses. *Physics Letters B*, 94(4):495–498, 1980.

[44] C. Giunti. *THEORY OF NEUTRINO OSCILLATIONS*. World Scientific Pub Co Pte Lt, 4 2005.

[45] K. Abe et al. Constraint on the matter–antimatter symmetry-violating phase in neutrino oscillations. *Nature 2020 580:7803*, 580:339–344, 4 2020.

[46] Y. Ashie et al. Evidence for an Oscillatory Signature in Atmospheric Neutrino Oscillations. *Phys. Rev. Lett.*, 93:101801, Sep 2004.

[47] Q. Ahmad et al. Direct Evidence for Neutrino Flavor Transformation from Neutral-Current Interactions in the Sudbury Neutrino Observatory. *Phys. Rev. Lett.*, 89:011301, Jun 2002.

[48] M. Aker et al. Improved Upper Limit on the Neutrino Mass from a Direct Kinematic Method by KATRIN. *Phys. Rev. Lett.*, 123:221802, Nov 2019.

[49] M. Aker et al. First direct neutrino-mass measurement with sub-eV sensitivity, 2021.

[50] M Aker et al. KATRIN: status and prospects for the neutrino mass and beyond. *Journal of Physics G: Nuclear and Particle Physics*, 49(10):100501, sep 2022.

[51] R. L. Workman and Others. Review of Particle Physics. *PTEP*, 2022:083C01, 2022. Accessed: 17-07-2023.

[52] X. Qian and P. Vogel. Neutrino mass hierarchy. *Progress in Particle and Nuclear Physics*, 83:1–30, 2015.

[53] A. Angelis and M. Pimenta. *The Properties of Neutrinos*. Springer International Publishing, Cham, 2018.

[54] Which neutrino is the lightest? | All Things Neutrino. https://neutrinos.fnal.gov/mysteries/mass-ordering/#moreinfo. Accessed: 17-07-2023.

[55] B. Aharmim et al. Combined analysis of all three phases of solar neutrino data from the Sudbury Neutrino Observatory. *Phys. Rev. C*, 88:025501, Aug 2013.

[56] G. Bellini et al. Neutrinos from the primary proton–proton fusion process in the Sun. *Nature 2014 512:7515*, 512:383–386, 8 2014.

[57] K. Abe et al. Solar neutrino results in Super-Kamiokande-III. *Phys. Rev. D*, 83:052010, Mar 2011.

[58] A. Gando et al. Reactor on-off antineutrino measurement with KamLAND. *Phys. Rev. D*, 88:033001, Aug 2013.

[59] D. Adey et al. Measurement of the Electron Antineutrino Oscillation with 1958 Days of Operation at Daya Bay. *Phys. Rev. Lett.*, 121:241805, Dec 2018.

[60] G. Bak et al. Measurement of Reactor Antineutrino Oscillation Amplitude and Frequency at RENO. *Phys. Rev. Lett.*, 121:201801, Nov 2018.

[61] H. de-Kerret et al. Double Chooz θ_{13} measurement via total neutron capture detection. *Nature Physics 2020 16:5*, 16:558–564, 4 2020.

[62] K. Abe et al. Search for *CP* Violation in Neutrino and Antineutrino Oscillations by the T2K Experiment with 2.2×10^{21} Protons on Target. *Phys. Rev. Lett.*, 121:171802, Oct 2018.

[63] K. Abe et al. Search for Electron Antineutrino Appearance in a Long-Baseline Muon Antineutrino Beam. *Phys. Rev. Lett.*, 124:161802, Apr 2020.

[64] M. Acero et al. Improved measurement of neutrino oscillation parameters by the NOvA experiment. *Phys. Rev. D*, 106:032004, Aug 2022.

[65] M. Aartsen et al. Determining neutrino oscillation parameters from atmospheric muon neutrino disappearance with three years of IceCube DeepCore data. *Phys. Rev. D*, 91:072004, Apr 2015.

[66] K. Abe et al. Atmospheric neutrino oscillation analysis with external constraints in Super-Kamiokande I-IV. *Phys. Rev. D*, 97:072001, Apr 2018.

[67] Esteban I, M. Gonzalez-Garcia, M. Maltoni, T. Schwetz, and A. Zhou. The fate of hints: updated global analysis of three-flavor neutrino oscillations. *Journal of High Energy Physics*, 2020:1–22, 9 2020.

[68] Hyper-Kamiokande Proto-Collaboration. Hyper-Kamiokande Design Report, 2018.

[69] B. Abi et al. Deep Underground Neutrino Experiment (DUNE), Far Detector Technical Design Report, Volume II: DUNE Physics, 2020.

[70] F. An et al. Neutrino physics with JUNO. *Journal of Physics G: Nuclear and Particle Physics*, 43(3):030401, feb 2016.

[71] Precision electroweak measurements on the Z resonance. *Physics Reports*, 427(5):257–454, 2006.

[72] S. Gariazzo, C. Giunti, M. Laveder, Y. Li, and E. Zavanin. Light sterile neutrinos*. *Journal of Physics G: Nuclear and Particle Physics*, 43(3):033001, jan 2016.

[73] A. Diaz, C. Argüelles, G. Collin, J. Conrad, and M. Shaevitz. Where are we with light sterile neutrinos? *Physics Reports*, 884:1–59, 2020. Where are we with light sterile neutrinos?

[74] J. Hardin, I. Martinez-Soler, A. Diaz, M. Jin, N. Kamp, C. Argüelles, J. Conrad, and M. Shaevitz. New Clues About Light Sterile Neutrinos: Preference for Models with Damping Effects in Global Fits, 2023.

[75] A. Aguilar et al. Evidence for neutrino oscillations from the observation of $\overline{\nu}_e$ appearance in a $\overline{\nu}_\mu$ beam. *Phys. Rev. D*, 64:112007, Nov 2001.

[76] A. Aguilar-Arevalo et al. Significant Excess of Electronlike Events in the MiniBooNE Short-Baseline Neutrino Experiment. *Phys. Rev. Lett.*, 121:221801, Nov 2018.

[77] A. Aguilar-Arevalo et al. Updated MiniBooNE neutrino oscillation results with increased data and new background studies. *Phys. Rev. D*, 103:052002, Mar 2021.

[78] L. Alvarez-Ruso and E. Saul-Sala. Neutrino interactions with matter and the MiniBooNE anomaly. *The European Physical Journal Special Topics 2021 230:24*, 230:4373–4389, 10 2021.

[79] B. Armbruster et al. Upper limits for neutrino oscillations $\overline{\nu}_\mu \to \overline{\nu}_e$ from muon decay at rest. *Phys. Rev. D*, 65:112001, Jun 2002.

[80] OPERA Collaboration. Final results of the search for $\nu_\mu \to \nu_e$ oscillations with the OPERA detector in the CNGS beam, 2018.

[81] P. Adamson et al. Search for Sterile Neutrinos in MINOS and MINOS+ Using a Two-Detector Fit. *Phys. Rev. Lett.*, 122:091803, Mar 2019.

[82] G. Cheng et al. Dual baseline search for muon antineutrino disappearance at 0.1 eV^2&$lt;\Delta m^2$&$lt;$100 eV^2. *Phys. Rev. D*, 86:052009, Sep 2012.

[83] R. Wendell et al. Atmospheric neutrino oscillation analysis with subleading effects in Super-Kamiokande I, II, and III. *Phys. Rev. D*, 81:092004, May 2010.

[84] M. Dentler, Á. Hernández-Cabezudo, J. Kopp, P. Machado, M. Maltoni, I. Martinez-Soler, and T. Schwetz. Updated global analysis of neutrino oscillations in the presence of eV-scale sterile neutrinos. *Journal of High Energy Physics*, 2018:1–35, 8 2018.

[85] S. Ajimura et al. Technical Design Report (TDR): Searching for a Sterile Neutrino at J-PARC MLF (E56, JSNS2), 2017.

[86] P. Abratenko. Search for Neutrino-Induced Neutral-Current Δ Radiative Decay in MicroBooNE and a First Test of the MiniBooNE Low Energy Excess under a Single-Photon Hypothesis. *Phys. Rev. Lett.*, 128:111801, Mar 2022.

[87] MicroBooNE collaboration. Search for an Excess of Electron Neutrino Interactions in MicroBooNE Using Multiple Final State Topologies, 2022.

[88] I. Alekseev et al. Search for sterile neutrinos at the DANSS experiment. *Physics Letters B*, 787:56–63, 2018.

[89] P. Serebrov et al. Search for sterile neutrinos with the Neutrino-4 experiment and measurement results. *Phys. Rev. D*, 104:032003, Aug 2021.

[90] M. Andriamirado et al. Improved short-baseline neutrino oscillation search and energy spectrum measurement with the PROSPECT experiment at HFIR. *Phys. Rev. D*, 103:032001, Feb 2021.

[91] H. Almazán et al. Improved sterile neutrino constraints from the STEREO experiment with 179 days of reactor-on data. *Phys. Rev. D*, 102:052002, Sep 2020.

[92] K. Abe et al. Search for light sterile neutrinos with the T2K far detector Super-Kamiokande at a baseline of 295 km. *Phys. Rev. D*, 99:071103, Apr 2019.

[93] M. Acero et al. Search for Active-Sterile Antineutrino Mixing Using Neutral-Current Interactions with the NOvA Experiment. *Phys. Rev. Lett.*, 127:201801, Nov 2021.

[94] K. Abe et al. Improved constraints on neutrino mixing from the T2K experiment with 3.13×10^{21} protons on target. *Phys. Rev. D*, 103:112008, Jun 2021.

[95] M. Acero et al. New constraints on oscillation parameters from ν_e appearance and ν_μ disappearance in the NOvA experiment. *Phys. Rev. D*, 98:032012, Aug 2018.

[96] T. Ngoc, S. Cao, N. Hong Van, and P. Quyen. Stringent constraint on *CPT* violation with the synergy of T2K-II, NOνA extension, and JUNO. *Phys. Rev. D*, 107:016013, Jan 2023.

[97] M. Ramírez et al. Updated T2K measurements of muon neutrino and antineutrino disappearance using 3.6×10^{21} protons on target, 2023.

[98] J. Nieves, F. Sánchez, I. Simo, and M. Vacas. Neutrino energy reconstruction and the shape of the charged current quasielastic-like total cross section. *Phys. Rev. D*, 85:113008, Jun 2012.

[99] M. Day and K. McFarland. Differences in quasielastic cross sections of muon and electron neutrinos. *Phys. Rev. D*, 86:053003, Sep 2012.

[100] J. Wolcott et al. Measurement of Electron Neutrino Quasielastic and Quasielasticlike Scattering on Hydrocarbon at $<E_\nu> = 3.6$ GeV. *Phys. Rev. Lett.*, 116:081802, Feb 2016.

[101] k. Abe et al. Measurement of the muon neutrino charged-current single π^+ production on hydrocarbon using the T2K off-axis near detector ND280. *Phys. Rev. D*, 101:012007, Jan 2020.

[102] T2K Collaboration. First measurement of muon neutrino charged-current interactions on hydrocarbon without pions in the final state using multiple detectors with correlated energy spectra at t2k, 2023.

[103] DUNE Collaboration. The DUNE Far Detector Interim Design Report Volume 1: Physics, Technology and Strategies, 2018.

[104] DUNE Collaboration. The DUNE Far Detector Interim Design Report, Volume 2: Single-Phase Module, 2018.

[105] DUNE Collaboration. The DUNE Far Detector Interim Design Report, Volume 3: Dual-Phase Module, 2018.

[106] C. Andreopoulos el al. The GENIE neutrino Monte Carlo generator. *Nuclear Instruments and Methods in Physics Research Section A: Accelerators, Spectrometers, Detectors and Associated Equipment*, 614(1):87–104, 2010.

[107] J. Hewett et al. Fundamental Physics at the Intensity Frontier, 2012.

[108] C. Llewellyn Smith. Neutrino reactions at accelerator energies. *Physics Reports*, 3(5):261–379, 1972.

[109] R. Subedi et al. Probing Cold Dense Nuclear Matter. *Science*, 320(5882):1476–1478, 2008.

[110] J. Nieves, I. Ruiz Simo, and M. Vacas. Inclusive charged-current neutrino-nucleus reactions. *Phys. Rev. C*, 83:045501, Apr 2011.

[111] R. Gran, J. Nieves, F. Sanchez, and M. Vacas. Neutrino-nucleus quasi-elastic and 2p2h interactions up to 10 GeV. *Phys. Rev. D*, 88:113007, Dec 2013.

[112] J. Amaro, M. Barbaro, J. Caballero, T. Donnelly, A. Molinari, and I. Sick. Using electron scattering superscaling to predict charge-changing neutrino cross sections in nuclei. *Phys. Rev. C*, 71:015501, Jan 2005.

[113] M. Martini, M. Ericson, G. Chanfray, and J. Marteau. Unified approach for nucleon knock-out and coherent and incoherent pion production in neutrino interactions with nuclei. *Phys. Rev. C*, 80:065501, Dec 2009.

[114] V. Pandey, N. Jachowicz, M. Martini, R. González-Jiménez, J. Ryckebusch, T. Van Cuyck, and N. Van Dessel. Impact of low-energy nuclear excitations on neutrino-nucleus scattering at MiniBooNE and T2K kinematics. *Phys. Rev. C*, 94:054609, Nov 2016.

[115] T. Katori. Meson exchange current (MEC) models in neutrino interaction generators. In *AIP conference proceedings*, volume 1663. AIP Publishing, 2015.

[116] D. Rein and L. Sehgal. Neutrino-excitation of baryon resonances and single pion production. *Annals of Physics*, 133(1):79–153, 1981.

[117] D. Rein and L. Sehgal. Coherent π^0 production in neutrino reactions. *Nuclear Physics B*, 223(1):29–44, 1983.

[118] C. Berger and L. Sehgal. Lepton mass effects in single pion production by neutrinos. *Phys. Rev. D*, 76:113004, Dec 2007.

[119] A. Bodek and U. Yang. Higher twist, ξ_w scaling, and effective LO PDFs for lepton scattering in the few GeV region. *Journal of Physics G: Nuclear and Particle Physics*, 29(8):1899, jul 2003.

[120] T. Yang, C. Andreopoulos, H. Gallagher, K. Hofmann, and P. Kehayias. A hadronization model for few-GeV neutrino interactions. *The European Physical Journal C 2009 63:1*, 63:1–10, 8 2009.

[121] R. Smith and E. Moniz. Neutrino reactions on nuclear targets. *Nuclear Physics B*, 43:605–622, 1972.

[122] M. Ascencio-Sosa. *From light neutrino decay phenomenology to muon neutrino cross-section measurement at MINERvA experiment*. PhD thesis, Pontificia Universidad Católica del Perú, 8 2022.

[123] J. Sobczyk. Intercomparison of lepton-nucleus scattering models in the quasielastic region. *Phys. Rev. C*, 96:045501, Oct 2017.

[124] W. Kohn and L. Sham. Self-Consistent Equations Including Exchange and Correlation Effects. *Phys. Rev.*, 140:A1133–A1138, Nov 1965.

[125] L. Alvarez-Ruso et al. Recent highlights from GENIE v3. *The European Physical Journal Special Topics 2021 230:24*, 230:4449–4467, 12 2021.

[126] G. Megias et al. Meson-exchange currents and quasielastic predictions for charged-current neutrino-^{12}C scattering in the superscaling approach. *Phys. Rev. D*, 91:073004, Apr 2015.

[127] R. Gran, J. Nieves, F. Sanchez, and M. Vicente Vacas. Neutrino-nucleus quasi-elastic and 2p2h interactions up to 10 GeV. *Phys. Rev. D*, 88:113007, Dec 2013.

[128] T. Golan, C. Juszczak, and J. Sobczyk. Effects of final-state interactions in neutrino-nucleus interactions. *Phys. Rev. C*, 86:015505, Jul 2012.

[129] S. Gollapinni. Neutrino Cross section Future, 2016.

[130] N. Metropolis, R. Bivins, M. Storm, A. Turkevich, J. Miller, and G. Friedlander. Monte Carlo Calculations on Intranuclear Cascades. I. Low-Energy Studies. *Phys. Rev.*, 110:185–203, Apr 1958.

[131] O. Buss, T. Gaitanos, K. Gallmeister, H. van Hees, M. Kaskulov, O. Lalakulich, A. Larionov, T. Leitner, J. Weil, and U. Mosel. Transport-theoretical description of nuclear reactions. *Physics Reports*, 512(1):1–124, 2012. Transport-theoretical Description of Nuclear Reactions.

[132] Júlia Tena-Vidal, Costas Andreopoulos, Adi Ashkenazi, Christopher Barry, Steve Dennis, Steve Dytman, Hugh Gallagher, Steven Gardiner, Walter Giele, Robert Hatcher, Or Hen, Libo Jiang, Igor D. Kakorin, Konstantin S. Kuzmin, Anselmo Meregaglia, Vadim A. Naumov, Afroditi Papadopoulou, Gabriel Perdue, Marco Roda, Vladyslav Syrotenko, and Jeremy Wolcott. Neutrino-nucleon cross-section model tuning in genie v3. *Phys. Rev. D*, 104:072009, Oct 2021.

[133] S. Dytman, Y. Hayato, R. Raboanary, J. T. Sobczyk, J. Tena-Vidal, and N. Vololoniaina. Comparison of validation methods of simulations for final state interactions in hadron production experiments. *Phys. Rev. D*, 104:053006, Sep 2021.

[134] W. Mann et al. Study of the Reaction $\nu + n \to \mu^- + p$. *Phys. Rev. Lett.*, 31:844–847, Sep 1973.

[135] S. Barish et al. Study of neutrino interactions in hydrogen and deuterium: Description of the experiment and study of the reaction $\nu + d \to \mu^- + p + p_s$. *Phys. Rev. D*, 16:3103–3121, Dec 1977.

[136] T. Kitagaki et al. High-energy quasielastic $\nu_\mu n \to \mu^- p$ scattering in deuterium. *Phys. Rev. D*, 28:436–442, Aug 1983.

[137] V. Bernard, L. Elouadrhiri, and U. Meißner. Axial structure of the nucleon. *Journal of Physics G: Nuclear and Particle Physics*, 28(1):R1, nov 2001.

[138] A. Aguilar-Arevalo et al. First measurement of the muon neutrino charged current quasielastic double differential cross section. *Phys. Rev. D*, 81:092005, May 2010.

[139] et al. S. Barish. Study of the Isospin Properties of Single-Pion Production by Neutrinos. *Phys. Rev. Lett.*, 36:179–183, Jan 1976.

[140] G. Radecky et al. Study of single-pion production by weak charged currents in low-energy νd interactions. *Phys. Rev. D*, 25:1161–1173, Mar 1982.

[141] S. Adler. Photo-, electro-, and weak single-pion production in the (3,3) resonance region. *Annals of Physics*, 50(2):189–311, 1968.

[142] T. Kitagaki et al. Charged-current exclusive pion production in neutrino-deuterium interactions. *Phys. Rev. D*, 34:2554–2565, Nov 1986.

[143] H. Grabosch et al. Cross-section measurements of single pion production in charged current neutrino and antineutrino interactions. *Zeitschrift für Physik C Particles and Fields*, 41:527–531, 12 1989.

[144] D. Allasia et al. Investigation of exclusive channels in $\nu/\bar{\nu}$ deuteron charged current interactions. *Nuclear Physics B*, 343(2):285–309, 1990.

[145] O. Lalakulich, E. Paschos, and G. Piranishvili. Resonance production by neutrinos: The second resonance region. *Phys. Rev. D*, 74:014009, Jul 2006.

[146] T. Leitner, L. Alvarez-Ruso, and U. Mosel. Charged current neutrino-nucleus interactions at intermediate energies. *Phys. Rev. C*, 73:065502, Jun 2006.

[147] E. Hernández, J. Nieves, and M. Valverde. Weak pion production off the nucleon. *Phys. Rev. D*, 76:033005, Aug 2007.

[148] T. Leitner, O. Buss, L. Alvarez-Ruso, and U. Mosel. Electron- and neutrino-nucleus scattering from the quasielastic to the resonance region. *Phys. Rev. C*, 79:034601, Mar 2009.

[149] D. Casper. The nuance neutrino physics simulation, and the future. *Nuclear Physics B - Proceedings Supplements*, 112(1):161–170, 2002.

[150] Y. Hayato. Neut. *Nuclear Physics B - Proceedings Supplements*, 112(1):171–176, 2002.

[151] H. Gallagher. The NEUGEN neutrino event generator. *Nuclear Physics B - Proceedings Supplements*, 112(1):188–194, 2002.

[152] Y. Kurimoto et al. Measurement of inclusive neutral current π^0 production on carbon in a few-GeV neutrino beam. *Phys. Rev. D*, 81:033004, Feb 2010.

[153] Joan Cataì Pérez. *Measurement of neutrino induced charged current neutral pion production cross section at SciBooNE.* PhD thesis, University of Valencia, 11 2013.

[154] C. Mariani et al. Measurement of inclusive π^0 production in the charged-current interactions of neutrinos in a 1.3-GeV wide band beam. *Phys. Rev. D*, 83:054023, Mar 2011.

[155] A. Aguilar-Arevalo et al. Measurement of ν_μ-induced charged-current neutral pion production cross sections on mineral oil at $E_\nu \in 0.5 - -2.0$ GeV. *Phys. Rev. D*, 83:052009, Mar 2011.

[156] A. Aguilar-Arevalo et al. Measurement of neutrino-induced charged-current charged pion production cross sections on mineral oil at $E_\nu \sim 1$ GeV. *Phys. Rev. D*, 83:052007, Mar 2011.

[157] O. Lalakulich and U. Mosel. Pion production in the MiniBooNE experiment. *Phys. Rev. C*, 87:014602, Jan 2013.

[158] E. Hernández, J. Nieves, and M. Vacas. Single π production in neutrino-nucleus scattering. *Phys. Rev. D*, 87:113009, Jun 2013.

[159] L. Alvarez-Ruso, Y. Hayato, and J. Nieves. Progress and open questions in the physics of neutrino cross sections at intermediate energies. *New Journal of Physics*, 16(7):075015, jul 2014.

[160] C. Wilkinson, P. Rodrigues, S. Cartwright, L. Thompson, and K. McFarland. Reanalysis of bubble chamber measurements of muon-neutrino induced single pion production. *Phys. Rev. D*, 90:112017, Dec 2014.

[161] P. Rodrigues, C. Wilkinson, and K. McFarland. Constraining the GENIE model of neutrino-induced single pion production using reanalyzed bubble chamber data. *The European Physical Journal C 2016 76:8*, 76:1–16, 8 2016.

[162] T. Le et al. Single neutral pion production by charged-current $\overline{\nu}_\mu$ interactions on hydrocarbon at $\langle E_\nu \rangle$ =3.6 GeV. *Physics Letters B*, 749:130–136, 2015.

[163] O. Altinok et al. Measurement of ν_μ charged-current single π^0 production on hydrocarbon in the few-GeV region using MINERvA. *Phys. Rev. D*, 96:072003, Oct 2017.

[164] C. McGivern et al. Cross sections for ν_μ and $\overline{\nu}_\mu$ induced pion production on hydrocarbon in the few-GeV region using MINERvA. *Phys. Rev. D*, 94:052005, Sep 2016.

[165] P. Stowell et al. Tuning the genie pion production model with MINERvA data. *Phys. Rev. D*, 100:072005, Oct 2019.

[166] P. Adamson et al. Study of quasielastic scattering using charged-current ν_μ-iron interactions in the MINOS near detector. *Phys. Rev. D*, 91:012005, Jan 2015.

[167] C. Rubbia. The Liquid Argon Time Projection Chamber: A New Concept for Neutrino Detectors. *CERN*, 5 1977.

[168] C. Adams et al. First measurement of ν_μ charged-current π^0 production on argon with the MicroBooNE detector. *Phys. Rev. D*, 99:091102, May 2019.

[169] T. Golan, J. Sobczyk, and J. Żmuda. NuWro: the Wrocław Monte Carlo Generator of Neutrino Interactions. *Nuclear Physics B - Proceedings Supplements*, 229-232:499, 2012. Neutrino 2010.

[170] Li. Yichen et al. Measurement of longitudinal electron diffusion in liquid argon. *Nuclear Instruments and Methods in Physics Research, Section A: Accelerators, Spectrometers, Detectors and Associated Equipment*, 816:160–170, 4 2016.

[171] R. Acciarri et al. Design and construction of the MicroBooNE detector. *Journal of Instrumentation*, 12(02):P02017, feb 2017.

[172] L. Bassi et all ICARUS collaborators. *ICARUS I: an optimized, real time detector of solar neutrinos*. CERN, Geneva, 1989.

[173] S. Bonetti et al. A study of the electron image due to ionizing events in a two-dimensional liquid argon TPC with a 24 cm drift gap. *Nuclear Instruments and Methods in Physics Research Section A: Accelerators, Spectrometers, Detectors and Associated Equipment*, 286(1):135–146, 1990.

[174] S. Amerio et al. Design, construction and tests of the icarus t600 detector. *Nuclear Instruments and Methods in Physics Research Section A: Accelerators, Spectrometers, Detectors and Associated Equipment*, 527(3):329–410, 2004.

[175] A. Ankowski et al. Measurement of through-going particle momentum by means of multiple scattering with the icarus t600 tpc. *The European Physical Journal C - Particles and Fields 2006 48:2*, 48:667–676, 10 2006.

[176] M. Antonello et al. Experimental observation of an extremely high electron lifetime with the icarus-t600 lar-tpc. *Journal of Instrumentation*, 9(12):P12006, dec 2014.

[177] C. Anderson el al. The ArgoNeuT detector in the NuMI low-energy beam line at Fermilab. *Journal of Instrumentation*, 7(10):P10019, oct 2012.

[178] R. Acciarri et al. Detection of back-to-back proton pairs in charged-current neutrino interactions with the argoneut detector in the numi low energy beam line. *Phys. Rev. D*, 2014.

[179] C. Anderson et al. First measurements of inclusive muon neutrino charged current differential cross sections on argon. *Phys. Rev. Lett.*, 108:161802, Apr 2012.

[180] R. Acciarri et al. Measurements of inclusive muon neutrino and antineutrino charged current differential cross sections on argon in the numi antineutrino beam. *Phys. Rev. D*, 89:112003, Jun 2014.

[181] R. Acciarri et al. First measurement of neutrino and antineutrino coherent charged pion production on argon. *Phys. Rev. Lett.*, 113:261801, Dec 2014.

[182] R. Acciarri et al. Measurement of ν_μ and $\overline{\nu}_\mu$ neutral current $\pi^0 \to \gamma\gamma$ production in the argoneut detector. *Phys. Rev. D*, 96:012006, Jul 2017.

[183] R. Acciarri et al. First measurement of the cross section for ν_μ and $\overline{\nu}_\mu$ induced single charged pion production on argon using argoneut. *Phys. Rev. D*, 98:052002, Sep 2018.

[184] R. Acciarri et al. First measurement of electron neutrino scattering cross section on argon. *Phys. Rev. D*, 102:011101, Jul 2020.

[185] R. Acciarri et al. The liquid argon in a testbeam (lariat) experiment. *Journal of Instrumentation*, 15(04):P04026, apr 2020.

[186] E. Gramellini et al. Measurement of the π^--Ar total hadronic cross section at the LArIAT experiment. *Phys. Rev. D*, 106:052009, Sep 2022.

[187] P. Abratenko et al. First Measurement of Inclusive Muon Neutrino Charged Current Differential Cross Sections on Argon at $E_\nu \sim 0.8$ GeV with the MicroBooNE Detector. *Phys. Rev. Lett.*, 123:131801, Sep 2019.

[188] P. Abratenko et al. First Measurement of Differential Charged Current Quasielasticlike ν_μ-Argon Scattering Cross Sections with the MicroBooNE Detector. *Phys. Rev. Lett.*, 125:201803, Nov 2020.

[189] P. Abratenko et al. Search for Neutrino-Induced Neutral-Current Δ Radiative Decay in MicroBooNE and a First Test of the MiniBooNE Low Energy Excess under a Single-Photon Hypothesis. *Phys. Rev. Lett.*, 128:111801, Mar 2022.

[190] MicroBooNE collaboration. Search for an Excess of Electron Neutrino Interactions in MicroBooNE Using Multiple Final State Topologies, 2022.

[191] B. Abi et al. The Single-Phase ProtoDUNE Technical Design Report, 2017.

[192] J. Asaadi et al. First Demonstration of a Pixelated Charge Readout for Single-Phase Liquid Argon Time Projection Chambers. *Instruments*, 4(1), 2020.

[193] D. Dwyer et al. LArPix: demonstration of low-power 3D pixelated charge readout for liquid argon time projection chambers. *Journal of Instrumentation*, 13(10):P10007, oct 2018.

[194] D. E. Groom and S. R. Klein. 23. passage of particles through matter. *Physical Review D - Particles, Fields, Gravitation and Cosmology*, pages 163–173, 2000.

[195] C. Adams et al. Reconstruction and measurement of $\mathcal{O}(100)$ MeV energy electromagnetic activity from $\pi^0 \to \gamma\gamma$ decays in the MicroBooNE LArTPC. *Journal of Instrumentation*, 15(02):P02007, 02 2020.

[196] W. et al. Foreman. Calorimetry for low-energy electrons using charge and light in liquid argon. *Phys. Rev. D*, 101:012010, Jan 2020.

[197] B. Abi et al. Volume IV. The DUNE far detector single-phase technology. *Journal of Instrumentation*, 15(08):T08010, 08 2020.

[198] L. Onsager. Initial Recombination of Ions. *Phys. Rev.*, 54:554–557, Oct 1938.

[199] R. Acciarri et al. A study of electron recombination using highly ionizing particles in the ArgoNeuT Liquid Argon TPC. *Journal of Instrumentation*, 8(08):P08005, Aug 2013.

[200] M. Miyajima, T. Takahashi, S. Konno, T. Hamada, S. Kubota, H. Shibamura, and T. Doke. Average energy expended per ion pair in liquid argon. *Phys. Rev. A*, 9:1438–1443, Mar 1974.

[201] J. Thomas and D. Imel. Recombination of electron-ion pairs in liquid argon and liquid xenon. *Phys. Rev. A*, 36:614–616, Jul 1987.

[202] J. Birks. Scintillations from Organic Crystals: Specific Fluorescence and Relative Response to Different Radiations. *Proceedings of the Physical Society. Section A*, 64(10):874, oct 1951.

[203] R. Acciarri et al. Oxygen contamination in liquid Argon: combined effects on ionization electron charge and scintillation light. *Journal of Instrumentation*, 5(05):P05003, May 2010.

[204] E. Segreto. Evidence of delayed light emission of tetraphenyl-butadiene excited by liquid-argon scintillation light. *Phys. Rev. C*, 91:035503, Mar 2015.

[205] M. Antonello et al. Detection of Cherenkov light emission in liquid argon. *Nuclear Instruments and Methods in Physics Research Section A: Accelerators, Spectrometers, Detectors and Associated Equipment*, 516(2):348–363, 2004.

[206] The MicroBooNE collaboration. Measurement of the longitudinal diffusion of ionization electrons in the MicroBooNE detector. *Journal of Instrumentation*, 16(09):P09025, sep 2021.

[207] Michael Mooney. The MicroBooNE Experiment and the Impact of Space Charge Effects, 2015.

[208] P. Abratenko. Measurement of space charge effects in the MicroBooNE LArTPC using cosmic muons. *Journal of Instrumentation*, 15(12):P12037, Dec 2020.

[209] DUNE Collaboration. Design, construction and operation of the ProtoDUNE-SP Liquid Argon TPC, 2021.

[210] G.M. Seidel, R.E. Lanou, and W. Yao. Rayleigh scattering in rare-gas liquids. *Nuclear Instruments and Methods in Physics Research Section A: Accelerators, Spectrometers, Detectors and Associated Equipment*, 489(1):189–194, 2002.

[211] N. Ishida et al. Attenuation length measurements of scintillation light in liquid rare gases and their mixtures using an improved reflection suppresser. *Nuclear Instruments and Methods in Physics Research Section A: Accelerators, Spectrometers, Detectors and Associated Equipment*, 384(2):380–386, 1997.

[212] R.Teague and C. Plngs. Refractive Index and the Lorentz–Lorenz Function for Gaseous and Liquid Argon, Including a Study of the Coexistence Curve near the Critical State. *The Journal of Chemical Physics*, 48:4973–4984, 6 1968.

[213] D. Garcia-Gamez, P. Green, and A. Szelc. Predicting transport effects of scintillation light signals in large-scale liquid argon detectors. *The European Physical Journal C 2021 81:4*, 81:1–21, 4 2021.

[214] J. Joshi and X. Qian. Signal Processing in the MicroBooNE LArTPC, 2015.

[215] R. Acciarri et al. Noise Characterization and Filtering in the MicroBooNE Liquid Argon TPC. *Journal of Instrumentation*, 12(08):P08003, Aug 2017.

[216] J. Asaadi, M. Auger, A. Ereditato, D. Goeldi, R. Haenni, U. Kose, I Kreslo, D. Lorca, M. Luethi, C. Rudolf Von Rohr, J. R. Sinclair, F. Stocker, C. Tognina, and M. Weber. First demonstration of a pixelated charge readout for single-phase liquid argon time projection chambers. *Instruments 4 (2020)*, 1 2018.

[217] B. Aimard et al. A 4 tonne demonstrator for large-scale dual-phase liquid argon time projection chambers. *Journal of Instrumentation*, 13(11):P11003, nov 2018.

[218] A.A. Machado and E. Segreto. ARAPUCA a new device for liquid argon scintillation light detection. *Journal of Instrumentation*, 11(02):C02004, feb 2016.

[219] A. Machado, E. Segreto, D. Warner, A. Fauth, B. Gelli, R. Máximo, A. Pissolatti, L. Paulucci, and F. Marinho. The X-ARAPUCA: an improvement of the ARAPUCA device. *Journal of Instrumentation*, 13(04):C04026, apr 2018.

[220] D. Totani, G. Cancelo, F. Cavanna, C. Escobar, E. Kemp, F. Marinho, L. Paulucci, D. Phan, S. Mufson, C. Macias, and D. Warner. A measurement of absolute efficiency of the ARAPUCA photon detector in liquid argon. *Journal of Instrumentation*, 15(06):T06003, jun 2020.

[221] A. Falcone et al. Cryogenic SiPM arrays for the DUNE photon detection system. *Nuclear Instruments and Methods in Physics Research Section A: Accelerators, Spectrometers, Detectors and Associated Equipment*, 985:164648, 2021.

[222] M. Bonesini. The short baseline neutrino program at fermilab, 2022.

[223] P. Machado, O. Palamara, and D. Schmitz. The short-baseline neutrino program at fermilab. *Annual Review of Nuclear and Particle Science*, 69(1):363–387, 2019.

[224] N. Kamp and M. Hostert and C. Argüelles and J. Conrad and M. Shaevitz. Implications of MicroBooNE's low sensitivity to electron antineutrino interactions in the search for the MiniBooNE excess. *Phys. Rev. D*, 107:092002, May 2023.

[225] SBN-doc-27037-v1: SBN Oscillation Sensitivity Technical Note (2021). https://sbn-docdb.fnal.gov/cgi-bin/sso/ShowDocument?docid=27037. Accessed: 10-06-2023.

[226] K. Mahn et al. Dual baseline search for muon neutrino disappearance at 0.5 ev^2&lt;Δm^2&lt;40 ev^2. *Phys. Rev. D*, 85:032007, Feb 2012.

[227] M. Aartsen et al. eV-Scale Sterile Neutrino Search Using Eight Years of Atmospheric Muon Neutrino Data from the IceCube Neutrino Observatory. *Phys. Rev. Lett.*, 125:141801, Sep 2020.

[228] L. Alvarez-Ruso et al. NuSTEC White Paper: Status and challenges of neutrino–nucleus scattering. *Progress in Particle and Nuclear Physics*, 100:1–68, 2018.

[229] A. Donini, P. Hernández, J. López-Pavón, M. Maltoni, and T. Schwetz. The minimal 3 + 2 neutrino model versus oscillation anomalies. *Journal of High Energy Physics*, 2012:1–20, 7 2012.

[230] H. Nunokawa P. Machado and R. Funchal. Testing for large extra dimensions with neutrino oscillations. *Phys. Rev. D*, 84:013003, Jul 2011.

[231] P. Masjuan M. Masip and D. Meloni. Heavy neutrino decays at MiniBooNE. *Journal of High Energy Physics*, 2013:1–16, 1 2013.

[232] F. Sala Y. Ema and R. Sato. Light Dark Matter at Neutrino Experiments. *Phys. Rev. Lett.*, 122:181802, May 2019.

[233] A. Aguilar-Arevalo et al. Neutrino flux prediction at MiniBooNE. *Phys. Rev. D*, 79:072002, Apr 2009.

[234] M. Catanesi et al. Measurement of the production cross-section of positive pions in the collision of 8.9 GeV/c protons on beryllium. *The European Physical Journal C 2007 52:1*, 52:29–53, 8 2007.

[235] E. Valencia et al. Constraint of the MINERνA medium energy neutrino flux using neutrino-electron elastic scattering. *Phys. Rev. D*, 100:092001, Nov 2019.

[236] R. Acciarri. Construction of precision wire readout planes for the Short-Baseline Near Detector (SBND). *Journal of Instrumentation*, 15(06):P06033, jun 2020.

[237] M. Auger et al. A novel cosmic ray tagger system for liquid argon tpc neutrino detectors, 2016.

[238] E. Snider and G. Petrillo. LArSoft: toolkit for simulation, reconstruction and analysis of liquid argon TPC neutrino detectors. *Journal of Physics: Conference Series*, 898(4):042057, oct 2017.

[239] C. Green, J. Kowalkowski, M. Paterno, M. Fischler, L. Garren, and Q. Lu. The art framework. *Journal of Physics: Conference Series*, 396(2):022020, dec 2012.

[240] R. Brun and F. Rademakers. ROOT — An object oriented data analysis framework. *Nuclear Instruments and Methods in Physics Research Section A: Accelerators, Spectrometers, Detectors and Associated Equipment*, 389(1):81–86, 1997. New Computing Techniques in Physics Research V.

[241] D. Heck, J. Knapp, J. Capdevielle, G. Schatz, and T. Thouw. CORSIKA: A Monte Carlo code to simulate extensive air showers. 2 1998.

[242] C. Adams et al. Ionization electron signal processing in single phase LArTPCs. Part I. Algorithm Description and quantitative evaluation with MicroBooNE simulation. *Journal of Instrumentation*, 13(07):P07006, jul 2018.

[243] D. Garcia-Gamez. Developing scintillation light readout simulation for the SBND experiment. *Journal of Instrumentation*, 11(01):C01080, jan 2016.

[244] D. Garcia-Gamez, P. Green, and A. Szelc. Predicting transport effects of scintillation light signals in large-scale liquid argon detectors. *The European Physical Journal C 2021 81:4*, 81:1–21, 4 2021.

[245] MicroBooNE Collaboration. Ionization electron signal processing in single phase LArTPCs. Part I. Algorithm Description and quantitative evaluation with MicroBooNE simulation. *Journal of Instrumentation*, 13(07):P07006, jul 2018.

[246] MicroBooNE Collaboration. Ionization electron signal processing in single phase LArTPCs. Part II. Data/simulation comparison and performance in MicroBooNE. *Journal of Instrumentation*, 13(07):P07007, jul 2018.

[247] GausHitFinder module. https://github.com/LArSoft/larreco/blob/86b7154f11685e67d424b40fe1be97a41bb87473/larreco/HitFinder/GausHitFinder_module.cc. Accessed: 08-05-2023.

[248] S. Gao. Low Noise Cold Electronics System for SBND LAr TPC. https://arxiv.org/abs/1910.06434v1, 2019. Accessed: 10-05-2023.

[249] D. Schmitz O. Palamara, M. Stancari. Technical Requirements of the SBND TPC Front-End Electronics, 2017. Accessed: 10-05-2023.

[250] Eric Brochu, Vlad M. Cora, and Nando de Freitas. A tutorial on bayesian optimization of expensive cost functions, with application to active user modeling and hierarchical reinforcement learning. *CoRR*, abs/1012.2599, 2010.

[251] J. S. Marshall and M. A. Thomson. The pandora software development kit for pattern recognition. *The European Physical Journal C 2015 75:9*, 75:1–16, 9 2015.

[252] C. Adams et al. R. Acciarri. The pandora multi-algorithm approach to automated pattern recognition of cosmic-ray muon and neutrino events in the microboone detector. *The European Physical Journal C 2018 78:1*, 78:1–25, 1 2018.

[253] Huong Lan Tran, K. Krüger, F. Sefkow, S. Green, J. Marshall, M. Thomson, and F. Simon. Software compensation in particle flow reconstruction. *The European Physical Journal C 2017 77:10*, 77:1–13, 10 2017.

[254] Lar pandora track creation module. https://github.com/LArSoft/larpandora/blob/589125cbf6536dc0b8e18e20cc5c9498ac62be0f/larpandora/LArPandoraEventBuilding/LArPandoraTrackCreation_module.cc. Accessed: 01-08-2023.

[255] Lartpc calorimetry module. https://github.com/LArSoft/larreco/blob/1d6058c32cd3513a652a5424017e2f6f89db8fee/larreco/Calorimetry/Calorimetry_module.cc. Accessed: 01-08-2023.

[256] P. Abratenko et al. Determination of muon momentum in the MicroBooNE LArTPC using an improved model of multiple Coulomb scattering. *Journal of Instrumentation*, 12(10):P10010, oct 2017.

[257] Lartpc calorimetry module. https://github.com/LArSoft/larpandora/blob/589125cbf6536dc0b8e18e20cc5c9498ac62be0f/larpandora/LArPandoraEventBuilding/LArPandoraShower/LArPandoraModularShowerCreation_module.cc. Accessed: 05-08-2023.

[258] Shower pfp vertex start position tool. https://github.com/LArSoft/larpandora/blob/f6cb58875c82eddd686ed7501a101c44e5f9b818/larpandora/LArPandoraEventBuilding/LArPandoraShower/Tools/ShowerPFPVertexStartPosition_tool.cc. Accessed: 05-08-2023.

[259] Shower pca direction tool. https://github.com/LArSoft/larpandora/blob/f6cb58875c82eddd686ed7501a101c44e5f9b818/larpandora/LArPandoraEventBuilding/LArPandoraShower/Tools/ShowerPCADirection_tool.cc. Accessed: 06-08-2023.

[260] Ian T. Jollife and Jorge Cadima. Principal component analysis: a review and recent developments. *Philosophical Transactions of the Royal Society A: Mathematical, Physical and Engineering Sciences*, 374, 4 2016.

[261] Shower incremental track hit finder. https://github.com/LArSoft/larpandora/blob/f6cb58875c82eddd686ed7501a101c44e5f9b818/larpandora/LArPandoraEventBuilding/LArPandoraShower/Tools/ShowerIncrementalTrackHitFinder_tool.cc. Accessed: 06-08-2023.

[262] Shower 3dcylinder track hit finder. https://github.com/LArSoft/larpandora/blob/f6cb58875c82eddd686ed7501a101c44e5f9b818/larpandora/LArPandoraEventBuilding/LArPandoraShower/Tools/Shower3DCylinderTrackHitFinder_tool.cc. Accessed: 06-08-2023.

[263] Shower trajpoint dedx. https://github.com/LArSoft/larpandora/blob/f6cb58875c82eddd686ed7501a101c44e5f9b818/larpandora/LArPandoraEventBuilding/LArPandoraShower/Tools/ShowerTrajPointdEdx_tool.cc. Accessed: 06-08-2023.

[264] R. Acciarri et al. First observation of low energy electron neutrinos in a liquid argon time projection chamber. *Phys. Rev. D*, 95:072005, Apr 2017.

[265] A. Hoecker et al. TMVA - Toolkit for Multivariate Data Analysis, 2009.

[266] Shower length percentile. https://github.com/LArSoft/larpandora/blob/f6cb58875c82eddd686ed7501a101c44e5f9b818/larpandora/LArPandoraEventBuilding/LArPandoraShower/Tools/ShowerLengthPercentile_tool.cc. Accessed: 07-08-2023.

[267] C. Tegeler, R. Span, and W. Wagner. A New Equation of State for Argon Covering the Fluid Region for Temperatures From the Melting Line to 700 K at Pressures up to 1000 MPa. *Journal of Physical and Chemical Reference Data*, 28(3):779–850, 05 1999.

[268] L. Pickering, P. Stowell, and J. Sobczyk. Event reweighting with the NuWro neutrino interaction generator. *Journal of Physics: Conference Series*, 888(1):012175, sep 2017.

[269] Booster Neutrino Flux Prediction at MicroBooNE. 7 2018.

[270] Y. Li, C. Thorn, W. Tang, J. Joshi, X. Qian, M. Diwan, S. Kettell, W. Morse, T. Rao, J. Stewart, T. Tsang, and L. Zhang. A 20-liter test stand with gas purification for liquid argon research. *Journal of Instrumentation*, 11:T06001, 6 2016.

[271] Omega. Introduction to PT100 RTD Temperature Sensors. https://www.omega.com/en-us/resources/rtd-hub. Accessed: 25-10-2022.

[272] Solid State Pressure Transducer. https://www.omega.co.uk/pptst/PX209_PX219.html. Accessed: 26-10-2022.

[273] GP:50 216 TRANSDUCER INSTALLATION MANUAL. https://www.manualslib.com/manual/1587421/Gp-50-216-316.html#manual. Accessed: 26-10-2022.

[274] Variable Area Flowmeters, G Series and M Series. https://www.swagelok.com/downloads/webcatalogs/en/ms-02-346.pdf. Accessed: 31-10-2022.

[275] X13 and GetterMax113, Water and Oxygen Removal. https://www.catalyst-central.com/product. Accessed: 31-10-2022.

[276] AFArmaFlex Class 0 THE FLEXIBLE & SUSTAINABLE INSULATION SYSTEM FOR ENERGY EFFICIENCY & CONDENSATION CONTROL-TRUSTED FOR OVER 40 YEARS. https://local.armacell.com/fileadmin/cms/uk/products/en/AFArmaFlexClassORangeUKROI.pdf. Accessed: 01-11-2022.

[277] Keysight Technologies. U5309a pcie high-speed digitizer - startup guide. https://www.keysight.com/us/en/assets/9018-04026/quick-start-guides/9018-04026.pdf. Accessed: 16-12-2022.

[278] CAEN Tools for Discovery. N417 8 channel low threshold discriminator. https://www.caen.it/download/?filter=N417. Accessed: 16-12-2022.

[279] Photomultiplier tube R11065-20 | Hamamatsu Photonics. https://www.hamamatsu.com/eu/en/product/optical-sensors/pmt/pmt_tube-alone/head-on-type/R11065-20.html. Accessed: 21-11-2022.

[280] CAEN Tools for Discovery. V6521 6 channel 6 kv/300 μa vme hv power supply module. https://www.caen.it/products/v6521/. Accessed: 18-12-2022.

[281] EMI Electronics. Emi photomultiplier tubes. https://frank.pocnet.net/other/EMI/EMI_Photomultiplier_Tubes_1970.pdf. Accessed: 21-12-2022.

[282] Et enterprises photomultiplier tubes. https://www.javanelec.com/CustomAjax/GetAppDocument/6ca0a372-97f1-4ebf-9009-2db1058d0ce5?type=1&inlineName=True. Accessed: 22-12-2022.

[283] SAINT-GOBAIN CRYSTALS. Scintillation Products, Organic Scintillators. https://seltokphotonics.com/upload/iblock/f5f/f5f21e0ae0abc57430fca2642873553a.pdf. Accessed: 27-12-2022.

[284] Damian Goeldi. *A Novel Liquid Argon Time Projection Chamber Detector: The ArgonCube Concept*. PhD thesis, University of Bern, 4 2018.

[285] Dominic Barker. *Developments Towards a νe CC Sterile Appearance Sensitivity in the Short-Baseline Neutrino Programme*. PhD thesis, The University of Sheffield, 7 2020.

[286] Gianluigi De Geronimo, Alessio D'Andragora, Shaorui Li, Neena Nambiar, Sergio Rescia, Emerson Vernon, Hucheng Chen, Francesco Lanni, Don Makowiecki, Veljko Radeka, Craig Thorn, and Bo Yu. "Front-end ASIC for a liquid argon TPC". In *IEEE Nuclear Science Symposuim & Medical Imaging Conference*, pages 1658–1666, 2010.

[287] arduino. Nano | Arduino Documentation | Arduino Documentation. https://docs.arduino.cc/hardware/nano. Accessed: 03-01-2023.

[288] CAEN Tools for Discovery. V1740-64 Channel 12 bit 62.5 MS/s Digitizer -CAEN-Tools for Discovery. https://www.caen.it/products/v1740/. Accessed: 03-01-2023.

[289] Tektronix. Tektronix mso3054 data sheet. https://www.testequipmenthq.com/datasheets/TEKTRONIX-MSO3054-Datasheet.pdf. Accessed: 05-01-2023.

[290] iseg Spezialelektronik GmbH. Nhq high voltage ps in nim. https://romtek.ro/uploads/products/files/NHQ.pdf. Accessed: 16-12-2022.

[291] J. Sondericker Y. Li and C. Thorn. Omega group noble liquid experiments: A discussion of lar time projection chamber (tpc) technology and cryogenic operating procedures for our tpc experiments. *Tech. Rep. v. 2.0, Brookhaven National Laboratory*, 2013.

[292] Liquid Argon | BOConline UK. https://www.boconline.co.uk/en/gases-and-equipment/bulk-gases/liquid-argon.html. Accessed: 18-01-2023.

[293] R. Brun and F. Rademakers. ROOT - An Object-Oriented Data Analysis Framework. Proceedings AIHENP'96 Workshop, Lausanne, Sep. 1996, Nucl. Inst. & Meth. in Phys. Res. A 389 (1997) 81-86. See also https://root.cern/. Date: 11th April 1997.

[294] SheffieldLAr, KeySight DAQDecoder. https://github.com/SheffieldLAr/LArAnalysis/blob/master/srcs/SubSystems/DAQDecoder/KeySight_DAQDecoder.cc. Accessed: 20-03-2023.

[295] Matthew Thiesse. *Research and Development Toward Massive Liquid Argon Time Projection Chambers for Neutrino Detection*. PhD thesis, The University of Sheffield, 10 2017.

[296] James W Cooley and John W Tukey. An algorithm for the machine calculation of complex fourier series. *ACM*, 1964.

[297] ROOT: TVirtualFFT Class Reference. https://root.cern.ch/doc/master/classTVirtualFFT.html#a68f66680ce0198f6ceddf380b55bedeb. Accessed: 22-03-2023.

[298] SheffieldLAr, FFT Noise Filter. https://github.com/AlaZglam/ShefLArRig/blob/f11e3ac7efba06b518df309d8938038abff3771c/SubSystems/Analysis/SubSystemCRT_FFTNoiseFilter.cc. Accessed: 24-03-2023.

[299] SheffieldLAr, Fast Fourier Transform (FFT). https://github.com/AlaZglam/ShefLArRig/blob/f11e3ac7efba06b518df309d8938038abff3771c/SubSystems/Analysis/SubSystemCRT_FourierTransform.cc. Accessed: 24-03-2023.

[300] SheffieldLAr, Noise Filter-2. https://github.com/AlaZglam/ShefLArRig/blob/f11e3ac7efba06b518df309d8938038abff3771c/SubSystems/Analysis/SubSystemCRT_NoiseFilter.cc. Accessed: 24-03-2023.

[301] V. Chepel and H. Araújo. Liquid noble gas detectors for low energy particle physics. *Journal of Instrumentation*, 8:R04001, 2013.

[302] SheffieldLAr, Pixel Software Trigger. https://github.com/SheffieldLAr/CAENDAQ/blob/3742df1f038084f0962faf75c5664f9bf0b64fb5/PixelDAQ/srcs/DAQConfig.txt. Accessed: 23-03-2023.

[303] SheffieldLAr, Pixel External Trigger. https://github.com/AlaZglam/ShefLArRig/blob/4c8bf3e7255e64dea84fe07d13df9a30bcb0c56f/CAENDAQ/PixelDAQ/srcs/PixelReadout.cc. Accessed: 23-03-2023.

[304] SheffieldLAr, PixelTPC DAQ Decoder. https://github.com/SheffieldLAr/LArAnalysis/blob/8eca644367ce16834985fd21f3ce2e5f6d622720/srcs/TPC/DAQDecoder/PixelTPC_DAQDecoder.cc. Accessed: 24-03-2023.

[305] SheffieldLAr, Pixel + CRT Selection. https://github.com/AlaZglam/ShefLArRig/blob/c5bd714d2071724801f5928154cb6a38e1ceaad2/LArAnalysis/TPC/Analysis/PixelTPC_PixelAndCRTsSelection.cc. Accessed: 25-03-2023.

[306] S Amoruso et al. Article in press analysis of the liquid argon purity in the icarus t600 tpc. *Nuclear Instruments and Methods in Physics Research A*, 516:68–79, 2004.

[307] The MicroBooNE Collaboration. A measurement of the attenuation of drifting electrons in the microboone lartpc. 2017.

[308] S. Rice H. Schnyders and L. Meyer. Electron drift velocities in liquefied argon and krypton at low electric field strengths. *Physical review*, 150, 1966.

Appendix A

Flux Parameters Systematic Uncertainties

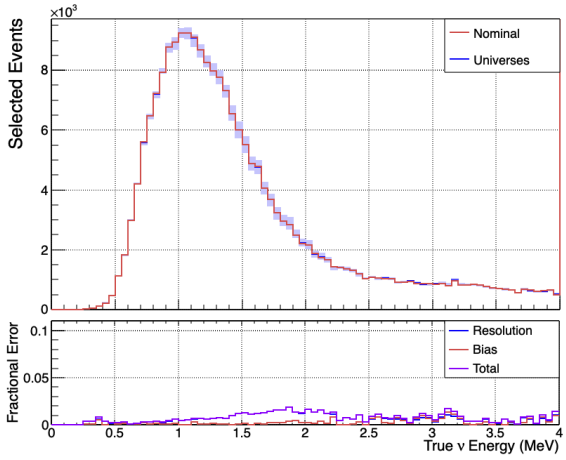

(a) Horn Current

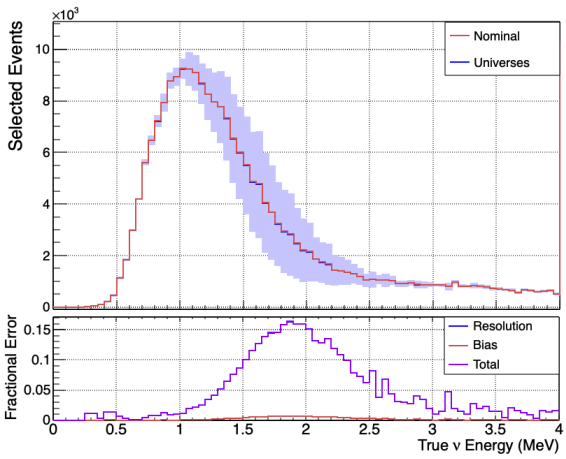

(b) Skin Current

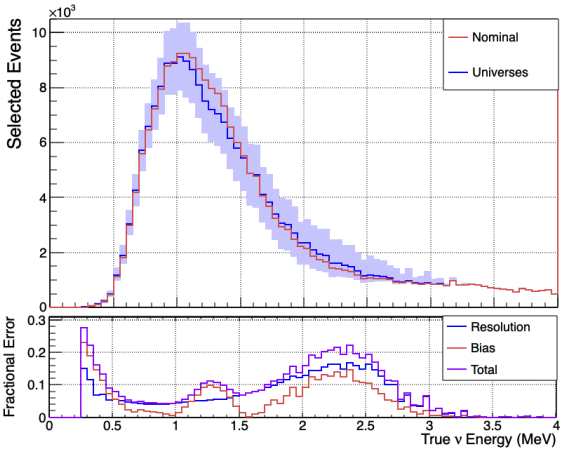

(c) σ_{π^+}

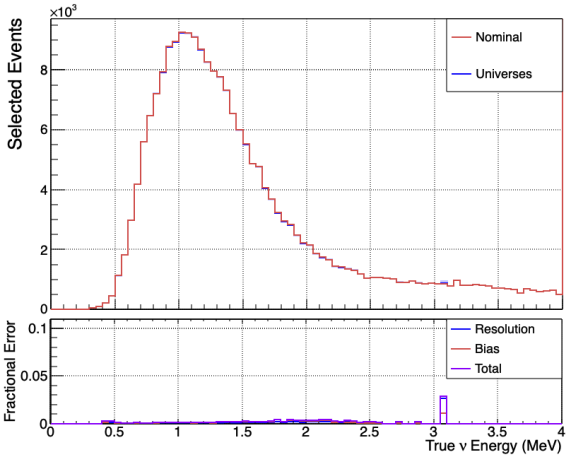

(d) σ_{π^-}

Figure A.1: The distribution of selected events with flux parameters systematic errors as a function of neutrino energy, including fractional uncertainty across universes shown below, split into resolution and bias, added in quadrature for the total.

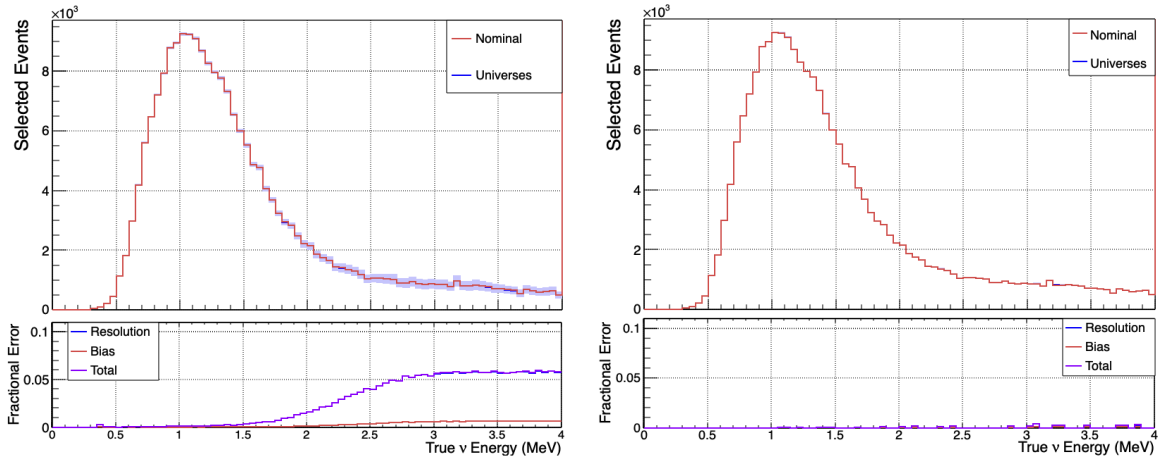

(a) σ_{K^+} (b) σ_{K^-}

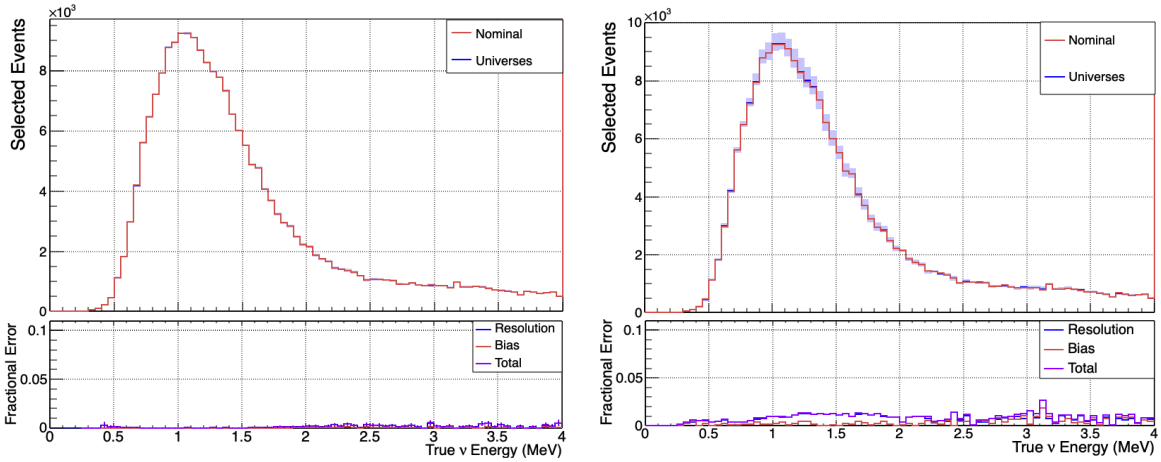

(c) σ_{K^0} (d) σ^{π}_{Tot}

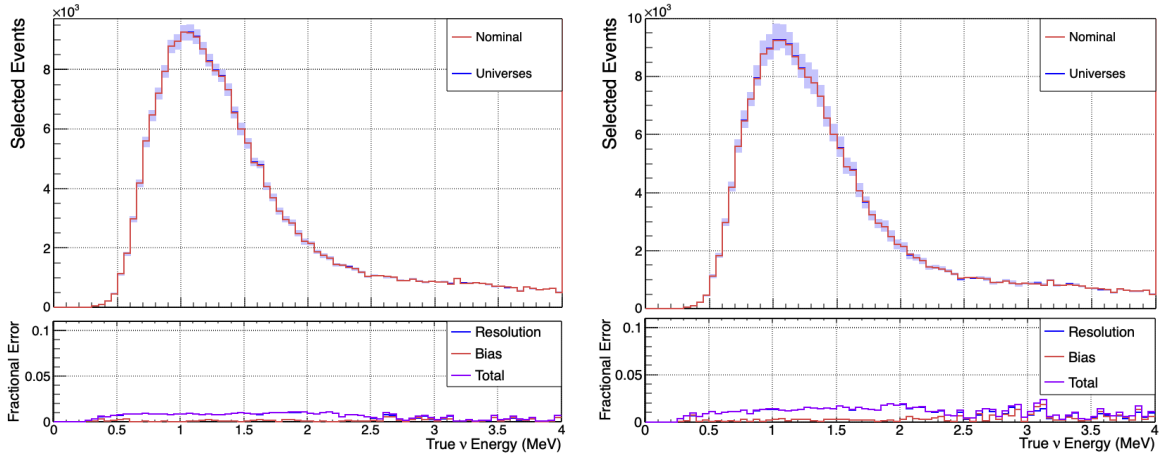

(e) σ^{π}_{QE} (f) σ^{π}_{Int}

Figure A.2: The distribution of selected events with flux parameters systematic errors as a function of neutrino energy, including fractional uncertainty across universes shown below, split into resolution and bias, added in quadrature for the total.

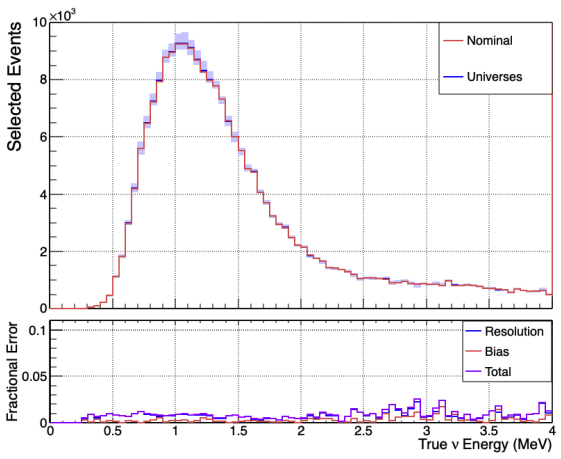

(a) σ^n_{Tot}

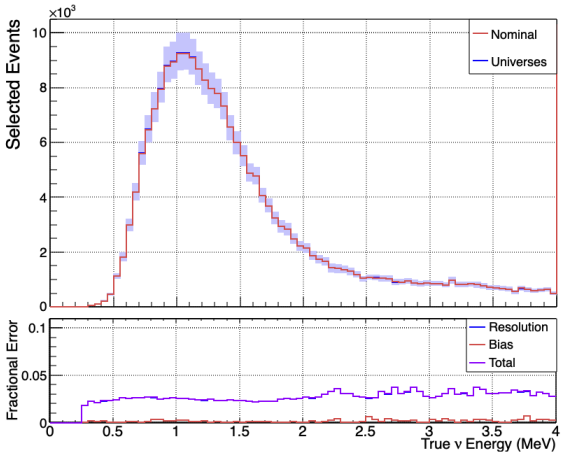

(b) σ^n_{QE}

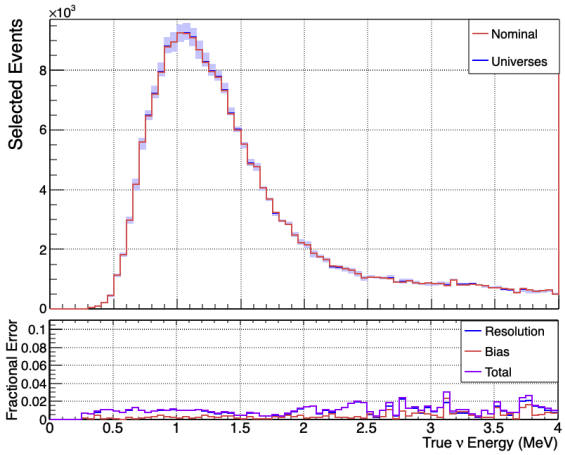

(c) σ^n_{Int}

Figure A.3: The distribution of selected events with flux parameters systematic errors as a function of neutrino energy, including fractional uncertainty across universes shown below, split into resolution and bias, added in quadrature for the total.

Appendix B

Interaction Parameters Uncertainties

Parameter	Description	$\sigma P/P$	Figure
	Axial Mass		
M_A^{CCQE}	CC Quasi-Elastic	$\pm 10\%$	FIG B.1a
M_A^{CCRES}	CC Resonant	$\pm 20\%$	FIG B.1b
M_A^{NCEL}	NC Elastic	$\pm 25\%$	FIG B.1c
M_A^{NCRES}	NC Resonant	$\pm 20\%$	FIG B.1d
$M_A^{COH}\pi$	CC/NC coherent π production	$\pm 50\%$	
	Vector Mass		
M_V^{NCRES}	NC Resonant	$\pm 10\%$	FIG B.1e
M_V^{CCRES}	CC Resonant	$\pm 10\%$	FIG B.1f
	Non-Resonant Background Normalisation		
$NR_{Bk}^{\nu p,CC1\pi}$	$\nu - p\ CC\ 1\pi$	$\pm 50\%$	FIG B.2a
$NR_{Bk}^{\nu n,CC1\pi}$	$\nu - n\ CC\ 1\pi$	$\pm 50\%$	FIG B.2b
$NR_{Bk}^{\nu p,CC2\pi}$	$\nu - p\ CC\ 2\pi$	$\pm 50\%$	FIG B.2c
$NR_{Bk}^{\nu n,CC2\pi}$	$\nu - n\ CC\ 2\pi$	$\pm 50\%$	FIG B.2d
$NR_{Bk}^{\nu p,NC1\pi}$	$\nu - p\ NC\ 1\pi$	$\pm 50\%$	FIG B.2e
$NR_{Bk}^{\nu n,NC1\pi}$	$\nu - n\ NC\ 1\pi$	$\pm 50\%$	FIG B.2f
$NR_{Bk}^{\nu p,NC2\pi}$	$\nu - p\ NC\ 2\pi$	$\pm 50\%$	FIG B.3a
$NR_{Bk}^{\nu n,NC2\pi}$	$\nu - n\ NC\ 2\pi$	$\pm 50\%$	FIG B.3b
$NR_{Bk}^{\overline{\nu} p,CC1\pi}$	$\overline{\nu} - p\ CC\ 1\pi$	$\pm 50\%$	FIG B.3c
$NR_{Bk}^{\overline{\nu} n,CC1\pi}$	$\overline{\nu} - n\ CC\ 1\pi$	$\pm 50\%$	FIG B.3d
$NR_{Bk}^{\overline{\nu} p,CC2\pi}$	$\overline{\nu} - p\ CC\ 2\pi$	$\pm 50\%$	FIG B.3e
$NR_{Bk}^{\overline{\nu} n,CC2\pi}$	$\overline{\nu} - n\ CC\ 2\pi$	$\pm 50\%$	FIG B.3f
$NR_{Bk}^{\overline{\nu} p,NC1\pi}$	$\overline{\nu} - p\ NC\ 1\pi$	$\pm 50\%$	FIG B.4a
$NR_{Bk}^{\overline{\nu} n,NC1\pi}$	$\overline{\nu} - n\ NC\ 1\pi$	$\pm 50\%$	FIG B.4b
$NR_{Bk}^{\overline{\nu} p,NC2\pi}$	$\overline{\nu} - p\ NC\ 2\pi$	$\pm 50\%$	FIG B.4c
$NR_{Bk}^{\overline{\nu} n,NC2\pi}$	$\overline{\nu} - n\ NC\ 2\pi$	$\pm 50\%$	FIG B.4d

For Nucleons			
x^N_{abs}	Intranuclear absorption probability	$\pm$20%	FIG B.4e
x^N_{CEx}	Intranuclear Charge Exchange probability	$\pm$50%	FIG B.4f
x^N_{El}	Intranuclear Elastic probability for nucleons	$\pm$30%	
x^N_{Ine}	Intranuclear Inelastic scatter probability	$\pm$40%	FIG B.5a
x^N_{mfp}	Intranuclear Nucleon mean free path	$\pm$20%	FIG B.5b
x^N_{π}	Nucleon π-production probability	$\pm$20%	FIG B.5c
For Pions			
x^{π}_{abs}	Intranuclear absorption probability	$\pm$20%	FIG B.5d
x^{π}_{CEx}	Intranuclear Charge Exchange probability	$\pm$50%	FIG B.5e
$xEl\pi$	Intranuclear Elastic probability for nucleons	$\pm$10%	
$xIne\pi$	Intranuclear Inelastic scatter probability	$\pm$40%	FIG B.5f
$xmfp\pi$	π mean free path	$\pm$20%	FIG B.6a
$x\pi\pi$	π π-production probability	$\pm$20%	FIG B.6b
Other			
η^{NCEL}	Strange axil form factor η for NC Elastic	$\pm$30%	FIG B.6c
A^{BY}_{HT}	A_{HT} twist parameter in Bodek-Yang model	$\pm$25%	FIG B.6d
B^{BY}_{HT}	B_{HT} twist parameter in Bodek-Yang model	$\pm$25%	FIG B.6e
$R^{COH}_0\pi$	Parameter controlling π absorption in RS model	$\pm$10%	
C^{BY}_{V1u}	C_{V1u} u valence GRV98 PDF correction parameter	$\pm$30%	FIG B.6f
C^{BY}_{V2u}	C_{V2u} u valence GRV98 PDF correction parameter	$\pm$40%	FIG B.7a

Table B.1: Interaction systematic uncertainties provided by GENIE [3].

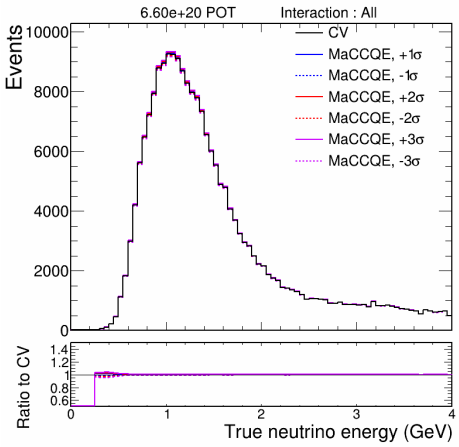

(a) M_A^{CCQE}

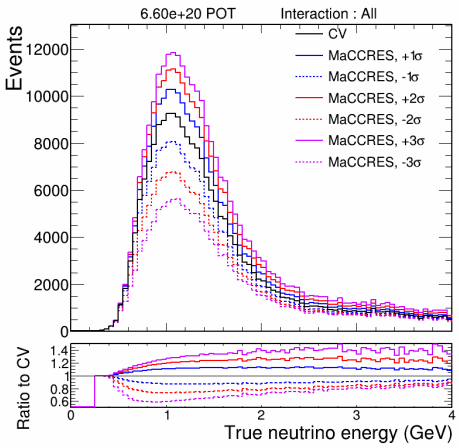

(b) M_A^{CCRES}

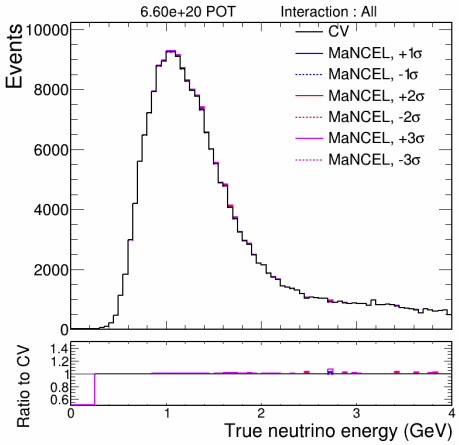

(c) M_A^{NCEL}

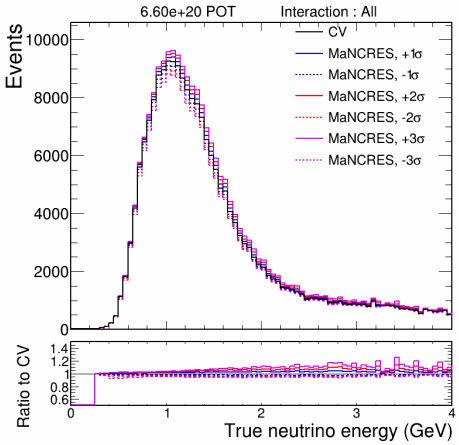

(d) M_A^{NCRES}

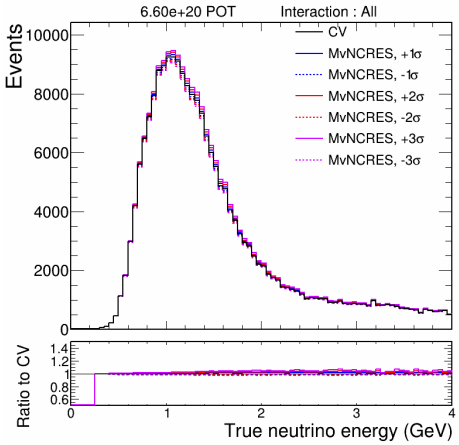

(e) M_V^{NCRES}

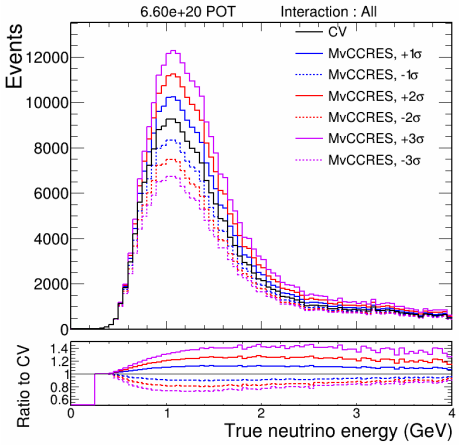

(f) M_V^{CCRES}

Figure B.1: The distribution of selected events with interaction parameters systematic errors as a function of neutrino energy.

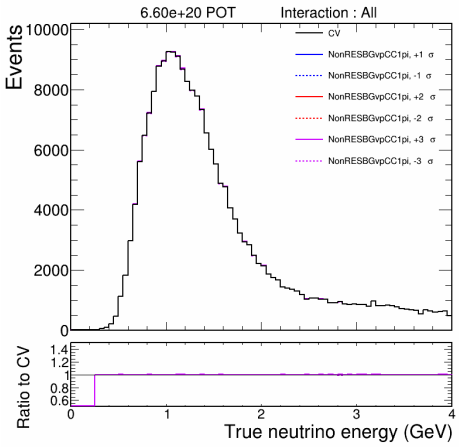

(a) $NR_{Bk}^{\nu p,CC1\pi}$

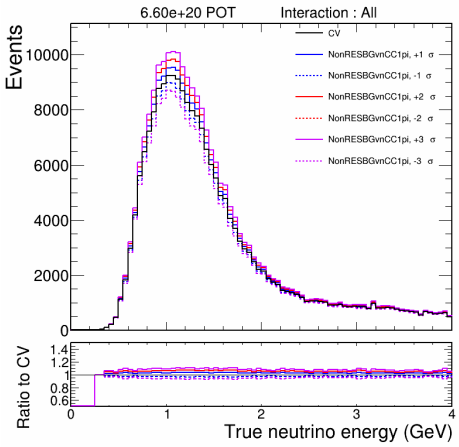

(b) $NR_{Bk}^{\nu n,CC1\pi}$

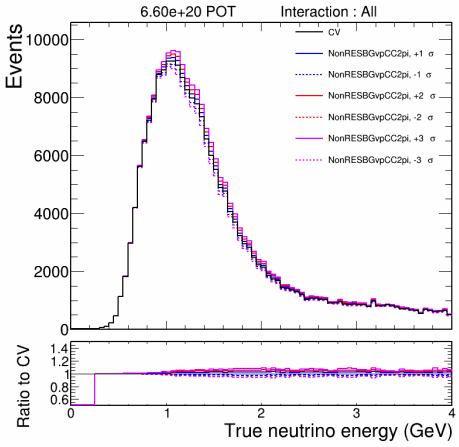

(c) $NR_{Bk}^{\nu p,CC2\pi}$

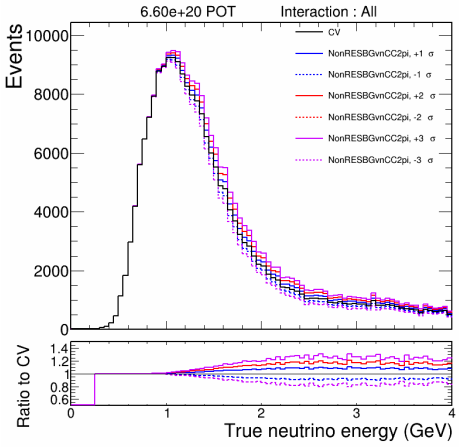

(d) $NR_{Bk}^{\nu n,CC2\pi}$

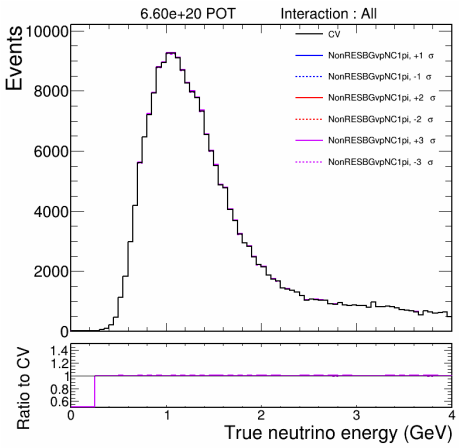

(e) $NR_{Bk}^{\nu p,NC1\pi}$

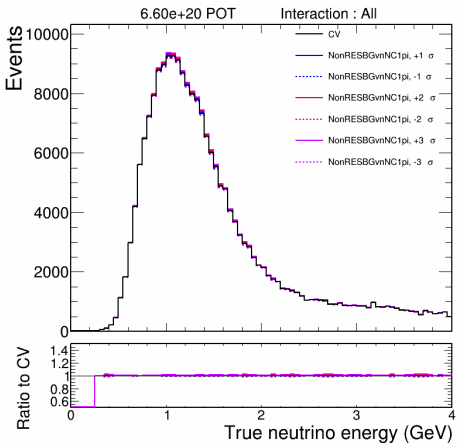

(f) $NR_{Bk}^{\nu n,NC1\pi}$

Figure B.2: The distribution of selected events with interaction parameters systematic errors as a function of neutrino energy.

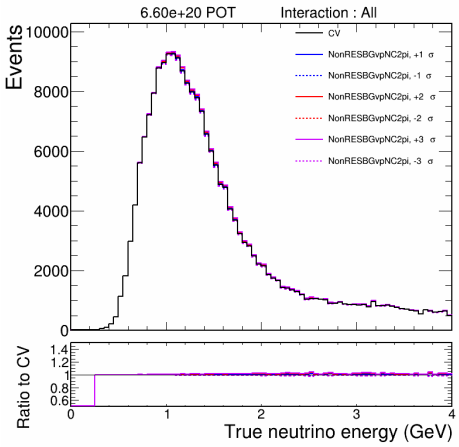

(a) $NR_{Bk}^{\nu p,NC2\pi}$

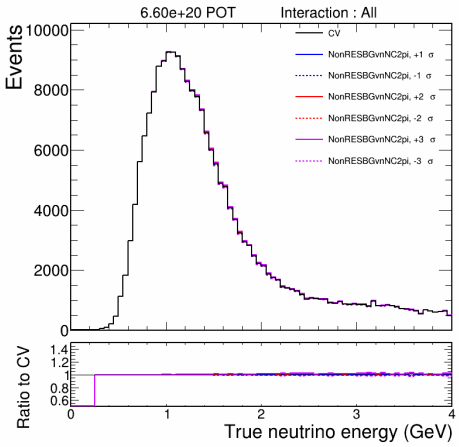

(b) $NR_{Bk}^{\nu n,NC2\pi}$

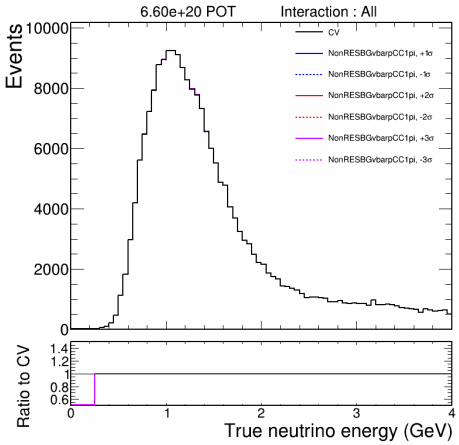

(c) $NR_{Bk}^{\overline{\nu}p,CC1\pi}$

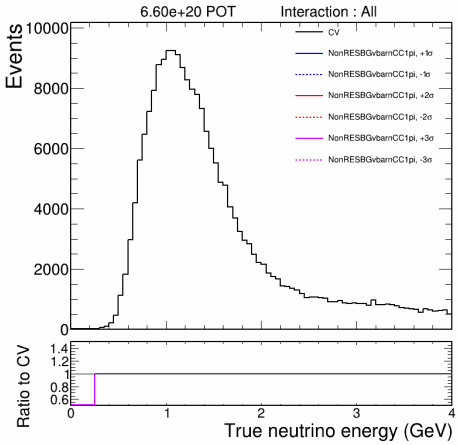

(d) $NR_{Bk}^{\overline{\nu}n,CC1\pi}$

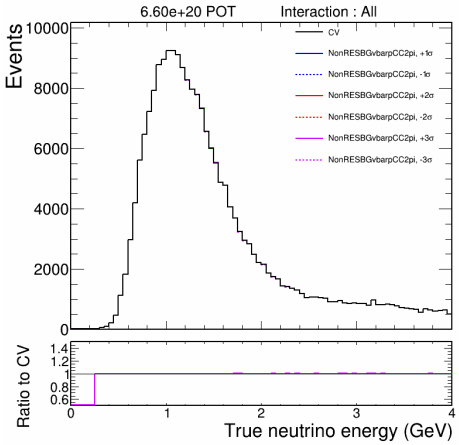

(e) $NR_{Bk}^{\overline{\nu}p,CC2\pi}$

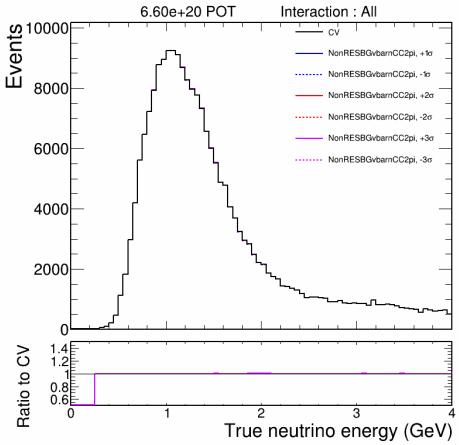

(f) $NR_{Bk}^{\overline{\nu}n,CC2\pi}$

Figure B.3: The distribution of selected events with interaction parameters systematic errors as a function of neutrino energy.

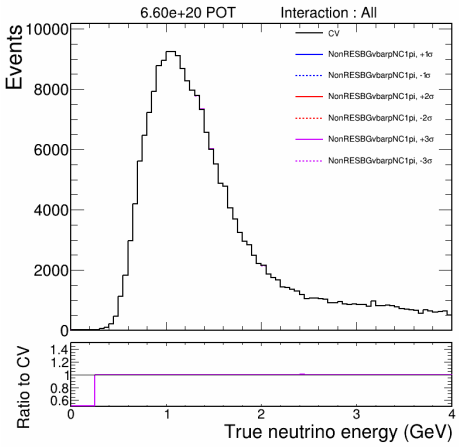

(a) $NR_{Bk}^{\overline{\nu}p,NC1\pi}$

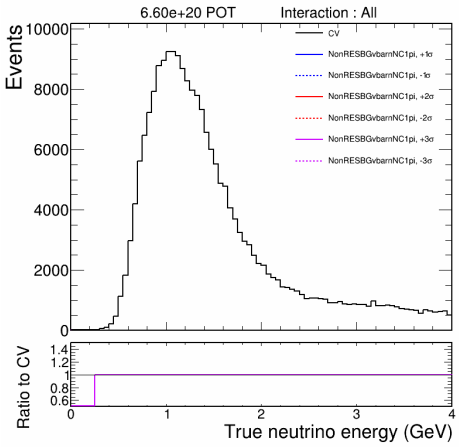

(b) $NR_{Bk}^{\overline{\nu}n,NC1\pi}$

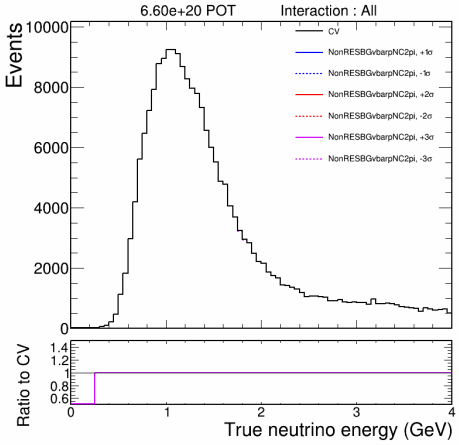

(c) $NR_{Bk}^{\overline{\nu}p,NC2\pi}$

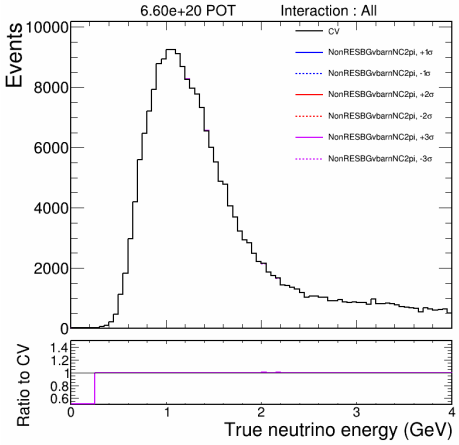

(d) $NR_{Bk}^{\overline{\nu}n,NC2\pi}$

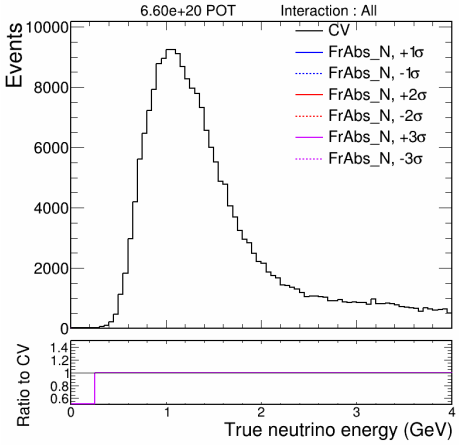

(e) x_{abs}^{N}

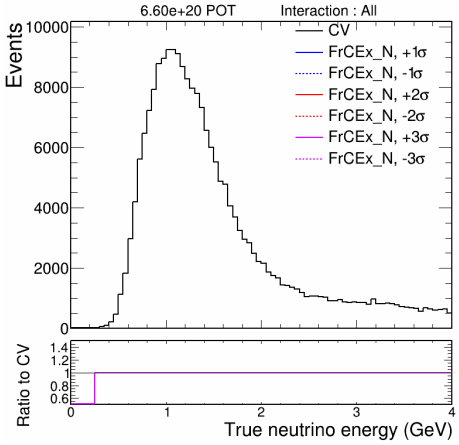

(f) x_{CEx}^{N}

Figure B.4: The distribution of selected events with interaction parameters systematic errors as a function of neutrino energy.

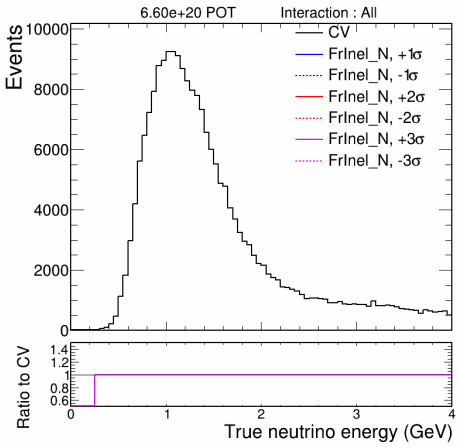

(a) x^N_{Ine}

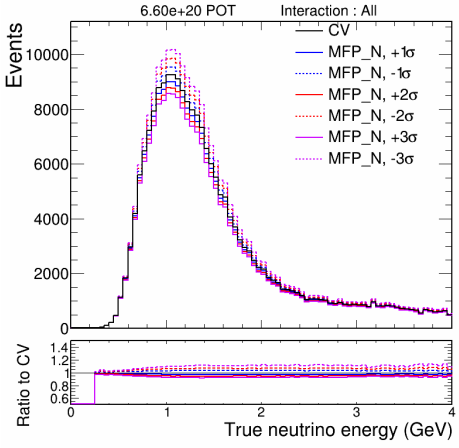

(b) x^N_{mfp}

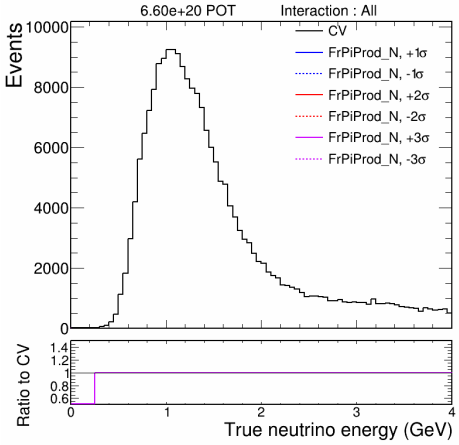

(c) x^N_{π}

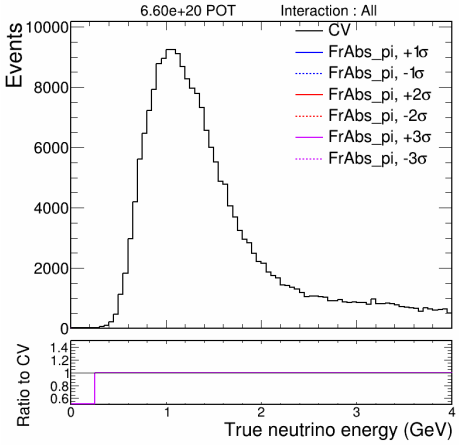

(d) x^{π}_{abs}

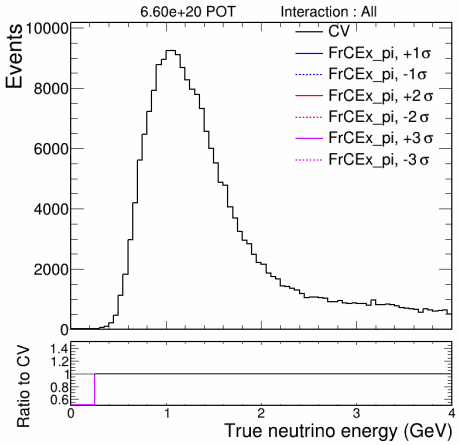

(e) x^{π}_{CEx}

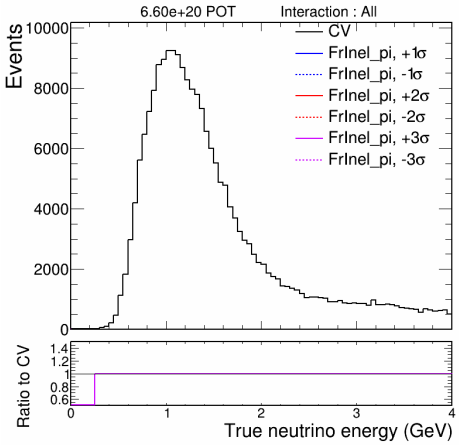

(f) $xIne\pi$

Figure B.5: The distribution of selected events with interaction parameters systematic errors as a function of neutrino energy.

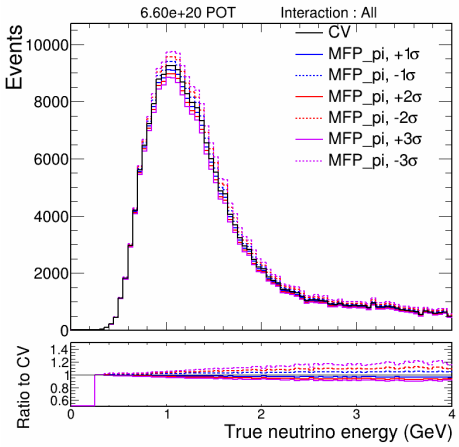

(a) $xmfp\pi$

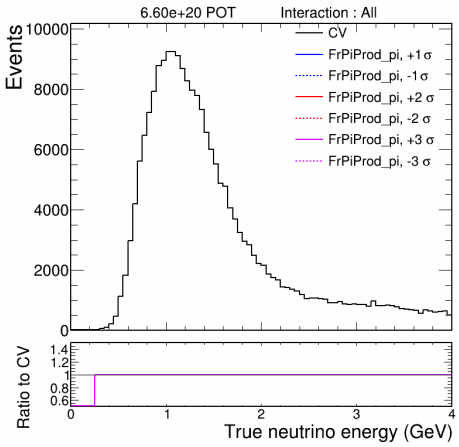

(b) $x\pi\pi$

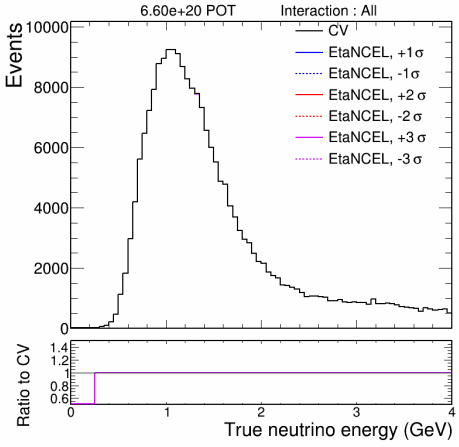

(c) η^{NCEL}

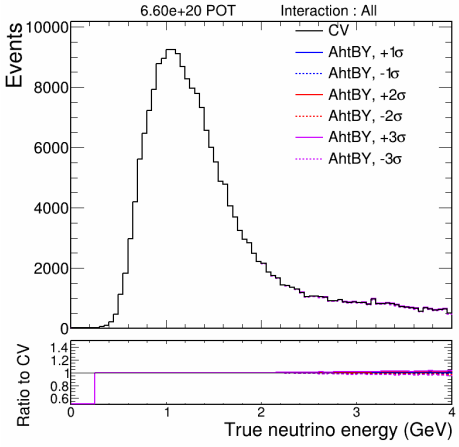

(d) A_{HT}^{BY}

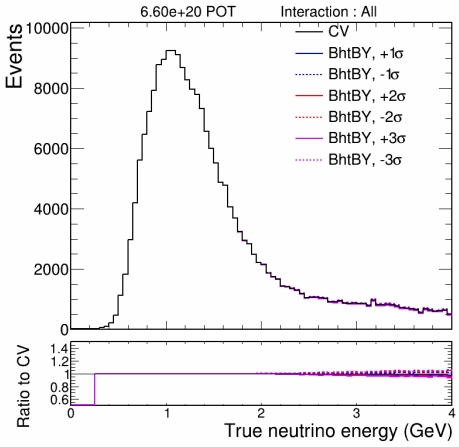

(e) B_{HT}^{BY}

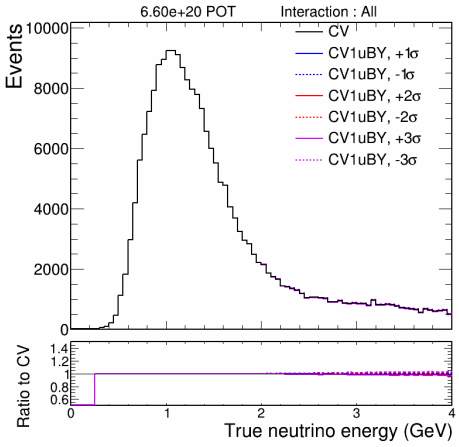

(f) C_{V1u}^{BY}

Figure B.6: The distribution of selected events with interaction parameters systematic errors as a function of neutrino energy.

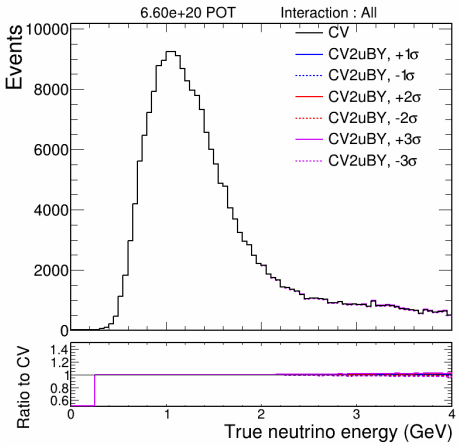

(a) C_{V2u}^{BY}

Figure B.7: The distribution of selected events with interaction parameters systematic errors as a function of neutrino energy.